Ab initio Molecular Dynamics Simulations of Storage Pond Radionuclides and Related Ions

Olivia Lynes

Thesis submitted for the Degree of

Doctor of Philosophy

September 2018

Lancaster University

Department of Chemistry

Supervisor:

Andrew Kerridge

Industrial Supervisor:

Jonathan Austin (NNL)

I, Olivia Lynes, confirm that the work presented in this thesis is my own work, and has not been submitted for the award of a higher degree elsewhere. Where information has been derived from other sources, I confirm that this has been indicated in the thesis. In addition, I confirm that this thesis does not exceed the permitted maximum length.

Abstract

An important problem in the nuclear power industry in the UK is the reprocessing of the legacy waste storage ponds at Sellafield in Cumbria. Understanding the solvation structure of the ions present in these ponds, as well as the stability of their hydroxide complexes, is vital for effective clean-up.

This work used *ab initio* molecular dynamics (AIMD) to characterise the solvation structure of Mg^{2+}, Ca^{2+}, Sr^{2+}, Cs^{+}, U^{6+} in the form of uranyl (UO_2^{2+}), La^{3+} and Lu^{3+}. These ions have been found in the legacy storage ponds and have previously been studied through gas phase or implicit solvation Density Functional Theory (DFT) methods. The properties of the first solvation shell have been categorised, and when compared to current experimental and computational literature the results are in excellent agreement, justifying the solvation model developed.

The understanding of the solvation structure of the ions in the storage ponds has been developed further, with the introduction of hydroxide ions to replicate the storage ponds alkaline conditions. The coordination and bonding of the hydroxide complexes was characterised, as was the proton transfer behaviour, through quantifying the Proton Transfer Events (PTEs) of each system. The introduction of hydroxides generally led to reduction in coordination number and bond length of the first solvation shell. It was found that PTEs were more prevalent away from the central ion of the system and occurred more frequently in the less charge dense ionic systems, where direct hydroxide coordination to the ion is less prevalent.

The final focus of the work was a DFT examination of the adsorption of Sr^{2+} onto a solvated $CeO_2(111)$ surface. The results showed a preference for some ion coordination to the surface, which lessened when hydroxide ions were introduced to the solvation model. The aim of this chapter was to investigate the validity of the surface-solvation model using a surface relevant to the nuclear waste disposal problem for use in future AIMD simulations of the fuel pond environment.

Acknowledgements

My first and greatest thanks go to Andy Kerridge, for the chance to do this research and for the last four years of seemingly unending patience and support. This research wouldn't have been possible without your ideas, our weekly meetings and the months trying to figure out how it all worked.

I would also like to thank Abi Trewin, my secondary supervisor at Lancaster, Jonathan Austin, my industrial supervisor, as well as Michael Peach and the rest of the CTC for the many useful discussions over the years. Additionally, I am grateful to the DISTINCTIVE consortium for their support, funding and the many opportunities to hone my presentation and poster making skills at various conferences and group meetings.

The work presented in this thesis would not have been possible without the HEC at Lancaster University and my thanks go to Mike Pacey for its maintenance, as well as the installation of CP2K and the continued updates.

To all the friends and family who have continually asked if I'm done yet, provided words of encouragement and listening ears. Thank you for your patience, this is finally it.

Lastly to Izaak, for agreeing to move to Lancaster in the first place so I could do this (then agreeing to move back again!), for all the hours of support and the copious amounts of M&Ms. Thank you for ensuring you wouldn't be the only one with a PhD.

Contents

List of Figures

List of Tables

Chapter 1: Introduction

Nuclear power has been a reliable source of low carbon electricity in the UK for over 60 years, and the government has remained committed to including nuclear power in efforts to ensure the 2050 targets for lower CO_2 emissions are met.[1] The storage and long term disposal of nuclear waste remains an issue across the UK, as does the decommissioning of nuclear sites, altogether amounting to costs of ~£3 billion annually.[2] On top of this, there is the continued disposing of nuclear waste from operational sites, such as Dungeness B, Hinkley Point and Heysham. The Nuclear Decommissioning Authority (NDA) forecast in 2018 states that future clean-up across the UK will cost £121 billion spread across the next 120 years.[3]

The Sellafield site in Cumbria houses legacy facilities from the early days of the UK's nuclear power program which began in the 1950s and is the UK's main nuclear fuel reprocessing and decommissioning plant. In 2018 the reprocessing of nuclear waste ended at Sellafield, with the complete closure of the Magnox reprocessing plant scheduled for 2020.[4] Part of the legacy of the Sellafield site is the storage ponds and silos where spent nuclear waste, such as used fuel rods, are stored. Over time, a large quantity of sand-like sludge has formed in these storage facilities, which has a varied composition and behaviour. These initial facilities were built with little thought for 'future-proofing' and the records of the contents of these ponds and silos no longer match the contents, further exacerbating this issue.[5] As the ponds are aging, the waste management and future storage of the nuclear waste is a top priority. However, these legacy waste storage ponds pose a difficult decommissioning challenge as the sludge, pond liquor and, indeed, the nuclear waste itself must be removed and dealt with via separate routes.

Working with nuclear waste materials is difficult and requires highly specialised facilities and training. As such, computational methods have become popular amongst the research fields associated with nuclear waste management as it enables research to be done without the risk, and cost, associated with working with radioactive substances. For example, modelling used by Sellafield Ltd and the National Nuclear Laboratory (NNL) provide detailed descriptions of the chemical reactions, speciation and solubility of solids which may exist in the ponds.[6]

The aims of this PhD project were to investigate the dynamics of radionuclides and other ions present in the aqueous environment of the storage ponds, including Mg^{2+}, Ca^{2+}, Sr^{2+}, Cs^{+}, U^{6+} in the form of uranyl (UO_2^{2+}), La^{3+} and Lu^{3+}. The work presented within focusses on the solvation structures of these ions and how they are impacted by the introduction of hydroxide ions, which are present in the ponds due to the high pH of the water. In addition, this thesis

examines the possibility of modelling radionuclide adsorption in an aqueous environment onto a CeO_2(111) mineral surface, to emulate ion adsorption to uranic components of the sludge in the storage ponds.

1.1 Nuclear Waste Problem

95% of the UK's radioactive waste arises from the nuclear power industry, including waste from the enrichment of uranium, making of nuclear fuel and the reprocessing of spent fuel.[7] The total volume of nuclear waste, as per the 2016 NDA inventory, is 132,000 m^3 of which 75% is generated at Sellafield. Nuclear waste is classified according to its level of radioactivity and is either low-level (LLW), intermediate-level (ILW), or high-level (HLW) waste.[7] LLW comprises 90% of the volume of radioactive waste but contributes only 1% of the radioactivity, it does not require shielding and can be disposed of in near surface facilities. ILW requires some shielding, comprises of resins, sludge and contaminated materials and contributes 4% of the radioactivity of waste. HLW contains the fission products and transuranic elements from the burning of uranium fuel and the reactor core, and is responsible for 95% of the total radioactivity.

Radioactive waste from nuclear reactors result from the nuclear fission process, which is used to generate heat, and hence electricity.[8] In the nuclear fission process, ^{235}U is bombarded with neutrons and will capture a free neutron to form ^{236}U, a short lived isotope which will split apart into smaller fission products, releasing neutrons and heat energy.[9,10] If the liberated neutrons then collide with surrounding ^{235}U isotopes, the process repeats and a fission chain reaction occurs.[8,9,11] From a nuclear waste management perspective, understanding the fission products with longer half-lives is crucial as they will be the source of the radioactivity in the waste storage facilities. For example, the fission of ^{235}U results in a ~6% yield of ^{137}Cs ($t_{1/2}$ = 30.2 y)[12] and ^{90}Sr ($t_{1/2}$ = 28.8 y)[12 13] which are among the most abundant radioactive elements in the HLW and ILW, other fission products include minor actinides Np, Am, Cm and lanthanides.[6,13–15]

1.2 Magnox Fuel Reactors

A total of 26 Magnox reactors were built in the UK in the 1950s to 1970s, which were initially designed to run for only 20 years. However, most ran for twice as long, with the last reactor shutting down in 2015.[16–19] Magnox reactors used unenriched uranium metal as the fuel source, containing around 0.7% ^{235}U, which was cast and machined into rods.[11] The uranium rods were sealed with an external cladding made from a magnesium aluminium alloy called

Magnox (Magnesium Non-Oxidising).[7] The composition of the alloy used varied, for example the A12 alloy was composed of between 0.7 and 0.9 % aluminium, while the ZA alloy was composed of between 0.45 and 0.65 % zirconium, though both had a magnesium content of up to 90%.[20–22] The fully formed fuel rods were loaded into vertical channels in a graphite block core which was cooled by blowing pressurised carbon dioxide (CO_2) gas past the fuel cans. The gas carried the heat from the reactor core to heat exchangers which generated steam to power turbines which generated then electricity.[7] A typical fuel rod is depicted in **Figure 1.1**, the shape of the cladding was often ribbed or finned to improve heat transfer to coolant gas in the reactor.[11]

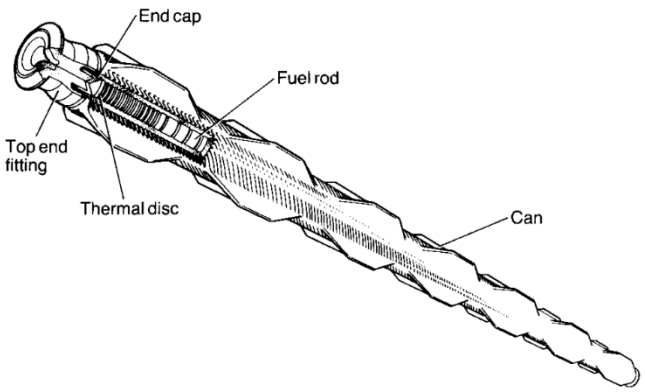

Figure 1.1: Typical magnox fuel element[7]

In a Magnox reactor the fuel rod has a useful life of 5 to 7 years before it must be replaced. Upon removal from the reactor, fuel rods were stored in underwater cooling ponds at the reactor site for a minimum of 90 days to allow the short-lived radioactivity to decay and heat generation to reduce. After the 90 days, the rods were packed into flasks of thick steel and transported to the Magnox reprocessing plant at Sellafield where they were housed in storage ponds to await reprocessing.[7]

The use of Magnox alloys as cladding came with drawbacks, namely a lower operating temperature compared to other alloys. At temperatures higher than 500 °C the grain structure of Magnox changes and there is a loss of strength impacting cladding integrity.[11,18,20] Another downside of the Magnox cladding is its tendency to corrode in water. The main product of cladding corrosion is magnesium hydroxide $(MgOH)_2$, or brucite, which is soluble at neutral and acidic pHs.[23,24] Excessive corrosion of the Magnox cladding would result in the exposure of the uranium fuel rod in the storage ponds. To overcome these difficulties, later reactors used stainless steel cladding and a uranium dioxide fuel which increased the possible

operating temperatures to 650 °C and as such made the reactors more efficient, with a higher power output, reducing capital costs.[25]

1.3 First Generation Magnox Storage Ponds

The Magnox fuel reprocessing plant at Sellafield in Cumbria began operations in 1964 after the First Generation Magnox Storage Ponds (FGMSP) were constructed in the 1950s[26], a recent image of the FGMSP is shown in **Figure 1.2**.[27] The FGMSP are open air, reinforced concrete structures filled with water to act as a radioactivity shield.[26] The storage ponds are dosed with NaOH to maintain a pH range of 10 to 12 to inhibit the corrosion of the Magnox cladding.[22–24,28] Fuel was transported from the reactor sites and transferred to the FGMSP for cooling and storage while awaiting reprocessing.[7,26,29]

Figure 1.2: Sellafield's First-Generation Magnox Storage Pond[27]

The corrosion of the Magnox cladding was accelerated by a long period of reprocessing shutdown in the 1970s, variation outside of ideal pond pH, and the continued addition of spent fuel into the 1990s. As a result, a layer of Corroded Magnox Sludge (CMS) has formed at the base of the ponds, made up of significant quantities of waste materials, fuel fragments, and fuel skips as well as organic matter which has fallen or been blown into the ponds.[7] Currently around 1000 to 2000 m^3 of the waste housed at Sellafield is defined as sludge.[30]

The legacy storage ponds are an aging facility and continue to degrade. The nuclear fuel, sludge, ILW and pond water contained within all need to be safely removed and either processed or sent for long term storage through separate routes.[7,26,30,31] The processing route of the waste depends on the radioactivity content and the chemical speciation of the waste,

i.e. whether the radioactive ion is found in the solid phase of the storage ponds or the liquid phase. Currently, the main disposal method for ILW waste is cement encapsulation in 500 litre drums, which will then be transferred to a purpose built store in a geological disposal facility.[7]

The approximate elemental composition of a single sample of CMS was reported by the NNL[32,33] and contained 12.9% Mg, 4.28 % U and 0.18% Ca, as well as ~2.64% of other elements including Al, Na, Fe, Ba, Zn, B, Cu and Si, with the remainder being water. This sludge sample was taken from the 'main pond area' of the FGMSP, rather than the more contaminated areas or the skips held inside the ponds. The sludge sample was analysed by Gregson *et al*.[34] who identified the solid phase as mainly brucite, a mineral which readily adsorbs radionuclides and other ions which are present in the liquor[31,35,36], as well as solid uranium oxide particles typically formed from the oxidation of the fuel rod.

Based on the sample analysed by Gregson *et al*.[34] and knowledge of the nuclear fission process the primary radionuclides across the different storage ponds are thought to be ^{238}U and its two fission products, ^{137}Cs, ^{90}Sr, as well as much smaller amounts of U^{235} and trace U^{232} and U^{236}.[6,37] The ions in the ponds exist as both aquo and hydroxide complexes, as well other species such as carbonates.[6,34,38] In an aqueous environment, uranium readily forms the highly soluble uranyl ion (UO_2^{2+}) which most likely will be present in both the liquid and solid phase, as well as forming uranium hydride (UH_3) and releasing diatomic hydrogen(H_2).[34] The ground water outside the legacy storage ponds and in the surrounding areas of Sellafield have been shown to contain ^{137}Cs, ^{90}Sr and UO_2^{2+}, these ions have also been found at other reactor sites as well as in the cooling water of damaged power plants such as Fukushima Daiichi.[39–44]

The leaching of products of the nuclear fuel cycle into the groundwater surrounding Sellafield poses a risk to both the environment and human health.[45,46] Both ^{137}Cs and ^{90}Sr are water soluble, however ^{137}Cs binds strongly to soil so is less likely to move through the groundwater than ^{90}Sr.[47] Due to the biochemical behaviour similarity of Sr^{2+} to Ca^{2+} it easily deposits in bones, bone marrow and teeth and its build up can cause cancer in humans.[37,48–50] The radioactive ^{137}Cs is also a risk to human health, where upon ingestion it evenly distributes through the body with the highest concentrations found in soft tissue.[51]

Understanding the solvation structure of the different species in the legacy storage ponds and how they are affected by changes in pond conditions, such as pH, can help inform the nuclear waste clean-up process. Many of the radionuclides listed above have been well studied in previous computational investigations, however information on how the dynamics and

presence of bulk water impacts their solvation is sparse. The focus of this PhD thesis is to build on this foundation of understanding regarding these ions and expand it in a novel way.

An overview of the theory which underpins the computational calculations used in this thesis is given in **Chapter 2**. The investigation into the solvation structure of the alkaline earth metals Mg^{2+}, Ca^{2+} and Sr^{2+} using *ab initio* Molecular Dynamics (AIMD), along with a justification for the analysis methodology used throughout the thesis, is given in **Chapter 3**. The focus of the work then turns to the impact of hydroxides on the solvation structure of the alkaline earth metals in **Chapter 4**, including an in-depth explanation of the analysis of hydroxide environments and how proton transport is quantified. The investigation of the more complex uranyl ion (UO_2^{2+}) and the results of AIMD simulations of its solvation structure in an aquo, monohydroxide and dihydroxide environment are summarised in **Chapter 5**. The work detailed in **Chapter 6** investigates solvation structure and hydroxide complexation as a function of increasing cation charge, examining the ions Sr^{2+}, Cs^{+}, La^{3+} and Lu^{3+}. Specifically, the monohydroxide environment of Sr^{2+}, the aquo and monohydroxide environments of Cs^{+} and the aqueous and trihydroxide environments of the lanthanides La^{3+} and Lu^{3+} are examined. Finally, in **Chapter 7** the viability of modelling Sr^{2+} adsorption on a CeO_2(111) surface, analogous to the UO_2 surface, is explored. The work in this chapter uses DFT geometry optimisations, rather than AIMD, on a 4x3x2 CeO_2(111) surface with a water model of 32 waters. In this final chapter ion adsorption of Sr^{2+} ion and the impact of hydroxide ions on the ion adsorption is investigated.

1.4 Aims and Objectives

Understanding the interactions of the chemical species held within the legacy waste storage ponds at Sellafield is key for the development of strategies for the continued storage and disposal of nuclear waste. This research project aims to investigate the dynamic behaviour and structure of various radionuclides and ions present in the legacy waste storage ponds at Sellafield. It also aims to examine the impact of hydroxide ions as a proxy for increasing pH has on the solvation structure of the ions of interest. Finally, the research will focus on investigating how a mineral surface interacts with the ions of interest.

In order to fulfil the research aims *ab initio* molecular dynamics (AIMD) will be used in all calculations relating to the dynamics of solvation structure, and density functional theory (DFT) will be used to investigate the energetic favourability of surface ion interactions. Initially the solvation structure of Mg^{2+}, Ca^{2+}, Sr^{2+} in an aqueous environment will be characterised to benchmark the methodology against existing literature. Then hydroxide ions will be included

in the alkaline earth metal aqueous environment to examine the impact of increasing pH on the solvation structure. The investigation into the effects of increasing pH on the solvation structure of ions will be broadened to include more complex ions including Cs^{+}, UO_2^{2+}, La^{3+} and Lu^{3+}.

Finally, a model surface of CeO_2(111) will be optimised to investigate the interactions between water, hydroxide ions and previously investigated radionuclides with the mineral surface, to ascertain which environments are most energetically favourable. It is intended that the research findings will inform the nuclear industry on the speciation of various ions in the nuclear waste storage ponds and provide an insight into how the ions are likely to behave in proximity to a mineral surface.

Chapter 2: Methodology

This chapter provides an overview of the quantum chemical theory and computational techniques used in the work given. For a more in-depth derivation of these techniques the reader is directed to the referenced sources.

2.1 Bra-Ket Notation

In parts of this chapter, where necessary, bra-ket notation is used to describe the quantum states using the following abbreviations:

$$\langle f| = f^*(\mathbf{a}) \quad ('bra') \qquad \textbf{Eq. 2.1}$$

$$|f\rangle = f(\mathbf{a}) \quad ('ket') \qquad \textbf{Eq. 2.2}$$

For every vector ket there is a bra which corresponds to its complex conjugate. The combination of a bra and a ket describes the overlap of states, for example:

$$\langle \Psi|\Psi\rangle = \int \Psi^*(\mathbf{a})\Psi(\mathbf{a})\, d\mathbf{a} \qquad \textbf{Eq. 2.3}$$

Using bra-ket notation the expectation value of an observable represented by an operator $\hat{A}$ for a system in the state $|\Psi\rangle$ is:

$$\langle \Psi|\hat{A}|\Psi\rangle \qquad \textbf{Eq. 2.4}$$

2.2 The Schrödinger Equation

In order to solve the wavefunction for a given system, the time-independent Schrödinger equation must be solved, which is as follows:[52]

$$\hat{H}\Psi = E\Psi \qquad \textbf{Eq. 2.5}$$

where $\hat{H}$ is the Hamiltonian operator and E is the energy of the system represented by the wavefunction, Ψ. It is possible to calculate the exact solution for a single electron system, i.e. a hydrogen atom,[53] but for a many electron system the Schrödinger equation is impossible to solve. Hence it is necessary to make approximations to solve the Schrödinger equation in order to evaluate the ground state of a many electron system. Two examples of quantum chemical approaches to approximating the solution to the Schrödinger equation are Hartree-Fock theory and Density Functional theory (DFT), which are discussed in **Sections 2.9** and **2.10**.

2.3 The Hamiltonian

The Hamiltonian, $\widehat{H}$, is an operator corresponding to the total energy of the system and is defined explicitly in terms of kinetic, $\hat{T}$, and potential energy, $\hat{V}$, operators:

$$\widehat{H} = \hat{T} + \hat{V} \qquad \textbf{Eq. 2.6}$$

where the kinetic energy operator, $\hat{T}$, for a molecular system is defined as:

$$\hat{T} = -\frac{\hbar^2}{2m}\sum_{i}^{n}\nabla_i^2 - \sum_{A}\frac{1}{2m_A}\nabla_A^2 \qquad \textbf{Eq. 2.7}$$

where i indicates that the operator only acts on the ith electron, $\hbar$ is the reduced Planck's constant, A indexes the nucleus, m is the mass of an electron, and ∇_i^2 is the Laplacian operator defined as:

$$\nabla_i^2 = \frac{\partial^2}{\partial {x_i}^2} + \frac{\partial^2}{\partial {y_i}^2} + \frac{\partial^2}{\partial {z_i}^2} \qquad \textbf{Eq. 2.8}$$

The potential energy operator, $\hat{V}$, can be further defined as the sum of the terms of the electron-electron interactions, $\hat{V}_{ee}$, nuclear-nuclear interactions, $\hat{V}_{nn}$, and electron-nuclear interactions, $\hat{V}_{ne}$. Which are defined as follows:

$$\hat{V}_{ee} = \frac{1}{4\pi\varepsilon_0}\sum_{i}\sum_{j>i}\frac{e^2}{\mathbf{r}_{i,j}} \qquad \textbf{Eq. 2.9}$$

$$\hat{V}_{nn} = \frac{1}{4\pi\varepsilon_0}\sum_{A}\sum_{B>A}\frac{Z_A Z_B e^2}{\mathbf{r}_{A,B}} \qquad \textbf{Eq. 2.10}$$

$$\hat{V}_{ne} = -\frac{1}{4\pi\varepsilon_0}\sum_{i}\sum_{A}\frac{Z_A e^2}{\mathbf{r}_{A,i}} \qquad \textbf{Eq. 2.11}$$

where ε_0 is the permittivity of free space, Z_A is the charge on nucleus A, e is the elementary charge, and $\mathbf{r}_{A,B}$ and $\mathbf{r}_{A,i}$ are the distances from nucleus A to nucleus B and from nucleus A to electron i, respectively.

The Hamiltonian, $\widehat{H}$, can then be written in atomic units, (a.u.) for simplicity, where the m, e, $\hbar$ and $4\pi\varepsilon_0$ equal one:

$$\widehat{H} = -\sum_{i}\frac{1}{2}\nabla_i^2 - \sum_{A}\frac{1}{2m_A}\nabla_A^2 - \sum_{A,i}\frac{Z_A}{\mathbf{r}_{A,i}} + \sum_{A}\sum_{B>A}\frac{Z_A Z_B}{\mathbf{r}_{A,B}} + \sum_{i}\sum_{j>i}\frac{1}{\mathbf{r}_{i,j}} \qquad \textbf{Eq. 2.12}$$

2.4 The Variational Principle

The variational method can be used to find approximations to the ground state or lowest energy of a system. First, a trial wavefunction, Ψ', which contains variational parameters, is chosen. These parameters are adjusted until the energy is minimised. The minimised trial wavefunction and its energy are variational approximations to the exact wavefunction, Ψ_0 , and exact energy, E_0.

The variational principle states that the energy of Ψ' must be greater than or equal to the energy of the exact wavefunction Ψ_0. The energy of the trial wavefunction is defined as the expectation value of the wavefunction:

$$E_{\Psi'} = \frac{\langle \Psi' | \hat{H} | \Psi' \rangle}{\langle \Psi' | \Psi' \rangle} \qquad \textbf{Eq. 2.13}$$

The exact energy, E_0, of a system can then be written in terms of the trial wavefunction according to the variational principle:

$$E_0 \leq \frac{\langle \Psi' | \hat{H} | \Psi' \rangle}{\langle \Psi' | \Psi' \rangle} \qquad \textbf{Eq. 2.14}$$

This forms a basis for convergence in optimisation calculations. The difficulty is finding the wavefunction which minimises the energy of the system.

2.5 The Born-Oppenheimer Approximation

Born and Oppenheimer simplified the problem of determining the electronic structure of a many body system by assuming that the position of the nuclei are fixed on the timescale of electron motion.[54] The basis of the Born-Oppenheimer approximation is that nuclei are several thousand times heavier than electrons, and move much more slowly. Due to the large difference in timescales of electronic and nuclear motion, electrons respond instantaneously to the motion of the nuclei. The Born-Oppenheimer approximation states that the wavefunction for a molecule can be separated into electronic and nuclear components.

The electronic part of the Schrödinger equation can be solved with nuclear positions assumed to be fixed, and the resulting potential energy surface is solved according to nuclear

coordinates being constant. The Hamiltonian can be simplified by removing the nuclear kinetic energy term, giving the electronic Hamiltonian as follows:[55]

$$\widehat{H}_{el} = -\sum_{i}\frac{1}{2}\nabla_i^2 - \sum_{A,i}\frac{Z_A}{\mathbf{r}_{A,i}} + \sum_{A}\sum_{B>A}\frac{Z_A Z_B}{\mathbf{r}_{A,B}} + \sum_{i}\sum_{j>i}\frac{1}{\mathbf{r}_{i,j}} \qquad \textbf{Eq. 2.15}$$

2.6 Basis Sets

A basis set is a set of basis functions which can be used to build a mathematical description of the molecular orbitals of a system. For a molecular calculation, the molecular orbitals are built using the linear combination of atomic orbitals (LCAO) approach, written as:

$$\varphi_k(\mathbf{r}) = \sum_{i} c_{ik}\phi_i(\mathbf{r}) \qquad \textbf{Eq. 2.16}$$

where φ_k is a molecular orbital, ϕ_i are the atomic orbitals which constitute the basis set and c_{ik} are the expansion coefficients which can be varied to minimise the energy of the system and hence obtain the molecular orbitals which correspond to the minimum energy. In general, a better description of the orbitals of a molecule and hence a higher quality calculation comes from using a larger basis set, although computational cost becomes a limiting factor.

2.6.1 Atom Centred Basis Sets

Slater Type Orbitals (STOs)[56] and Gaussian Type Orbitals (GTOs)[57] are the main types of atom centred basis functions used for defining atomic orbitals. The form of STOs and GTOs can be seen in **Figure 2.1**.

STOs are defined as:

$$\phi_{\zeta,n,l,m}(r,\theta,\phi) = \mathrm{N}Y_{l,m}(\theta,\phi)r^{(n-1)}e^{-\zeta r} \qquad \textbf{Eq. 2.17}$$

GTOs are used in most quantum chemistry programs and are defined as:

$$\phi_{\zeta,n,l,m}(r,\theta,\phi) = \mathrm{N}Y_{l,m}(\theta,\phi)r^{(2n-2-l)}e^{-\zeta r^2} \qquad \textbf{Eq. 2.18}$$

where N is a normalisation constant, $Y_{l,m}$ are spherical harmonic functions, r is the distance from the nucleus, ζ is used to define the rate of decay of the basis function, and n, l and m are quantum numbers.

STOs are a more accurate description of the atomic orbital, they exhibit exponential decay at long range and a cusp at the atomic nucleus. STOs have a e^{-r} dependence while GTOs have an e^{-r^2} dependence, GTOs fall off too rapidly from the nucleus and have no cusp and are less

accurate at describing long range behaviour. For a given level of accuracy, more GTOs are needed than STOs to make up the basis set. However, the integrals of GTOs are easier to solve, and by taking linear combinations of GTOs the same level of accuracy as STOs can be achieved. It is computationally more efficient to use multiple GTOs and they are preferentially used for most computational calculations.

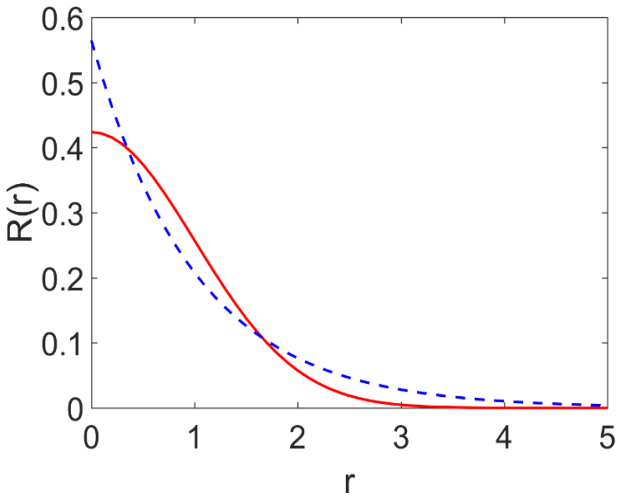

Figure 2.1: Example of a STO (blue) and a GTO (red).

The smallest number of basis functions which describe all electrons of a system is the minimal basis set or single-ζ (SZ) basis set. For hydrogen and helium the minimal basis set would include a single *s*-function, whereas for first row periodic elements a basis set would include two *s* functions, and one set of *p* functions. The number of basis functions for each atomic orbital can be increased to introduce more flexibility and a higher level of accuracy. Doubling the basis functions for each atomic orbital produces a double-ζ (DZ) type basis set, tripling the basis functions for each atomic orbital produces a triple-ζ (TZ) type basis set, and so on. However, the increase in accuracy from increasing the number of basis functions comes with an increased computational cost. This cost can be reduced by increasing the basis functions for only the valence electrons, since these are the ones involved in bonding interactions, maintaining a minimal basis for the core electrons. This is denoted as valence double zeta ('VDZ'), valence triple zeta ('VTZ'), etc.

Further increased accuracy can be achieved by adding polarisation and diffuse functions. Polarisation functions introduce functions of a higher angular momentum than those of the basis function of the orbital they are added to, for example *s* orbitals can be polarised by adding *p* functions. They account for the asymmetric distortion of the electron density which occurs during bonding. When polarisation functions are added to the basis set, the notation

becomes DZVP, TZVP etc. Polarised basis sets are good general purpose basis sets for describing chemical bonding in neutral molecules. Diffuse functions have small exponents and they are designed to give an accurate representation of the regions of the orbital most distant from the nucleus. The addition of diffuse functions can be important for anionic systems or excited states.

2.6.2 Plane Wave Basis Sets

Plane wave basis sets are used in computational calculations of periodic systems; first a periodic system must be defined. A periodic system is made up of a fundamental unit cell, as shown in **Figure 2.2**, which is repeated to form an infinite system. Three dimensional unit cell periodicity is defined by the lattice vectors $\mathbf{a}_1$, $\mathbf{a}_2$, and $\mathbf{a}_3$.[58] The combination of a unit cell and the positions of atoms or molecules within the unit cell is known as the Bravais lattice. It is the translation of the Bravais lattice along $\mathbf{R}$, the translation vector which generates the periodic system.

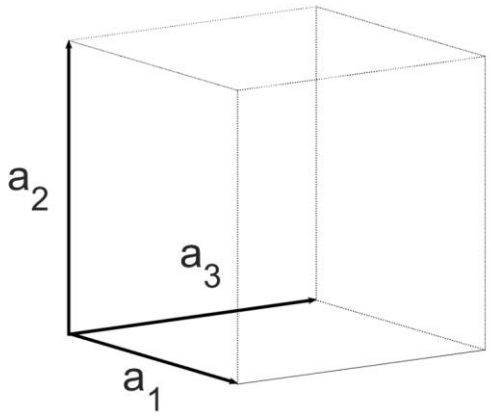

Figure 2.2: A cubic unit cell defined by three vectors.

The expansion of plane waves as basis functions follows Blöch's theorem[59] which states that wave functions must be composed of a wave-like part and a periodic part which satisfies $V(\mathbf{r}) = V(\mathbf{r} + \mathbf{R})$, where in a periodic system the external potential, V, felt by the electrons will also be periodic.

The wavefunction can be written as:

$$\Psi(\mathbf{r}) = e^{(i\mathbf{kr})} u_{ik}(\mathbf{r}) \qquad \textbf{Eq. 2. 19}$$

where $u_{ik}(\mathbf{r})$ is the periodic part with the same periodicity as the potential V and $e^{(i\mathbf{k}.\mathbf{r})}$ is the wave-like part where $\mathbf{k}$ is the wave vector related to the frequency of the wave.

u_{ik} can be expanded as a set of plane waves:

$$u_{ik}(\mathbf{r}) = \sum_{\mathbf{G}} c_{i,\mathbf{G}} e^{(i\mathbf{G}.\mathbf{r})} \qquad \textbf{Eq. 2.20}$$

where c_i is the expansion coefficient, and $\mathbf{G}$ is the wave vector related to the wavelength.

The wavefunction can then be written as the sum of the plane waves:

$$\Psi(\mathbf{r}) = \sum_{\mathbf{G}} c_{i,\mathbf{G}} e^{(i(\mathbf{G}+\mathbf{k}).\mathbf{r})} \qquad \textbf{Eq. 2.21}$$

The quality of plane wave basis sets are typically described by the energy cutoff which sets the maximum magnitude of $\mathbf{G}$. The cutoff energy controls the accuracy of the basis set, for a given system it is not known in advance and must be converged for a calculation to be successful. Plane wave basis functions are ideal for describing delocalised slowly varying electron densities such as the valence bands in metal, and larger systems. However, for the core electrons where the electron density varies rapidly, a plane wave function with a high $\mathbf{G}$ value is needed, increasing computational cost**.** Instead plane wave functions which adequately describe the valence electrons can be used, with pseudopotentials to describe the core electrons.

2.7 Pseudopotentials

Pseudopotentials can be used to describe the core regions of an atom implicitly, since electrons in this region do not generally participate in bonding, excitations, or conductivity, while the valence electrons can be treated explicitly.[55,58] This reduces the size of the basis set necessary to describe molecular orbitals and reduces the cost of a calculation.[58,60]

Using a relativistic pseudopotential for the core electrons also provides indirect relativistic effects to the valence electrons. The relativistic motion of core electrons is partly responsible for the chemical and physical properties of heavy atoms, such as the lanthanides and actinides, although it is less important for lighter atoms. A notable example of the importance of including relativistic effects is the yellow colour of gold.[61,62] Non-relativistic calculations of the excitation energies of gold predict the transition responsible for its yellow colour to be in the ultraviolet region. It is only with the inclusion of relativistic effects that this transition is predicted in the visible region. The inclusion of relativistic effects increases the accuracy of the pseudopotentials used with little impact on the computational cost.

2.6.1 Goedecker, Teter and Hutter Pseudopotentials

The pseudopotentials used in this thesis were developed by Goedecker, Teter and Hutter (GTH-pseudopotentials).[63] The pseudopotential is separated into a local one electron term, and a non-local two electron term, as follows:

$$V^{\mathrm{PP}}(\mathbf{r},\mathbf{r}') = V_{\mathrm{loc}}^{\mathrm{PP}}(\mathbf{r}) + V_{\mathrm{nl}}^{\mathrm{PP}}(\mathbf{r},\mathbf{r}') \qquad \mathbf{Eq.2.22}$$

the GTH-pseudopotentials were developed for use with plane wave basis sets. These pseudopotentials are relativistic, norm-conserving, separable and dual-space meaning they are defined in both real and Fourier space.

2.8 The Hartree Approximation

The many-electron wavefunction can be approximated by the Hartree or orbital approximation using the product of n one-electron orbitals. This is known as the Hartree product:[55,64]

$$\Psi_{\mathrm{HP}}(\mathbf{x}_1,\mathbf{x}_2,..,\mathbf{x}_n) = \varphi_1(\mathbf{x}_1)\varphi_2(\mathbf{x}_2)\ldots\ \varphi_n(\mathbf{x}_n) \qquad \mathbf{Eq.2.23}$$

where $\mathbf{x}_n$ is the spin and spatial coordinates of one electron in spin-orbitals φ_n. Spin orbitals are the product of a spatial orbital and a spin function i.e. $\varphi_n(\mathbf{x}_{\mathrm{n}}) = \varphi_i(\mathbf{r}_i)\sigma(i)$ where $\mathbf{r}_i$ is the spatial coordinates of electron i and $\sigma(i)$ is the z-component of the spin of the electron which can be either spin up (α) or spin down (β).

The Hartree product neglects electron-electron interactions and treats the electrons as distinguishable particles rather than indistinguishable spin ½ particles (fermions). It violates the antisymmetry principle, which states that a wavefunction of a system of fermions must be antisymmetric with respect to the exchange of any two of the fermions.[55]

2.9 Hartree-Fock Method

The defects of the Hartree product were corrected by Pauling[65], Slater[66] and Fock[67]. The Hartree-Fock method improves upon the Hartree approximation by approximating the total molecular wavefunction Ψ using a Slater determinant composed of occupied spin orbitals: [55]

$$\Psi_{\mathrm{HF}}(\mathbf{x}_1,\mathbf{x}_2\ldots\mathbf{x}_n) = \frac{1}{\sqrt{n!}}\begin{vmatrix} \varphi_1(\mathbf{x}_1) & \varphi_2(\mathbf{x}_1) & \cdots & \varphi_N(\mathbf{x}_1) \\ \varphi_1(\mathbf{x}_2) & \varphi_1(\mathbf{x}_2) & \ldots & \varphi_N(\mathbf{x}_2) \\ \vdots & \vdots & \ddots & \vdots \\ \varphi_1(\mathbf{x}_n) & \varphi_2(\mathbf{x}_n) & \cdots & \varphi_N(\mathbf{x}_n) \end{vmatrix} \qquad \mathbf{Eq.2.24}$$

The Slater determinant satisfies the antisymmetry principle, as when two rows are exchanged the sign changes, and the wavefunction is zero if any two rows are identical which satisfies the Pauli principle.[55]

Fock developed the explicit form of the Fock operator, $\hat{F}_i$, which acts on the molecular spin-orbitals, to produce the energy of each orbital, as shown in the Hartree-Fock equations:[55]

$$\hat{F}_i \varphi_i(\mathbf{r}) = E_i \varphi_i(\mathbf{r}) \qquad \textbf{Eq. 2.25}$$

where φ_i are the set of spin-orbitals used to generate the Hartree-Fock potential. The Fock operator takes the form:

$$\hat{F}_i = \hat{h}_i + \sum_{j=1}^{n} \left[2\hat{J}_j(i) - \hat{K}_j(i)\right] \qquad \textbf{Eq. 2.26}$$

where $\hat{h}_i$ is the one electron Hamiltonian, $\hat{J}_j$ and $\hat{K}_j$ are the electron-electron Coulomb and exchange operators respectively.

The Hartree-Fock energy is minimised iteratively with respect to the variational parameters. The initial set of molecular spin-orbitals making up a wavefunction generate an initial potential. The energy of the wavefunction is minimised with respect to the initial potential, forming a new set of molecular spin-orbitals and in turn a new potential. This new potential is again used to minimise the energy of the wavefunction and this cycle is repeated until self-consistency is achieved, i.e. the energy of the molecular orbitals generated is the same as the energy of the input molecular orbitals to within a predefined tolerance.[55] This is known as the self-consistent field procedure.

2.10 Electron Correlation

A major deficiency of the Hartree-Fock method is that electron-electron repulsion is treated as if a single electron moves through an average electrostatic field from all other electrons, rather than being influenced by the repulsion of individual electrons. Fermi correlation, or exchange, which is due to the fact that two electrons of like spin cannot occupy the same space, is dealt with by the Slater determinant in Hartree-Fock Theory. However, Coulomb correlation, which is the correlation in motion due to electrostatic repulsion between electrons, is neglected by the Hartree-Fock method.[55] This leads to an overestimation of the repulsion and an increase in the electronic energy of a system regardless of the size of the basis set.

The Hartree-Fock energy, E_{HF}, is always greater than the exact energy, E_0, of the system. Therefore the correlation energy is defined as the difference between them:[55,68]

$$E_{\mathrm{C}} = E_0 - E_{\mathrm{HF}} \qquad \textbf{Eq. 2.27}$$

2.11 Density Functional Theory

Density Functional Theory (DFT) is an alternative method to Hartree-Fock theory for obtaining the ground state electronic structure of many-body systems. Using DFT, the properties of a many electron system can be determined via the use of functionals i.e. functions of another function. DFT derives the positions of atomic nuclei and the ground state energy of a system from its electron density, or charge density, $\rho(\mathbf{r})$, rather than from the wavefunction. It improves how electron-electron interactions are dealt with and recovers the correlation energy. It is one of the most routinely applied computational investigative techniques and is instrumental for understanding the electronic, structural and thermodynamic properties of molecular systems.

2.11.1 Thomas-Fermi Theory

Thomas[69] and Fermi[70] proposed calculating the energy of an electronic system solely in terms of the electronic density, it was a precursor to the modern Density Functional Theory. The Thomas-Fermi expression for the total electronic energy is as follows:

$$E_\alpha[\rho] = \int \rho(\mathbf{r})\varepsilon_\alpha[\rho(\mathbf{r})]d\mathbf{r} \qquad \textbf{Eq. 2.28}$$

where $\varepsilon_\alpha[\rho(\mathbf{r})]$ is the energy density of contribution α (kinetic, exchange or correlation energies), calculated locally at every point in space. This is a local density approximation, or LDA.[68] The original Thomas-Fermi approximation was too crude a description of the electronic ground state as only the kinetic energy of electrons was considered, while the nuclear-electron and electron-electron contributions were treated completely classically.[71]

2.11.2 Hohenberg-Kohn Theorems

In 1964, Hohenberg and Kohn introduced two theorems which form the basis for modern density functional theory.[72] The first theorem states that all the ground state properties of a molecule can be determined from the electron density $\rho_0(\mathbf{r})$. Therefore the ground state energy of a many electron system can be calculated given $\rho_0(\mathbf{r})$, represented as:[55]

$$\rho_0(\mathbf{r}) \rightarrow \mathrm{E}_0 \qquad \textbf{Eq. 2.29}$$

the second theorem states that the variational principle applies to the density of a system and therefore any value of the molecular energy calculated from the density will be greater than or equal to the true energy. The ground state energy of the system can be minimised by varying the density, and the exact ground state energy is given by the density which minimises the total energy. The second theorem can be stated as: [55]

$$E[\rho_t] \geq E_0[\rho_0] \qquad \textbf{Eq. 2.30}$$

where ρ_t is a trial electronic density, and E_0 is the true ground state energy corresponding to the true electronic density ρ_0.[55]

Electrons move under the influence of an external potential, $V_{\text{ext}}(\mathbf{r})$, which is determined by $\rho(\mathbf{r})$. The total energy of a system, $E[\rho(\mathbf{r})]$, is a functional of the electron density and can be written in terms of the external potential:

$$E[\rho(\mathbf{r})] = F[\rho(\mathbf{r})] + \int \rho(\mathbf{r}) V_{\text{ext}}(\mathbf{r})\, \mathrm{d}\mathbf{r} \qquad \textbf{Eq. 2.31}$$

where $F[\rho(\mathbf{r})]$ is the Hohenberg Kohn universal functional. Knowing the universal functional would allow the computation of the exact ground state energy as the second term in $\textbf{Eq. 2.31}$ can be calculated exactly. Unfortunately, it is not known, and so approximations must be made.

The two theorems provide a basis for an electronic structure theory based on the electron density, rather than the wavefunction. Hohenberg and Kohn proved the existence of the dependence of the total energy on the electron density and showed that the universal functional exists, however, they did not provide a way to calculate the total energy using this approach.

2.11.3 Kohn-Sham Equations

Kohn and Sham[73] later provided an efficient method to evaluate the ground state energy of a system using the density. The premise of the Kohn-Sham equations is that the exact ground state density of a real fully interacting system can be written as the ground state density of a fictitious system of non-interacting particles. Rather than needing to find the universal H-K functional, the challenge is to find a fictitious system with the same density as the real one. This allows more accurate DFT calculations as the expression for the kinetic energy of non-interacting electrons is in terms of orbitals.

A general expression for the Kohn-Sham DFT energy, E_{KS}, can be written as:

$$E_{\mathrm{KS}}[\rho(\mathbf{r})] = T_{\mathrm{NI}}[\rho(\mathbf{r})] + V_{\mathrm{ne}}[\rho(\mathbf{r})] + J[\rho(\mathbf{r})] + E_{\mathrm{xc}}[\rho(\mathbf{r})] \qquad \mathbf{Eq.2.32}$$

T_{NI} is the kinetic energy of the non-interacting system, V_{ne}, the interactions between the nuclei and the electrons and J, the Coulombic interactions. The only unknown term, E_{xc}, is the exchange-correlation term which includes the small amount of remaining kinetic energy from the interaction of particles and the exchange-correlation interactions between electrons:

$$E_{\mathrm{xc}}[\rho(\mathbf{r})] = T[\rho(\mathbf{r})] - T_{\mathrm{NI}}[\rho(\mathbf{r})] + V_{\mathrm{ee}}[\rho(\mathbf{r})] - J[\rho(\mathbf{r})] \qquad \mathbf{Eq.2.33}$$

The Kohn-Sham equation $\mathbf{Eq.2.34}$ is a Schrödinger-like equation of a single electron interacting with the external potential V_{KS} where ε_i is the energy corresponding to the orbital φ_i. The effective potential needed to generate the same electron density as the fully interacting system:

$$\left(-\frac{1}{2}\nabla^2 + V_{\mathrm{KS}}(\mathbf{r})\right)\varphi_i(r) = \varepsilon_i\varphi_i(\mathbf{r}) \qquad \mathbf{Eq.2.34}$$

Kohn-Sham one electron molecular orbitals, $\varphi_i^{\mathrm{KS}}(\mathbf{r})$, are used to solve $\mathbf{Eq.2.34}$ and the total electron density is given in terms of the occupied Kohn-Sham orbitals:

$$\rho(\mathbf{r}) = \sum_i \left|\varphi_i^{\mathrm{KS}}(\mathbf{r})\right|^2 \qquad \mathbf{Eq.2.35}$$

The Kohn-Sham equations can be solved, as in HF theory, with an initial set of approximate molecular orbitals and a self-consistent field procedure. As the $\mathrm{E_{xc}}$ term is only known for a free electron gas and must be approximated for all other systems.

2.11.4 Exchange-Correlation Functionals

Different approximations of various levels of accuracy exist for E_{xc} which allow for the calculation of ground state energies of molecular systems. They are categorised in **Figure 2.3** as a ladder approaching the goal of Chemical accuracy from the starting point of the Hartree Fock theory.

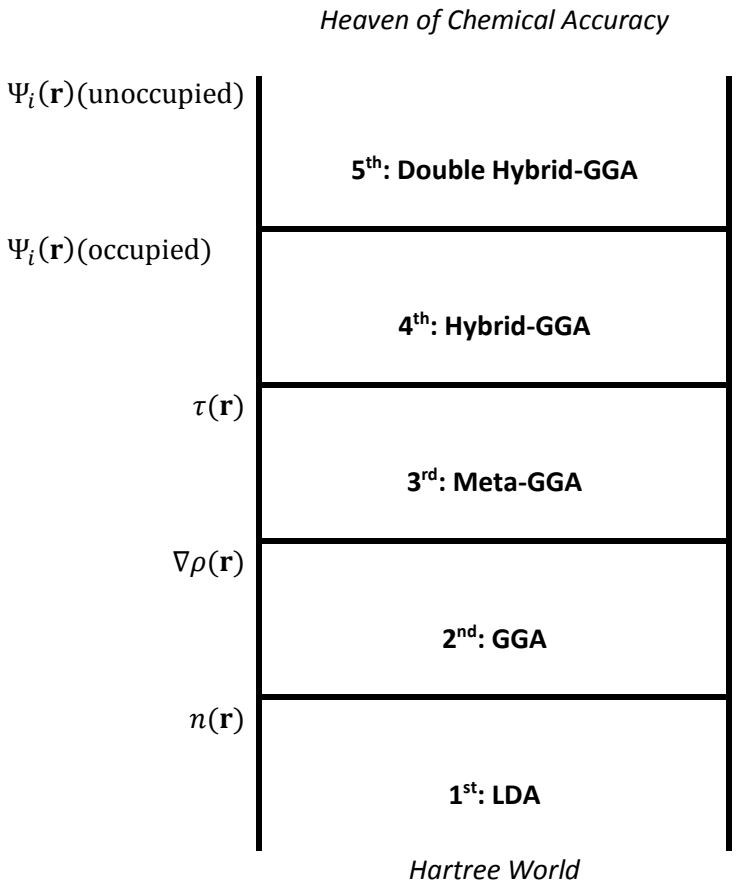

Figure 2.3: The Jacob's Ladder of Chemical Accuracy, reproduced from Perdew J.P. and Schmidft, K. ref[74].

2.11.4.1 The Local Density Approximation

The bottom rung of the DFT Jacob's ladder is the simplest form of the exchange-correlation functional, the Local Density Approximation (LDA). LDA does not assume that the electron density in a molecule is homogenous. It assumes that the E_{xc} density is only dependent on the value of ρ at each point in space. The LDA functional can be written as:

$$E_{\mathrm{xc}}^{\mathrm{LDA}}[\rho(\mathbf{r})] = \int \rho(\mathbf{r})\varepsilon_{\mathrm{xc}}[\rho(\mathbf{r})]\,\mathrm{d}\mathbf{r} \qquad \mathbf{Eq.2.36}$$

The LDA has several problems, it is exact for an uniform electron gas but it fails for molecules which have strongly varying electron density, the total energy is underestimated and it tends to cause over-binding between atoms in molecules.[55,60]

2.11.4.2 The Generalised Gradient Approximation

The Generalised Gradient Approximation (GGA) for the exchange correlation energy improves on the LDA by considering both the electron density at a given point and the gradient, $\nabla\rho$, at that point:

$$E_{\mathrm{xc}}^{\mathrm{GGA}}[\rho(\mathbf{r})] = \int \rho(\mathbf{r})\varepsilon_{\mathrm{xc}}[\rho(\mathbf{r}), \nabla\rho(\mathbf{r})]\,\mathrm{d}\mathbf{r} \qquad \mathbf{Eq.2.37}$$

Multiple GGA functionals exist which increase the accuracy of ground state calculations without a large increase in computational cost compared to LDA. The parameters of GGA functionals can be non-empirical, for example the Perdew-Burke-Ernzerhof (PBE)[75,76] functional, or semi-empirical, for example the BLYP[77] functional, which is dependent upon parameters fitted to experimental data.

2.11.4.3 Meta-GGA and Hybrid-GGA xc-Functionals

An improvement over standard GGA functionals can be gained using meta-GGA functionals, such as TPSS[75,78] which consider the second derivatives of ρ:

$$\mathrm{E}_{\mathrm{xc}}^{\mathrm{mGGA}}[\rho(\mathbf{r})] = \int \rho(\mathbf{r})\varepsilon_{\mathrm{xc}}[\rho(\mathbf{r}), \nabla\rho(\mathbf{r}), \nabla^2\rho(\mathbf{r})]\,\mathrm{d}\mathbf{r} \qquad \mathbf{Eq.2.38}$$

Hybrid-GGA functions, such as PBE0[75,79,80] and B3LYP,[77,81,82] can also be used which combine a percentage of exact Hartree-Fock exchange energy with the approximate DFT exchange. These can be more accurate than standard GGA functionals, but this comes with an increase in computational cost.

2.11.5 DFT+U

One of the failures of DFT is the inability of LDA and GGA functionals to account for the strong correlation of localised *d* and *f* electrons, often leading to incorrect orbital occupation numbers. Failure to describe these correlations can misrepresent physical properties, for instance in the case of uranium dioxide GGA functionals predict metallic character.[83] The DFT+U correction proposed by Liechtenstein *et al.*[84] corrects this using an additional Hubbard-like term. The effective Coulomb correction is given as:

$$U_{eff} = U - J \qquad \mathbf{Eq.2.39}$$

where U and J describe the strength of the on-site interactions for the Coulomb and exchange parameters respectively. The addition of the U_{eff} term applies a penalty to delocalised electrons which forces their orbital occupancy so they become localised instead of being shared by several atoms.

The determination of U_{eff} can be done empirically or obtained from a series of total energy calculations where the occupancy of localised *d* or *f* orbitals is varied.[85,86] DFT+U is often used when investigating actinide dioxides where DFT functionals find the AnO_2 systems to be insulators.[87–89] It is also used when investigating catalytic materials such as silver, copper and iron oxides, which often have variable occupations of *d* or *f* states in their catalytic phase.[90]

2.11.6 DFT with Dispersion

Dispersion is defined as the response of electron density to fluctuations of density in other regions of space. Standard LDA and GGA DFT functionals fail to account for long-range $\frac{1}{r^6}$ electron correlations that are responsible for van der Waals dispersion forces between atoms.[55,91]

Grimme *et al*.[92,93] developed a method for calculating the dispersion forces for a small addition to computational cost. The DFT-D method adds an additional term to the DFT total energy to account for dispersion forces:

$$\mathrm{E_{DFT-D}} = \mathrm{E_{DFT}} + \mathrm{E_{Disp}} \qquad \textbf{Eq. 2.40}$$

In D2 dispersion the coefficients are empirically derived and the D2 dispersion correction is given by an attractive semi-empirical pair potential:

$$\mathrm{E_{D2}} = \sum_{AB} \sum_{n=6,8,10,\ldots} s_n \frac{C_n^{AB}}{r_{AB}^{\mathrm{n}}} f_{d,n}(r_{AB}) \qquad \textbf{Eq. 2.41}$$

Where the first sum is over all atom pairs in the system, C_n^{AB} is the n^{th} order dispersion coefficient for atom pair AB, s_n is a global scaling factor, r_{AB} is the interatomic distance and $f_{d,n}$ is a damping function defined as:

$$f_{d,n}(r_{AB}) = \frac{1}{1 + 6\left(\frac{r_{AB}}{s_{r,n} R_0^{AB}}\right)^{-\alpha_n}} \qquad \textbf{Eq. 2.42}$$

where $s_{r,n}$ is the order dependent scaling factor of the cutoff radii R_0^{AB}.

Grimme *et al*.[93] later improved upon their initial dispersion correction with DFT-D3. In this case E_{disp} is the sum of two and three body energies:

$$\mathrm{E}_{D3} = \mathrm{E}_2 + \mathrm{E}_3 \qquad \textbf{Eq. 2.43}$$

E_2 takes the form of the $\mathbf{Eq.\,2.41}$ but n is truncated at 8, and E_3 is defined as:

$$\mathrm{E}_3 = \sum_{ABC} f_{d,(3)}(\bar{r}_{ABC}) E^{ABC} \qquad \textbf{Eq. 2.44}$$

where the sum is over all atom triples ABC, the geometric radii $\bar{r}_{ABC}$ is used as a dampening factor with f_d, $\mathbf{Eq.\,2.42,}$ which has the parameters $\alpha = 16$ and $s_r = \frac{4}{3}$, and E^{ABC} describes the long range interactions between atoms ABC.

For small molecules the two centre terms dominate the dispersion correction so that the E_3 has no impact on the value of dispersion correction, and so the three body term is neglected and the D2 term is calculated with $n = 6{,}8$ for atoms AB, as in $\mathbf{Eq.\,2.41}$. The improved D3 method for calculating dispersion introduced atom-pairwise specific dispersion effects and a cutoff radii computed from first principles. The descriptions of dispersion have been calculated for elements with nuclear charge Z = 1-94.[93]

2.11.7 Density Functional Theory Implementation in CP2K

The CP2K Quickstep[94] DFT module implements a mixed Gaussian and plane wave method. This combines the advantages of two representations of density in terms of Gaussians and plane waves using the Gaussian and plane wave method (GPW)[95] or the Gaussian Augmented Plane wave method (GAPW)[96] where augmented plane waves are used.

2.11.7.1 Gaussian and Plane Wave Method

The starting point for the GAPW method is the hybrid Gaussian and Plane Wave (GPW) method.[95] The GPW method uses an atom-centred Gaussian type basis to describe the wave function and plane wave basis to describe the density. Using a dual representation allows for an efficient treatment of the electrostatic interactions, and results in a scheme which has linear scaling cost for the computation of the total energy with respect to the number of atoms in a system.[94]

The representation of the electron density $\rho(\mathbf{r})$ can be written in terms of Gaussian functions:

$$\rho(\mathbf{r}) = \sum_{ij} P_{ij} \varphi_i(\mathbf{r})\, \varphi_j(\mathbf{r}) \qquad \textbf{Eq. 2.45}$$

where P_{ij} is the density matrix element in the atomic basis, and $\varphi_i(\mathbf{r})$ are contracted Gaussian basis functions. Core electrons are represented using pseudopotentials such as GTH pseudopotentials described in **Section 2.6.2**.

The representation of the electron density in plane waves is given by:

$$\tilde{\rho}(\mathbf{r}) = \frac{1}{\Omega}\sum_{\mathbf{G}} \tilde{\rho}(\mathbf{G}) e^{(i\mathbf{G}.\mathbf{r})} \qquad \textbf{Eq. 2.46}$$

where Ω is the volume of the unit cell, and $\mathbf{G}$ are the reciprocal lattice vectors. The expansion coefficients $\tilde{\rho}(\boldsymbol{G})$ are such that $\rho(\mathbf{r})$ is equal to $\tilde{\rho}(\mathbf{r})$ on a regular grid in a unit cell. Conversion between the two representations is achieved by expressing Gaussians numerically on a real space grid and the use of Fast Fourier Transforms (FFTs).

The Kohn-Sham DFT energy expression as employed within the GPW framework is defined in $\textbf{Eq. 2.32}$. All integrals and derivatives are computed using Gaussian basis functions, except for the integrals of the Coulomb term $J[\rho]$ which is evaluated using plane waves according to $\textbf{Eq. 2.46}$. $\mathrm{E_{XC}}[\rho]$ is approximated by functionals such as those described in **Section 2.11.4**.

The GPW method combines the benefits of Gaussians and plane waves as basis sets. The use of FFTs to convert between real and reciprocal space makes the algebraic manipulations simple in the plane wave basis set. However, a combination of high energy plane waves is needed to reproduce the wavefunction close to the nuclei to compute the Coulomb term. While this is alleviated by the use of pseudopotentials it can lead to unreasonably large basis sets with some elements. In regions of empty space, a plane wave basis set needs to represent empty space with the same accuracy as the atom filled region which can be very computationally demanding. To remedy these deficiencies while preserving the advantages the Gaussian Augmented Plane wave (GAPW) method can be used.[95,96]

2.11.7.2 Gaussian Augmented Plane Wave Method

The GAPW method[96] as used in this thesis extends the GPW method using augmented plane waves instead of pure plane waves to describe the electron density. The GPW method assumes that the plane wave cutoff is high enough that the plane wave basis is sufficiently large to describe the electron density correctly. However, even with the use of pseudopotentials, the cutoff needed for a converged calculation can lead to an unfavourably high number of FFT grid points. The use of augmented plane waves in the GAPW method reduces the energy cutoff needed, and as a result reduces the number of FFT grid points needed for the plane wave representation of the density.

The electron density of a molecular system has different characteristics depending on the region in space. U_A is the spherical atomic region around nucleus A where the density is strongly varying. In the interstitial region, *I*, away from the nucleus the density varies slowly.

It can be assumed the total density is the sum of three contributions:

$$\rho(\mathbf{r}) = \tilde{\rho}(\mathbf{r}) - \tilde{\rho}^1(\mathbf{r}) + \rho^1(\mathbf{r}) \qquad \textbf{Eq. 2.47}$$

where $\tilde{\rho}(\mathbf{r})$ is smoothed and distributed over all space, and $\rho^1(\mathbf{r})$ and $\tilde{\rho}^1(\mathbf{r})$ are the sums of atom-centred contributions, $\rho_A^1(\mathbf{r})$ and $\tilde{\rho}_A^1(\mathbf{r})$, which are hard and soft respectively.

$$\rho^1(\mathbf{r}) = \sum_A \rho_A^1(\mathbf{r}) \qquad \textbf{Eq. 2.48}$$

$$\tilde{\rho}^1(\mathbf{r}) = \sum_A \tilde{\rho}_A^1(\mathbf{r}) \qquad \textbf{Eq. 2.49}$$

It is assumed the difference between ρ_A^1 and $\tilde{\rho}_A^1$ is zero outside U_A. For U_A it is assumed that the atomic regions around different atoms do not overlap. Inside U_A, the soft density, $\tilde{\rho}$ is equal to its atom-centred contribution $\tilde{\rho}^1$:

$$\tilde{\rho}(\mathbf{r}) = \tilde{\rho}^1(\mathbf{r}) \text{ for } \mathbf{r} \in U_A \qquad \textbf{Eq. 2.50}$$

Outside the atomic regions in the interstitial region, I, it is assumed that the soft density is equal to the total density:

$$\tilde{\rho}(\mathbf{r}) = \rho(\mathbf{r}) \text{ for } \mathbf{r} \in I \qquad \textbf{Eq. 2.51}$$

These requirements lead to the four assumptions made to set up the GAPW representation of the electron density:

$$\rho(\mathbf{r}) - \tilde{\rho}(\mathbf{r}) = 0 \text{ for } \boldsymbol{r} \in I \qquad \textbf{Eq. 2.52}$$

$$\rho_A^1(\mathbf{r}) - \tilde{\rho}_A^1(\mathbf{r}) = 0 \text{ for } \boldsymbol{r} \in I \qquad \textbf{Eq. 2.53}$$

$$\tilde{\rho}(\mathbf{r}) - \tilde{\rho}_A^1(\mathbf{r}) = 0 \text{ for } \boldsymbol{r} \in U_A \qquad \textbf{Eq. 2.54}$$

$$\rho(\mathbf{r}) - \rho_A^1(\mathbf{r}) = 0 \text{ for } \boldsymbol{r} \in U_A \qquad \textbf{Eq. 2.55}$$

Partitioning the density in this way means that the Coulomb and exchange correlation terms can be calculated independently for $\tilde{\rho}$, ρ^1 and $\tilde{\rho}^1$. The Coulomb potential is separated into smooth non-local contributions expanded in planewaves and local contributions described with Gaussians and treated analytically.

The exchange correlation functional for the GAPW method can be written as:

$$\mathrm{E_{XC}}[\rho] = \mathrm{E_{XC}}[\tilde{\rho}] - \sum_{A} \mathrm{E_{XC}}[\tilde{\rho}_A^1] + \sum_{A} \mathrm{E_{XC}}[\rho_A^1] \qquad \textbf{Eq. 2.56}$$

The first term can be evaluated according using plane waves as in the GPW method, and the last two terms are evaluated using atom centred expanded Gaussians.

The GAPW method maintains the advantages of the plane basis sets, including periodic boundary conditions naturally but reducing the planewave cutoff needed to converge the system which reduces the computational cost of calculations.

2.12 Molecular Dynamics

Molecular dynamics allows the study of thermodynamic and dynamic properties of a many body system over a set time period. There are two main groups of molecular dynamics simulations, classical molecular dynamics (MD) and *ab initio* molecular dynamics (AIMD), which describe the interatomic interactions in different ways. In MD, simulation particles are treated as classical objects and potentials are used to describe interatomic interactions, whereas in AIMD interatomic interactions are calculated from first principles. Both the classical and *ab initio* methods aim to describe the interatomic interactions sufficiently to approximate the movement of ions at equilibrium. However, due to differences in the way the forces are calculated MD is suitable for dynamic studies of large systems made up of many thousands of atoms for nanosecond timescales while the computational cost of AIMD becomes unfeasible for systems and timescales of this size.[97]

2.12.1 Classical Molecular Dynamics

In MD, molecules are treated as classical objects obeying the laws of classical mechanics which describe the position, velocity and acceleration of each atom as they vary with time.[98,99] For the system of interest a set of initial conditions are specified which define the positions and velocities of all particles, and an interaction potential which derives the forces between particles. The trajectory of a system is followed by solving the differential equations from Newton's equation of motion, ($\mathbf{F}_i = m_i a_i$), where a_i is the acceleration of each particle:[98]

$$\mathbf{F}_i = m_i \frac{d^2 \mathbf{r}_i(t)}{dt^2} \qquad \textbf{Eq. 2.57}$$

Where $\mathbf{F}$ is the force acting upon the particle i at position $\mathbf{r}$ at time t and m is the mass of the particle.

The force can also be expressed as the gradient of the potential energy of the system:

$$\mathbf{F}_i = -\nabla_i V \qquad \textbf{Eq. 2. 58}$$

combining equations $\textbf{Eq. 2. 57}$ and $\textbf{Eq. 2. 58}$ relates the derivative of the potential energy to changes in the position of atoms as a function of time:

$$-\frac{dV}{d\mathbf{r}_i} = m_i \frac{d^2\mathbf{r}_i(t)}{dt^2} \qquad \textbf{Eq. 2. 59}$$

New atomic positions from time t to $t + \delta t$ are progated through the solving of integrators such as the Verlet algorithm.[100–103] The time step, δt, has to be chosen carefully in order to guarantee the stability of the integrator and reduce drift in the system's energy. Interaction models or potentials, such as the Lennard-Jones pair potential,[104] describe the interaction a systems constituents. The pressure, temperature or the number or particles of a simulation are controlled using a statistical ensemble. For example, in the micro canonical (NVE) ensemble the number of atoms (N), the volume (V) of the simulation cell, and the energy (E) are kept constant, essentially representing an isolated system. These three parts, the integrator, the interaction model and the ensemble, define a MD simulation and are varied to describe the system precisely over the timescale of a simulation.

In systems where temperature control is essential a thermostat can be used such as in an NVT ensemble.[97] The Nosé-Hoover thermostat[105,106] is an algorithm for constant temperature simulations used across MD and AIMD simulations. The thermostat introduces a fictitious 'heat bath' term with an associated mass, Q. At the correct value of Q, the thermal interaction between the heat reservoir and the dynamic system maintains the temperature of the system. A Q value which is too high would result in slow energy flow between the system and the reservoir while a Q value which is too low results in rapid temperature fluctuations. The Nosé -Hoover thermostat is commonly used as one of the most accurate and efficient methods for constant-temperature molecular dynamic simulations.[107]

The use of potentials instead of describing particle interactions means that MD is an ideal method for examining the dynamics within a system of millions of atoms for timescales in the nanosecond range without an excessive computational cost. However, there are limitations to the atom-atom interactions which can be simulated using potentials and as electron configurations are undefined any changes in bonding and reactions between molecules cannot be easily simulated.[103,108]

2.12.2 *Ab Initio* Molecular Dynamics

Ab initio molecular dynamics (AIMD) unifies molecular dynamics and electronic structure theory by computing the forces acting on the nuclei from electronic structure calculations performed "on-the-fly" as the dynamic trajectory is generated. One of the advantages of this method over the classical molecular dynamics approach is that electrons are explicitly included, meaning that it is possible to see how chemical processes occur over the timescale of the calculation. However, the introduction of the first principles (*ab initio*) basis for calculations comes at significant computational cost.

The computational cost of calculating the ground state energy of each step reduces a AIMD calculation to a few hundred atoms and a few picoseconds of length compared to the million atom, nanosecond long classical molecular dynamics calculations.[109] A shorter timescale raises concerns that a chemical system is not fully equilibrated, resulting in a highly variable energy, temperature or pressure.[110] In the case of the total energy of a system, an erratic energy or a system where the energy drifts across the timescale of a simulation can be controlled with a well-chosen SCF convergence criteria.[111] In contrast to 0 K static gas phase DFT calculations, a carefully parameterised thermostat and barostat can maintain a constant temperature and pressure.[97]

The periodic nature of AIMD calculations and the relatively small periodic box compared to classical MD means that self-interaction error can be a concern.[112] Self-interaction error is where a molecule or atom in one periodic box will interact with itself in an adjacent box. The size of simulation box must be large enough that the distance between a molecule and its periodic image minimises any self-interaction.[113] In the case of bulk solid calculations or material slabs, a vacuum between periodic boxes can also be used.[97]

In spite of these concerns with AIMD, for the calculations laid out in the subsequent chapters, it is the appropriate computational method, and the theory behind all AIMD techniques is the time-dependent Schrödinger equation. In principle the use of the time-dependent Schrödinger equation describes how a molecular system evolves over time:

$$\widehat{H}\Psi = \imath\hbar\frac{\partial\Psi}{\partial t} \qquad \textbf{Eq. 2. 60}$$

Where $\widehat{H}$ is the standard Hamiltonian given in $\textbf{Eq. 2. 12}$. There are three approaches to AIMD, Ehrenfest molecular dynamics (EMD)[97], Car-Parrinello molecular dynamics (CPMD)[114] and Born-Oppenheimer molecular dynamics (BOMD).[54]

EMD is a mixed approach where the classical equations of motion for electrons are solved simultaneously with the Schrödinger equation for the electrons. The energy of a molecular system is minimised in the first time step, the time scale and time step are determined by the dynamics of the electrons and thus EMD needs a very short time-step to allow the integration of the electronic equations of motion. This confines the MD trajectory to much smaller time scales than BOMD which depends on nuclear motion.

CPMD also calculates the forces at each time step using DFT, however the electrons and nuclei are considered to be moving at the same time, and the electrons are kept close to the ground state by use of "fictitious dynamics" which keeps the electrons in a low electronic fictitious temperature oscillation around a constant value. The evolution of a trajectory according to CPMD does not require an energy minimum to be reached in each time step.

Born-Oppenheimer molecular dynamics (BOMD)[54], is the AIMD method used for the calculations presented in this thesis, and in the CP2K package.[115] It uses the assumptions of the Born-Oppenheimer Approximation, described in **Section 2.5**. BOMD includes the electronic structure in dynamics simulations by solving the static electronic structure problem at each trajectory step using the set of fixed nuclear positions at that time step.

The BOMD method can be written: [97]

$$m_i \frac{d^2 \boldsymbol{R}_I(t)}{dt^2} = -\nabla_i \, min_{\Psi}\{\langle \Psi | \widehat{H}_{el} | \Psi \rangle\} \qquad \textbf{Eq. 2. 61}$$

for the nuclear, $\mathbf{R}_I$, degrees of freedom, where $\widehat{H}_{el}$ is the electronic Hamiltonian ($\mathbf{Eq. 2. 15}$) and m_i is the mass of electron i. An energy minimum has to be reached in each time step using Kohn-Sham DFT, described in **Section 2.10.3**, to ensure accurate results.[97] The electronic structure is solved from the time-independent Schrödinger equation, $\mathbf{Eq. 2. 5}$, while the nuclei positions are propagated according to $\mathbf{Eq. 2. 61}$. Therefore, the time-dependence of the electronic structure is a consequence of nuclear motion. As the energy must be minimised at each time step the efficiency of the BOMD approach depends on how effectively ground state energy can be reached.

2.12 Software Packages

The work presented in this thesis makes use of the software packages described below:

CP2K (https://www.cp2k.org/)

CP2K[115–117] is an open source quantum chemistry and solid state software package able to perform atomistic and molecular simulations of the solid state, liquid, molecular and biological systems. The CP2K Quickstep module provides a framework for DFT and AIMD using periodic boundary conditions and the mixed Gaussian and plane wave approaches GPW and GAPW. CP2K is capable of other methods not used in this work such as Hartree-Fock, post-Hartree-Fock methods (MP2, RPA), classical molecular dynamics, and mixed QM/MM calculations. All DFT and AIMD calculations in this work were performed using CP2K.

VMD (http://www.ks.uiuc.edu/Research/vmd/)

Visual Molecular Dynamics (VMD)[118] is a molecular graphics program used for the display and analysis of large molecular systems. VMD has a graphical user interface and a script parser to allow the analysis of structure files. VMD was used in this work to visualise .xyz files and to generate radial distribution functions.

Matlab (https://uk.mathworks.com/products/matlab.html)

Matlab[119] is a multi-functional computing environment and programming language, capable of intense data manipulation. The analysis and presentation of data can be achieved either through prewritten scripts or using the graphical interface. All the data analysis and figures present in this work have been done with the use of Matlab scripts.

GaussView (http://gaussian.com/)

Gaussview[120] is a graphical interface used to construct and view molecular systems of interest. In this work Gaussview was used to modify, build and inspect starting structures for both DFT and AIMD calculations.

Chapter 3: Aquo Complexes of the Alkaline Earth Metals: Mg^{2+}, Ca^{2+}, Sr^{2+}

In this chapter, the results of investigations into the solvation structure of Mg^{2+}, Ca^{2+} and Sr^{2+} from 75 ps of *ab initio* Molecular Dynamics trajectories are analysed and compared to existing computational and experimental literature. In addition, the parameters for the computational model used to investigate the solvation structure are presented. The analysis methodology used in this and later chapters of this thesis is explained in detail.

The coordination environment of aqueous Mg^{2+}, Ca^{2+} and Sr^{2+} complexes have been well studied with both computational and experimental methods and Sr^{2+} is a direct product of the nuclear fission process with the other ions present in the nuclear waste storage ponds. These initial studies provide a way to test the validity of the solvation model and computational methodology against existing literature.

3.1 Introduction

The liquid of the nuclear waste storage ponds contains aquo complexes of Mg^{2+}, Ca^{2+} and Sr^{2+}, as well as hydroxide and carbonate species, and all three species have been found in the groundwater around Sellafield.[121–123] To fully investigate the dynamics of the ion behaviour in aqueous solution an accurate model of their solvation environment is necessary. This model provides a useful benchmarking opportunity for the underlying methodology presented in this thesis as the hydration structure of these alkaline earth metals have been studied previously both experimentally and computationally.

The literature on the hydration structure of Mg^{2+} is relatively unambiguous. X-ray Diffraction (XRD)[124,125], Neutron Diffraction (ND)[126], Raman Spectroscopy[127,128], Density Functional Theory (DFT)[129,130], Classical Molecular Dynamics(MD)[124,127,131] and *ab initio* Molecular Dynamics(AIMD)[46,132–134] investigations all report a coordination number (CN) of 6. One gas phase DFT study investigating the successive binding energies of water to Mg^{2+} by Pavlov *et al*.[135] found stable structures up to a CN of 7. A CN of 6.8 was reported in an XRD study by Albright[136] but the author warned that the poor resolution of the peaks was the likely cause of the inconsistent result and a lower CN of 6 was more likely. The first shell Mg—O distance is found experimentally to be between 2.10 and 2.12 Å.[126–128,136–139] Computationally, the Mg—O distance varies to a slightly greater extent, with CPMD studies reporting bond lengths of 2.08 Å[46], 2.10 Å[133], 2.13 Å[132,134]. The molecular dynamics study of Obst *et al.*[140] reported a CN

of 6.2 and a longer bond length of 2.20 Å, which has not been replicated in the literature and is untypical.

The hydration structure of Ca^{2+} is less well-defined, with experimental investigations reporting CNs between 6[141,142] and 7.9[136], and Ca—O distances of 2.40[143] to 2.45 Å.[141] Combined experimental computational investigations report CNs of 6[144] to 9.5[145], and Ca—O distances of 2.45[146] to 2.51 Å[145]. Katz *et al.*[147] used *ab initio* molecular orbital calculations to examine experimental crystal structures of Ca^{2+}, similar total energies were found for CNs 6, 7, and 8 while all other CNs had considerably larger energies. A DFT study into the successive binding energies of Ca^{2+} by Pavlov *et al.*[135] found the most stable CN to be 6 with a Ca—O distance of 2.35 Å but identified stable structures up to a CN of 8. MD calculations report similar variation with CNs ranging from 5.95[148] to 8[140] and Ca—O lengths of 2.35[148] to 2.45 Å[149]. The Quantum Chemical Statistical Mechanical Simulations (QMSTAT) study by Tofteberg *et al.*[150] reported a CN of 6.9 with a Ca—O length of 2.50 Å.

Various Car-Parrinello Molecular Dynamics (CPMD) studies of the hydration structure of Ca^{2+} calculated CNs in the range 5.9[46] to 7.2[151] and Ca—O distances of 2.36[46] to 2.45 Å[152]. A 22 ps CPMD study by Ikeda *et al.*[132] took snapshots of hydrated Ca^{2+} at CNs of 5.4, 6.9 and 7.6 with associated Ca—O distances of 2.36 Å, 2.52 Å and 2.58 Å respectively. Noor *et al.*[151] conducted a CPMD study on the hydration properties of Ca^{2+} and found the CN fluctuated between 7 and 8, with an average value of 7.2 over a 14.2 ps simulation.[151] A Born-Oppenheimer Molecular Dynamics (BOMD) study by Mehandzhiyski *et al.*[153] found a CN of 7 with a Ca—O distance of 2.45 Å, in agreement with earlier CPMD studies.

The hydration structure of Sr^{2+} is similarly varied in the literature. Extended X-ray Absorption Fine Structure (EXAFS) studies identified structures with CNs from 6[154] to 10.3[155], with CNs around 8 being typical and first shell Sr—O distances of 2.57[154] to 2.63 Å.[155] X-ray Absorption Fine Structure (XAFS) studies report a smaller CN range of 6.22[156] to 7.3[157] and first shell Sr—O distances of 2.60[156] to 2.62 Å[157], while XRD studies report a CN of around 8[128,136,158–160] and first shell distances of 2.60[136] to 2.64 Å[128]. A ND study by Neilson *et al.*[161] of $Sr(ClO_4)_2$ reported a much higher CN of 15 with a Sr—O first shell distance of 2.65 Å, however this data was later found to be inaccurate and was re-examined in conjunction with an Anomalous X-ray Diffraction (AXD) study to find a CN of 9.[160]

Many computational methods have been used to evaluate the first shell solvation structure of Sr^{2+} including DFT[162], Quantum Mechanical/Molecular Mechanics (QMMM)[163], QMSTAT[150] as well as MD[131] and AIMD[46,153,164] and report widespread CNs between 6.7[46] and 9.8[139] and Sr—

O distances of 2.58[131] to 2.69.[150] A recent paper by D'Angelo *et al.*[165] combined experimental and computational techniques to investigate the coordination shell of Sr^{2+} using X-ray Absorption Near-Edge Spectroscopy (XANES) of $[Sr(H_2O)_8](OH)_2$, MD (using both the Åqvist and Dang potentials), and CPMD. The authors concluded that a CN of 8 with a first shell Sr—O distance of 2.60 Å was the most accurate description, reporting that the 2.72 Å bond length calculated with CPMD was inaccurate compared to their classical simulations and other AIMD literature. Earlier AIMD investigations report a Sr—O distance of 2.60 Å[164] and 2.65 Å[46] and coordination numbers of 6.7 and 8.0. A BOMD study by Mehandzhiyski *et al.*[153] included a DFT-D2 dispersion correction to better model the interactions of the water molecules, something absent from other AIMD investigations, and found a CN of 7.6 with 2.60 Å Sr—O first shell distance.

3.2 Computational Details

Born-Oppenheimer molecular dynamics simulations were performed using the QUICKSTEP module of CP2K, version 3.0 on simulations cells with periodic boundary conditions containing a single dication of either Mg^{2+}, Ca^{2+} or Sr^{2+} and 64 water molecules.[94,115] Temperature and pressure were kept constant using a NPT_I ensemble, where the simulation cell is isotropic. A 0.5 fs time step was used, the average temperature $T = 400\ \mathrm{K}$ was maintained using a Nosè-Hoover thermostat and a barostat maintained pressure of 1 atm.[105] Initial cubic cell parameters were set to $a = b = c = 11.99\ \text{Å}$. The computational parameters are discussed in length later in this chapter.

The Gaussian Augmented Plane Wave method (GAPW) was used for the calculation of forces and energies.[96] The PBE[75,76] functional was used including the DFT-D2 dispersion correction as proposed by Grimme.[76,166] The calculations used double-ζ plus polarization quality Gaussian basis set (DZVP-MOLOPT-SR-GTH), a planewave cutoff of 500 Ry and a relative cutoff of 60 Ry.[167]

Charge neutrality is achieved through the use of a uniform neutralising background charge. Each calculated trajectory was 20 ps long, the first 5 ps of each trajectory was treated as an equilibration period, and was not considered in subsequent analysis. A total of 100 ps of trajectory time was collected for each system, with 75 ps used in analysis once the equilibration period was discarded.

Convergence test results for the planewave cutoff and the relative cutoff can be found in **Appendix A1, A2 and A3** for Mg^{2+}, Ca^{2+} and Sr^{2+} respectively.

The DFT-D2 dispersion correction has been used for the alkaline earth metals in **Chapters 3** and **4**. For other ions considered in this thesis in **Chapters 5** to **7** the improved DFT-D3 dispersion correction is used as there are no DFT-D2 dispersion corrections available. A comparison of the difference between using the D2 correction and the D3 correction for Sr^{2+} in water can be found in **Appendix B**.

3.3 Simulation Parameter Investigation

In order to ensure the validity of the water model used to study the solvation structure of the alkaline earth metals, and other ions presented in later chapters, certain parameters needed to be chosen to accurately represent the bulk structure of water. These parameters are investigated below and compared to available experimental data to ensure accuracy in the calculations.

3.3.1 Temperature Dependence

Initial geometry optimisations were carried out on a simulation cell containing 64 water molecules using the Grimme D2 dispersion correction.[166] Pure GGA functionals, such as PBE, have a tendency to overbind in water simulations.[168–170] The overbinding manifests by over structuring water to such an extent that at room temperature PBE simulations do not accurately represent liquid water.[171,172] To overcome the effects of overbinding, previous studies[46,170,173,174] have selected a simulation temperature of 400 K in order to ensure a liquid phase. As such, an appropriate simulation temperature for the studies presented in this thesis needed to be selected to accurately represent liquid water.

Figure 3.1 presents O—H, O—O and H—H radial distribution functions (RDFs) obtained from simulations at 300 and 400 K and compares them to experimental data for liquid water. The experimental data used for comparison discarded the peak which appears at approximately 1 Å in **Figure 3.1a**. Each RDF shows a clear improvement in agreement with experimental data for the higher temperature simulations, in particular when considering the second and third peaks in the O—H and O—O RDFs. Although there is still deviation from the experimental data which might perhaps be improved with further optimisation of the simulation temperature, 400 K is used throughout the remainder of this thesis in line with other literature to allow for better comparison.[46,170,173,174]

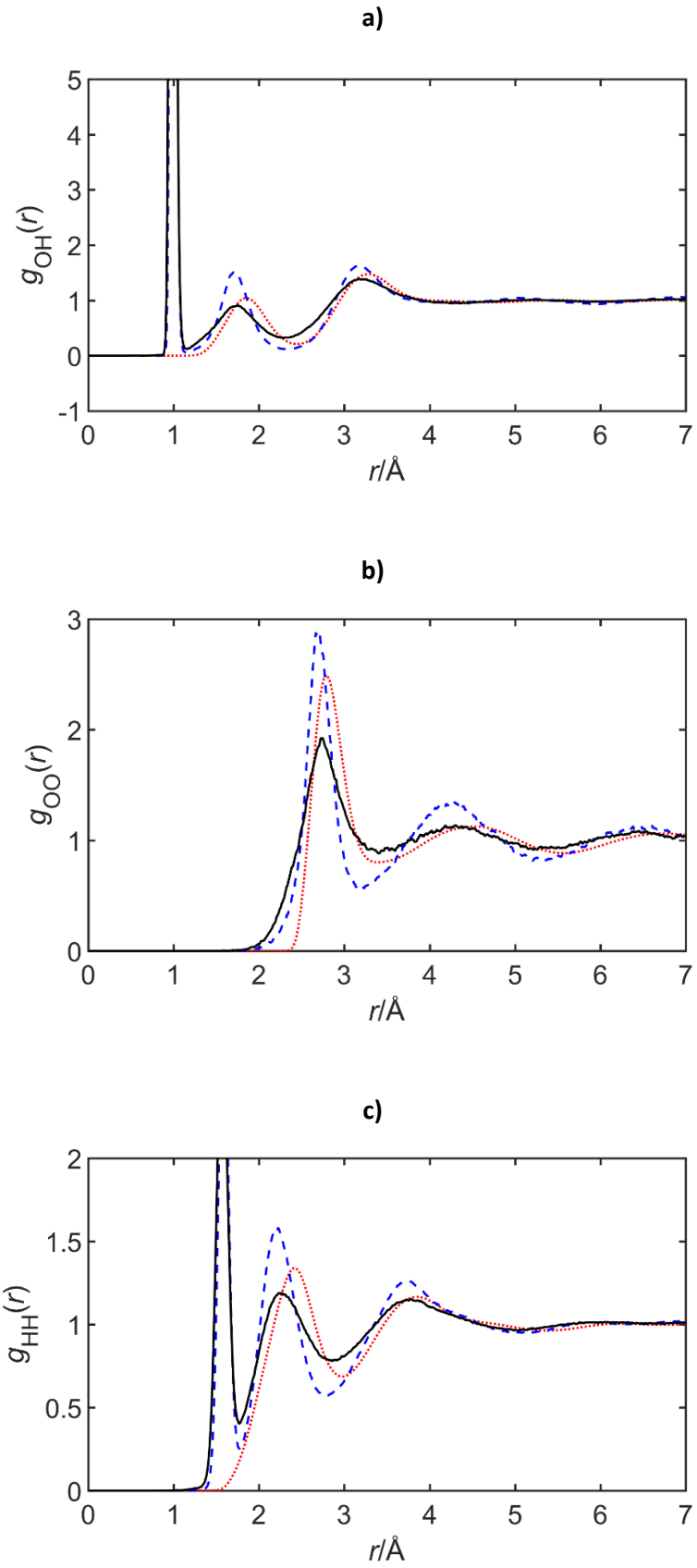

Figure 3.1: a) O—H, **b)** O—O and **c)** H—H radial distribution functions, $g(r)$, generated using simulation temperatures of 300 K (dashed blue) and 400 K (solid black), compared to experimental data from reference [ref[175]] (dotted red).

3.3.2 Impact of Temperature on Ion Solvation Structure

As a simulation temperature of 400 K is essential to ensure a liquid water environment for the ions it is important to investigate if this has an impact on any calculated M—O bonds lengths. To investigate this further, the effect of temperature was considered in simulations of the Sr^{2+} ion in a simulation cell with 64 water molecules. A 20 ps AIMD trajectory at temperatures of 300 and 400 K were run, and the resulting 15 ps of non-equilibration data was analysed.

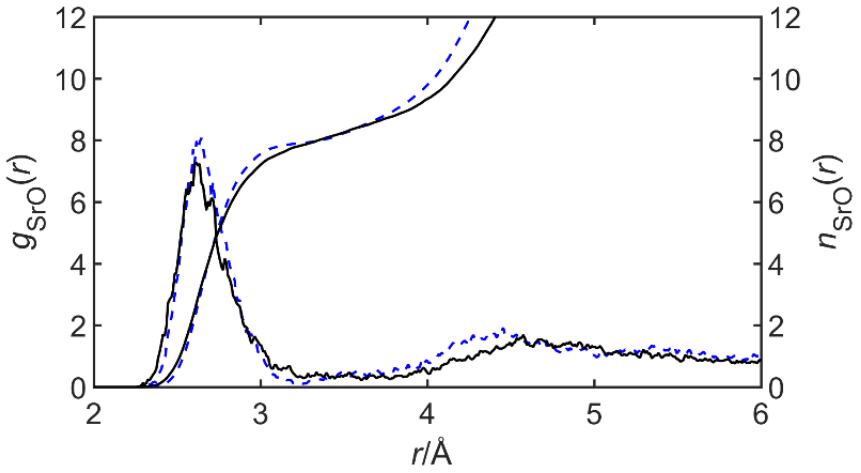

Figure 3.2: Sr—O radial distribution function, g(r), generated from 15ps simulations at 300K (dashed blue) and 400k (solid black).

Figure 3.2 compares the RDFs from each trajectory, with peaks indicating the Sr—O bond distance at 2.65 and 2.62 Å at 300 and 400 K, respectively. While both these values are within the literature ranges presented for the Sr—O bond distance, the 2.62 Å value from the 400 K calculation agrees better with the range of the experimental data from 2.57[154] to 2.63 Å[155]. In particular the calculated value of 2.62 Å agrees excellently with the 2.62 Å value obtained by the XAFS study of Pfund *et al*.[157] and the XRD study of Persson *et al*.[176] Due to the agreement of the Sr—O bond lengths with the literature values it was apparent that an increased simulation temperature of 400 K did not negatively impact the bonding of the ions and could be used going forward.

3.3.3 Dispersion Effects

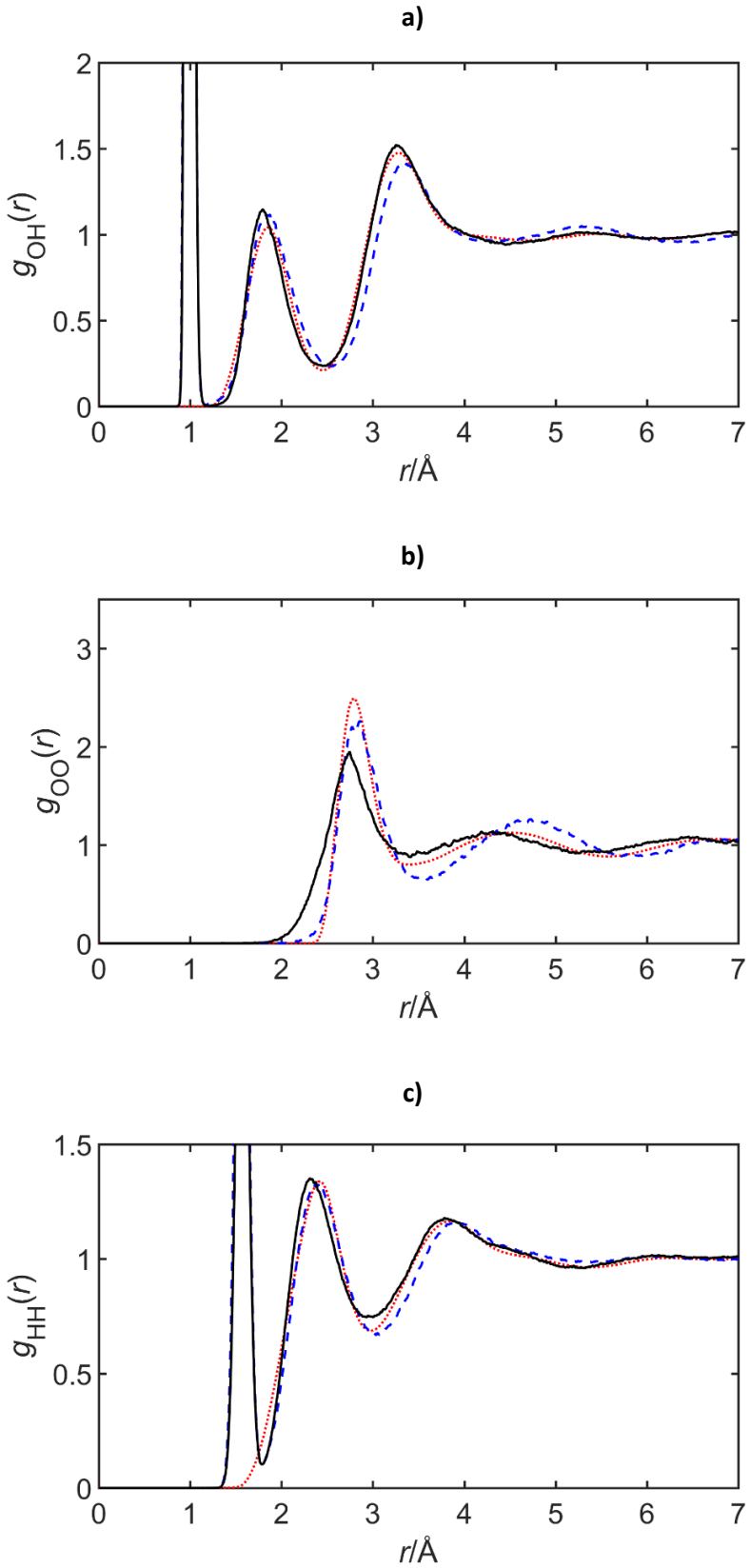

Figure 3.3: a) O—H, **b)** O—O and **c)** H—H radial distribution functions , g(r), calculated at 400 K with (solid black) and without (dashed blue) Grimme's D2 dispersion correction, and compared to experimental data from reference [ref[175]] (dotted red)

While GGA functionals can describe the hydrogen bonds with good accuracy they fail to account for the long-range dispersion interactions or van der Waals interactions in water. The effect of introducing a dispersion correction on the structure of water was investigated by applying the Grimme D2 dispersion correction.[166] Two AIMD simulations of 64 water molecules at 400 K with and without the dispersion correction were run for 20 ps. The resulting 15 ps of non-equilibration trajectory time was used to generate RDFs.

Figure 3.3 presents the O—H, O—O and H—H RDFs obtained for these simulations and compares them to experimental data for liquid water. The experimental data used for comparison discarded the peak which appears at approximately 1 Å in **Figure 3.3a**. Each RDF shows an improvement in agreement with experimental data at longer separation when the dispersion correction is included. As a result of this small improvement and the modest additional computational cost, a dispersion correction was included in all AIMD simulations to better represent bonding interactions and again leads to improved agreement with experimental data at 400K.

3.3.4 Choice of Ensemble

As detailed in **Chapter 2.22** the choice of ensemble used in molecular dynamics simulations is important in order to accurately describe the parameters of the simulation shell. Two different ensembles were investigated for use in the AIMD simulations. An NVT ensemble, which maintains a constant Number of atoms, Volume, and Temperature, and an NPT_I ensemble, which maintains a constant Number of atoms, Pressure, and Temperature. The NPT_I ensemble uses an isotropic cell which can expand and contract keeping the cell lengths and angles constant.

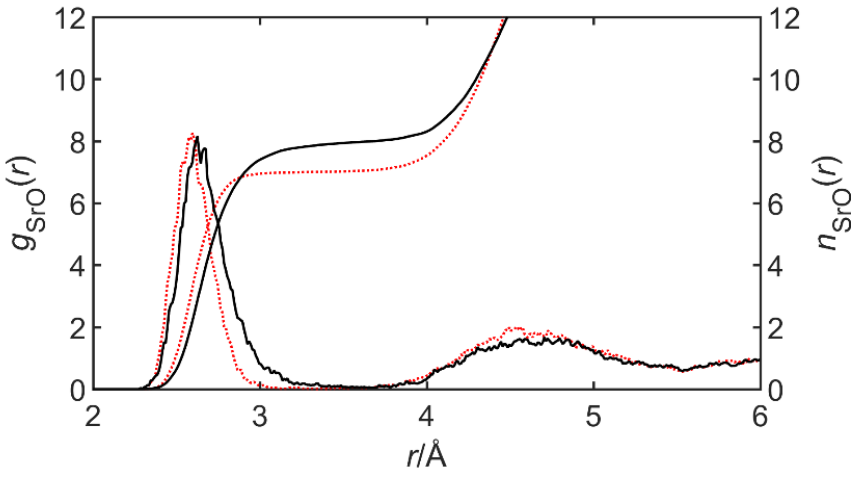

Figure 3.4: Sr—O radial distribution functions, $g(r)$, generated from NVT trajectories (dotted red) or NPT_I trajectories (solid black).

A 20 ps AIMD simulation of the Sr^{2+} ion surrounded by 64 molecules was performed using the NVT and a second AIMD simulation using the NPT_I ensemble was performed to consider the effect of the simulation box parameters varying through a trajectory. **Figure 3.4** compares the RDFs for the Sr—O distance obtained with the NVT ensemble to one generated using the NPT_I ensemble. The first peak of the Sr—O RDF occurs at 2.60 Å and 2.63 Å, for the NVT and NPT_I simulations, respectively. Both within the experimental literature range of 2.57[154] to 2.63 Å[155]. While the differences in using the NPT_I ensemble are small, the improved agreement with literature values obtained led this approach to be adopted for the remainder of the study.

3.4 Results

3.4.1 Aquo Analysis Method

Each CP2K AIMD trajectory generates a large volume of output files detailing the bonding, coordination and charge information for each of the 40 000 time steps, which corresponds to 20 ps of trajectory time. As 5 ps is discarded as the equilibration zone the remaining 15 ps of data or 30 000 time steps needs to be fully analysed to obtain meaningful results. A robust analysis method was developed and tested on the alkaline earth metals and water simulations in preparation for use in all subsequent AIMD simulations presented in this thesis. This analysis method is presented below.

3.4.1.1 Solvation Shell Cutoff

To fully characterise the first solvation shell for the ions used in AIMD simulations, a cutoff distance was selected. This cutoff value needed to identify when water molecules surrounding the ion were no longer considered to be bonded to the ion, or in the first solvation shell. Initially, RDFs were calculated averaged over the entire 75 ps of analysable simulation time, as shown in **Figure 3.5**, which resulted in M—O peak values of 2.10, 2.44 and 2.63 Å for Mg^{2+}, Ca^{2+} and Sr^{2+}, respectively.

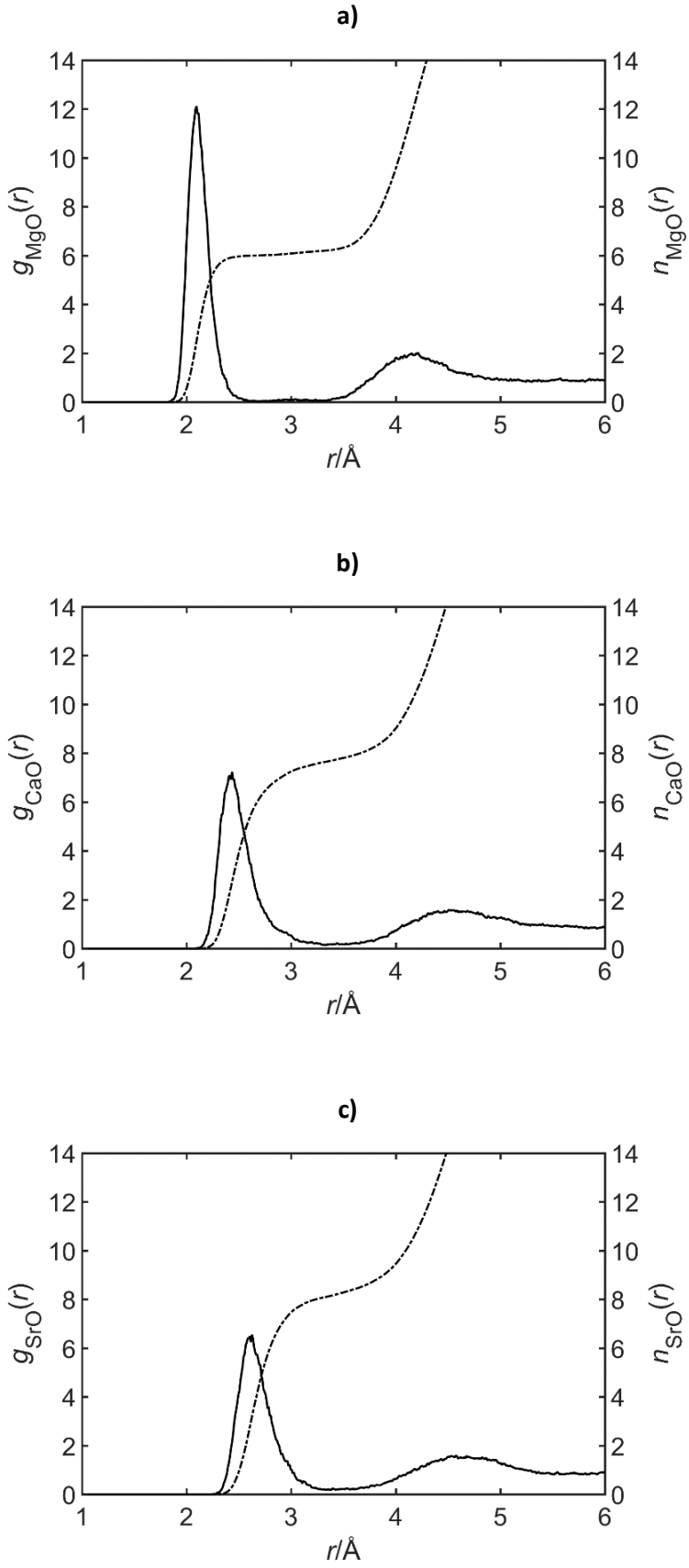

Figure 3.5: M—O radial distribution functions, g(r), generated using a total of 75 ps of simulation time for **a)** Mg^{2+}, **b)** Ca^{2+}, **c)** Sr^{2+}.

A trajectory plot of all of the Mg—O bonds at a distance of less than 4 Å from the ion is shown in **Figure 3.6a**. The first solvation shell for Mg^{2+} can be clearly identified around 2.10 Å, however it is not easy to identify the number of oxygens which surround the ion at any one point. A simpler way of depicting the first solvation shell is with a single line plot of the total coordination number (CN), that is how many oxygens are coordinated to the metal ion. Initially the RDF peak of 2.10 Å was used as the first solvation shell cutoff, as in **Figure 3.6b**, however it was clear from examining **Figure 3.6b** that it fails as a useful representation of **Figure 3.6a** and that simply using the RDF peak does not account for slightly longer Mg—O bonds or bond stretching character across the timescale of trajectory. This results in a large amount of variation in the total CN, rather than identifying genuine changes in CN.

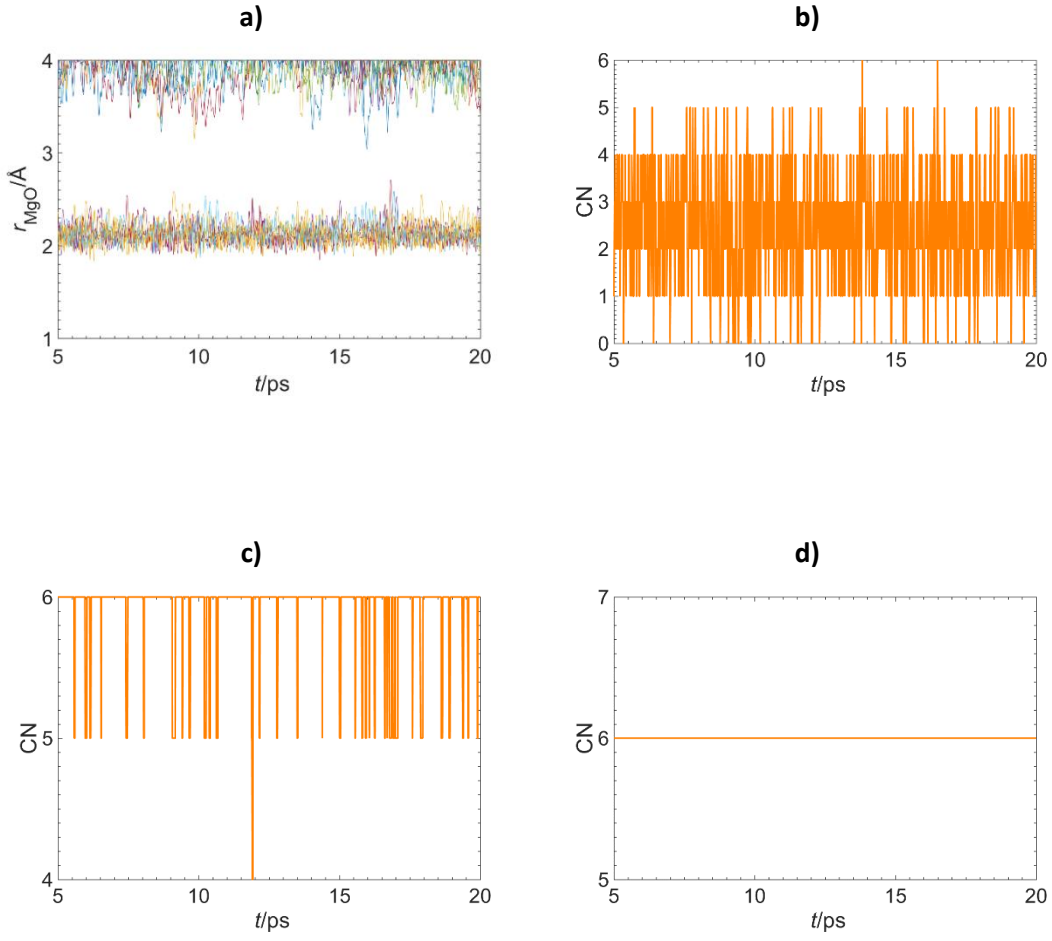

Figure 3.6: **a)** Trajectory plot for all Mg—O bonds at a distance of < 4 Å from the ion. Coordination number plot of Mg^{2+} using a first shell cutoff of **b)** 2.10 Å, **c)** 2.40 Å, **d)** 2.7 Å for a representative 15 ps AIMD run.

In order to make an accurate representation of **Figure 3.6a** as a total CN plot, a larger first shell cutoff was needed. Total CN plots using a cutoff value of the RDF peak + 0.30 Å, 2.40 Å, is shown in **Figure 3.6c** and the RDF peak + 0.60 Å, 2.70 Å, shown in **Figure 3.6d,** all cutoffs are

rounded to 2 decimal places. Examining all **Figure 3.6b** to **d** it is clear that **Figure 3.6d** produced the most accurate representation of the total CN for the first solvation shell of Mg^{2+}. Therefore, a first solvation shell cutoff of 2.70 Å was identified for use in all further analysis of Mg^{2+}.

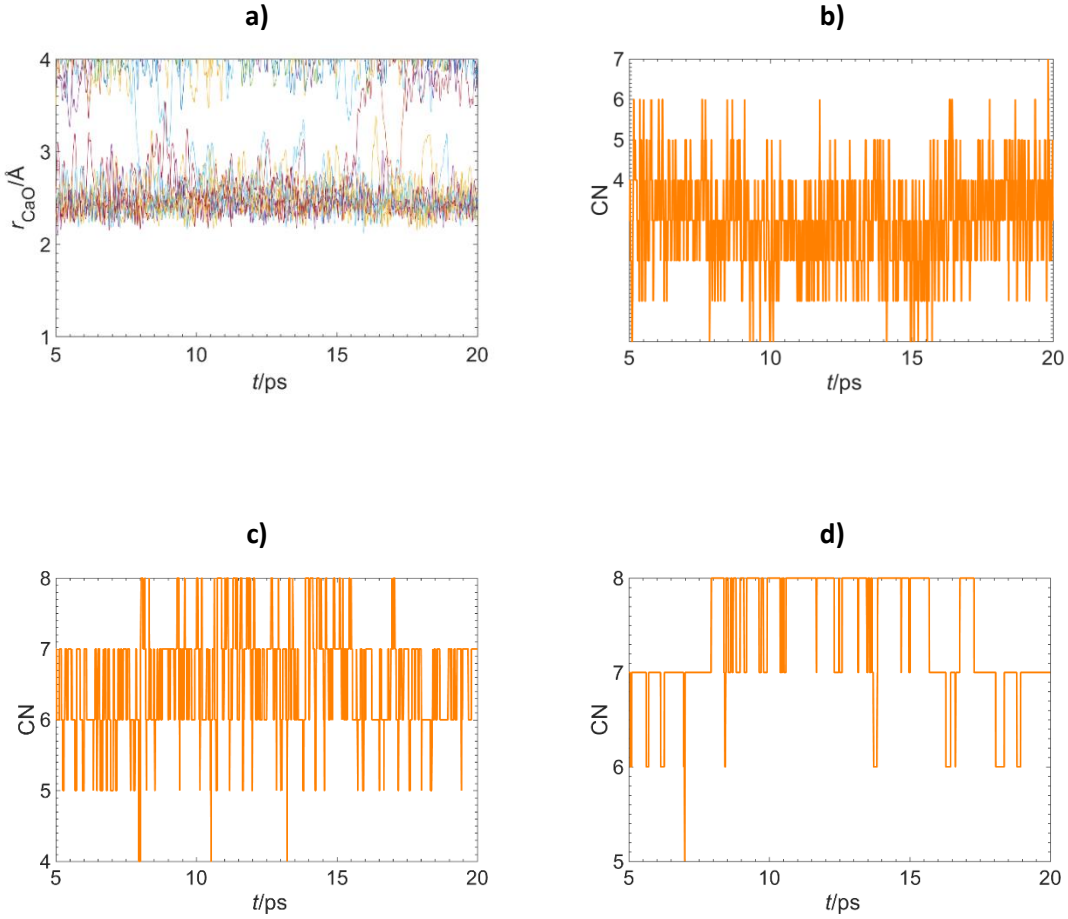

Figure 3.7: **a)** Trajectory plot for all Ca—O bonds at a distance of < 4 Å from the ion. Coordination number plots of Ca^{2+} using a first shell cutoff of **b)** 2.44 Å, **c)** 2.7 Å, **d)** 3 Å. For a representative 15 ps AIMD run.

Appropriate first solvation shell cutoffs are also needed for Ca^{2+}, and Sr^{2+}. It is evident from **Figure 3.7a** and **Figure 3.8a**, which are trajectory plots of all the M—O bonds at a distance of less than 4 Å from the ion for Ca^{2+} and Sr^{2+} respectively, that the first solvation shell for these ions are more labile. Therefore, the process to identify an appropriate solvation cutoff was repeated for Ca^{2+} and Sr^{2+} as with Mg^{2+}. Three first shell cutoffs were tested based on the value given for the RDF peak, the RDF peak + 0.30 Å and the RDF peak + 0.60 Å, all cutoffs are rounded to 2 decimal places. For Ca^{2+} this corresponded to cutoffs of 2.44 Å (**Figure 3.7b**), 2.70 Å (**Figure 3.7c**) and 3.00 Å (**Figure 3.7d**), whereas for Sr^{2+} the cutoffs used were 2.63 Å (**Figure 3.8b**), 2.90 Å (**Figure 3.8c**) and 3.20 Å (**Figure 3.8d**). For both ions adding 0.6 Å to the RDF peak provided the best representation of the first solvation shell trajectory plot as seen in **Figure 3.7a** and **3.8a**. The final first shell cutoffs were therefore 2.70 Å, 3.00 Å and 3.20 Å for Mg^{2+},

Ca^{2+} and Sr^{2+} respectively. The analysis of all AIMD trajectories in this and the following chapters use a first solvation shell cutoff of the RDF peak value +0.60 Å.

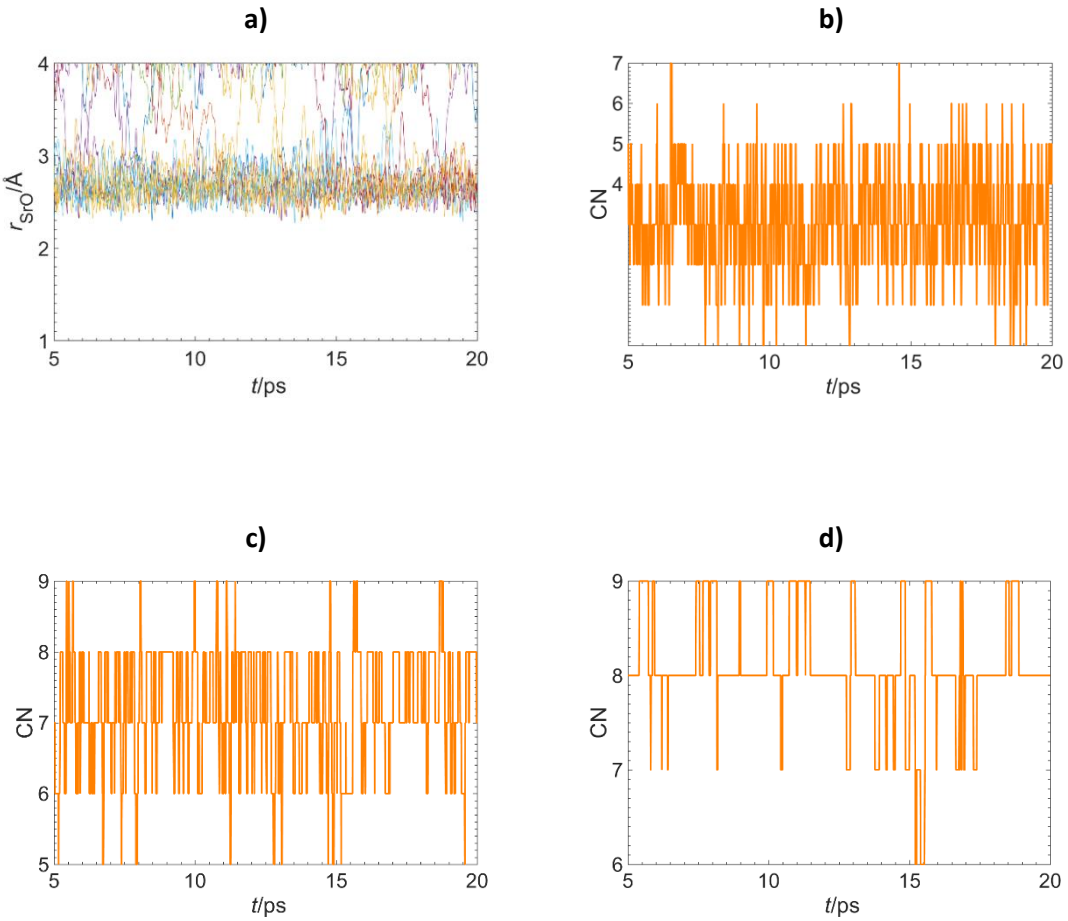

Figure 3.8: a) Trajectory plot for all Sr—O bonds at a distance of < 4 Å from the ion. Coordination number plots of Sr^{2+} using a first shell cutoff of **b)** 2.63 Å, **c)** 2.9 Å, **d)** 3.2 Å. For a representative 15 ps AIMD run.

3.4.1.2 Analysing Large Volumes of Data

Initially, data for each AIMD trajectory was analysed using data from every timestep. However, as the complexity of simulations increased so did the amount of data produced at each timestep, which became too large to effectively analyse. In an attempt to make the data produced more manageable, the impact on accuracy of using only every 10^{th} timestep in analysis was investigated.

The total CN plots for using each timestep for analysis are shown in, **Figures 3.9a**, **3.9c**, and **3.9e** for Mg^{2+}, Ca^{2+} and Sr^{2+} respectively. The same data has been analysed using every 10^{th} time step shown in **Figures 3.9b**, **3.9d**, and **3.9f** for Mg^{2+}, Ca^{2+} and Sr^{2+} respectively. Comparing the CN plots using every timestep to those using every 10^{th} timestep there is no loss in accuracy

when using only every 10th timestep, therefore the analysis method was adapted to use data from every 10th timestep.

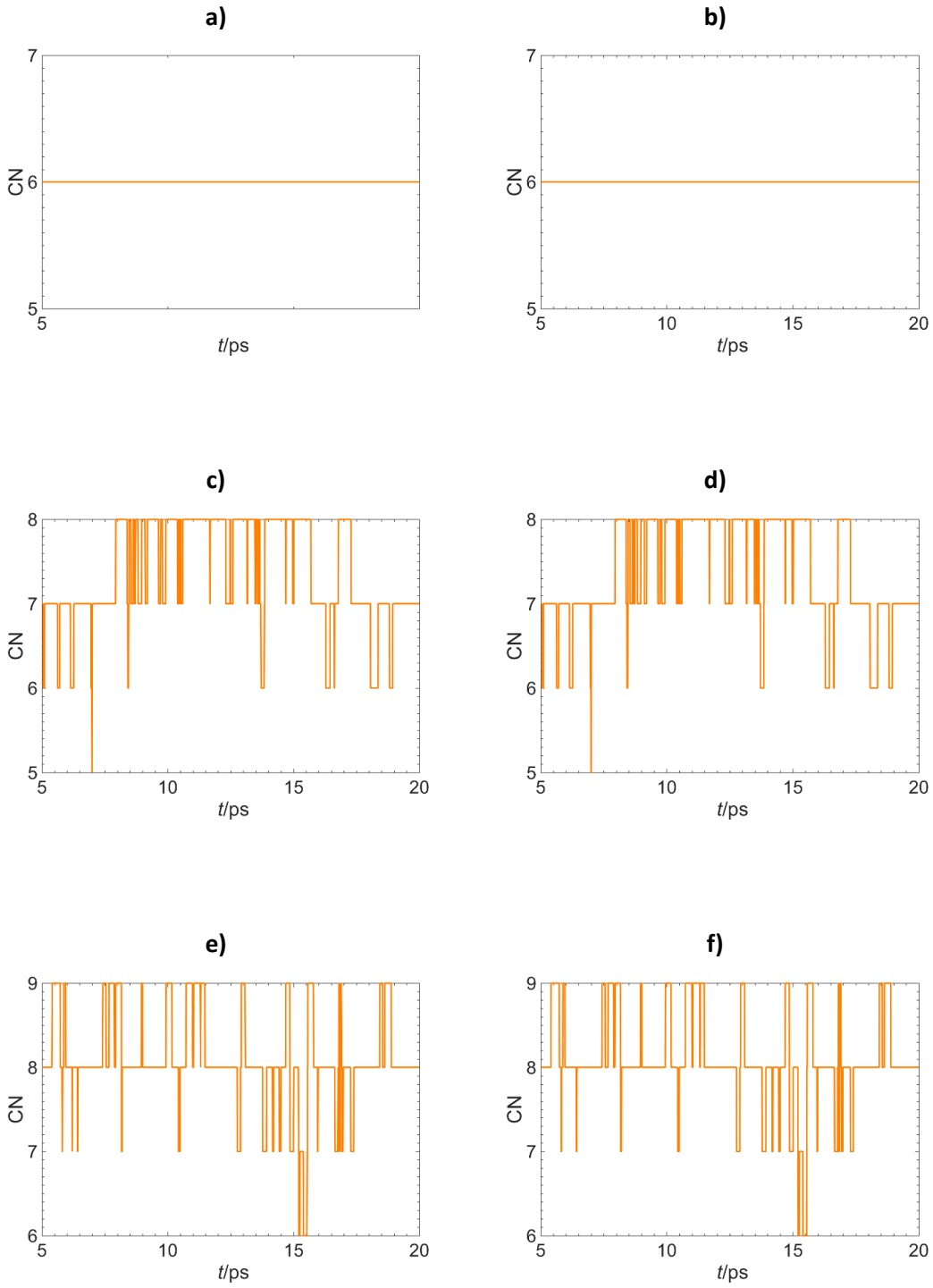

Figure 3.9: Coordination number plot for a representative 15 ps trajectory of; Mg^{2+} **a)** using all time steps **b)** using every 10th timestep; Ca^{2+} **c)** using all timesteps, **d)** using every 10th timestep; Sr^{2+} **e)** using all timesteps, **f)** using every 10th timestep.

3.4.1.3 True Coordination Number Changes

In order to accurately analyse any coordination number (CN) changes for the first solvation shell, any noise in the data, whereby waters move in and out of the first solvation shell for only a brief amount of time needed to be removed. This can be done with the use of a smoothing value whereby a change in CN is discounted unless the change occurs for a set period of time. This has previously been done with the direct method approach as per Hofer *et al*.[177] who detail the best approach to identify true transitions is to ignore any change in CN that occurs for less than 0.5 ps: in the work presented in this thesis this corresponds to 100 data steps. However, when approaching the analysis for the hydroxide trajectories, as described in **Chapter 4**, a shorter timescale was needed to capture the motion of protons throughout the simulation box. As proton transfer events occur on the scale of 0.1 ps[178–180], using a value of 0.5 ps to eliminate CN changes could also eliminate any visible proton transfer in the system. For this reason, two smoothing values for CN changes were tested: CN changes needed to last for either 0.1 ps (equivalent to 20 steps) or 0.5 ps (equivalent to 100 steps) in order to see which was most likely to capture the true coordination changes of the AIMD trajectories.

Figures 3.10a to **3.10c** plot the CN changes for representative examples of Mg^{2+}, Ca^{2+} and Sr^{2+} using both of 20 step and 100 step smoothing values represented by orange dots and blue dashes respectively. **Table 3.1** compares the total CN and average bond distances for all the aquo complexes using the two smoothing values. **Table 3.2** and **Table 3.3** show the percentage time that each ion spends at each different CNs, or residence time, across the 75 ps of simulation time collected. A wider variation in CN is seen in the **Figure 3.10b** and **Figure 3.10c** when using the 20 step smoothing value, and when comparing the calculated percentage residence times in **Tables 3.2** and **3.3**. However, when examining the calculated CN and bond lengths in **Table 3.1** there is only a small reduction for both calculated values of Ca^{2+} and Sr^{2+}. Combining the information for the CN and average bond length data the first solvation shell for each ion can be accurately characterised when using the 20 step smoothing approach, reducing the risk that any proton transfer or proton migration behaviour will be unnecessarily ignored in the later analysis of the hydroxide systems as described in **Chapter 4**.

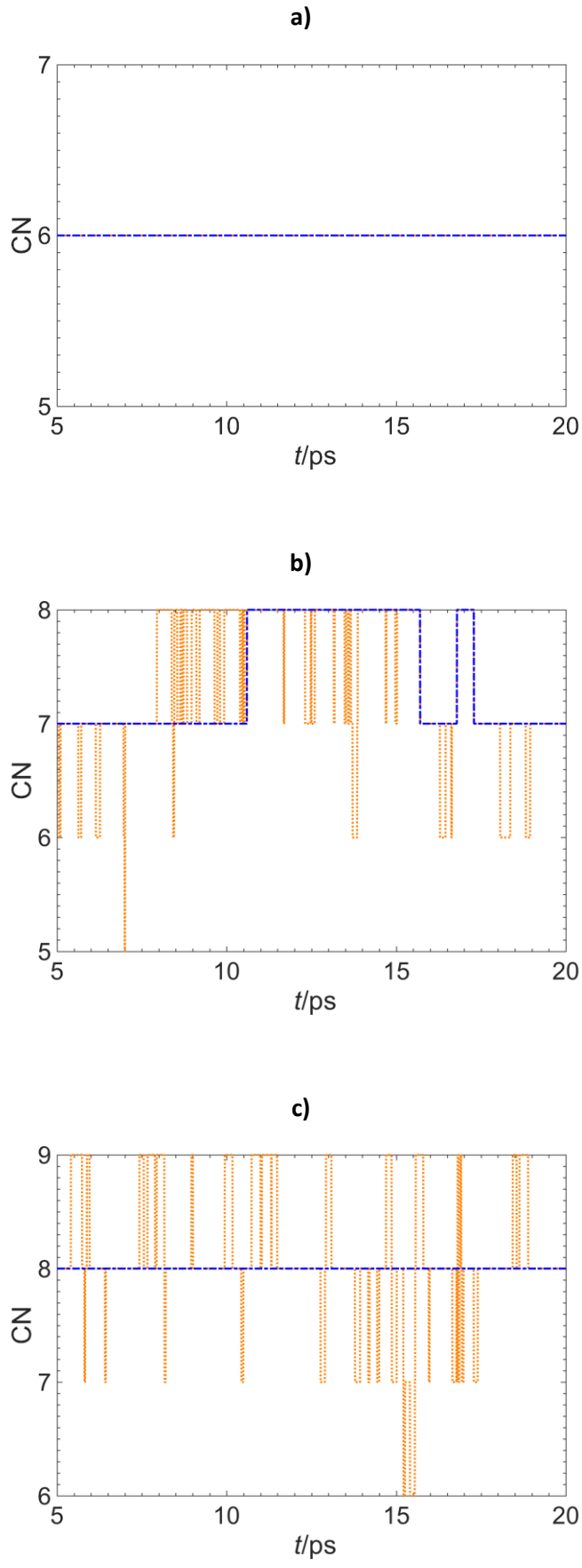

Figure 3.10: Coordination number plot comparing smoothing every 20 steps (orange dots) and every 100 steps (blue dash) for **a)** Mg—O **b)** Ca—O **c)** Sr—O.

Table 3.1: Coordination numbers (CN) and Average bond distances for r_{M-O} for using both 20 step and 100 step smoothing accompanying standard deviation (SD).

Ion	CN		r_{M-O} (Å)	
	20 step	100 step	20 step	100 step
Mg^{2+}	6.00 (0.01)	6.00 (0.00)	2.134 (0.02)	2.134 (0.02)
Ca^{2+}	7.50 (0.24)	7.39 (0.29)	2.508 (0.02)	2.507 (0.02)
Sr^{2+}	8.02 (0.14)	7.99 (0.03)	2.692 (0.01)	2.696 (0.01)

Table 3.2: Percentage residence time of different coordination environments, averaged over a total of 75 ps for each ion with 20 step smoothing.

Ion	CN					
	5	6	7	8	9	10
Mg^{2+}	0.35	99.65	0.00	0.00	0.00	0.00
Ca^{2+}	0.00	3.38	45.69	48.29	2.63	0.00
Sr^{2+}	0.00	0.23	14.09	69.57	15.28	0.83

Table 3.3: Percentage residence time of different coordination environments, averaged over a total of 75 ps for each ion with 100 step smoothing.

Ion	CN					
	5	6	7	8	9	10
Mg^{2+}	0.00	100.00	0.00	0.00	0.00	0.00
Ca^{2+}	0.00	0.57	60.27	39.16	0.00	0.00
Sr^{2+}	0.00	0.00	5.65	90.13	4.29	0.00

3.4.2 Characterisation of Alkaline Earth Aquo Complexes

In order to accurately benchmark the solvation structure of the alkaline earth metals against existing literature, 5 separate starting structures each of Mg^{2+}, Ca^{2+} or Sr^{2+} surrounded by 64 water molecules were generated for use in the AIMD calculations. These 15 structures underwent a cell optimisation whereby both the geometry and the cell size were optimised simultaneously. The resulting 75 ps of trajectory time for each ion, after the 5ps equilibration period was discarded, was analysed using the analysis methodology described above.

The calculated M—O bond lengths and metal coordination numbers for each simulation are summarised in **Table 3.4** and compared to the experimental literature ranges. There is an increase in the M—O bond distances down the group from Mg^{2+} to Sr^{2+} along with an increase in first shell coordination number. While the calculated M—O bond lengths are slightly longer

than the experimentally reported values the literature values are predominately defined by the M—O peaks of the RDFS. As stated in **Section 3.4.1.2**, the RDF peaks obtained from the total 75ps of AIMD simulations were 2.10, 2.44 and 2.63 Å for Mg^{2+}, Ca^{2+} and Sr^{2+}, which are well within the literature reported ranges.

Table 3.4: Calculated M—O separations (r_{M-O}) and mean coordination numbers (CN) for each AIMD trajectory (Traj.) and accompany standard deviation (SD).

Traj.	r_{M-O} (Å)			CN		
	Mg^{2+}	Ca^{2+}	Sr^{2+}	Mg^{2+}	Ca^{2+}	Sr^{2+}
1	2.133	2.499	2.701	6.00	7.45	8.12
2	2.133	2.521	2.702	6.00	7.71	8.19
3	2.136	2.526	2.677	5.99	7.61	7.91
4	2.130	2.487	2.692	5.99	7.11	8.06
5	2.137	2.510	2.688	6.00	7.64	7.83
Mean	2.134	2.508	2.692	6.00	7.50	8.02
(SD)	(0.023)	(0.017)	(0.009)	(0.01)	(0.24)	(0.14)

The literature values, both experimental and computational, for the Mg—O bond distance cluster around 2.12 Å, in excellent agreement with the calculated value of 2.13 Å. Experimentally reported bond lengths for Ca^{2+} and Sr^{2+} aquo complexes vary by 0.11 Å and 0.15 Å respectively, indicating significant uncertainty and dependence on experimental conditions. Typical experimental values for the Ca—O are reported around 2.45 Å, in excellent agreement with the calculated RDF value of 2.44 Å. The calculated value also compares well to other simulation data, which range from 2.35[147] to 2.68[151] Å, comparing excellently with the Mehandzhyski *et al.*[153] BOMD study which also reported a Ca—O distance of 2.45 Å. Experimentally reported values of the Sr—O distance cluster around 2.63 Å, again in excellent agreement with the value of 2.63 Å obtained from the simulations. This value is, again, in agreement with existing simulation data, which range from 2.59[164] to 2.69[163] Å.

The CN values calculated are, in all cases, within the range of values reported experimentally. The largest variation in the CN is for Ca^{2+}, as evidenced by a standard deviation of 0.24. This is reflected in the percentage residence times of different coordination environments as reported in **Table 3.5** for each ion. The CN plots for each AIMD trajectory are given in **Figure 3.11**, **Figure 3.12** and **Figure 3.13** for Mg^{2+}, Ca^{2+} and Sr^{2+} respectively.

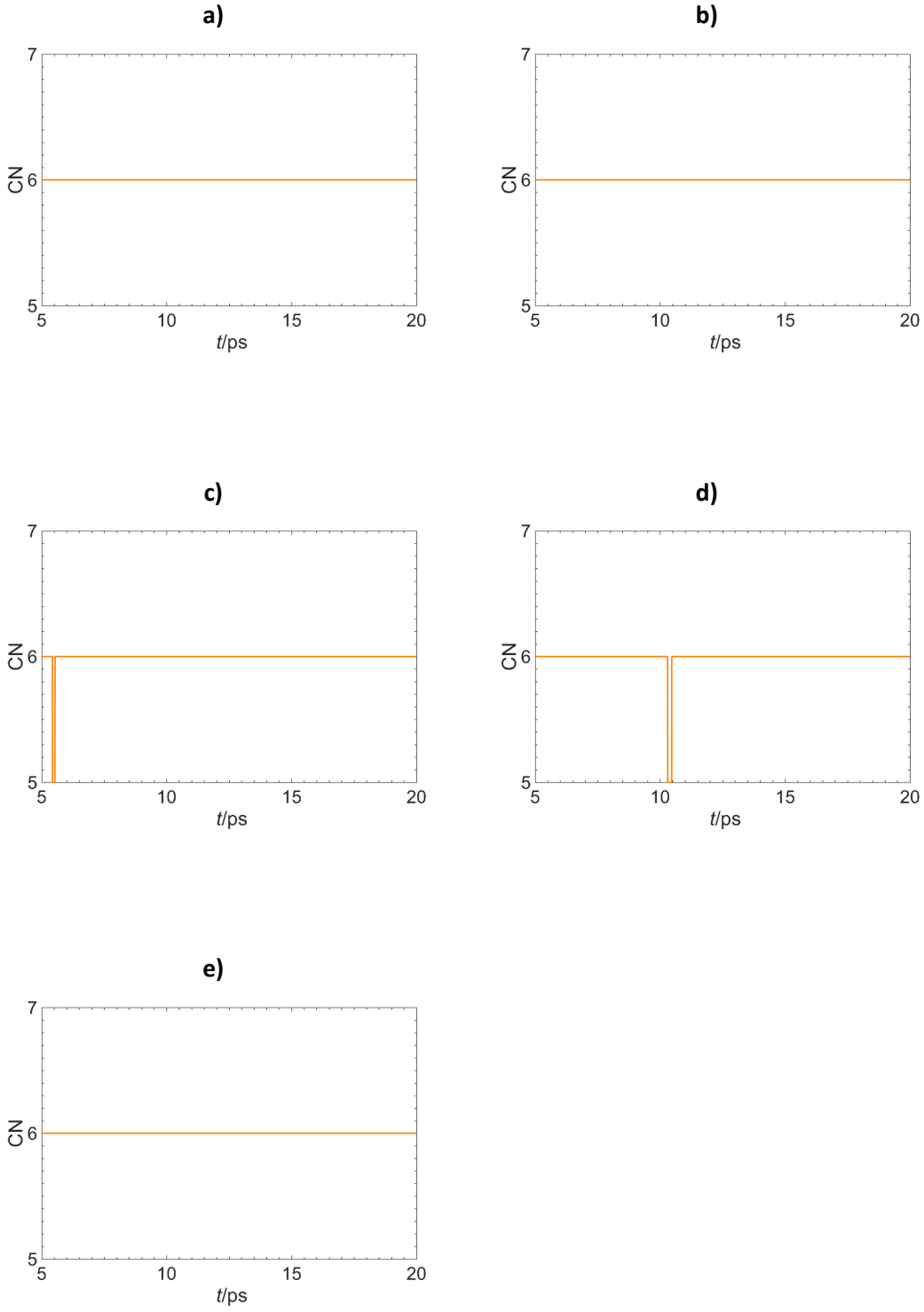

Figure 3.11(a-e): Total coordination number plots for each 15 ps AIMD trajectory of Mg^{2+}.

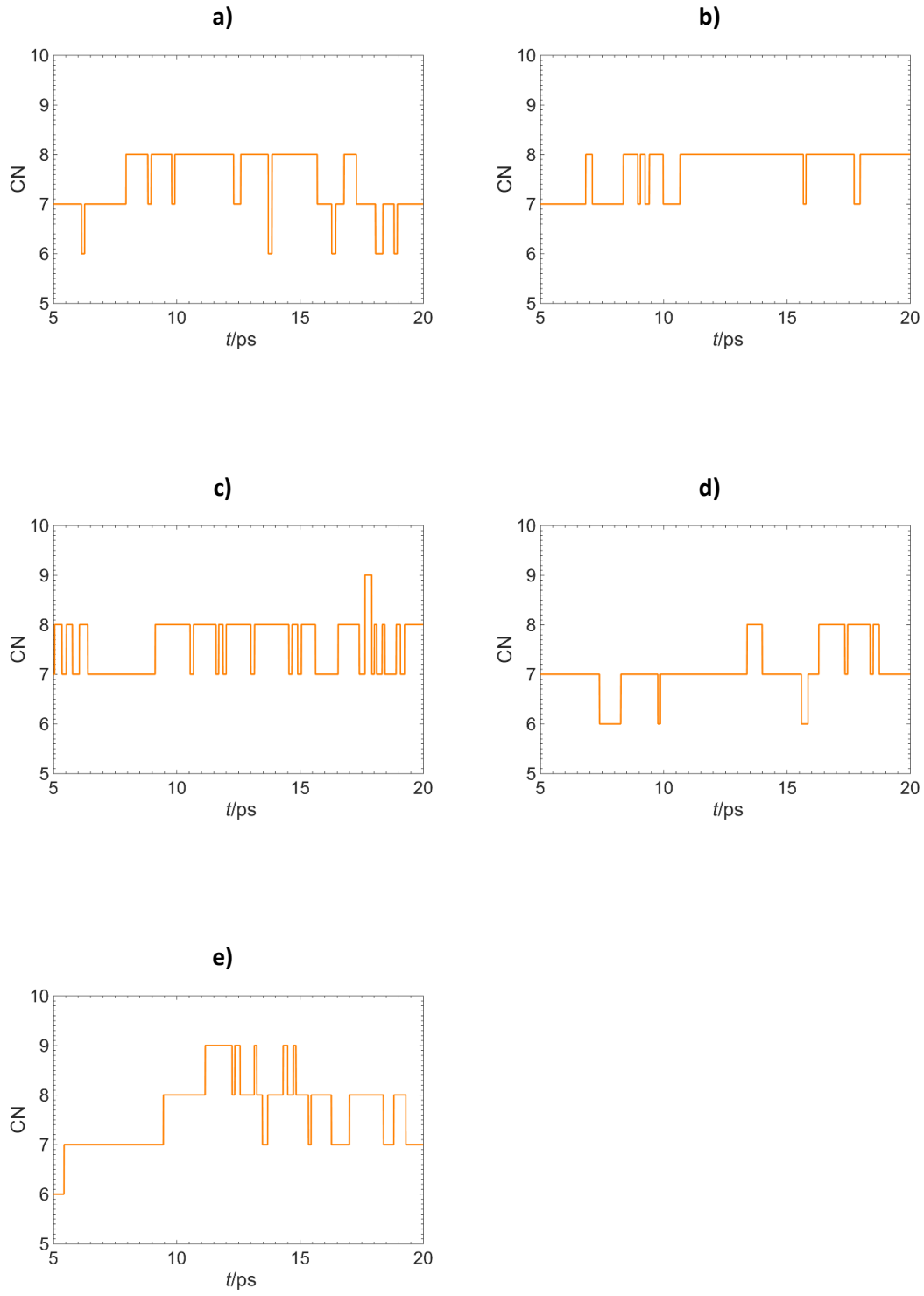

Figure 3.12(a-e): Total coordination number plots for each 15 ps AIMD trajectory of Ca^{2+}.

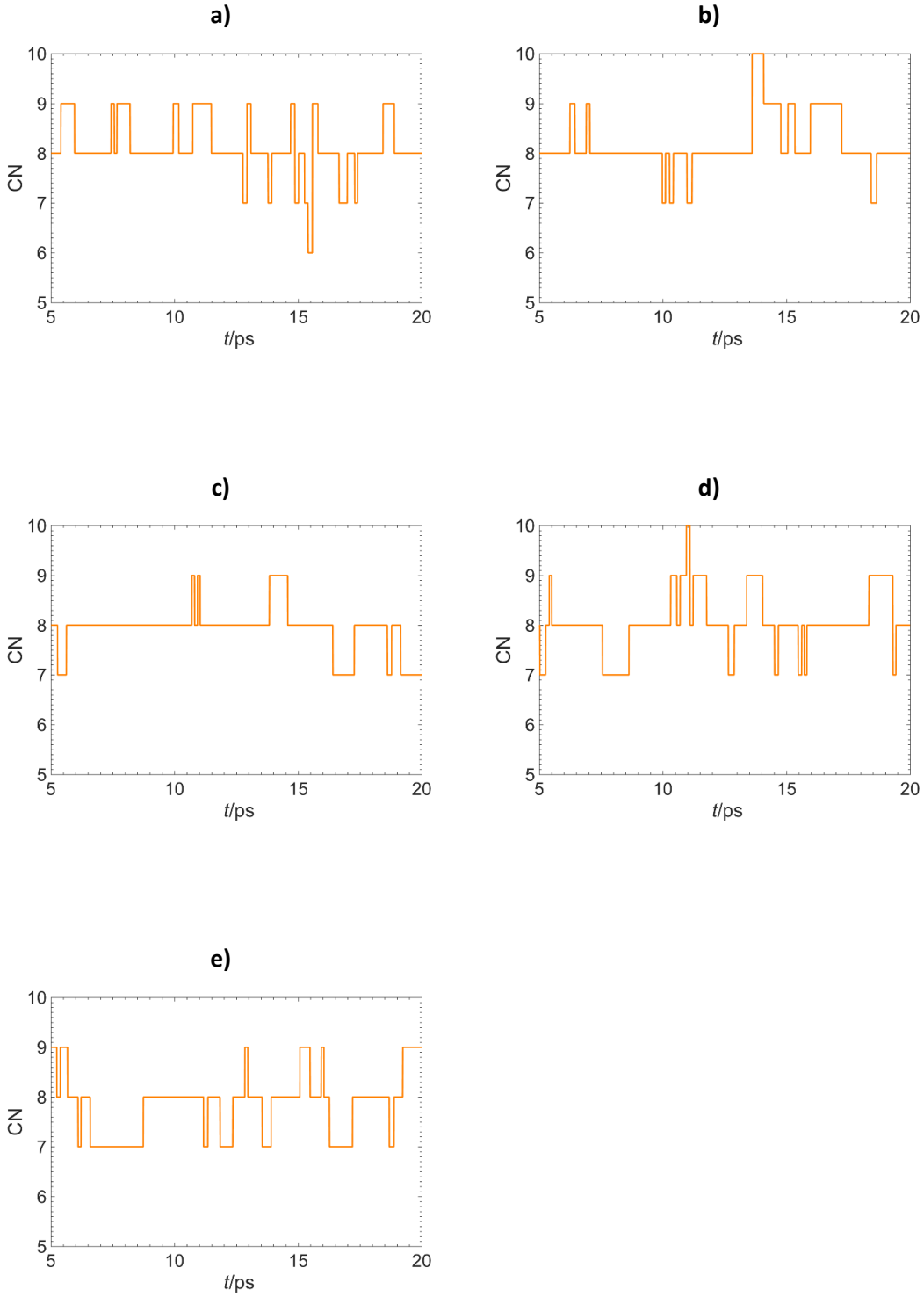

Figure 3.13(a-e): Total coordination number plots for each 15 ps AIMD trajectory of Sr^{2+}.

Table 3.5: Percentage residence time of different coordination environments (CN), averaged over a total of 75 ps for each ion.

Cation	CN					
	5	6	7	8	9	10
Mg^{2+}	0.35	99.65	0.00	0.00	0.00	0.00
Ca^{2+}	0.00	3.38	45.69	48.29	2.63	0.00
Sr^{2+}	0.00	0.23	14.09	69.57	15.28	0.83

While Mg^{2+} has a stable CN of 6 and only spends a brief percentage of time at a CN of 5, Ca^{2+} exists as the 7 and 8 coordinated complex for approximately equal periods of time. This indicates the significant lability of the eighth coordinating water molecule and, along with the brief time periods in which the 6- and even 9 coordinated complexes exist, explains the large standard deviation in the calculated coordination number. The larger Sr^{2+} more easily accommodates an eighth water molecule, spending the majority of the simulation time as an eight coordinated species, but also exists for significant periods of time with coordination numbers of both 7 and 9. These results are in excellent agreement with previous computational literature which found CNs of 6[181] for Mg^{2+}, CNs of 6[135] to 8[135] for Ca^{2+}, and CNs of 7[162] to 9[163] for Sr^{2+}.

3.5 Conclusion

This chapter focused on developing the computational and analysis method used throughout this thesis, by examining the solvation structure of the alkaline earth metals Mg^{2+}, Ca^{2+} and Sr^{2+}. As these ions are well studied in literature, as well as being relevant to nuclear waste storage and treatment, they are ideal candidates to develop a robust computational model which can be taken forward and used on more complex systems.

The parameters for the proposed computational model were explained and justified, using existing literature parameters and experimental results to ensure an accurate solvation model was used in the subsequent AIMD simulations. The analysis methodology for full AIMD trajectories was then explained with the testing for each analysis parameter included.

Finally, 75 ps of analysable AIMD trajectories for each of the alkaline earth metal ions in an aqueous environment were collected. These initial structures were optimised using the PBE functional with a DFT-D2 dispersion correction and AIMD calculations were run using Born-Oppenheimer molecular dynamics. The structure of the first solvation shell was characterised by averaging the radial distribution functions over the entire trajectory time, and calculating

average M—O bond lengths. First shell coordination numbers were also calculated with accompanying percentage residence times.

The results from characterising the first solvation shell compared excellently to existing literature, particularly with experimental literature. Highlighting that this method can be accurately used to investigate the solvation structure of these and other ions found in the nuclear waste storage ponds. An increase in both average bond length and coordination number was identified descending the alkaline earths from Mg^{2+} to Sr^{2+}. Correctly identifying this trend and demonstrating the accuracy of these results in comparison to current literature indicates that an accurate solvation model has been developed and that the analysis method is correctly representing the data obtained from each AIMD trajectory.

Chapter 4: Proton Transfer or Hydroxide Migration? Exploring the Alkaline Earth Metal Hydroxides

In this chapter, a novel investigation into the dynamics and solvation structure of the Mg^{2+}, Ca^{2+} and Sr^{2+} hydrated hydroxides is presented, as a way to probe how the solvation structure of the ions alters with increasing pH. It builds on the aquo complexes studied in **Chapter 3**, to characterise the nature of the hydrated hydroxide complexes in bulk water environments, 225 ps of analysable AIMD trajectories have been collected for each of the ions.

The analysis method used to investigate the solvation structure and the method of proton transport through the bulk system is discussed, alongside testing done to ensure the validity of the method. The results of the AIMD trajectories are presented and discussed in the context of the prevalence of proton transfer and stabilities of the hydroxides residing in the first or second solvation shell.

4.1 Introduction

As previously discussed, the pH level of the nuclear waste storage ponds is maintained in the range 10 to 12. As a result of the alkaline pH hydroxide complexes form in the storage ponds. Little is known about the microsolvation environments of the alkaline earth hydroxides species, especially with regards to the dynamics of the hydroxide ions. However, there is some literature which has begun to probe both the structure and behaviour of the alkaline earth metal hydroxides.

Kluge *et al*.[182] used gas phase Density Functional Theory (DFT) with the B3LYP exchange-correlation functional and found that in Mg^{2+} complexes the introduction of a hydroxide ligand reduces the total coordination number (CN) of the first solvation shell from 6 to 5. In repeat calculations it was found that on the inclusion of a hydroxide ion, one water molecule migrated to the second solvation sphere causing a change in coordination geometry from octahedral to bipyramidal. It was also found that the inclusion of a second hydroxide ion causes a further change to tetrahedral coordination.

The gas phase DFT studies of Felmy *et al*.[183] explored the hydrolysis of both Ca^{2+} and Sr^{2+} aquo complexes. In hydrolysing calcium aquo species from $[Ca(H_2O)_6]^{2+}$ to $[Ca(H_2O)_5OH]^{+}$, there was no change in first solvation shell CN, and no migration of the hydroxyl group from Ca^{2+}. However, the removal of a proton from $[Sr(H_2O)_6]^{2+}$ and $[Sr(H_2O)_8]^{2+}$ had different effects. The $[Sr(H_2O)_5OH]^{+}$ structure predicted the OH^{-} directly bonded to the Sr^{2+}, whereas for

$[Sr(H_2O)_7OH]^+$ the OH^- dissociated from the central ion and formed hydrogen bonds with three first shell H_2O molecules. This difference in behaviour suggested that the addition of successive water molecules has a destabilising effect on the OH^- although the authors note that lack the of an explicit second solvation shell in their calculations may have overestimated this effect.

There is a larger body of information on strontium hydroxides, the structure of $Sr(OH)_2.8H_2O$, has been examined with X-ray Diffraction (XRD)[155,184], Neutron Diffraction (ND)[185] and X-ray Absorption Near Edge Structure (XANES)[165] which all indicated that 8 water molecules coordinate to the ion, but find the hydroxide ions do not coordinate directly to the Sr^{2+} centre. Instead the hydroxide oxygen forms chains of acceptor and donor bonds with the first coordination shell, and forms hydrogen bonds with neighbouring waters.

Kerridge and Kaltsoyannis[186] used DFT to investigate the gas phase structures of the strontium hydroxide complexes with the form $[Sr(H_2O)_{8-n}(OH)_n]^{(2-n)}$ up to n = 4. A broad trend was found that the coordination of Sr^{2+} by n hydroxyl groups resulted in the destabilisation of complexes with a coordination number greater than 8 – n. Quantum Theory of Atoms in Molecules (QTAIM) calculations revealed the hydroxide ions have a weakening effect on the Sr^{2+} interactions with water oxygens. This results in waters preferentially occupying the second solvation shell rather than directly coordinating the Sr^{2+} ion.

The effects of the inclusion of an explicit second solvation shell on the microsolvation of strontium hydroxides was studied using DFT by Makkos *et al*.[187] who used the COSMO continuum solvation model to investigate bulk solvation. Overall they found that as the number of hydroxides increased the Sr-O_w bond distances increased, as the extra hydroxide coordination weakens the bonds. The authors found a low energetic barrier to proton transfer for the most stable dihydroxide species. When both hydroxide ions resided in the first solvation shell the complex was 3.0 kJ mol^{-1} higher in energy than a species with only one hydroxide in the first solvation shell.

4.2 Computational Details

Born-Oppenheimer molecular dynamics simulations were performed using the QUICKSTEP module of CP2K version 3.0. All simulation cells had periodic boundary conditions and contain a single cation of either Mg^{2+}, Ca^{2+} or Sr^{2+}, 62 water molecules and 2 OH^- ions.[94,115] A NPT_I ensemble, where the simulation cell is isotropic, was used with the initial cubic cell parameters set to $a = b = c = 11.99$ Å, the temperature was set at $T = 400\ K$ and was maintained using a Nosè-Hoover thermostat and a barostat maintained pressure of 1 atm.[105]

The Gaussian Augmented Plane Wave method (GAPW) was used for the calculation of energies and forces.[96] The Perdew-Burke-Ernzerhof (PBE) generalised gradient approximation was used including the DFT-D2 dispersion correction as proposed by Grimme.[76,166] The calculations used a double-ζ plus polarization Gaussian basis set (DZVP-MOLOPT-SR-GTH), a planewave cutoff of 500 Ry, and a relative cutoff of 60 Ry.[167] The Mulliken charge[188] was calculated on each atom throughout the trajectory.

Each calculated trajectory was 20 ps long, with a timestep of 0.5 fs, the first 5 ps of each trajectory were treated as an equilibration time, and was not considered in subsequent analysis. In total 300 ps of trajectory time was collected for each ionic system, which resulted in 225 ps of analysable trajectory time per ion.

4.3 Results

Each AIMD trajectory generated output files with bonding, coordination and charge information for each timestep, it was therefore possible to identify and track the movement of hydroxides across the timescale of a trajectory. Initially all trajectories were analysed according to the methodology described in **Chapter 3.4.1** to gain information on the bonding and coordination of the first solvation shell. Additional analysis was done, as described below, to provide information on the movement of hydroxide ions, proton transfer events and hydroxide coordination.

For consistency the first solvation shell cutoff for the hydroxide environments was maintained as those identified in **Chapter 3** for the aquo complexes. While the pH of the storage ponds was kept between pH 10 and 12, the inclusion of two hydroxide ions into the simulations presented herein result in a pH of 14, due to the relatively smaller number of water molecules in the simulation cells. The cutoff was used to calculate the total number of oxygens coordinated to the central metal ion, and to identify hydroxide coordination to the ion. The analysis method described below was based on Mg^{2+} dihydroxide environments, however testing was done with the Ca^{2+} and Sr^{2+} structures which indicated the same results.

4.3.1 Hydroxide Analysis Method

4.3.1.2 Identifying Hydroxides

A representative magnesium dihydroxide system is used to illustrate the analysis approach used for all AIMD trajectories involving hydroxides in this thesis. Each oxygen in the simulation cell is numbered, and the calculated Mulliken charge is used to differentiate the hydroxide

oxygens, O_{OH}, from water oxygens, O_w. An example of how the number of the oxygens associated with hydroxides, n_O, varies over an AIMD trajectory is shown in **Figure 4.1**.

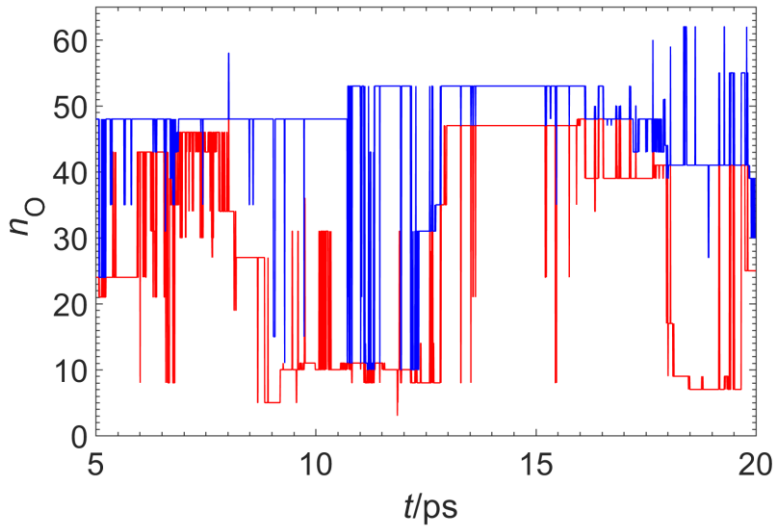

Figure 4.1: The hydroxide oxygen number, n_O, changing over a representative 15ps Mg^{2+} AIMD trajectory, for both hydroxides.

As is evident from **Figure 4.1** there is a large amount of variation in n_O followed by periods of stability. The change in n_O indicates that the hydroxides migrate through the water of the simulation cell by proton transfer, rather than by hydroxide migration. If hydroxide migration were the main method of hydroxide transport, then n_O would not change as the simulation progressed.

The mechanism of proton transfer through water is known as the Grotthuss mechanism[189], and has previously been thought of as a stepwise process whereby a proton from a water molecule transfers to a OH^- or from a H_3O^+ to a water molecule. However, more recently this mechanism has been examined and the mechanism of transfer of charge through water is no longer thought to be stepwise, but rather through specific chains of water molecules known as proton wires.[178,190,191] Bursts of activity involving several protons along the proton wires leads to a new hydroxide, followed by periods of stability. This mechanism appears to be evident in **Figure 4.1** where on multiple occasions n_O varies wildly before settling on a single n_O value for a period.

While the variation in the data presented in **Figure 4.1** potentially identifies the mechanism by which proton transfer occurs, for the purposes of quantifying proton transfer and the whereabouts of the hydroxides in the simulation cell it is most useful to only consider the periods of hydroxide stability. Therefore, the variation in the data where n_O varies or oscillates

between two numbers should be discounted for analysis purposes. Initially n_O was smoothed using the timescale prescribed in the Hofer *et al*.[177] direct method, where any transition in coordination which resulted in a new hydroxide but did not last 0.5 ps or 100 timesteps was removed, as shown in **Figure 4.2**. However, this is not an accurate representation of the different stable hydroxides which exist in **Figure 4.1**, and reduces the change in hydroxide to once over the 20 ps timescale.

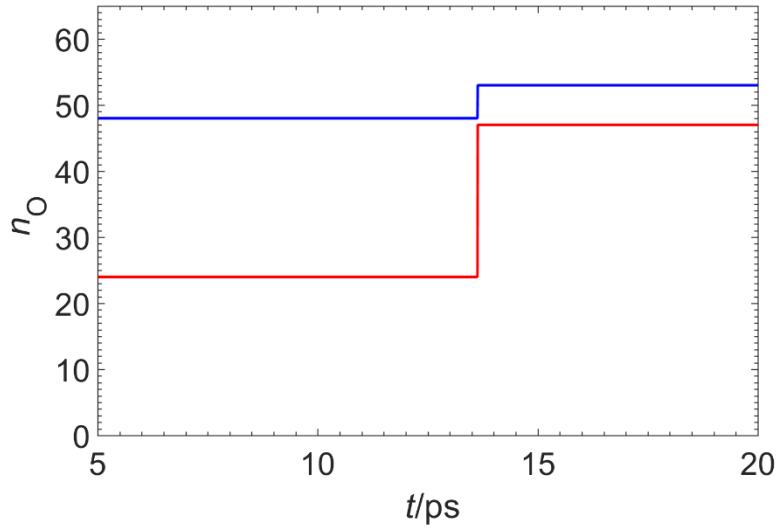

Figure 4.2: Hydroxide oxygen number, $n_{O,}$ against time ignoring any change which lasted less than 100 steps, for both hydroxides.

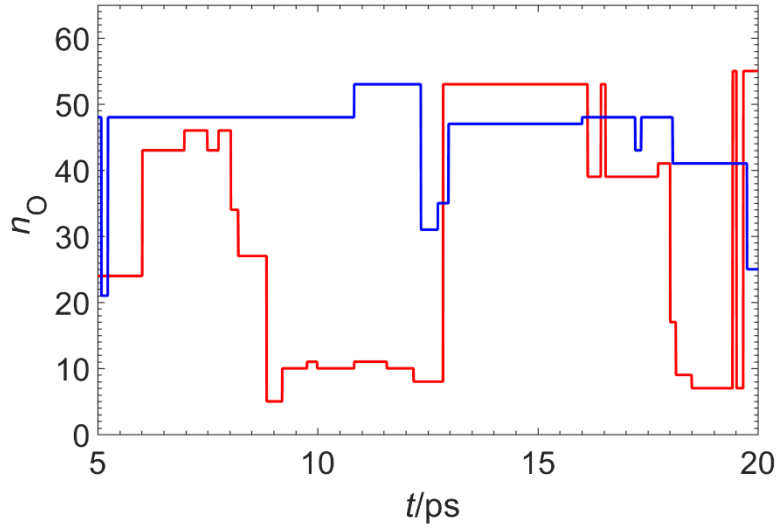

Figure 4.3: Hydroxide oxygen number, $n_{O,}$ against time ignoring any change which lasted less than 20 steps, for both hydroxides.

The entire Grotthuss mechanism is thought to take place on a timescale of 1 to 2 ps[189] with the bursts of activity which result in a full proton transfer occurring on a shorter timescale of

hundredths of a femtosecond.[178,179,192] However, there is evidence that proton transfer can occur on a timescale of < 0.1 ps.[189,193–195] Therefore, an alternative smoothing value of 0.1 ps, equivalent to 20 steps, was used to identify proton transfers, as shown in **Figure 4.3**. This smoothing value appears to have identified the periods of hydroxide stability, as evidenced in **Figure 4.1**, and was also verified against other AIMD trajectories to confirm it was an appropriate value to use in the analysis of hydroxide systems.

4.3.1.3 First Shell Hydroxide Coordination

Identifying each hydroxide at each step of the AIMD simulation means the distance of the hydroxide from the central ion and first solvation shell residence time, the total time each ion spent at a given CN, can be calculated. **Figure 4.4** is an example plot of the distance from the central Mg^{2+} ion of each hydroxide ion at each point of the simulation. However, this plot only relays that at each point there are two hydroxides, rather than where the hydroxides have travelled from in relation to the ion.

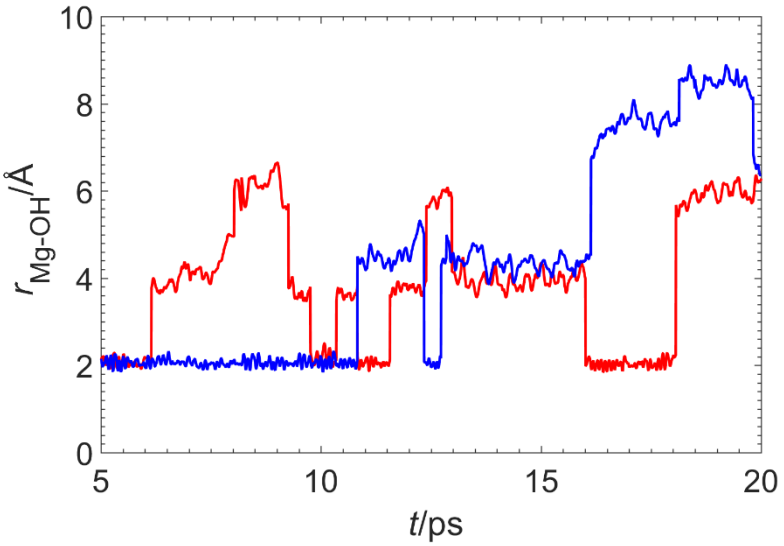

Figure 4.4: Mg—OH distance for each hydroxide at each step of a representative 15 ps AIMD trajectory.

The distance of each hydroxide from the metal ion is used to summarise if the hydroxide is in the first solvation shell, as in **Figure 4.5**, as an alternative to **Figure 4.4**. Both the total Mg—O coordination, and Mg—O_{OH} CN, and how they vary across a trajectory are shown in **Figure 4.5**.

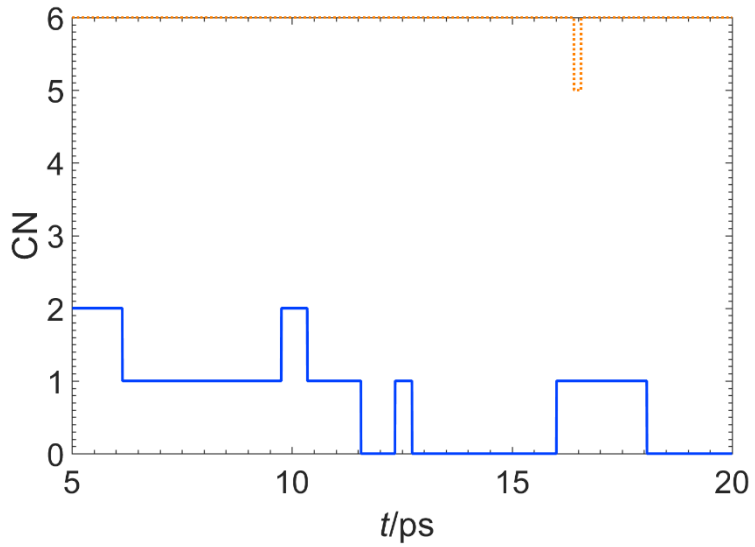

Figure 4.5: Coordination Number (CN) plot for total first shell CN (orange dotted line) and hydroxide first shell CN (blue solid line) for a representative 15 ps Mg^{2+} dihydroxide AIMD trajectory.

4.3.1.4 Identifying Proton Transfer Events

The process of a proton transferring which generates a new hydroxide, or Proton Transfer Event (PTE), can be quantified in relation to the distance from the ion that the new hydroxide is identified. Initially a smoothing value of 20 ps was used on the AIMD trajectory data to identify any true PTEs. However, due to the variation in **Figure 4.1** of the unsmoothed n_o, three smoothing values, of 10 steps, 20 steps and 30 steps, equivalent to 0.05 ps, 0.1 ps and 0.15 ps, were used to detect PTEs.

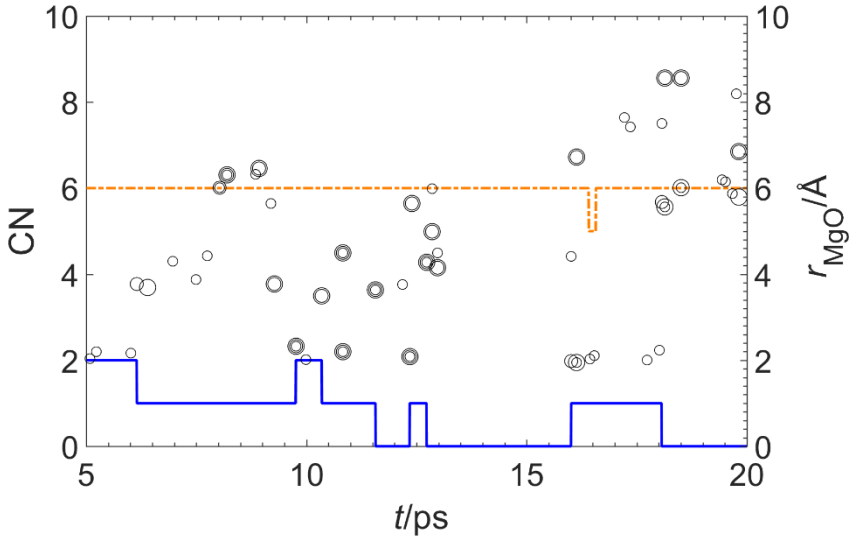

Figure 4.6: Total trajectory plot for Mg^{2+} dihydroxide system showing total CN (orange dashed line), hydroxide CN in the first shell (blue solid line), and PTEs based on the (○), 20 (○) or 30(○) step smoothing value. PTEs are plotted at the distance which the new hydroxide appears.

Figure 4.6 presents the total first shell coordination number, total hydroxide coordination number in the first shell and the circles each represent a PTE at the distance from the ion that the proton was donated from. The size of the circle indicates the smoothing value which detected the PTE, 10 (○), 20 (○) or 30 (○). When visually inspecting the data used in **Figure 4.6** for which smoothing value was the most appropriate, the 10 step smoothing value resulted in PTEs being identified which were a result of bond vibration rather than proton transfer, while the 30 step smoothing proved to be overcautious and resulted in not identifying PTEs which had occurred. The initially chosen 20 step smoothing value proved to be the most robust value with which to find true PTEs in an AIMD trajectory.

While the information presented in **Figure 4.6** is accurate it does not tell us if the proton is transferring into or out of the first solvation shell. There are four possibilities for proton transfer which relate the direction of proton transfer to the first solvation shell cutoff. Proton transfer can either be:

1. 1^{st} shell to 1^{st} shell (○) – this results in a new hydroxide in first shell and number of hydroxides in the first solvation shell staying the same.
2. 1^{st} shell to 2^{nd} shell (Δ) – this results in a new hydroxide in first solvation shell and the number of hydroxides in the first solvation shell increases.
3. 2^{nd} shell to 2^{nd} shell (○) – this results in a new hydroxide outside the first solvation shell with no change in the number of hydroxides in the first solvation shell.
4. 2^{nd} shell to 1^{st} shell (∇) – this results in a new hydroxide outside the first solvation shell and the number of hydroxides in the first solvation shell decreases.

The intrashell proton transfers are marked with the same symbol, ○, whereas the intershell proton transfers are indicated by arrows in the direction of proton transfer across the first shell cutoff. Collating all the information regarding coordination of the first solvation shell and proton transfers it is possible to present an entire AIMD trajectory on a single graph. As in **Figure 4.7**, which summarises an AIMD trajectory for Mg^{2+} with 2 hydroxides and 62 water molecules, displaying both the total and hydroxide CN, the first shell cutoff and classifies the PTEs at the distance they occur.

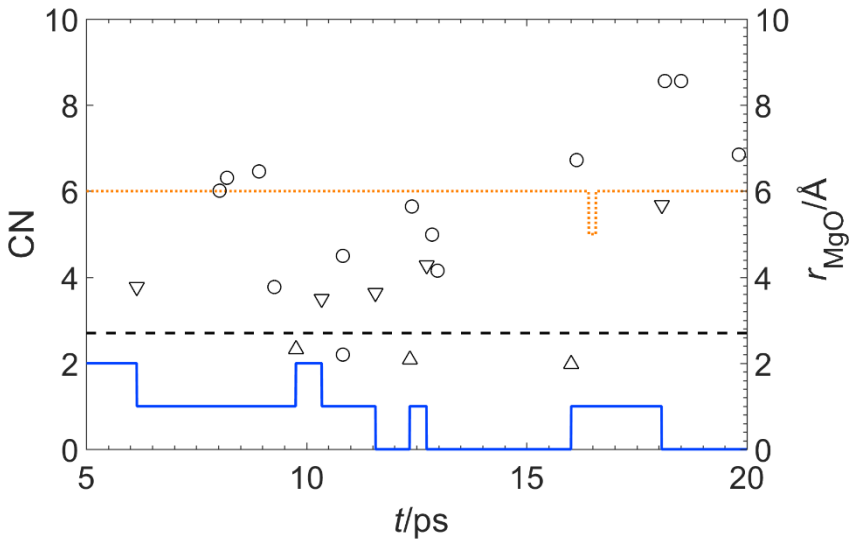

Figure 4.7: Total (dotted orange line) and hydroxide (solid blue line) coordination numbers, and proton transfer events (Δ: 1st shell → 2nd shell, ∇: 2nd shell → 1st shell, ○: intrashell) for an example Mg^{2+} dihydroxide AIMD trajectory. The dashed black line indicates the first shell cutoff distance of 2.7 Å.

4.3.2 Characterisation of Alkaline Earth Dihydroxide Complexes

To investigate alkaline earth metals in dihydroxide environments DFT and AIMD were employed. The dihydroxide starting structures were generated by taking snapshots of aquo AIMD trajectories of Mg^{2+}, Ca^{2+} and Sr^{2+}, from **Chapter 3**, and removing two protons from waters. These structures then underwent cell optimisation to optimise both the cell size and the geometry. The initial hydroxide placement was varied such that the starting structure had either both hydroxides coordinated to the ion, one hydroxide coordinated the ion or the ion was uncoordinated by hydroxides. This resulted in 5 structures for each dihydroxide starting placement, a total of 15 unique dihydroxide environments per metal ion.

RDFs were calculated over the entire 225 ps simulation time, as shown in **Figure 4.8**, which gave peak positions of 2.12, 2.41 and 2.59 Å for Mg^{2+}, Ca^{2+} and Sr^{2+} respectively. There is a slight change in the peak positions compared to the aquo simulations with Mg^{2+} peak increasing by 0.02 Å and peaks for Ca^{2+} and Sr^{2+} decreasing by 0.03 and 0.04 Å respectively. The single peak indicating the first solvation shell shows that in terms of bond length the metal hydroxide bonds, M—O_{OH}, and metal water bonds, M—O_w, are indistinguishable from the RDFs.

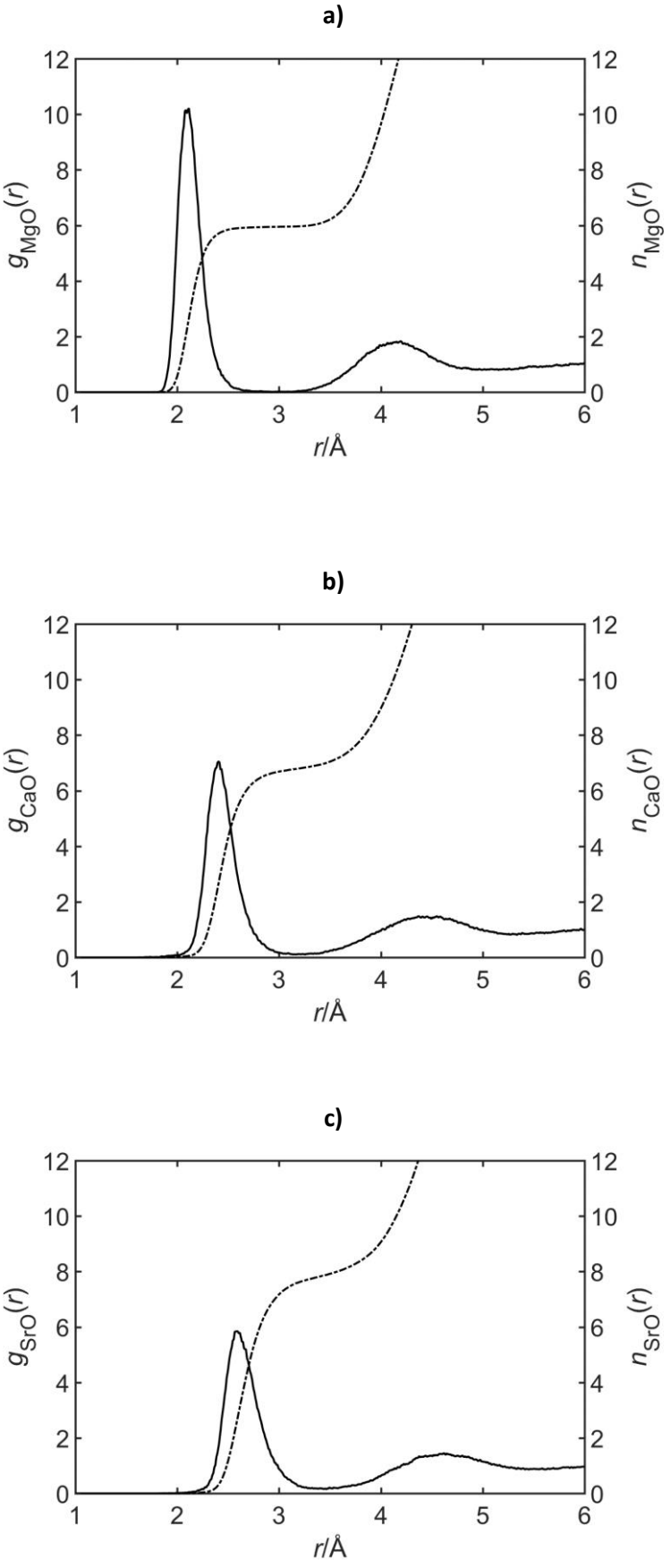

Figure 4.8: M—O radial distribution functions, *g*(r), generated using a total of 225 ps of simulation time for the dihydroxide environment of **a)** Mg^{2+}, **b)** Ca^{2+}, **c)** Sr^{2+}.

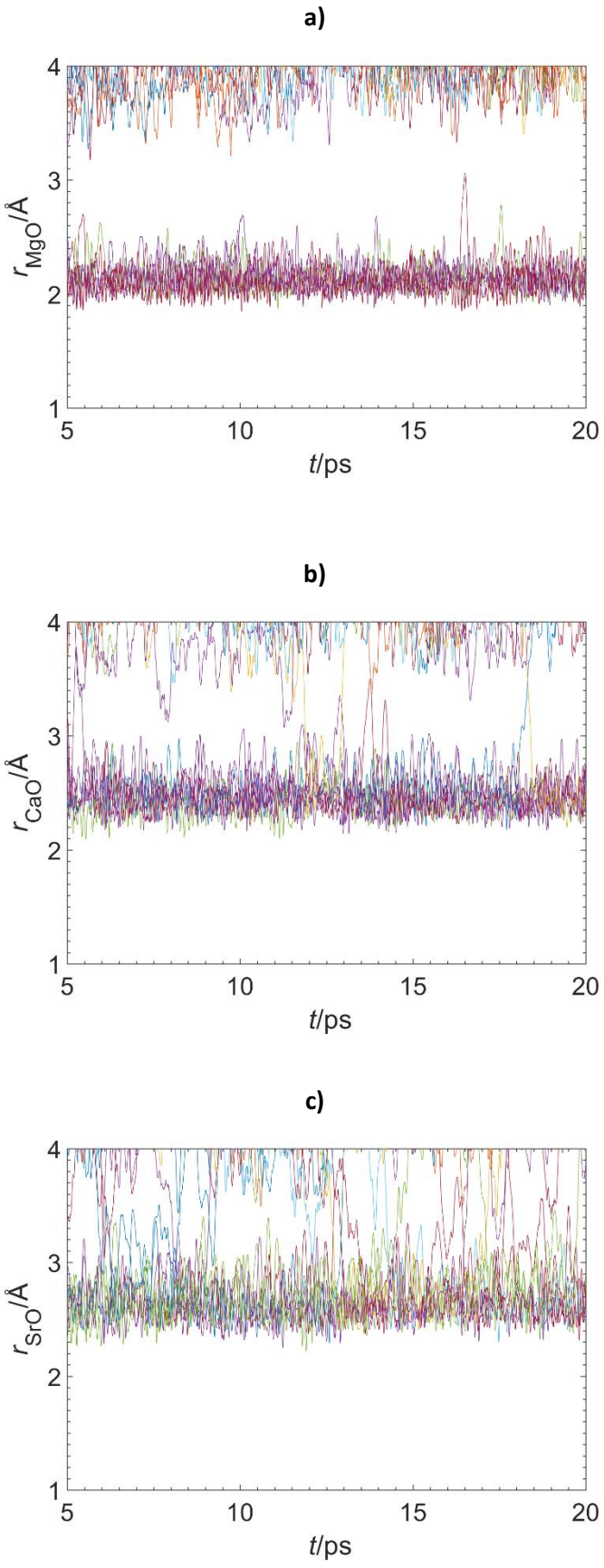

Figure 4.9: Example of a first shell plot for all M—O bonds across the time of a trajectory at a distance <4 Å for **a)** Mg^{2+}, **b)** Ca^{2+}, **c)** Sr^{2+} in a dihydroxide environment.

Examples of the first shell trajectory for all M—O bonds at a distance of less than 4 Å from the central ion of either Mg^{2+}, Ca^{2+}, Sr^{2+} in a dihydroxide environment are shown in **Figure 4.9a** to **c**. The calculated average M—O bond lengths for each trajectory are summarised in **Table 4.1**, the total and hydroxides CNs for each trajectory and the overall CN, hydroxide CN and bond lengths averaged over 225 ps are also given.

Table 4.1: Calculated M—O separations ($r_{M\text{-}O}$), total coordination numbers (CN) and hydroxide coordination numbers (CN_{OH}) and accompanying standard deviation (SD) for each AIMD trajectory (Traj.) considered in this study.

Traj.	r_{M-O} (Å)			CN			CN_{OH}		
	Mg^{2+}	Ca^{2+}	Sr^{2+}	Mg^{2+}	Ca^{2+}	Sr^{2+}	Mg^{2+}	Ca^{2+}	Sr^{2+}
1	2.150	2.471	2.705	5.97	6.84	7.99	0.51	0.61	0.41
2	2.151	2.449	2.681	5.97	6.43	7.56	0.88	1.08	0.20
3	2.149	2.470	2.708	5.98	6.61	7.84	0.80	0.75	0.26
4	2.159	2.436	2.676	6.00	6.15	7.44	1.38	0.98	0.25
5	2.155	2.473	2.668	5.98	6.69	7.36	1.39	0.52	0.60
6	2.149	2.488	2.688	5.99	6.97	7.49	0.72	0.46	0.52
7	2.148	2.435	2.667	6.00	6.15	7.42	0.67	1.28	0.11
8	2.127	2.458	2.689	5.57	6.48	7.64	1.23	0.92	0.06
9	2.151	2.470	2.689	5.95	6.63	7.73	0.98	0.78	0.14
10	2.153	2.490	2.686	5.98	6.96	7.51	0.99	0.51	0.77
11	2.141	2.490	2.699	5.67	6.82	7.97	1.56	0.71	0.05
12	2.152	2.472	2.681	6.00	6.55	7.53	0.98	1.03	0.13
13	2.154	2.481	2.679	5.99	6.83	7.61	0.97	0.60	0.15
14	2.155	2.471	2.682	5.85	6.72	7.63	1.29	0.35	0.08
15	2.147	2.479	2.683	5.99	6.82	7.47	0.38	0.32	0.57
Mean	2.150	2.469	2.685	5.93	6.64	7.61	0.98	0.73	0.29
(SD)	(0.008)	(0.018)	(0.012)	(0.13)	(0.26)	(0.19)	(0.34)	(0.28)	(0.23)

Compared to the aquo environments explored in **Chapter 3** the average M—O bond length for Mg^{2+} increased by ~0.02 Å, while the average bond length for Ca^{2+} and Sr^{2+} decreased by ~0.04 Å and 0.01 Å, respectively. In all cases the inclusion of hydroxide species resulted in a decrease in mean coordination number of 0.07, 0.86 and 0.39 for Mg^{2+}, Ca^{2+} and Sr^{2+} when compared to the aquo complexes. This reduction in CN can be understood when examining the results presented in **Table 4.2** which reports the residence times of each CN identified for each ion as a percentage of total trajectory time. As in **Chapter 3**, Ca^{2+} exhibited the greatest lability, with comparable time spent 6 and 7 coordinated in the dihydroxide environment, compared to equal time spent as 7 and 8 coordinated in aquo complexes. This shift in coordination

environments combined with higher 9 coordinated Ca^{2+} not found is reflected in the substantial reduction in the average CN reported in **Table 4.1**. The Sr^{2+} complex, showed a propensity for an 8 coordination complex, also spent significant time in 7 coordinated, but the higher CN of 10 was not seen. While Mg^{2+} retained a CN close to 6, the time spent at lower CN of 4 and 5 increased compared to the aquo environments.

Table 4.2: Percentage residence time of different coordination environments (CN) averaged over a total of 225 ps for each ion.

Cation	CN					
	4	5	6	7	8	9
Mg^{2+}	0.13	6.54	93.33	0.00	0.00	0.00
Ca^{2+}	0.00	0.21	41.29	52.46	6.03	0.00
Sr^{2+}	0.00	0.21	2.67	37.97	54.16	4.99

The decrease in total CN for Mg^{2+} with the inclusion of hydroxides is not as pronounced as suggested by the gas phase calculations of Kluge *et al*.[182] and the decrease in CN for Ca^{2+} was not evidenced in the studies of Felmy *et al*.[183] However, the CN decrease for Sr^{2+} mirrors that found in previous literature.[183,186] Both Kluge *et al*.[182] and Felmy *et al*.[183] used gas phase DFT calculations with only the first shell waters explicitly included. It is likely that the explicit inclusion of 62 water molecules in the AIMD solvation model more accurately models the bulk solvent and allow the water molecules to structure into first and second shells around the central ion as shown in the RDFs of **Figure 4.7**.

The percentage residence time of each hydroxide coordination environment is summarised in **Table 4.3** with the mean hydroxide coordination number (CN_{OH}) averaged over 225 ps for each ion. The CN_{OH} for Mg^{2+} is close to one, however a static view of the hydroxide coordination number is not accurate when examining the percentage residence times in **Table 4.3**: while Mg^{2+} spends half the trajectory time coordinated to one hydroxide, the remaining time is divided between dihydroxide and uncoordinated species. The hydroxide coordination is similarly dynamic for Ca^{2+} with a lower CN of 0.73 indicating that it is not often coordinated by a hydroxide, however the percentage residence times in **Table 4.3** show that for 57 % of the trajectory time Ca^{2+} is coordinated by either one or two hydroxide ions. A low coordination number of 0.29 was found for Sr^{2+} which spends the majority of trajectory time uncoordinated by hydroxides for the majority, although both the monohydroxide and dihydroxide species are found, albeit the latter only for 3% of the simulation time.

Table 4.3: Percentage residence time of different hydroxide coordination environments, (CN_{OH}) along with mean coordination number < CN_{OH}> standard deviation in parentheses, averaged over a total of 225 ps for each ion.

Cation	CN_{OH}			<CN_{OH}>
	0	1	2	
Mg^{2+}	23.45	54.95	21.60	0.98 (0.34)
Ca^{2+}	42.99	41.36	15.65	0.73 (0.28)
Sr^{2+}	74.22	23.00	2.78	0.29 (0.23)

When examining this data in the context of the reduced charge density of the alkaline earth metals, as in **Figure 4.10**, as the ions get larger the strength of the interaction of the ion with both water and hydroxide species reduces. This is reflected in both the increased lability of water CN and the decrease in hydroxide coordination from Mg^{2+} to Sr^{2+}. The charge dense Mg^{2+} ion preferentially binds to one hydroxide which replaces a water to maintain a CN of 6 as in the aquo complexes, rather than ejecting a 6th water to the second solvation shell. Ca^{2+} also preferentially binds to a single hydroxide, however its reduction in charge density also leads to a reduction in coordination number from aquo to hydroxide species. The charge density of Sr^{2+} has reduced such that it is no longer energetically favourable for a hydroxide to bind to the ion and only small reduction in CN is seen compared to that of the aquo complex

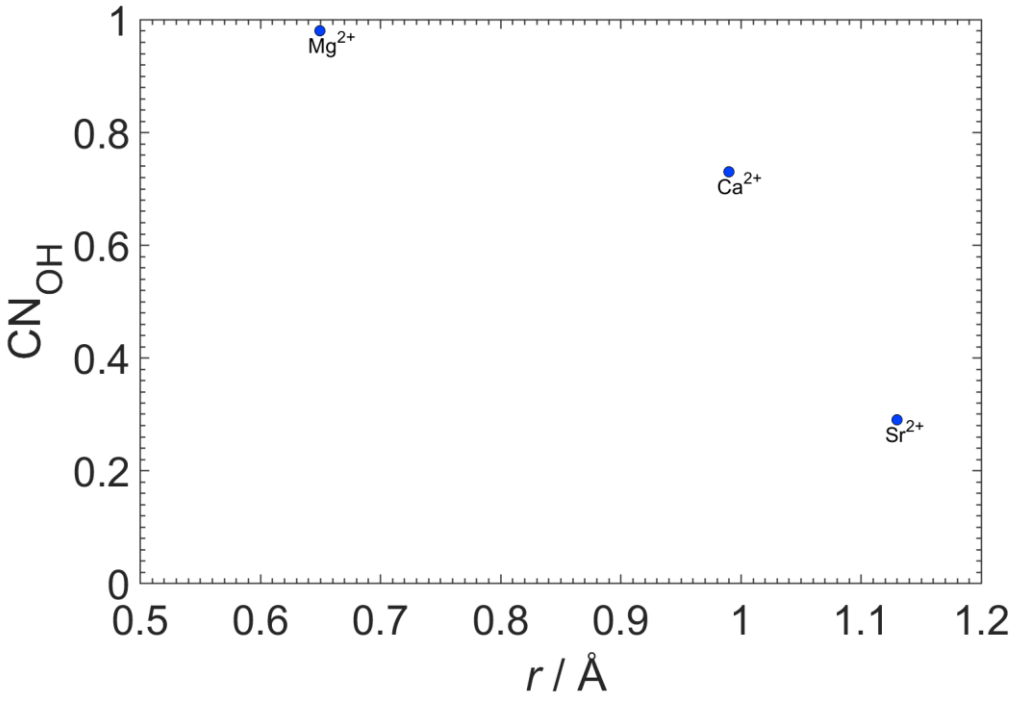

Figure 4.10: The hydroxide coordination (CN_{OH}) against the ionic radius[123] of each cation Mg^{2+}, Ca^{2+}, Sr^{2+}.

4.3.2.1 Dynamics of Hydroxide Coordination

Each trajectory has been analysed in accordance with the methodology described in **Section 4.3.1**. Care was taken to ensure that the starting position of the hydroxides did not influence the variation in the position of the hydroxides in the AIMD trajectories. The full trajectory plots are shown in **Figure 4.11** to **Figure 4.19**, indicating total and the hydroxide coordination numbers. These show the significant variation in both across the course of each simulation, particularly prevalent for the larger Ca^{2+} and Sr^{2+} ions. The total CN exhibits higher values when the hydroxide CN is low as discussed previously. The PTEs for each trajectory are indicated on **Figure 4.11** to **Figure 4.19** with the position of each symbol indicating the distance between the ion and the oxygen in the water molecule donating the proton. While in almost all cases a change in hydroxide coordination is accompanied by a PTE, there are a few occasions where no PTE takes place, such as in **Figure 4.18b** at 8 ps, and the hydroxide coordination change is a result of hydroxide migration into or out of the first solvation shell.

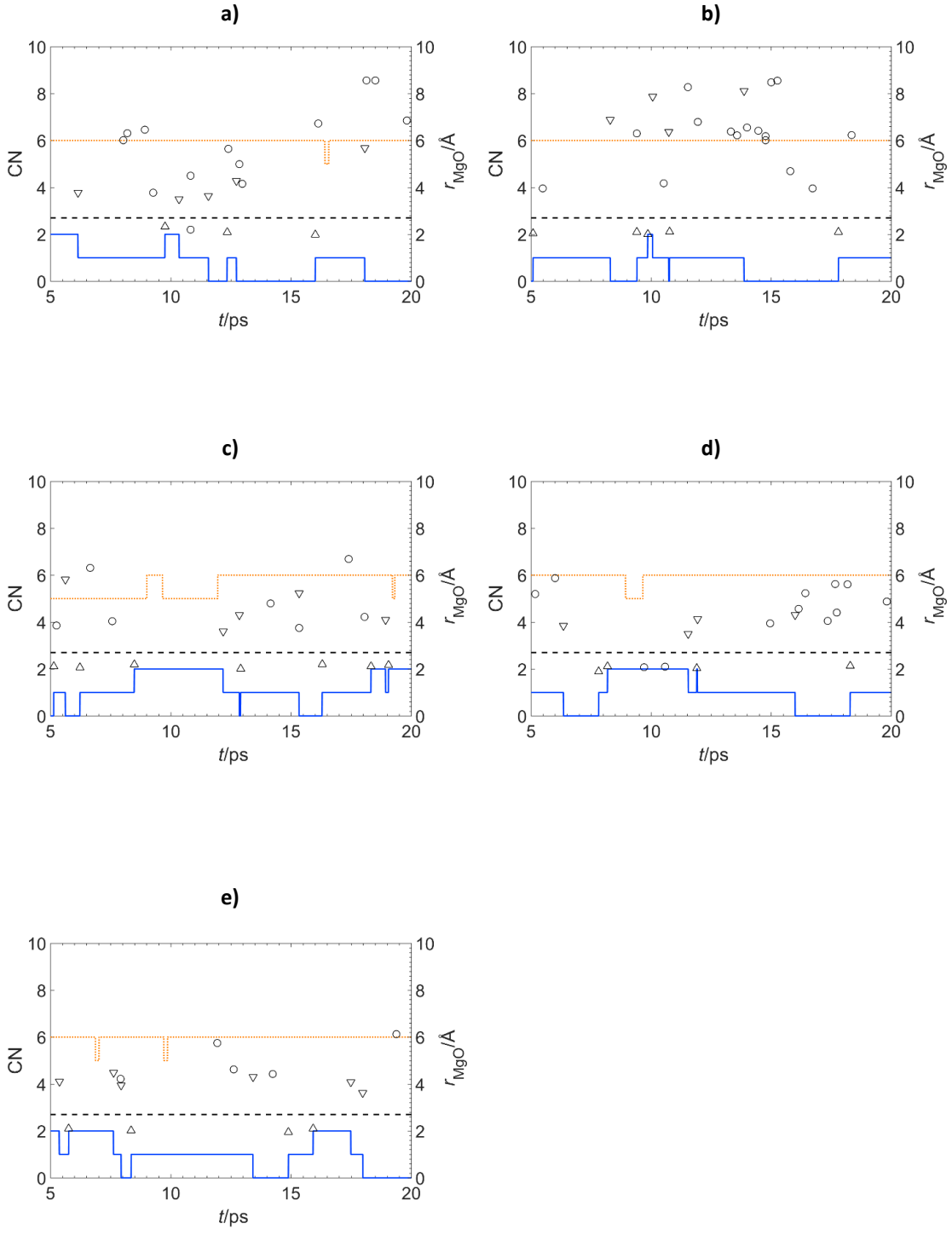

Figure 4.11: Total (dotted orange) and hydroxide (solid blue) coordination number and proton transfer events (Δ: 1st shell → 2nd shell, ∇: 2nd shell → 1st shell, ○: intrashell) for each Mg^{2+} 15 ps dihydroxide AIMD trajectory where both hydroxides started in the first solvation shell. The dashed black line indicates the first shell cutoff distance of 2.7 Å.

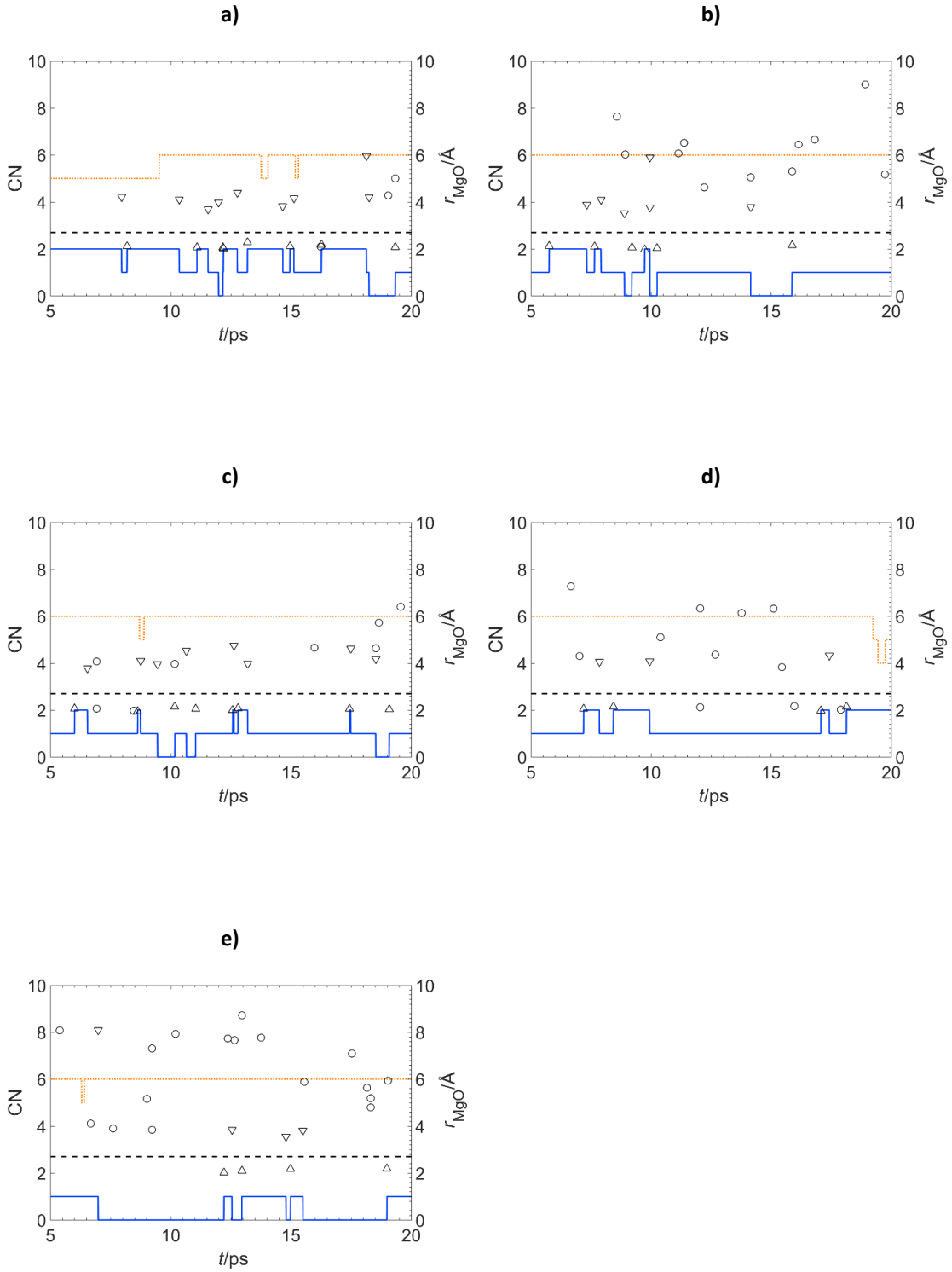

Figure 4.12: Total (dotted orange) and hydroxide (solid blue) coordination number and proton transfer events (Δ: 1st shell → 2nd shell, ∇: 2nd shell → 1st shell, ○: intrashell) for each Mg^{2+} 15 ps dihydroxide AIMD trajectory where neither hydroxide started in the first solvation shell. The dashed black line indicates the first shell cutoff distance of 2.7 Å.

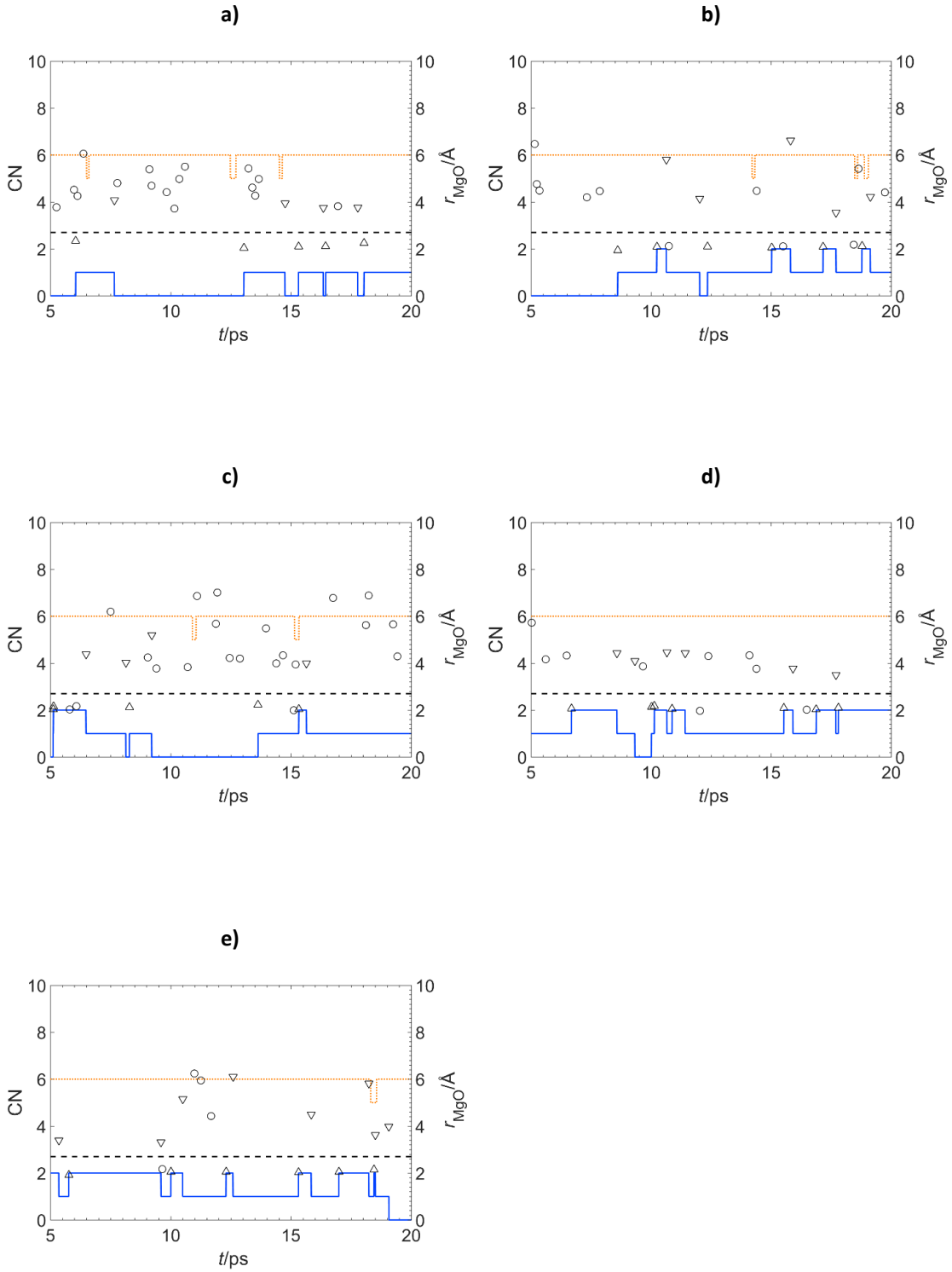

Figure 4.13: Total (dotted orange) and hydroxide (solid blue) coordination number and proton transfer events (Δ: 1st shell → 2nd shell, ∇: 2nd shell → 1st shell, ○: intrashell) for each Mg^{2+} 15 ps dihydroxide AIMD trajectory where one hydroxide started in the first solvation shell. The dashed black line indicates the first shell cutoff distance of 2.7 Å.

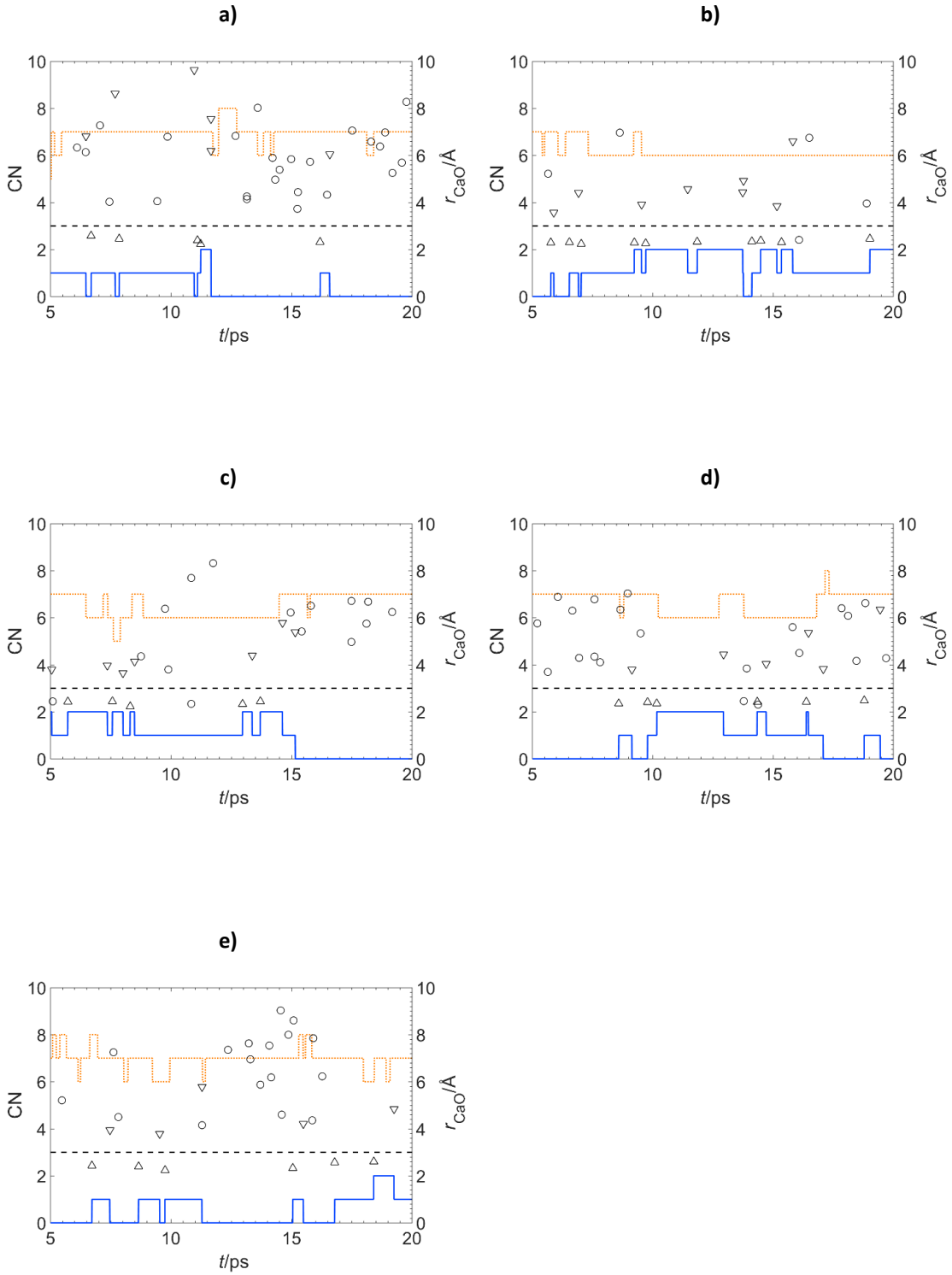

Figure 4.14: Total (dotted orange) and hydroxide (solid blue) coordination number and proton transfer events (Δ: 1st shell → 2nd shell, ∇: 2nd shell → 1st shell, ○: intrashell) for each Ca^{2+} 15 ps dihydroxide AIMD trajectory where both hydroxides started in the first solvation shell. The dashed black line indicates the first shell cutoff distance of 3.0 Å.

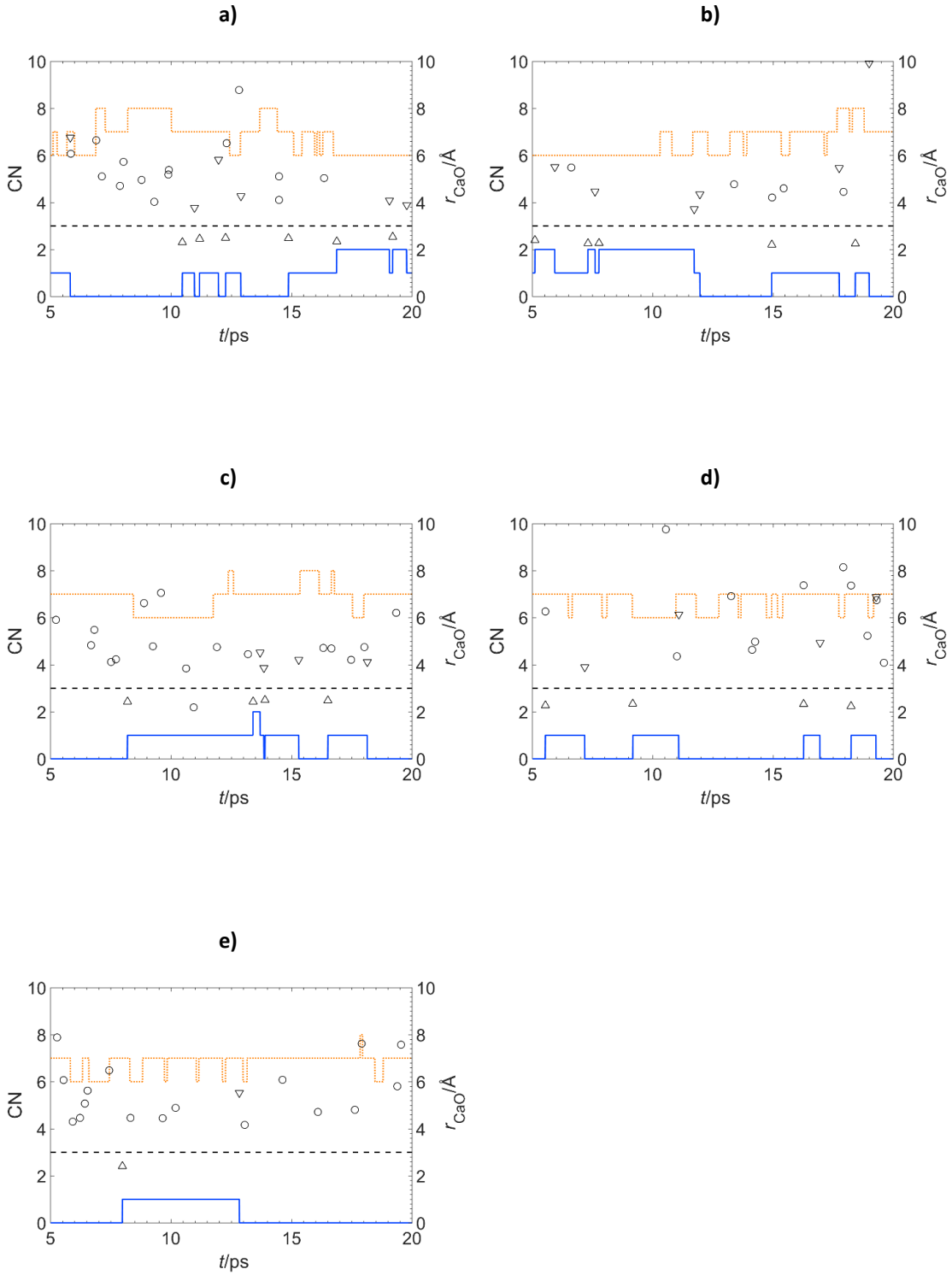

Figure 4.15: Total (dotted orange) and hydroxide (solid blue) coordination number and proton transfer events (Δ: 1st shell → 2nd shell, ∇: 2nd shell → 1st shell, ○: intrashell) for each Ca^{2+} 15 ps AIMD dihydroxide trajectory where neither hydroxide started in the first solvation shell. The dashed black line indicates the first shell cutoff distance of 3.0 Å.

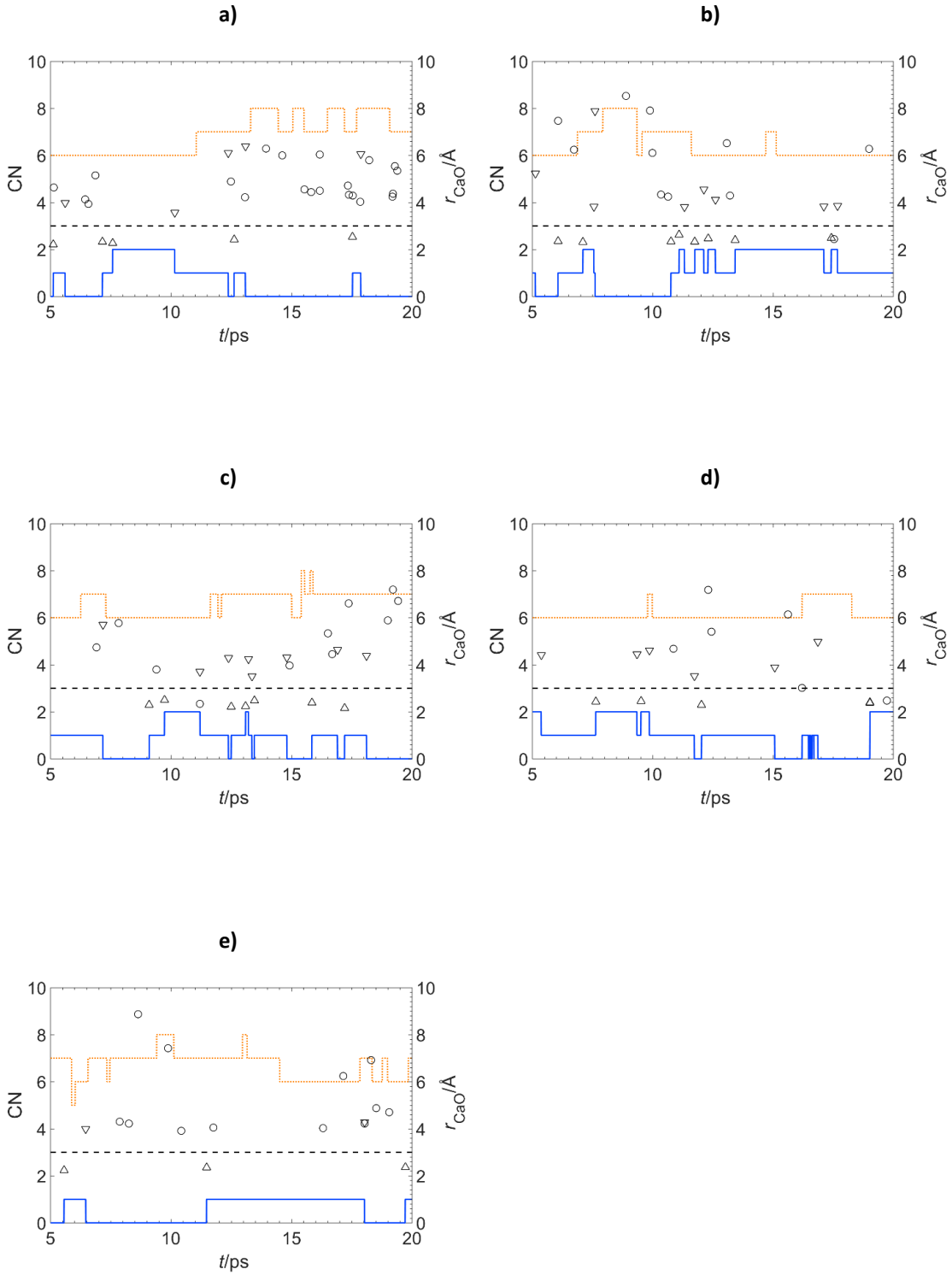

Figure 4.16: Total (dotted orange) and hydroxide (solid blue) coordination number and proton transfer events (Δ: 1st shell → 2nd shell, ∇: 2nd shell → 1st shell, ○: intrashell) for each Ca^{2+} 15 ps AIMD dihydroxide trajectory where one hydroxide started in the first solvation shell. The dashed black line indicates the first shell cutoff distance of 3.0 Å.

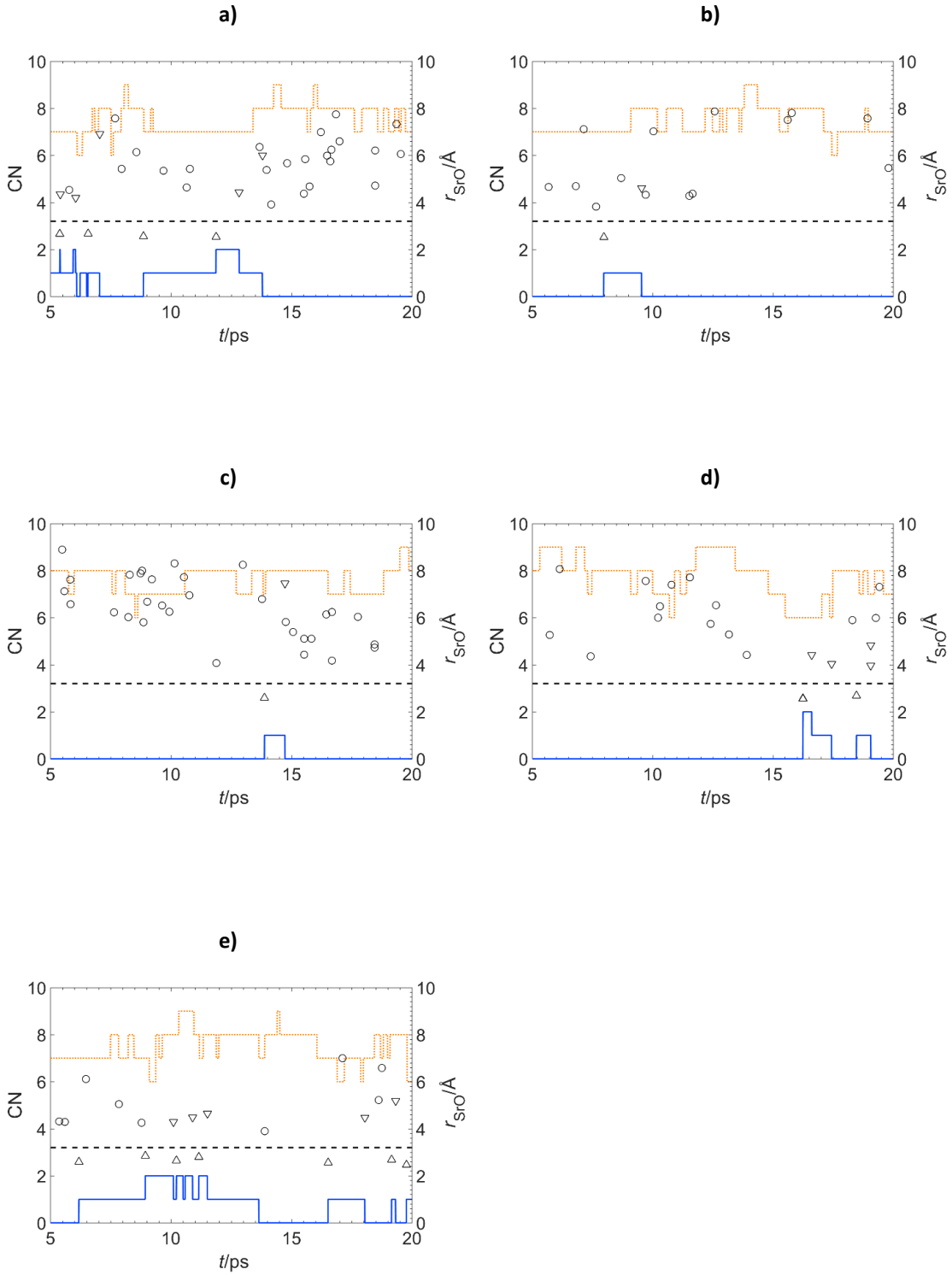

Figure 4.17: Total (dotted orange) and hydroxide (solid blue) coordination number and proton transfer events (Δ: 1st shell → 2nd shell, ∇: 2nd shell → 1st shell, ○: intrashell) for each Sr^{2+} 15 ps AIMD dihydroxide trajectory where both hydroxides started in the first solvation shell. The dashed black line indicates the first shell cutoff distance of 3.2 Å.

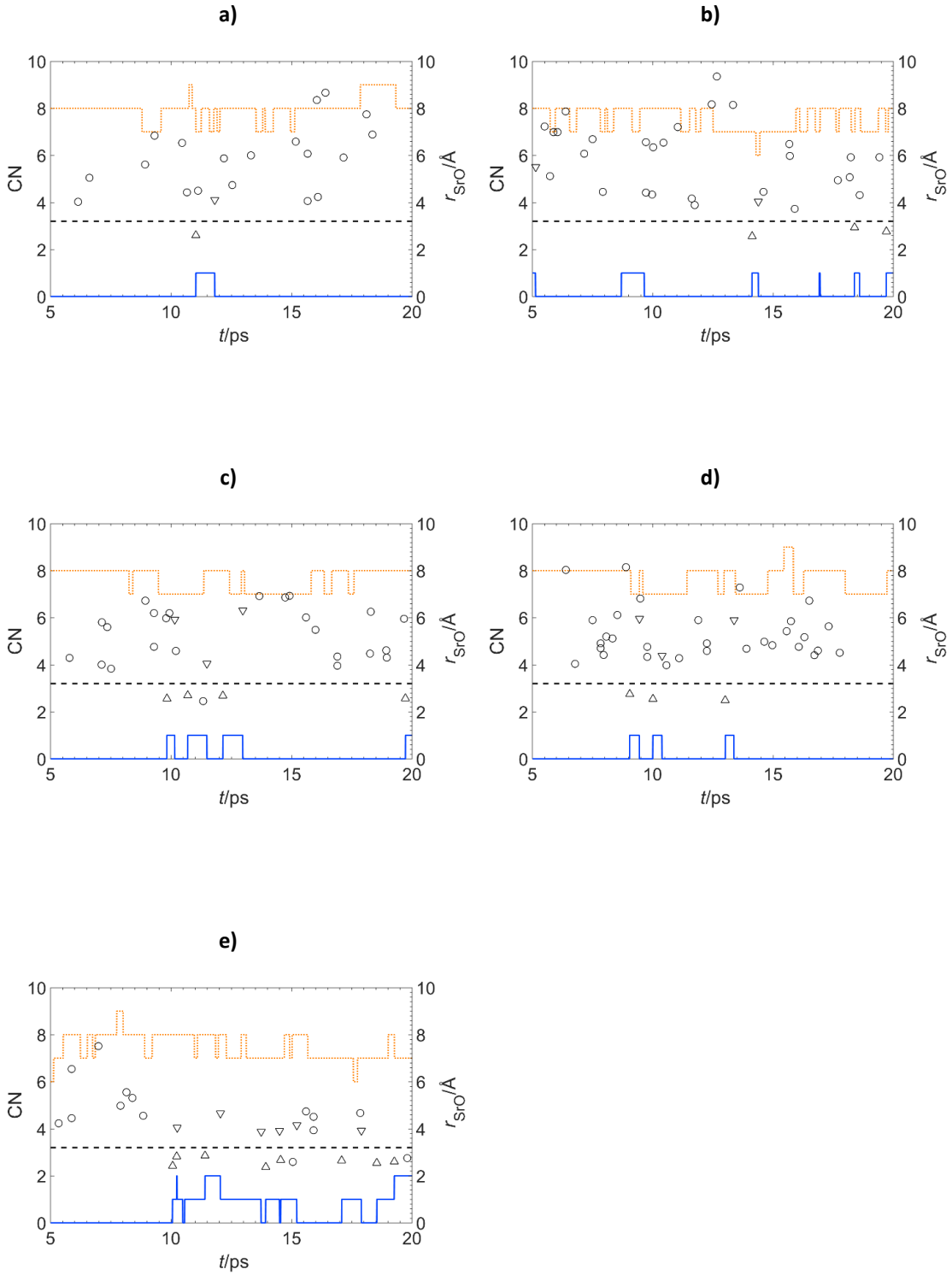

Figure 4.18: Total (dotted orange) and hydroxide (solid blue) coordination number and proton transfer events (Δ: 1st shell → 2nd shell, ∇: 2nd shell → 1st shell, ○: intrashell) for each Sr^{2+} 15 ps AIMD dihydroxide trajectory where neither hydroxide started in the first solvation shell. The dashed black line indicates the first shell cutoff distance of 3.2 Å.

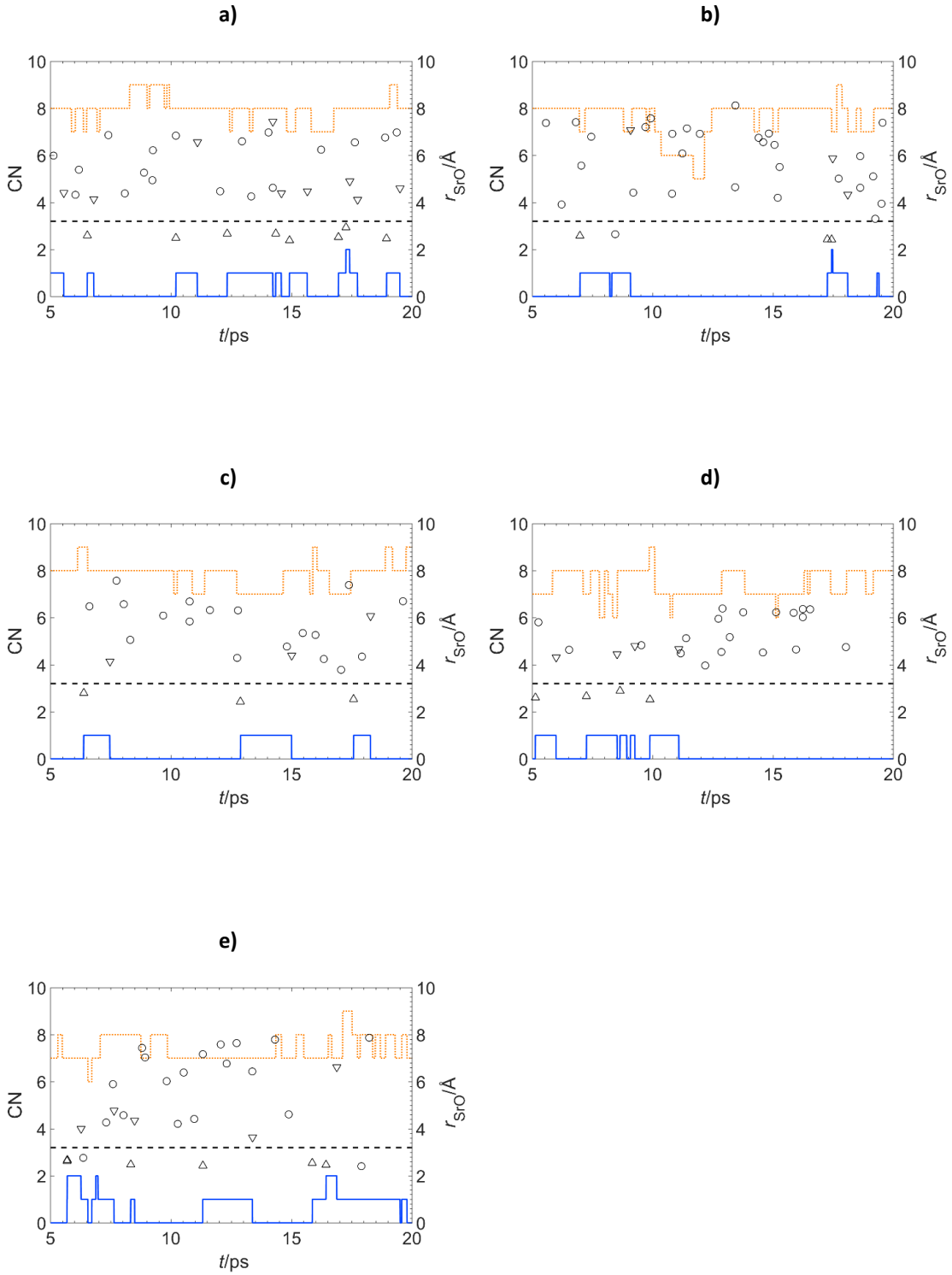

Figure 4.19: Total (dotted orange) and hydroxide (solid blue) coordination number and proton transfer events (Δ: 1st shell → 2nd shell, ∇: 2nd shell → 1st shell, ○: intrashell) for each Sr^{2+} 15 ps AIMD dihydroxide trajectory where one hydroxide started in the first solvation shell. The dashed black line indicates the first shell cutoff distance of 3.2 Å.

Table 4.4: Number and type of proton transfer events (PTE), obtained from 225 ps of AIMD data for each ion. Percentage values are given in parentheses

Cation	PTE				
	1^{st}—1^{st}	1^{st}—2^{nd}	2^{nd}—1^{st}	2^{nd}—2^{nd}	Total
Mg^{2+}	15 (4)	77 (24)	79 (24)	155(48)	326
Ca^{2+}	9 (2)	80 (22)	82 (22)	200 (54)	371
Sr^{2+}	6 (1)	59 (14)	55 (13)	306 (72)	426

The total number of PTEs found during the simulations is summarised by the direction of proton transfer, with respect to the first solvation shell cut off, in **Table 4.4**. There is a significant increase in the number of PTEs from Mg^{2+} to Sr^{2+}, due to the increase in intrashell PTEs outside the first solvation shell. The intrashell PTEs in the first solvation shell decrease down the group, although this should be considered in the context of a lower probability of a hydroxide coordinating to the large metal ions, as in **Table 4.3**. For all the ions the number of PTEs involving a transfer into the first solvation shell is generally equal to the number involving transfer out of the shell, further indication of the lack of bias in the starting configuration. The total number of intershell PTEs also reduces with increasing ion size and this decrease can be explained with the results presented in **Table 4.3** indicating the reduced probability of a hydroxide coordinating with the larger ions.

The increase in intrashell PTEs outside the first solvation shell can partly be attributed to the increase in hydroxide species outside of the first solvation shell for the large ions. However, this does not explain the corresponding increase in total PTEs. The classical simulations of Hellström and Behler[196] have demonstrated that proton transfer from water molecules directly coordinating to an Na^{+} ion is less likely than that from a bulk water molecule. This difference in probability is due to an increase energetic barrier to donation when the water molecules are coordinated to the ion. The authors also suggested that, generally, proton transfer is affected by the change in hydrogen bonding in waters surround the ion, compared to the waters in the bulk. As is seen **Figure 4.8a** and **4.9a** the Mg^{2+} structures water into well-defined first and second solvation shells, more than Ca^{2+} and Sr^{2+}, which provides credence to the argument that a well-structured solvation environment suppresses proton transfer, and explains the increase in PTEs for the large Ca^{2+} and Sr^{2+} ions.

4.3.2.2 Relative Energetics of Strontium Hydroxides

The static DFT simulations of strontium hydroxides using the meta-GGA TPSS exchange-correlation functional by Makkos *et al*.[187] used 22 explicit water molecules to represent the first and second hydration shells of the Sr^{2+} ion, with bulk solvation effects modelled using the COSMO continuum solvation model. These investigations found that the most stable dihydroxide species was just 3.0 kJ mol^{-1} higher in energy than the monohydroxide species.

To investigate if the energy difference could be replicated with the more realistic solvation structure used in the AIMD simulations, analogous complexes were optimised. Snapshots of the dynamic simulations with either one or two hydroxide species in the first solvation shell were optimised. To ensure calculated energies were comparable the simulation cell size was fixed to 11.99 Å. The results of the optimisations found that the complex with both hydroxides coordinated to the Sr^{2+} ion was 3.1 kJ mol^{-1} less stable than those with only one hydroxide coordinated to the ion, in excellent agreement with the previous study.

4.4 Conclusion

This chapter focuses on novel investigations of the coordination of alkaline earth metals in hydroxide environments. 225 ps of analysable AIMD trajectories were collected for the dihydroxide environments of the Mg, Ca and Sr ions. Initial structures were randomised by varying the hydroxide placement and optimised using the PBE functional with a DFT-D2 dispersion correction. AIMD simulations were carried out using Born-Oppenheimer molecular dynamics.

A robust analysis for dynamics of hydroxide movement through the simulation box over the timescale of an AIMD reaction was presented. This chapter also describes a novel way to analyse proton transfer events for them to be characterised for further discussion. The full analysis method was thoroughly tested on multiple chemical environments and is applicable to all other hydroxide environments beyond the alkaline earth metals to allow for easy comparison.

Bonding in the first solvation shell was characterised by averaging the radial distribution functions over the entire AIMD trajectory time and by calculating the average bond lengths of M—O, for M = Mg^{2+}, Ca^{2+} or Sr^{2+}. For both the total coordination and hydroxide coordination the percentage of trajectory time for each coordination mode was also calculated with an average total coordination number and average hydroxide coordination number.

The resulting data was compared to the aquo environments investigated in **Chapter 3** and in the context of the available literature. Overall a decrease in total CN with hydroxides of each metal ion system was found as a result of the improved solvation model used in the AIMD simulations compared to those of previous literature investigations. Changes in average bond length reflected those found in existing literature but in the context of both total and hydroxide coordination number identified a different trend. The average bond for magnesium complexes increased compared to its aquo complexes, in contrast the average bond length for both calcium and strontium complexes decreased in the hydroxide environments.

From the results presented in this chapter it could be inferred that in the higher pH environment, such as those of the nuclear waste storage ponds at Sellafield, magnesium and calcium are likely to exist as a mono or di hydroxide. However, in the case of strontium it will most likely not be present as a hydroxide. A further study investigating the competing interactions of multiple radionuclides in a hydroxide rich environment would further inform this.

Proton transfer events were quantified and found to be most prevalent in the strontium hydroxide systems, likely due to the lack of hydroxide coordination to the central ion. In all cases the intrashell proton transfers which occurred outside of the first solvation shell were most prevalent, with the numbers of proton transfer events from the first to second shell and vice versa roughly equal. This corroborates the Hellström and Behler[196] investigation which, although used a different methodology, found a similar pattern with PTEs most likely occurring away from the ion. 225 ps of analysable data was obtained to reduce the bias in the starting structures due to placement of the hydroxide ions, however there seem to be no correlation between the starting structure and the resulting level of PTEs and hydroxide CN when analysed.

Snapshots of the strontium dihydroxide AIMD simulations were optimised to obtain the energy difference of structures where the ion was coordinated by either one or both hydroxides were performed. A small energy difference between the two coordination modes was found, which was in excellent agreement with a previously reported DFT investigation.

The investigation presented in this chapter applies the solvation model developed in **Chapter 3** and expands it to a new area of interest; the solvation structure of the alkaline earth metals in the presence of hydroxide ions. The dynamics of the cations, has been thoroughly analysed to highlight the effects a hydroxide environment for the solvation structure of each alkaline earth metal.

Chapter 5: Aquo and Hydrated Hydroxide Complexes of UO_2^{2+}

In this chapter, the results of an investigation into the bulk solvation of the hydrated uranyl ion (UO_2^{2+}) in both the absence and presence of hydroxide are reported. 5 AIMD trajectories were simulated for each of the aquo, monohydroxide and dihydroxide environments and then summarised and compared to current literature. In addition, the dynamics and proton transfer events of the hydroxide systems are contrasted with the results from the alkaline earth metals presented in **Chapters 3** and **4**. As well as being industrially relevant, due to the prevalence of UO_2^{2+} in the nuclear waste storage ponds, the study of UO_2^{2+} was an opportunity to investigate a more complex dication, which has uranium centre in the +6 oxidation state.

5.1 Introduction

In the aqueous environment uranium readily forms uranyl (UO_2^{2+}) which has a linear structure, shown in **Figure 5.1**, and been found to be present in nuclear waste storage ponds as both aquo and hydroxide complexes, as well as carbonate species such as $UO_2(CO_3)_2^{2-}$ and $UO_2CO_3(OH)_3^-$.[6,34,197] At increasing pH uranyl complexation with hydroxide ions increases, species at a lower pH range of 3 to 6 include UO_2OH^+ and $(UO_2)_3(OH)_5^+$ whereas at a higher pH range of 9 to 12 complexes include $UO_2(OH)_3^-$, $(UO_2)_3(OH)_8^{2-}$ and $(UO_2)_3(OH)_{10}^{4-}$.[198,199] In addition to being contained in the ponds the uranyl ion is the dominant uranium species in contaminated groundwater systems around both reactor sites and uranium mines.[44] Due to the solubility and the strength of the metal-oxygen bonds in uranyl its presence in the ponds makes effective clean-up difficult.[38]

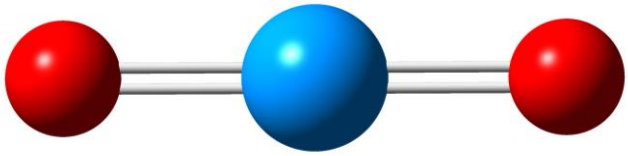

Figure 5.1: The structure of uranyl $[UO_2]^{2+}$.

Experimental techniques such as Extended X-ray Fine Structure Spectroscopy (EXAFS)[200,201], High Energy X-ray Scattering (HEXS)[202], High Field Nuclear Magnetic Resonance (NMR)[203], X-ray Absorption Fine Structure (XAFS)[204], X-Ray Scattering[205] and X-ray Adsorption Near Edge Spectroscopy (XANES)[206] have been used to probe the solvation structure of aquo complexes of UO_2^{2+}. They report equatorial coordination numbers (CN) of 4.5[200] to 5.3[207], axial uranyl (U—

O_{yl}) bond distances of 1.70[208] to 1.77 Å[205] and equatorial (U—O) bond distances of 2.41[200,207,209] to 2.45 Å[210]. Both the HEXS study Soderholm *et al*.[202] and the X-ray scattering investigation by Neuefeind *et al.*[205] of various concentrations of $UO_3.0.8H_2O$ in dissolved in perchloric acid by found a dynamic equilibrium between a four and five coordinated uranyl, $[UO_2(H_2O)_4]^{3+}$ and $[UO_2(H_2O)_5]^{2+}$ respectively, in which the five coordinated species was favoured. XAFS spectra were collected for uranyl in aqueous solution as a function of chloride concentration by Allen *et al*.[207] and a CN of 5.3 and U—O of 2.41 Å were found at low chloride concentration. As the concentration of chloride was increased the CN of uranyl decreased due to chloride complexation and the U—O bond length increased.

Various density functional theory (DFT) investigations of the aquo solvation structure of uranyl found a equatorial CN of uranyl as 5[211–218], with equatorial U—O bond lengths of 2.4[215] to 2.53 Å[214,217]. Siboulet *et al.*[211] used DFT, with the hybrid functional B3LYP, to investigate the effect of including an explicit second solvation shell on the solvation structure of UO_2^{2+}. They identified a shortening of the U—O equatorial bond distance of 0.06 - 0.08 Å with the inclusion of a 10 water molecule second solvation sphere for both the 4 and 5 coordinated species from 2.44 Å to 2.36 Å and from 2.50 Å to 2.44 Å respectively. Kumar *et al.*[213] found a similar, albeit less significant, shortening in bond lengths from 2.47 to 2.45 Å when using a conductor-like polarizable continuum model and the hybrid functional B3PW91.

In general both *ab initio* Molecular Dynamics (AIMD)[219–221] and Classical Molecular Dynamics (MD)[206,222–225] simulations of the uranyl solvation environment indicate a coordination number of 5 and the U—O bond distance is identified as 2.36[222] to 2.48 Å.[224,225] The Classical MD study by Rodríguez-Jeangros *et al.*[226] identified an average CN of 4.39 as uranyl is equatorially coordinated by either 4 or 5 waters. In their *ab initio* Quantum Mechanical Charge Field Molecular Dynamics (QMCF-MD) study or uranyl in aqueous solution, Frick *et al*.[227] used Hartree-Fock theory to investigate the first solvation shell of uranyl and found a CN of 4 with a U—O average distance of 2.51 Å. The Car-Parrinello Molecular Dynamics (CPMD) study of Bühl *et al*.[219], using the functional BLYP, initially optimised different geometries of gaseous $[UO_2(H_2O)_5]^{2+}$ followed by aqueous AIMD simulations for 2 ps. They found an average U—O distance of 2.54 Å in the gas phase for 5 CN structures and when the same 5 CN structure was placed in a water box the average U—O distance decreased to 2.47 Å.

The impact of hydroxide on the first solvation shell of uranyl has been documented in both experimental and computational literature alike. Experimental EXAFS and X-ray Diffraction (XRD) data indicate U—O_{yl} distances of 1.79[228] to 1.83[200,229]. EXAFS investigations of solid

$[UO_2(OH)_4]^{2-}$ by Moll *et al.*[229] identified a U—O_{yl} distance of 1.83 Å and U—O_{OH} distance of 2.26 Å.[229] The EXAFS and XRD analysis by Clark *et al*.[228] crystals of of $UO_2(OH)_n^{2-n}$ (n = 4,5) found U—O_{yl} distances of 1.80 to 1.82 Å and U—O_{OH} distances of 2.21 to 2.26 Å. The combined computational and experimental investigation of Wahlgren *et al.*[200] used EXAFS and DFT calculations, at the MP2 level of approximation, to investigate the structure of uranyl with hydroxide ions. For the fixed structure $[UO_2(OH)_4]^{2-}$, U—O_{yl} distances of 1.8 Å and U—O_{OH} distances of 2.36 to 2.38 Å were found with computational methods. Their EXAFS data suggested a CN of 5 +/- 0.5 oxygens and a U—O_{OH} distance of 2.25 Å with a U—O_{yl} bond length of 1.82 Å. However, the authors note that EXAFS is more accurately able to measure bond length than CN and suggest a CN of 4 due to the decrease in bond length compared to aquo species, in line with their computational calculations.

Various DFT[217,218,238,239,230–237] studies investigate the impact on the solvation structure of uranyl with hydroxide ions. DFT investigations have found U—O_{yl} distances of 1.75[239] to 1.88[233] Å, U—O_{OH} distances of 2.09[218] to 2.46[232] Å, U—O_w distances of 2.47[240] to 2.60[238] Å. However, these bond distances are dependent on the number of hydroxides coordinating the uranyl ion. In the hybrid DFT study of $UO_2(OH)_2$ by Hratchian *et al*.[218], using B3LYP, shorter U—O_{OH} bond distances of 2.09 to 2.11 Å, and U—O_{yl} distances of 1.78 to 1.82 Å were found, whereas multiple DFT studies of $[UO_2(OH)_4]^{2-}$ found longer distances of 1.84[231] to 1.88[233] Å for U—O_{yl} and 2.29[233] to 2.31[232] U—O_{OH}. The gas phase DFT investigation, using the GGA functionals BP86, PW91 and PBE,by Ingram *et al.*[234] into the relative energies and ground state structures of $[UO_2(H_2O)_m(OH)_n]^{(2-n)}$) ($n$ + m = 5) using PBE found that as successive hydroxides are added to uranyl's first solvation shell the U—O_{yl} distance lengthened from 1.77 to 1.88 Å, the U—O_w distance increased from 2.49 to 2.80 Å, while the U—O_{OH} distance increased from 2.11 to 2.46 Å.

Cao *et al*.[239] used B3LYP and MP2 with 20 explicit water molecules and a continuum solvent model to investigate the solvation structure of uranyl with a one or two hydroxides. In each case a CN of 5 was found, with the first solvation structure of $UO_2(OH)(H_2O)_4^+$ for the monohydroxide system and $UO_2(OH)_2(H_2O)_3$ for the dihydroxide system. For the monohydroxide structure they found U—O_{yl} distances of 1.76 to 1.79 Å, U—O_{OH} distances of 2.16 to 2.19 Å and U—O_w distance of 2.47 to 2.60 Å. For the dihydroxide structure these bond lengths increased to distances of 1.79 to 1.82 Å for U—O_{yl} and 2.53 to 2.66 Å for U—O_w. Compared to the monohydroxide structures a wider range of U—O_{OH} bond lengths was found from 2.04 to 2.21 Å.

There is little dynamic data on the presence of hydroxides in the first solvation shell of uranyl. The computation investigation of Austin *et al.*[236] into $[UO_2(OH)_5]^{3-}$ used MD simulations to obtain solvated uranyl hydroxide structures which were then optimised using DFT with the BP86 and B3LYP functionals and a continuum solvation model. This investigation found a U—O_{yl} distance of 1.88 Å and U—O_{OH} distance of 2.42 Å. Bühl and Schreckenbach[241] used CPMD with an explicit 55 water molecule solvent and an NH_4^+ counter ion and the BLYP functional to examine the exchange of the axial and equatorial oxygen atoms in $[UO_2(OH)_4]^{2-}$. They found that the structure can be deprotonated to form $[UO_3(OH)_3]^{3-}$ which then undergoes proton transfer via *cis*-$[UO_2(OH)_4]^{2-}$ complex. The rate limiting step in the transformation is the proton transfer which is assisted by a water molecule from the solvent, there was a computed barrier for the exchange of 12.5 kcal mol^{-1}.

5.2 Computational Details

Born-Oppenheimer molecular dynamics simulations were performed using the QUICKSTEP module of CP2K version 3.0 and simulation cells with periodic boundary conditions.[94,115] Temperature and pressure were kept constant using a NPT_I ensemble, where the simulation cell is isotropic. The average temperature $T = 400\ K$ was maintained using a Nosè-Hoover thermostat and a barostat maintained pressure of 1 atm.[105] The GAPW[96] method was implemented using the PBE functional with Grimme's DFT-D3 dispersion correction applied.[76,166] The calculations used a double-ζ plus polarization quality Gaussian basis set (DZVP-MOLOPT-SR-GTH) and a planewave cutoff of 600 Ry with a relative cutoff of 80 Ry.[167] The results from converging the relative and planewave cutoff can be found in **Appendix A7**.

The DFT+U approach was taken for all calculations with an effective $U_{eff} = U - J$ value of 3.96 eV applied to the f orbitals. The U value of 4.5 eV and J value of 0.54 eV has been employed in keeping with many previous studies,[83,87,242–245] this value is based on the XRD measurements of Kotani and Yamazaki.[246] This value was used for both the cell optimisation and the generation of AIMD trajectories.

All initial structures underwent a cell optimisation prior to the start of the AIMD trajectory run, where both the cell parameters and the geometry were optimised simultaneously. The final cell parameters for each structure were then used for the starting AIMD trajectory, and allowed to vary as in the NPT_I ensemble. For the aquo and monohydroxide systems charge neutrality was achieved through the use of a uniform neutralising background charge. Each AIMD trajectory was 20 ps long and was comprised of 40,000 steps, each of length 0.5 fs. The

first 5 ps of each trajectory was treated as an equilibration period and was not considered in subsequent analysis.

A total trajectory time of 100, 100 and 120 ps for the aquo uranyl, uranyl monohydroxide and uranyl dihydroxide respectively was collected. Once the equilibration time was discarded 75, 75 and 90 ps of trajectory time were analysed for the aquo uranyl, uranyl monohydroxide and uranyl dihydroxide systems respectively.

5.3 Results

5.3.1 Characterisation of the Uranyl Aquo Complexes

To investigate the solvation structure of uranyl in an aqueous environment, 5 separate starting structures of 64 waters with a central UO_2^{2+} underwent a cell optimisation. These 5 structures were used for AIMD trajectories with initial cubic cell parameters of $a = b = c = 12.31$ Å for the first structure, and 11.99 Å for the final 4 structures. The resulting 75 ps of trajectory was analysed in the same method as described in detail in **Chapters 3** and **4**.

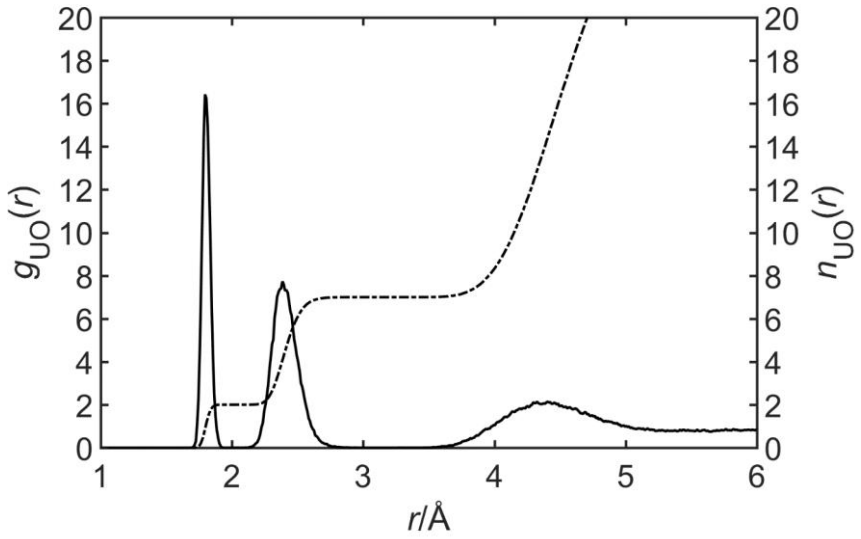

Figure 5.2: U—O radial distribution function, g(r), generated from a total 75 ps of simulation time for the uranyl aqueous environment.

Radial distribution functions (RDFs) were calculated for the entire 75 ps simulation time, as shown in **Figure 5.2**. The RDF yielded peak positions of 1.80 Å and 2.39 Å, clearly defining the U—O_{yl} bond distances and the U—O bond distances, respectively. As in various DFT investigations including that of Siboulet *et al.*[211] and Kumar *et al.*[213] the shorter equatorial bond length has resulted in a lengthening of the U—O_{yl} bond length as indicated in the RDFs.

These values are in generally good agreement with the experimental data, with most literature reporting a U—O_{yl} distance of 1.76 Å[201,202,205,207] and U—O distance of 2.42 Å[202,205,208].

The calculated average U—O_{yl} and U—O bond lengths and uranium coordination number are summarised in **Table 5.1**. The experimental literature data has a range of 1.70 to 1.76Å for the uranyl bond and 2.41 to 2.45 Å for the U—O bonds, while the computational literature data differs from 1.70 to 1.85 Å for the uranyl bond and 2.36 to 2.53 Å for the U—O Å bonds which indicates that the bond distances obtained are dependent on the methodology used to obtain them.

Table 5.1: Calculated U—O_{yl}, U—O bond lengths and mean coordination numbers (CN) for each AIMD trajectory run and accompanying standard deviation (SD) in parenthesis.

Trajectory	r_{M-O} (Å)		CN
	U—O_{yl}	U—O	
1	1.809	2.417	5
2	1.806	2.420	5
3	1.806	2.416	5
4	1.804	2.422	5
5	1.806	2.420	5
Mean (SD)	1.806 (0.002)	2.419 (0.003)	5(0.00)

The average U—O_{yl} bond distances of 1.81 Å from the AIMD simulations are slightly longer than those obtained experimentally but fall in the middle of the range given by computational literature, comparing excellently with the CMPD[219] calculated value of 1.81 Å. The average U—O bond length of 2.42 Å compares excellently with the U—O distance of 2.42 Å found experimentally from a range of techniques including XRD[208], XAFS[207], XANES[206], EXAFS [200,201] and X-ray scattering[205]. It also falls within the range of both computational and experimental literature of 2.36[222] to 2.53[214,217] Å.

Table 5.2: Percentage residence time for coordination environments averaged over 75 ps.

CN	4	5
%	0	100

Analysis of the trajectories yielded percentage residence times as summarised in **Table 5.2**. The calculated CN of 5 agreed with the available experimental and computational literature. While some studies[202,205,226] reported a variation in the coordination number between 4 and 5 with a dominance for 5 CN, this was not seen in the AIMD data. The chosen first shell cutoff of 3 Å for the first solation shell ensured a complete picture of how the coordination environment

varied across a trajectory, eliminating any noise in the data from bond stretching and bending which did not produce a true coordination change. The analysis of the trajectory showed that the first solvation shell did not vary in coordination number across the whole 75 ps of trajectory time.

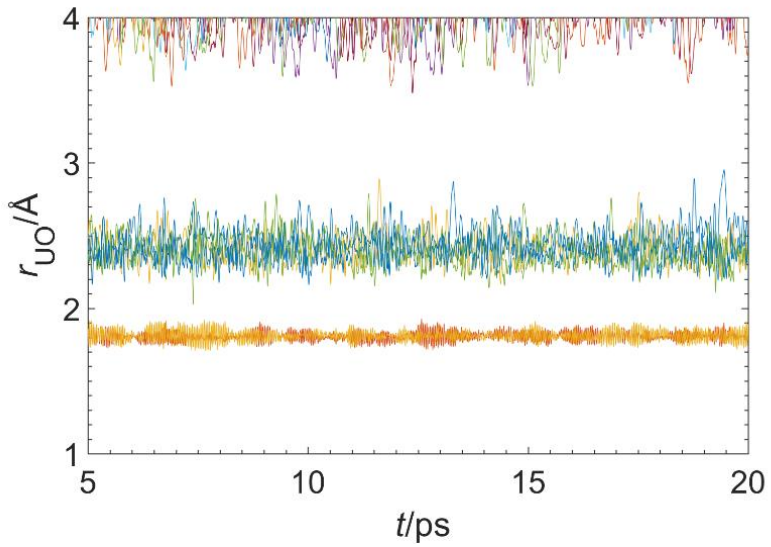

Figure 5.3: Example of a first shell trajectory plot for all U—O bonds at a distance of < 4 Å for uranyl aqueous environment.

An example of a trajectory plot for the first solvation shell of uranyl is shown in **Figure 5.3** plotting the distance of all U—O bonds within 4 Å. The U—O_{yl} bonds can be seen in the orange and yellow lines varying around 1.8 Å, whereas the U—O bonds indicating the first solvation shell can be seen around 2.4 Å. For ease of analysis the trajectory plots are redrawn as coordination plots indicating the CN of the first solvation shell across the time of a trajectory such as those show in **Figure 5.4 (a-e)**.

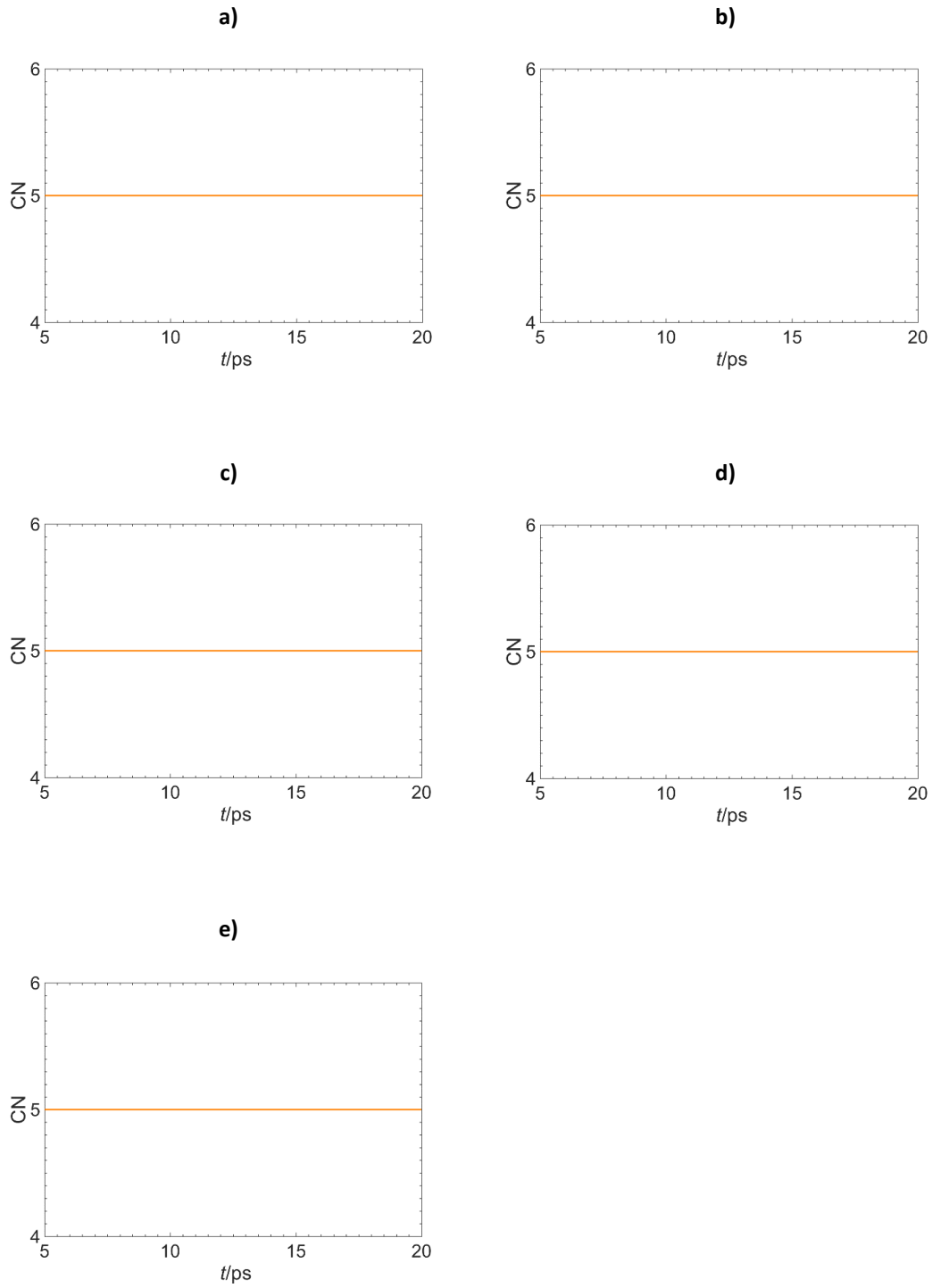

Figure 5.4(a-e): Total coordination number plots for each 15 ps AIMD trajectory of UO_2^{2+}.

5.3.2 Characterisation of Uranyl Monohydroxide Complexes

To investigate the impact of a single hydroxide on the solvation structure of uranyl, DFT and Born-Oppenheimer Molecular Dynamics were employed. The monohydroxide simulation structures were generated using 5 separate simulation snapshots from the aquo AIMD trajectories in **section 5.3.1** with a single proton removed. These monohydroxide systems underwent cell optimisations and the initial cubic cell parameters for the AIMD trajectories were set to $a = b = c = 12.60$ Å for all 5 structures based on cell optimisations. The initial 5 ps of trajectory time for each AIMD run were discarded for equilibration for a total of 75 ps of trajectory time. The data was analysed in the same method as described in detail in **Chapter 4**. In the mono-hydroxide systems the initial hydroxide placement was varied before geometry optimisation. Several attempts were made to optimise a geometry with a hydroxide outside of the first solvation shell, however these resulted in the proton migrating out of the first shell to generate a hydroxide inside the first solvation shell.

The RDFs were calculated over the entire 75 ps simulation time, as shown in **Figure 5.5**. The RDF gave peak positions of 1.83 Å, defining the U—O_{yl} bond distances, and 2.47 Å, identifying the U—O_w bond distance. A new maximum at 2.12 Å clearly indicates the U—O_{OH} distance, a peak which is absent in the aquo RDF in **Figure 5.2** and in the RDFs of the simulations of the alkaline earth metals with hydroxide presented in **Chapter 4**. This new peak could be due to the increased oxidation state of the uranium metal centre in comparison to the alkaline earth metals, causing the uranium centre to bind more tightly to the hydroxide than the water.

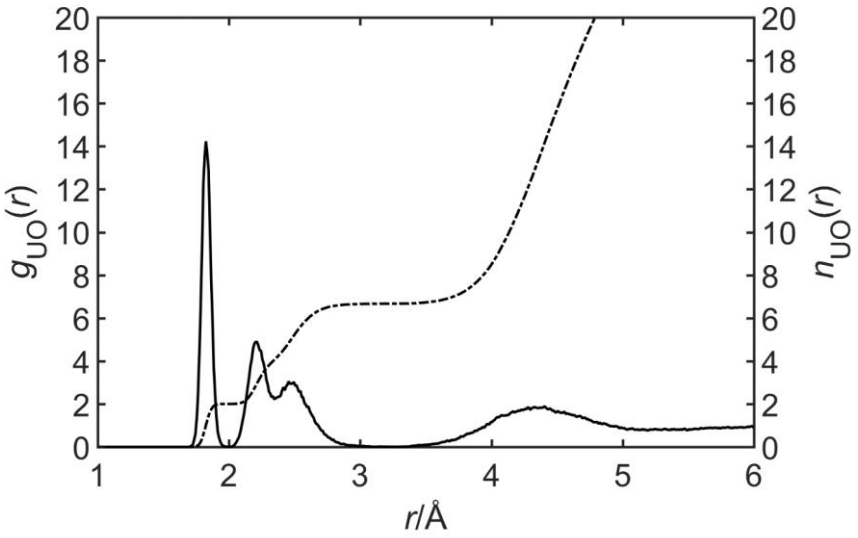

Figure 5.5: U—O radial distribution function, g(r), generated from a total of 75 ps of simulation time for the uranyl monohydroxide system.

To appropriately analyse the impact of the hydroxides on the first solvation shell the bond lengths have been calculated separately for the U—O_{OH}, U—O_w and the uranyl bond U—O_{yl} and are summarised in **Table 5.3**. The introduction of a hydroxide ion into the first solvation shell impacts both the axial and equatorial bond lengths. The average U—O_{yl} bond length increases by 0.02 Å and the U—O_w bond length increased by 0.07 Å compared to those obtained the aquo AIMD trajectories. Combined with the shorter U—O_{OH} bond distances suggests that the U—O_{OH} interaction is stronger than the U— O_{Ow} interaction. The increase in bond length mirrors the trend seen in the DFT study by Ingram *et al.*[234] where the introduction of a hydroxide ion induced a U—O_{yl} lengthening of 0.03 Å and U—O lengthening of 0.1 Å.

Table 5.3: Average bond distances for r_{M-O} and coordination numbers (CN) and hydroxide coordination numbers (CN_{OH}) for each AIMD trajectory (Traj.) with accompanying standard deviation (SD) in brackets.

Traj.	r_{M-O} (Å)			CN	CN_{OH}
	U—O_{yl}	U—O_w	U—O_{OH}		
1	1.827	2.491	2.167	5	1
2	1.821	2.481	2.182	5	1
3	1.820	2.482	2.191	5	1
4	1.817	2.496	2.198	5	1
5	1.820	2.482	2.205	5	1
Mean (SD)	1.821 (0.003)	2.486 (0.007)	2.189 (0.015)	5 (0.00)	1 (0.00)

The average U—O_{OH} value of 2.19 Å is significantly longer than the Ingram *et al.*[234] value of 2.12 Å for a monohydroxide. However it is best compared to the Cao *et al*.[239] DFT investigation, as their systems included 20 explicit water molecules and a continuum solvent model. For their monohydroxide system they obtained a U—O_{OH} bond distance of 2.19 Å, U—O_w bond distances of 2.47 to 2.50 Å and a U—O_{yl} bond distance of 1.79 Å yielding a 5 CN system comprised of 1 hydroxide and 4 waters.

There is no dynamic data on uranyl monohydroxide systems to compare the calculated values in **Table 5.3** against. However, given the accuracy of the aquo systems when compared to experimental data and how well the calculated average bond lengths for the monohydroxide compare to the available computational literature it is reasonable to assume these results based on dynamics have the same level of accuracy.

Analysis of the trajectories yielded coordination residence times as shown in **Table 5.4**. As for the aquo system the CN did not deviate from 5 over the 75ps of trajectory time. An example of a full trajectory plot of all U—O bond lengths at a distance less than 4 Å over the trajectory time can be seen in **Figure 5.6**. The shorter hydroxide bond as indicated in the RDF at 2.12 Å

is evidenced as the light blue line in **Figure 5.6** around 2.2 Å. The first shell coordination plots for all 5 AIMD trajectories can be seen in **Figure 5.7(a-e)** where the orange dotted line indicates the total U—O CN, the solid blue line indicates the total U—O_{OH} coordination number, and the dashed black line indicates the cutoff for the first solvation shell.

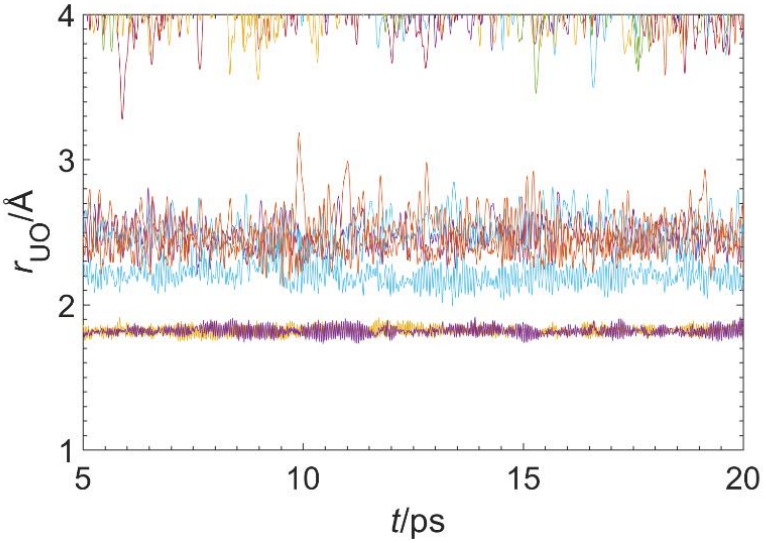

Figure 5.6: Example of a first shell trajectory plot for all U—O bonds at a distance < 4 Å for the uranyl monohydroxide system.

Table 5.4: Percentage residence time for each coordination environment (CN) averaged over 75 ps.

CN	4	5
%	0	100

Table 5.5: Percentage of hydroxide coordination (CN_{OH}) averaged over 75 ps.

CN_{OH}	0	1
%	0	100

Mulliken charges were calculated on each of the atoms and used to identify the hydroxide over the timescale of each AIMD run. The AIMD trajectories were analysed for proton transfer events in accordance with the methodology explained in **Chapter 4**. However, no proton transfer events were seen across the 75 ps simulation time. This is likely due to increased charge on the uranium ion and the strength of the metal-oxygen bonds compared to the metal-oxygen bonds of the alkaline earth metals. As established in **Chapter 4** proton transfer events are more likely to occur outside of the first solvation shell; the continued coordination of the hydroxide ion to the uranium metal therefore limits the potential for proton transfer.

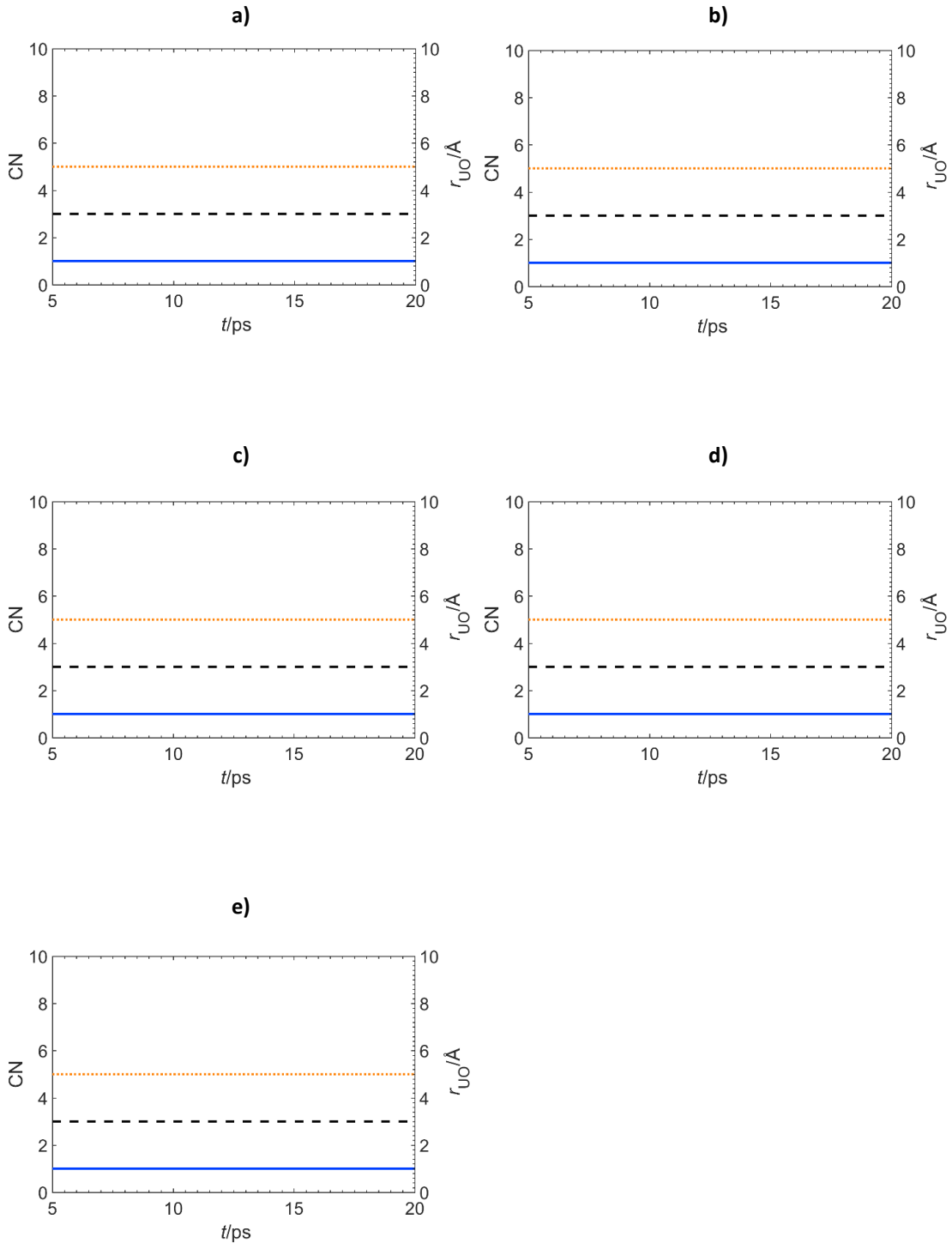

Figure 5.7(a-e): Total (dotted orange) and hydroxide (solid blue) coordination number for each UO_2^{2+} monohydroxide 15 ps AIMD trajectory. The dashed black line indicates the first shell cutoff distance of 3.0 Å.

5.3.3 Characterisation of the Uranyl Dihydroxide Complexes

To investigate the impact of two hydroxide ions on the first solvation shell of uranyl complexes DFT and Born-Oppenheimer Molecular Dynamics were employed. The dihydroxide systems were made by removing two hydrogens from each of the 6 separate simulation structures taken from the AIMD trajectories of the aquo complexes. These 6 structures underwent cell optimisations with the final cell parameters being used for the start of each AIMD trajectory. Initial cubic cell parameters were set to $a = b = c = 12.31$ Å for the first 5 systems with $a = b = c = 12.99$ Å used for the final 6th structure.

Initially only 5 structures were optimised and used for AIMD trajectories, as in **Chapter 4**, however the analysis of the structures appeared to indicate two separate uranyl environments: one environment where a 5 coordinated uranyl structure was constant, and one environment where the coordination number of uranyl easily dropped from 5 to 4. A 6th random snapshot was optimised and used for an AIMD trajectory to see if one environment was more prevalent than the other. On closer analysis there was nothing specific to the coordination environments or the water structure which could cause the drop in coordination number.

Each AIMD trajectory was 20 ps long with the initial 5 ps of trajectory time discarded for equilibration for a total of 90 ps of analysable trajectory time. The data was analysed in the same method as described in detail in **Chapter 4**. As in the monohydroxide systems the initial hydroxide placement was varied before geometry optimisation. Several attempts were made to optimise a geometry with a hydroxide outside of the first solvation shell however these all resulted in proton transfer from the first solvation shell to generate two hydroxides in the first solvation shell.

RDFs were calculated for the entire 90 ps simulation time, as shown in **Figure 5.8**, which yielded peak positions of 1.83 Å, 2.21 Å and 2.45 Å, identifying the U—O_{yl}, U—O_{OH} and the U—O_w bond distances respectively. The introduction of a second hydroxide did not have an impact on the U—O_{yl} bond distance, however the peak position for U—O_{OH} increased by 0.09 Å and the peak position for U—O_w decreased by 0.07 Å compared to the monohydroxide systems.

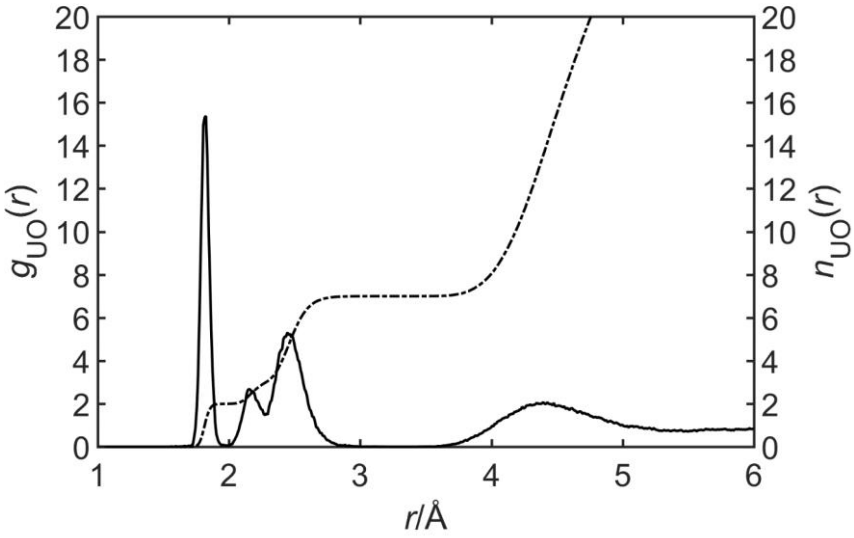

Figure 5.8: U—O radial distribution function, g(r), averaged over 75 ps simulation time for the uranyl dihydroxide system.

Figure 5.9 is an example of a full trajectory plot of all U—O bond lengths over the trajectory time at a U—O distance of < 4 Å. The shorter hydroxide bonds, which are indicated in the RDF at 2.21 Å, are shown by the red and purple lines in **Figure 5.9**.

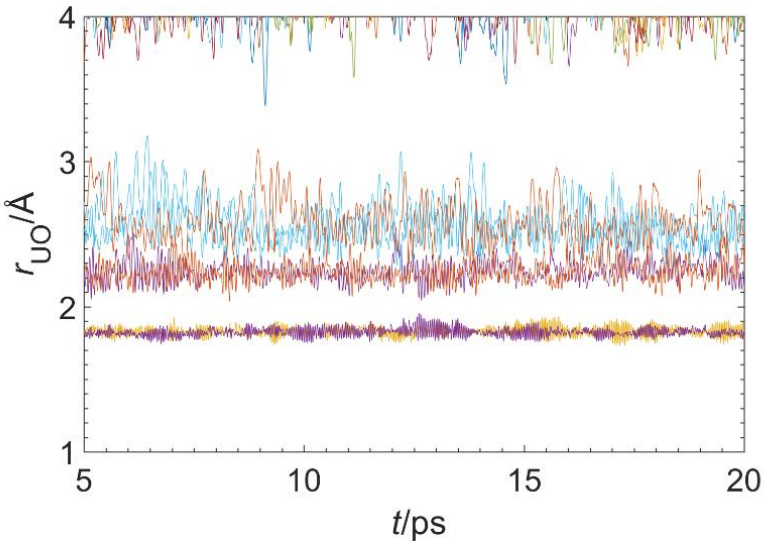

Figure 5.9: Example of a first shell trajectory plot for all U—O bonds at a distance < 4 Å for the uranyl dihydroxide system.

The calculated average U—O_{yl}, U—O_w and U—O_{OH} bond lengths and uranium coordination number are summarised in **Table 5.6**. A first shell cutoff of 3 Å was used for the calculation of bond lengths. Compared to the monohydroxide systems, the average bond lengths increased by 0.01 Å for the U—O_{yl} bond, 0.04 Å for U—O_w bonds and 0.04 Å for the U—O_{OH} bonds. This

increase in bond lengths reflects the trend reported by both Ingram *et al.*[234] and Cao *et al.*[239] who found that bond lengths increased as successive hydroxides were added to the system. The calculated average bond lengths for the first solvation shell for U—O_w and U—O_{OH} are 0.08 Å and 0.07 Å longer than those reported by Cao *et al.*[239], and 0.07 Å longer than those reported by Ingram *et al.*[234] However, neither of these DFT models included explicit water molecules beyond the first solvation shell, and used continuum solvent models to model the long range interactions of the water, which has been shown to impact the accuracy of the first solvation shell in studies with uranyl in water.[211,213,247]

Table 5.6: Average r_{M-O}, coordination numbers (CN) and hydroxide coordination numbers (CN_{OH}) for each trajectory (Traj.). Overall means for each value with accompanying standard deviation (SD) in brackets.

Traj.	r_{M-O} (Å)			CN	CN_{OH}
	U—O_{yl}	U—O_w	U—O_{OH}		
1	1.827	2.575	2.258	5.00	1.99
2	1.826	2.564	2.246	5.00	2.00
3	1.838	2.549	2.229	5.00	2.00
4	1.827	2.502	2.227	4.49	2.00
5	1.830	2.483	2.213	4.29	2.00
6	1.832	2.485	2.212	4.37	2.00
Mean (SD)	1.830 (0.005)	2.526 (0.041)	2.231 (0.018)	4.69 (0.34)	2.00 (0.01)

The total and hydroxide coordination environments for all 6 trajectories are shown in **Figure 5.10(a-e)** where the orange dotted line indicates the total U—O CN, the solid blue line indicates the total U—O_{OH} coordination number, and the dashed black line indicates the cutoff for the first solvation shell of 3.0 Å.

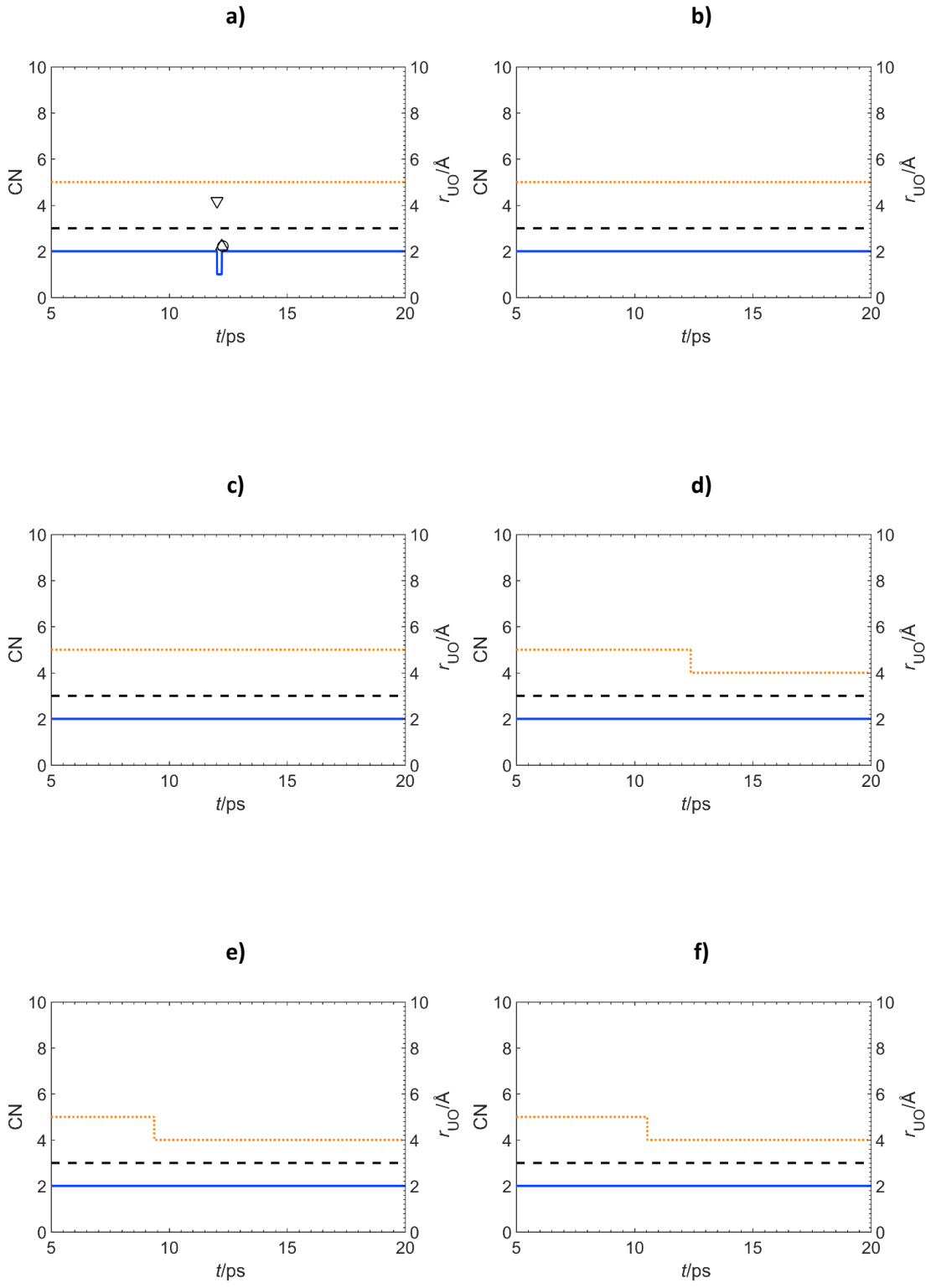

Figure 5.10(a-e): Total (dotted orange) and hydroxide (solid blue) coordination number and proton transfer events (Δ: 1st shell → 2nd shell, ∇: 2nd shell → 1st shell, ○: intrashell) for each UO_2^{2+} dihydroxide 15 ps AIMD trajectory. The dashed black line indicates the first shell cutoff distance of 3.0 Å.

Analysis of the trajectories yielded average residence times for the first shell as summarised in **Table 5.7**. Compared to the aquo and monohydroxide complexes where a CN of 5 is seen throughout, 30.1% of the trajectory time in the dihydroxide systems indicates a CN of 4. The introduction of a second hydroxide triggered a reduction in coordination number, from 5 to 4, in 3 of the dihydroxide systems as shown in **Figure 5.10(d-f)**. The overall CN reduced to 4.69. However, the 5 CN structure dominates with the majority of the trajectory time collected indicating that a 5 CN uranyl species is preferred.

Table 5.7: Percentage residence time for each coordination environment (CN) averaged over 90 ps.

CN	4	5
%	30.82	69.18

The percentage of time the uranyl ion spent coordinated by 1 or 2 hydroxide ions is summarised in **Table 5.8**. Only a short amount of time (0.23%) was spent with only 1 hydroxide coordinated to the uranium metal, suggesting that the strength of the U—O_{OH} bonds remain too great to overcome for a long period of time.

Table 5.8: Percentage of hydroxide coordination environment (CN_{OH}) averaged over 90 ps.

CN_{OH}	0	1	2
%	0	0.23	99.77

The dynamics of proton transfer were analysed in accordance with the methodology laid out in **Chapter 4**. These values are summarised in **Table 5.9**, over the 90 ps total trajectory time only 3 proton transfer events were identified, all in one dihydroxide trajectory. The PTEs are shown in **Figure 5.10a** at 12.5 ps., initially a proton moves into the first solvation shell (∇) reducing the number of hydroxides in the first solvation shell to 1. The proton then transfers out of the first solvation shell (Δ), before another proton transfers from an adjacent water (○).

Table 5.9: Number and characterisation of proton transfer events (PTE), obtained from 90 ps of AIMD data for the uranyl dihydroxide system.

PTE				
1^{st}—1^{st}	1^{st}—2^{nd}	2^{nd}—1^{st}	2^{nd}—2^{nd}	Total
1	1	1	0	3

The relative absence of PTEs and both hydroxides being coordinated to the uranyl for the majority of the trajectory time indicates the increased strength of the U—O_{OH} bond in comparison to the M—O_{OH} bonds in the alkaline earth metals, as mentioned earlier this is likely a result of the increased charge of the central uranium ion. In **Chapter 4** the number of PTEs inside the first solvation shell was less than outside the first solvation shell. As the uranyl ion

is only in one instance coordinated by less than 2 hydroxides the opportunity for intrashell PTEs, involving hydroxides which resulting in a new hydroxide outside the first solvation shell, is eliminated. However, it is worth noting that such a low number of PTEs may not be statistically relevant and any future work would need to probe the probability of proton transfer with uranyl carefully.

The increase in hydroxides from 1 to 2 in the system appears to have increased the likelihood of a proton transfer occurring. In the same way that in the Bühl and Schreckenbach[241] investigation the presence of hydroxide ions allows a solvent assisted proton transfer to occur in the first solvation shell, it appears that the presence of hydroxide in the system is weakening the equatorial bonding in the uranyl first solvation shell which allows proton transfer to occur.

5.4 Conclusion

This chapter focuses on the solvation structure of the uranyl ion in the absence and presence of hydroxide ions. The +6 oxidation state of the uranium dication introduced a more complex aspect to the investigations. 75 ps of analysable AIMD trajectories were collected for the aquo and monohydroxide environments and 90 ps were collected for the dihydroxide environment. Initial environments were optimised using the PBE functional with Grimme's DFT-D3 dispersion correction and the DFT+U Hubbard correction. AIMD simulations were carried out using Born-Oppenheimer molecular dynamics.

Bonding in the first solvation shell was characterised by averaging the radial distribution functions over the entire AIMD trajectory time and by calculating the average bond lengths of $U—O_{yl}$, $U—O_{w}$, as well as $U—O_{OH}$ for the last two investigations. An average coordination number of the first solvation shell was calculated, and for the hydroxide systems an average time where the ion was coordinated by either one or both hydroxide ions was also calculated. The first solvation shell of the aquo systems compared well to existing experimental and computational literature, with bond lengths well within values measured previously and coordination numbers in line with previously calculated values. The addition of successive hydroxides identified similar trends as in past literature, but with a novel computational methodology. The addition of hydroxides increased bond lengths in all cases, as previously identified through DFT and AIMD calculations. A reduction in coordination number was also seen when two hydroxides were present in the system.

Attempts were made to identify proton transfer events in both the mono- and dihydroxide systems and PTEs were more prevalent in the dihydroxide system. However, only three such events were identified in the dihydroxide environment, indicating the clear impact of the

increased charge density of uranium and its propensity for forming strong metal-oxygen bonds in aqueous solution. The impact on the metal-oxygen bonds is similar as that seen in the alkaline earth metals, as the more charge dense Mg^{2+} environments have significantly less PTEs than environments containing the less charge dense Sr^{2+}.

Overall the data presented here indicates that a good model for uranyl solvation has been developed. The investigation into the behaviour of the uranyl ion, commonly found in the nuclear waste storage ponds, in a high pH environment indicate that uranyl tightly binds to the hydroxide species and prohibits proton transfer.

Chapter 6: Impact of Increasing Ionic Charge

This chapter is separated into three parts which each apply the solvation model developed in previous chapters to different ionic systems to examine the impact of increasing pH and expand the understanding of proton transfer in different chemical environments. In **Part 1**, results from Sr^{2+} monohydroxide systems are reported and the difference in solvation structure of the strontium dication in a monohydroxide and dihydroxide system are summarised. **Part 2**, focuses on the aquo and monohydroxide complexes of Cs^{+}, a known by-product of the nuclear waste process, to contrast the impact of a single hydroxide interacting with a monocation compared to a dication. Finally, **Part 3** presents calculations of La^{3+} and Lu^{3+} in aquo and trihydroxide environments expanding the solvation model to include trications ions in the presence of hydroxide and examining further elements which have relevance to the nuclear industry. Investigating mono-, di- and tri cations allows a broad picture to be developed of the difference in of hydroxides complexation with increasing cation charge, while verifying the solvation models against existing aquo literature.

6.1 Part 1: Strontium Monohydroxide Complexes

Investigating the solvation structure, hydroxide coordination and proton transfer in a strontium monohydroxide system further applies the solvation model developed in **Chapters 3** and **4**. By investigating the monohydroxide environment and comparing it to the same dication in a dihydroxide environment the results should reveal if a single hydroxide is enough to alter the coordination and bonding of the first solvation shell, and highlight any differences between the two environments. While there is not extensive literature on strontium monohydroxide there are gas-phase Density Functional Theory (DFT) investigations on the impact of a single hydroxide ion on the microsolvation structure of strontium.

Kerridge and Kaltsoyannis[186] used DFT to optimise the molecular structures of the aquo complexes of strontium monohydroxides. The most highly coordinated complex found had a coordination number (CN) of 7, and all attempts to obtain complex with a CN of 8 resulted in the migration of one ligand to the second coordination shell. The most stable structure had a CN of 5 with the hydroxide ion in the second shell hydrogen bonded to waters in the first shell. For higher coordinated structures with CNs of 6 and 7 the lowest energy structures were just 3.0 and 2.1 kJ mol^{-1} higher in energy than the most stable CN = 5 structure, respectively. As the CN of the first solvation shell increased from 5 to 7 the calculated $Sr—O_{OH}$ bond lengths increased from 2.346 Å to 2.530 Å. Quantum Theory of Atoms in Molecules (QTAIM) analysis revealed a small reducing effect of the hydroxide ion with increasing coordination to the Sr^{2+}.

The strontium charge, which is formally +2, decreases from +1.87 to +1.84 going from mono to tri hydroxide. The authors note, however, that the use of the COSMO continuum solvation model alone is inadequate to accurately model the energetics of multi hydroxide systems and that an explicit water model is required.

Makkos *et al*.[187] used DFT at the meta-GGA level to build on the work of Kerridge *et al.*[186] using both COSMO and explicit water molecules to study the aqueous solvation of strontium mono-, di- and trihydroxides. The full first and second solvation shell was modelled by including 22 explicit waters in the solvation environment. It was found initially that the inclusion of only the first solvation shell led to unavoidable energetic instabilities due to gaps in the solvation structure. The inclusion of a second shell increased the CN of the most stable complex with a preference for a 6-coordinated structure preferred, compared to a 5-coordinated structure with only the first solvation shell modelled explicitly. As referred to previously in **Chapter 4** this investigation highlighted the small energetic difference of just 3.0 kJ mol^{-1} between a dihydroxide coordinated strontium and a monohydroxide coordinated strontium.

6.1.1 Computational Details

The computational details were kept in line with previous Sr^{2+} simulations. AIMD simulations were performed with the QUICKSTEP module of CP2K version 3.0.[94,115] All calculations involved simulation cells with periodic boundary conditions. A NPT_I ensemble, where the simulation cell is isotropic with initial cubic cell parameters were set to $a = b = c = 11.99$ Å. The average temperature was set at $T = 400$ K and was maintained using a Nosè-Hoover thermostat and a barostat maintained pressure of 1 atm.[105]

The Gaussian Augmented Plane Wave method (GAPW) was used for the calculation of forces and energies.[96] The Perdew-Burke-Ernzerhof (PBE) generalised gradient approximation was used including the DFT-D2 dispersion correction as proposed by Grimme.[76,166] The calculations used double-ζ plus polarization Gaussian basis sets (DZVP-MOLOPT-SR-GTH) and a planewave cutoff of 500 Ry and a relative cutoff of 60 Ry.[167] The Mulliken charge[188] was calculated on each atom throughout the trajectory.

Each AIMD trajectory was 20 ps long and each timestep was 0.5 fs. The first 5 ps of each trajectory was treated as an equilibration period and was not considered in subsequent analysis. A total of 100 ps of trajectory time was collected, with 75 ps used in analysis once the equilibration period was discarded.

6.1.2 Results

Both DFT and AIMD were employed to investigate the impact of a single hydroxide on the solvation environment of Sr^{2+}. 5 snapshots from the AIMD aquo trajectories of Sr^{2+} were taken, from which a single proton was removed to create a hydroxide ion. These systems then underwent a cell optimisation in which the cell parameters and geometry were optimised simultaneously. Each simulation cell contained 63 waters, 1 Sr^{2+} ion and 1 OH^- ion, the starting cell parameters were set to 11.99 Å. A total of 100 ps trajectory time was collected resulting in 75 ps of analysable simulation time.

Each trajectory was analysed in accordance with the methodology described in **Chapter 4**, but instead accounting for only one hydroxide in the system. For consistency with other Sr^{2+} calculations, a first shell cutoff of 3.2 Å was used for all relevant analysis. The RDF was calculated over the entire 75 ps of trajectory time, and is shown in **Figure 6.1**. The peak at 2.62 Å indicates the first shell Sr—O distance, there is a slight decrease in peak position of 0.01 Å compared to aquo complexes.

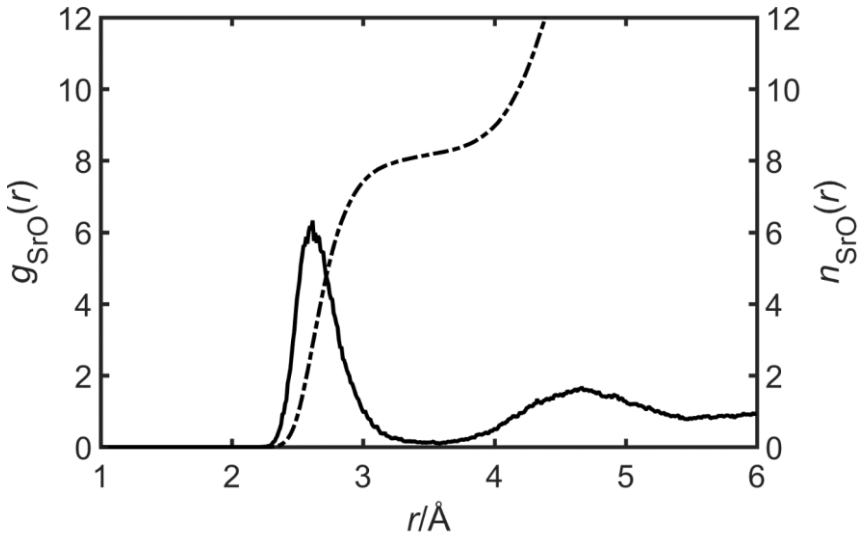

Figure 6.1: Sr—O radial distribution function, g(r), generated from 75 ps of simulation time for a monohydroxide environment.

The calculated average Sr—O bond lengths, total CN and hydroxide CN for each trajectory are summarised in **Table 6.1**. The average total CN of 7.92 is higher than the computationally predicted CN of 7 of Kerridge *et al.*[186], and the average Sr—O bond length is significantly longer than the reported 2.53 Å. However, this increase is likely to be due to the difference in methodology, as using AIMD and a larger solvation model of 64 waters both impact the CN and bond length, as discussed by Makkos *et al*.[187] The Sr—O distance and the average CN are

within the calculated experimental ranges for the aqueous investigations of 2.57[154] to 2.69[150] and 6.00[154] to 10.30[155], respectively.

Table 6.1: Calculated Sr—O separations (r_{Sr-O}), coordination numbers (CN) , and hydroxide coordination numbers (CN_{OH}) with accompanying standard deviation (SD), for each AIMD trajectory (Traj.) considered in this study.

Traj.	r_{Sr-O} (Å)	CN	CN_{OH}
1	2.693	7.91	0.00
2	2.683	7.74	0.00
3	2.690	7.90	0.02
4	2.706	8.19	0.15
5	2.694	7.88	0.15
Mean (SD)	2.693 (0.01)	7.92 (0.16)	0.06 (0.08)

Further analysis of the trajectories yielded the residence time for each total coordination environment, given in **Table 6.2**. Sr^{2+} is predominantly 8 coordinated with significant periods of time spent as a 7 and 9 coordinated species. The percentage of time the Sr^{2+} spent coordinated by a hydroxide is summarised in **Table 6.3**. For the majority of the time the hydroxide ion is not coordinated to the central Sr^{2+} ion, as evidenced by there being only 6 % of the trajectory time which shows a CN_{OH} of 1. The CN_{OH} in the dihydroxide environment was higher, with an overall CN_{OH} of 0.23 and with 26 % of trajectory time spent coordinated by either 1 or 2 hydroxides. The low CN_{OH} in **Table 6.1** and the low hydroxide residence time in **Table 6.3** provide further evidence that a single hydroxide ion has little to no impact on the first solvation shell, with two trajectories indicating no coordination by the anion at all and a third trajectory having a low CN_{OH} of just 0.02.

Table 6.2: Percentage residence time in different total coordination environments (CN), averaged over 75ps.

CN			
6	7	8	9
0.85	18.20	68.64	12.28

Table 6.3: Percentage residence time in different hydroxide coordination environments, (CN_{OH}), averaged over 75 ps.

CN_{OH}	
0	1
93.79	6.21

For ease of comparison, the RDF peak, average Sr—O bond distance, average total CN and average hydroxide CN are reported in **Table 6.4** for Sr^{2+} in the aqueous, monohydroxide and dihydroxide environments. The averages are calculated over the 75 ps of AIMD trajectory time, collected for each environment after 5 ps of equilibration time has been discarded. In all cases there is a more pronounced change when comparing the aqueous environment to the dihydroxide than the monohydroxide environment. The RDF peak and average CN decrease significantly with the introduction of two hydroxide species; however, the difference between the aqueous and monohydroxide environment is not as large as the difference between the monohydroxide and dihydroxide environment, as the RDF peak and Sr—O distance remains the same with the introduction of a single hydroxide. The introduction of a single hydroxide reduces the Sr^{2+} CN by 0.1 but with the introduction of a second hydroxide there is further reduction in the average CN of 0.3, again indicating that the second hydroxide has a larger impact on the bonding of the first solvation shell.

Table 6.4: Calculated Sr—O RDF peak, Sr—O bond distance (r_{Sr-O}), mean coordination numbers (CN), and mean hydroxide coordination numbers (CN_{OH}) averaged over 75ps with accompanying standard deviations (SD), for the aqueous, monohydroxide and dihydroxide environments.

	Aqueous	Monohydroxide	Dihydroxide
RDF Peak (Å)	2.630	2.620	2.590
r_{Sr-O} (Å)	2.692 (0.01)	2.693 (0.01)	2.685 (0.01)
CN	8.02 (0.14)	7.92 (0.16)	7.61 (0.19)
CN_{OH}	-	0.06 (0.08)	0.29 (0.23)

Table 6.5 summarises the percentage residence times for Sr^{2+} at different CNs for the aqueous, monohydroxide and dihydroxide investigations. Across all three investigations the 8 coordinated Sr^{2+} species dominates, with significant periods of time spent as 7 or 9 coordinated. As hydroxides are introduced, the range of total coordination numbers shifts from 6 to 10, to 5 to 9, with CNs of 5 and 10 only found in the dihydroxide and aqueous environments, respectively.

Table 6.5: Percentage residence time of different total coordination environments (CN), averaged over 75ps, for the aqueous, monohydroxide and dihydroxide environments.

	CN					
	5	6	7	8	9	10
Aqueous	0.00	0.23	14.09	69.57	15.28	0.83
Monohydroxide	0.00	0.85	18.20	68.64	12.28	0.00
Dihydroxide	0.21	2.67	37.97	54.16	4.99	0.00

The comparison of CN_{OH} in the mono and dihydroxide environments shown in **Table 6.4** indicates the small impact that a single hydroxide has on the solvation shell. Although the results in **Chapter 4** indicate that the Sr^{2+} is coordinated by a single hydroxide for 23% of the trajectory time, this is only when there is a second hydroxide present.

Table 6.6: Number and characterisation of proton transfer events (PTE), obtained from 75 ps of AIMD data considered in this study. Percentage values are given in parentheses.

PTE				
1^{st}—1^{st}	1^{st}—2^{nd}	2^{nd}—1^{st}	2^{nd}—2^{nd}	Total
0 (0)	6 (9)	5 (7)	57 (84)	68

The lack of coordination by the hydroxide ion in the monohydroxide environment has a clear effect on the classification of the PTEs found. **Table 6.6** lists the total number of PTEs classified by the direction of proton transfer across the first solvation shell cutoff. The majority of the PTEs are intrashell and outside the first solvation shell, with roughly an equal number of inter shell PTEs in both directions across the first solvation shell boundary. In contrast to the dihydroxides, no intrashell PTEs in the first solvation shell are identified. The periods of coordination by the hydroxide ion are seemingly too brief for intrashell proton transfer to occur. The rate of PTEs in monohydroxide environments is approximately 0.90 PTEs per ps, compared to the slightly more frequent rate of 0.94 PTEs per ps for each hydroxide present in the dihydroxide environments.

The low hydroxide coordination in the monohydroxide environment is further evidenced in the full trajectory plots in **Figures 6.2a** to **6.2e**. The full trajectory plots indicate the total first shell CN, CN_{OH} and PTEs for each trajectory, and the first solvation shell cutoff is also shown. **Figures 6.2a** and **6.2b** indicate no hydroxide coordination, whereas **Figures 6.2c** to **6.2e** indicate brief hydroxide coordination with longer periods of coordination lasting for around 2 ps, in contrast to the dihydroxide simulations where periods of a single hydroxide coordinating the Sr^{2+} are found for up to 10 ps.

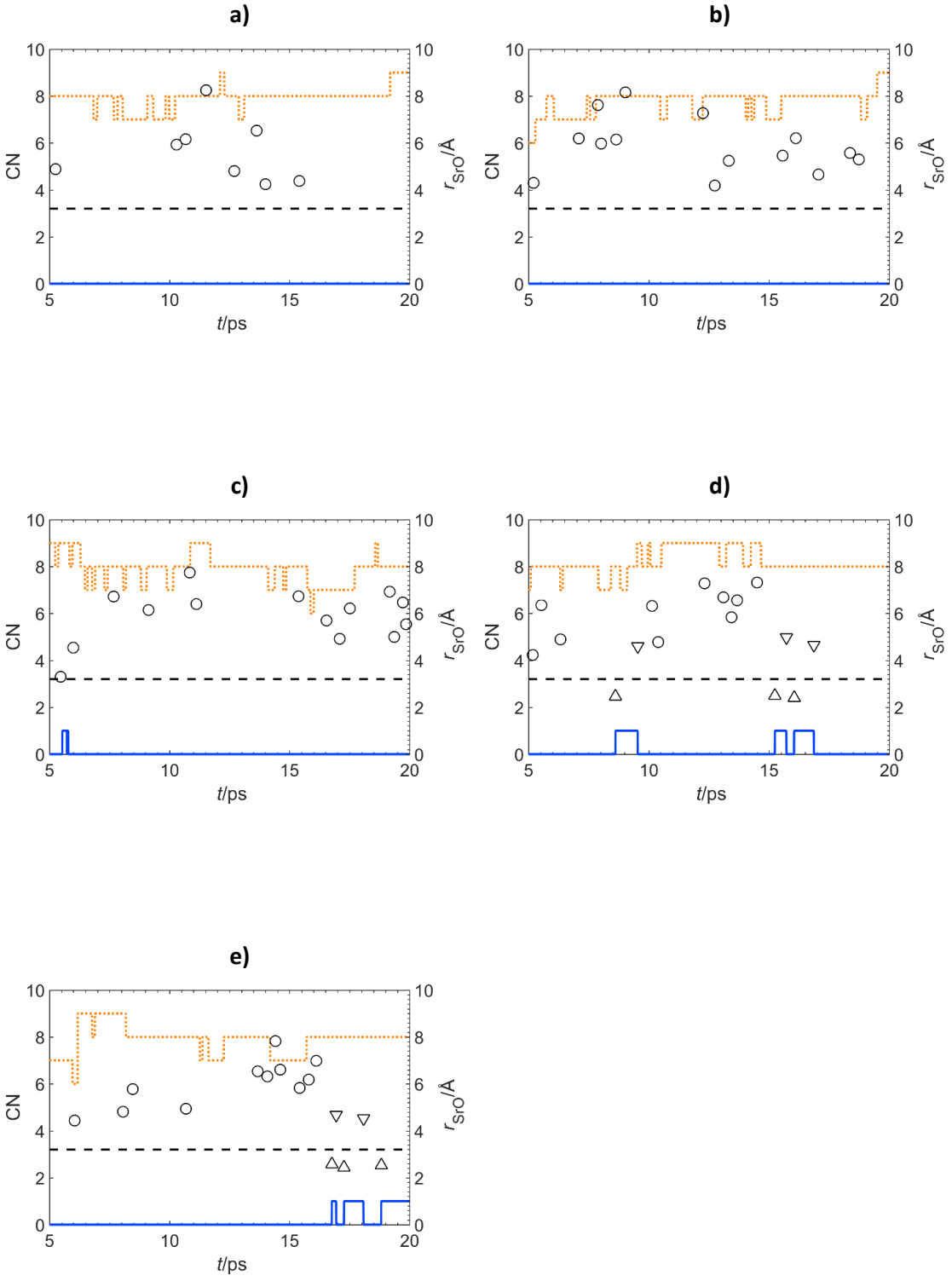

Figure 6.2(a-e): Total (dotted orange line) and hydroxide (solid blue line) coordination numbers, and proton transfer events ((Δ: 1st shell → 2nd shell, ∇: 2nd shell → 1st shell, ○: intrashell) for each Sr^{2+} monohydroxide 15 ps AIMD trajectory. The dashed black line indicates the first shell cutoff distance of 3.2 Å.

6.1.3 Part 1: Conclusion

This section examines the impact on the solvation structure of strontium by the introduction of a single hydroxide ion. 75 ps of trajectory time for a system with a central Sr^{2+} ion in the presence of 63 water molecules and a single hydroxide ion were collected. All AIMD simulations were carried out using Born-Oppenheimer molecular dynamics. Initial structures had randomised hydroxide placement and were optimised using the PBE functional with DFT-D2 dispersion correction applied.

Following the previous analysis of the solvation structure of strontium in both aquo and dihydroxide environments in **Chapter 3** and **4**, this further investigation of the monohydroxide environment provides a more complete overview of the effect of the increasing number of hydroxides. Both the bonding and the total coordination number of the strontium ion remain essentially unchanged compared to the aquo complexes. The introduction of a single hydroxide ion has a limited impact on the microsolvation of strontium compared to the dihydroxide systems, with essentially no change in coordination number or average bond length. The monohydroxide exhibits broadly similar proton transfer behaviour to the dihydroxide, and PTE frequency is also similar, with the majority of proton transfers occurring outside of the first solvation shell. However, in contrast to the dihydroxide environment, there are no proton transfers inside the first solvation shell for the monohydroxide environment due to the lack of coordination of the hydroxide ion to the central ion.

These results combined with those in **Chapter 4** indicate that the strontium ion is the least likely to form hydroxide species in the high pH environment of the nuclear waste storage ponds, and waste clean-up should be focused on removing the ion in its aqueous form, rather than as a hydrated hydroxide complex.

6.2 Part 2: Aquo and Hydrated Hydroxide Complexes of Cs^+

As was detailed in **Chapter 1** caesium is one of the most abundant species in nuclear waste and has a long half-life and as such it is of relevance to this thesis. In this section, the solvation structure of Cs^+ in both an aqueous environment and in the presence of hydroxide has been considered. Cs^+ has a large atomic radius and hence weaker ion-water electrostatic interactions as a hydrated ion compared to other metal cations. The examination of the solvation structure of a monocation in both the presence and absence of a single hydroxide provides a useful comparison to the same solvation environments for the Sr^{2+} dication.

Several experimental techniques have been used to investigate the solvation structure of caesium, including Anomalous X-ray Diffraction (AXD)[248,249], X-Ray Diffraction (XRD)[250–253], Large Angle X-ray Scattering (LAXS)[254], X-ray Scattering[255], Inelastic Neutron Scattering[256], Neutron Diffraction (ND)[257] and Nuclear Magnetic Resonance (NMR)[258]. Typically a coordination number (CN) of 8[248,252–254,256–258] is found in experimental investigations within the total range of 4.73[251] to 8.4[255]. The Cs—O distances for the first solvation shell were reported to be between 2.95[257] to 3.15[250,252] Å. Both Lawrence *et al*.[250] and Tamura *et al*.[251] used XRD to investigate the effect of increasing concentration of CsI on the solvation shell of Cs^+, and found a reduction of CN with increasing concentration as the water coordinating to the ion is replaced with the counter-ions. Tamura *et al*.[251] also found that the hydration shell was sensitive to an increase in temperature with an increase from 298 K to 343 K lowering the CN from 5.75 to 4.73 at the same CsI concentration of 2.78 M. The X-ray scattering investigation of Yongquan *et al*.[255] found a CN of 8.4 at an average Cs—O distance of 3.12 Å, the authors used Monte Carlo simulations to refine the results but were unable to identify a second hydration sphere. The lack of second hydration sphere is replicated by several other authors who attribute it and the formation of a weak first hydration shell to the low charge density of the Cs^+ ion.[248,249,253,255,256]

The combined experimental and computational investigation of Kolaski *et al.*[259] used B3LYP and MP2 levels of theory to investigate caesium water structures of the form $Cs(H_2O)_n$ (n=1 - 8) and compared them to IR absorption studies. The Cs—O separation for the first solvation shell was defined as less than 3.8 Å, while Cs—O separations greater than 4.5 Å defined the secondary hydration shell. The analysis of the results using these cutoff parameters gave a CN of 8 and an average Cs—O bond length between 3.40 Å to 3.46 Å.

Several classical MD studies[149,260–266] calculated the Cs—O distance to be between 3.10[262] and 3.30[261] Å with a CN between 7.8[261] to 10[260]. Deublein *et al*.[262] used classical MD to identify the first solvation shell of Cs^+ in aqueous solution as CsF, CsBr and CsI with the first shell cutoff set at 3.7 Å. In all cases the RDF yielded a Cs—O distance of 3.10 Å, a higher CN of 8 was found for Cs^+ when the counter ion was F^-, while a Cs^+ CN of 7.5 was found for the Br^- and I^- counter-ions. It was also found that an increase in salt concentration from 1 M to 5 M caused a reduction in CN.

Schewenk *et al*.[261] used QM/MM methodology at different levels of theory (HF, B3LYP and BP86) to investigate the structure breaking effect of Cs^+. Structure breaking ions, which are mainly large weak interacting ions, have little influence on water when they are solvated and fail to form a defined solvation shell. In all cases the Cs—O RDFs indicate the structure breaking behaviour of the ion, with a broad asymmetric first-shell peak and with a flat but recognisable second shell. A CN of 8 with a Cs—O RDF peak of 3.25 Å was found using HF whereas both B3LYP and BP86 calculations gave a CN of 9 with Cs—O RDF peaks of 3.20 Å and 3.30 Å, respectively. The CN of 5 to 11 were identified over the timescale of the simulation. This broad distribution of CNs indicates the extremely fast dynamics and rapidly changing character of the first hydration shell.

Ikeda *et al*.[267] used CPMD to investigate the hydration structure of Cs^+ in 63 water molecules, and were unable to define a first solvation shell. The CNs were therefore obtained using three first shell cutoff distances of 3.8, 3.9 and 4 Å, identifying overall CNs of 7 to 8.2. Upon investigating the distribution of coordination modes over the timescale of the simulation, a broad range of CNs from 4 to 11 was found. A similar CN range as found by Schewenk *et al*.[261] and mirroring the structure breaking effect of Cs^+ which they investigated.

There are no computational or experimental investigations into the solvation structure of caesium monohydroxide in an aqueous environment. Several studies exist reporting the length of the isolated Cs—OH bond. The microwave spectrum of Cs—OH investigated by Kuczkowski *et al*.[268] showed a Cs—OH distance of 2.40 Å, with their later study[269] refining the results to 2.391 Å. Theoretical investigations found longer Cs—OH distances, the molecular orbital study by Stiakaki *et al*.[270] found a Cs—OH bond length of 2.447 Å whereas Lee *et al*.[271] used Couple Cluster Singles and Doubles (CCSD) level theory to identify a Cs—OH distance of 2.635 Å. Bauschlicher *et al*.[272] used *ab initio* computational methods with a fixed O—H bond length to derive the Cs—OH bond length of 2.419 Å using SCF and CISD levels of theory. However, a lower Cs—OH distance of 2.393 Å was found by Brown *et al*.[273] using MP3 level calculations to determine the equilibrium geometries of the alkali hydroxides.

The dissociation of CsOH in water clusters was investigated by Odde *et al*.[274] using MP2 level calculations of CsOH.$(H_2O)_n$ *(n* = 0 to 4). The equilibrium structures were calculated using the B3LYP functional and MP2. On the addition of water molecules, the Cs—OH bond lengthened from 2.64 Å for *n* = 1 to 3.08 Å for *n* = 4. A total of 3 water molecules are needed for the dissociation of Cs—OH, compared to strong acid dissociation which requires a minimum of four waters.

6.2.1 Computational Details

Born-Oppenheimer molecular dynamics simulations were performed using the QUICKSTEP module of CP2K version 3.0 on simulation cells with periodic boundary conditions.[94,115] Temperature and pressure were kept constant using a NPT_I ensemble, where the simulation cell is isotropic and the average temperature $T = 400\ K$ was maintained using a Nosé-Hoover thermostat and a barostat maintained pressure of 1 atm.[105] The GAPW[96] method was implemented using the PBE functional with the DFT-D3 dispersion correction applied.[76,166] The calculations used a double-ζ plus polarization Gaussian basis set (DZVP-MOLOPT-SR-GTH) and a planewave cutoff of 600 Ry and a relative cutoff of 80 Ry, convergence test for both cutoffs can be found in **Appendix A4**.[167]

The solvation structure of caesium in an aqueous environment was studied using 5 separate starting structures of 64 waters and a central Cs^+ ion. All initial structures underwent a cell optimisation prior to the start of the AIMD trajectory run, where both the cell parameters and the geometry were optimised simultaneously. The resulting optimised cell parameters of $a = b = c = 12.50$ Å were used as the starting cell parameters for each AIMD trajectory. For the aquo systems charge neutrality was achieved through the use of a uniform neutralising background charge. Each AIMD trajectory was 20 ps long with a timestep of 0.5 fs. The first 5 ps of each trajectory was treated as an equilibration period and was not considered in subsequent analysis. A total of 100 ps of trajectory time was collected, with 75 ps used in analysis once the equilibration period was discarded.

6.2.2 Results

6.2.2.1 Characterisation of Caesium Aquo Complexes

The results from the AIMD simulations were analysed using the methodology described in **Chapter 3**. The RDF was calculated for the entire 75 ps of trajectory time and is given in **Figure 6.3**. The first solvation shell is ill defined, with a broad asymmetric peak with a maximum at 3.24 Å but no minima to indicate its end. The running integral, $n_{CsO}(r)$, does not indicate a first or second solvation shell.

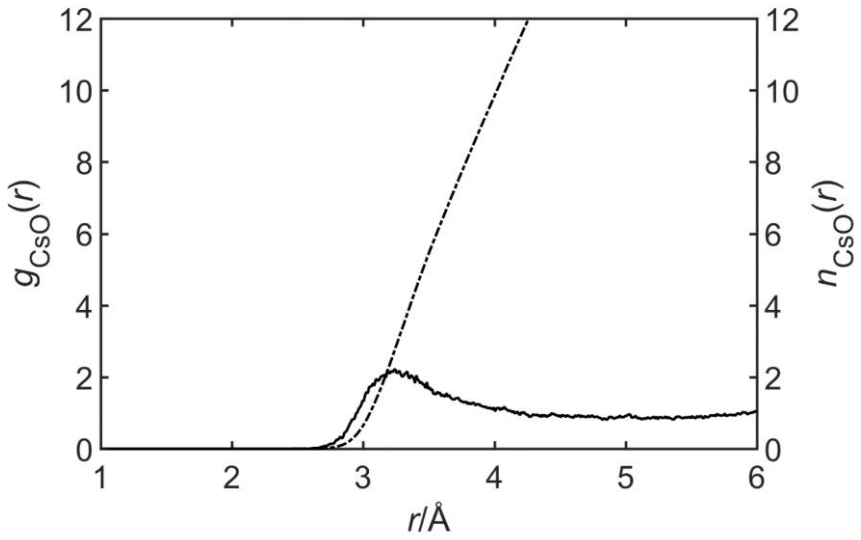

Figure 6.3: Cs—O radial distribution function, g(r), generated from 75 ps of aquo simulation time.

The lack definition of the first solvation shell is also evidenced in **Figure 6.4**, a plot of all Cs—O distances over the timescale of a single AIMD trajectory. In contrast to the previously investigated ions there is no clear first solvation shell surrounding the ion, rather a large distance of ~3 Å between Cs^+ and the 64 water molecules which form a seemingly bulk-like configuration.

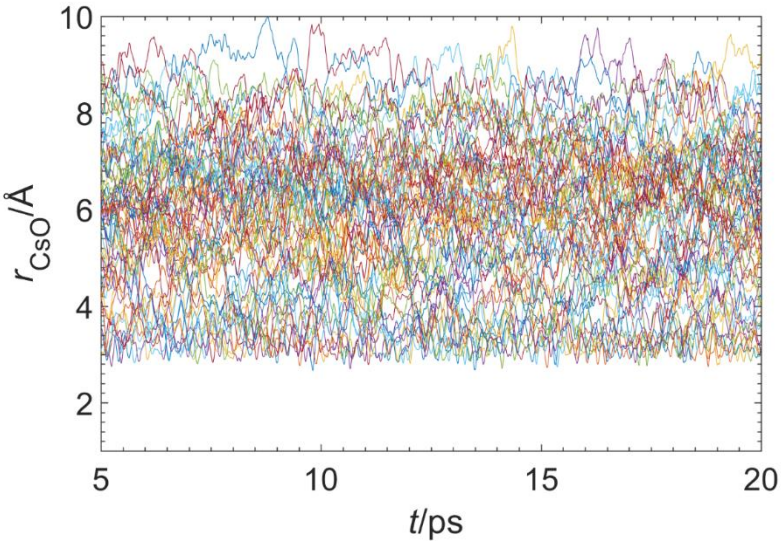

Figure 6.4: Full trajectory plot for all Cs—O distances over the timescale of an example AIMD trajectory.

The lack of a defined solvation shell adds a layer of complexity to the analysis method. The approach used in previous chapters where the cutoff for the first solvation shell is set as the RDF peak + 0.6 Å is potentially inappropriate given the lack of definition for the end of the solvation shell. However, this approach does provide a useful starting point for the investigation. The RDF peak (3.24 Å) + 0.6 Å, 3.80 Å, was used as the first shell cutoff, as well

as 3.7 and 3.9 Å, in a method the same as Ikeda *et al*.[267] who investigated using three first shell cutoffs of 3.7, 3.8 and 3.9 Å.

The calculated average Cs—O bond lengths are summarised in **Table 6.7**. While none of the calculated values agree with previous literature investigations, in all cases the average bond lengths are slightly larger than the experimental values of 2.95[257] to 3.15[250,252] Å, and outside the computationally obtained range of 3.10[262] to 3.30[261] Å. The mean bond lengths vary within a 0.08 Å range and are within 0.05 Å of the Cs—O distance of 3.38 Å calculated from the 3.8 Å cutoff.

Table 6.7: Calculated Cs—O bond lengths (r_{Cs-O}) and mean bond length for each AIMD trajectory run and accompanying standard deviation (SD), at cutoffs of 3.7, 3.8 and 3.9 Å.

Trajectory	r_{Cs-O} (Å)		
Cutoff (Å)	3.7	3.8	3.9
1	3.342	3.369	3.436
2	3.347	3.386	3.416
3	3.310	3.399	3.411
4	3.305	3.366	3.397
5	3.346	3.374	3.402
Mean (SD)	3.330 (0.02)	3.379 (0.01)	3.412 (0.02)

Table 6.8: Calculated total and mean coordination numbers (CN) for each AIMD trajectory run and accompanying standard deviation (SD), at cutoffs of 3.7, 3.8 and 3.9 Å.

Trajectory	CN		
Cutoff (Å)	3.7	3.8	3.9
1	7.40	7.85	9.15
2	7.62	8.36	8.97
3	6.87	8.59	8.78
4	6.46	7.61	8.18
5	6.99	8.96	8.27
Mean (SD)	7.07 (0.46)	8.27 (0.55)	8.67 (0.43)

There is a large difference in the range of calculated average CN, which are summarised in **Table 6.8** for each of the three cutoffs employed. The average CNs found vary from 7.07 to 8.67, which is slightly larger than the 7 to 8.2 range reported in the Ikeda *et al*.[267] AIMD study. Each calculated average CN has a standard deviation of around 0.5, indicating that there is a noticeable variation in the CN for each trajectory. Both computational and experimental literature values cluster around a CN of 8 for Cs^+, but the calculated value of a CN of 8.3 for

the 3.8 Å cutoff is longer, and within the range of 7.5[249] to 8.4[255] reported experimentally and 7.8[261] to 10[260] computationally. In addition, the calculated value agrees excellently with the CN of 8.3 obtained from the Koneshan *et al*.[149] MD investigation and the CN of 8.4 found from the X-ray Scattering investigation of Yongquan *et al*.[255]

Further evidence of the variation in CN is seen in the percentage residence times for each coordination environment as given in **Table 6.9**. The lower cutoff of 3.7 Å found coordination modes from 5 to 10, 3.8 Å found a wider range from 5 to 11 and 3.9 has the largest variation with coordination environments of 5 to 13 found. There is no clear preference for a particular coordination mode across the three cutoffs, with a CN of 6 most dominant for the lowest cutoff, 8 for the 3.8 Å cutoff and 9 for the highest cutoff. In contrast the Ikeda *et al*.[267] AIMD investigation found a smaller range of coordination environments from 4 to 11, and the majority of the trajectory time was 7 or 8 coordinated across all three cutoffs. For the 3.8 Å cutoff in particular ~35% of the simulation time was spent as a 7 coordinated structure and ~25 % of time Cs^+ was either 8 or 6 coordinated, with a total range of CNs from 4 to 10 identified.

Table 6.9: Percentage residence time for coordination environments (CN) at cutoffs of 3.7, 3.8 and 3.9 Å averaged over 75 ps.

Cutoff (Å)	CN								
	5	6	7	8	9	10	11	12	13
3.7	5.43	35.65	21.89	24.87	8.05	4.12	0.00	0.00	0.00
3.8	1.39	6.78	24.08	30.60	21.33	14.87	2.32	0.00	0.00
3.9	0.34	1.68	17.15	26.19	28.84	20.68	3.03	1.05	0.34

The total CN variation across each 15 ps trajectory are shown in **Figure 6.5**, **6.6** and **6.7** for the 3.7, 3.8 and 3.9 Å cutoffs, respectively. There appears to be no fluctuation around a single CN as reported in previous AIMD investigations of other ions. Instead there is considerable variation and rapid transitions between different coordination modes. The frequently altering coordination environment is further evidence of the lack of definition in the first solvation shell for Cs^+, and indication that the large size of the ion, and therefore low charge density, impacts its ability to form a defined solvation structure.

Based on the calculated values for each cutoff value, the cutoff of 3.8 Å provides the best approximation for the first solvation shell character of Cs^+ in an aquo environment. The calculated average CN is closer to the frequently reported value of 8, the average bond length of 3.38 Å within previously calculated ranges combined with the distribution of coordination

numbers from 5 to 10 in line with Ikeda *et al*.[267] all indicate that this is an appropriate cutoff value to use.

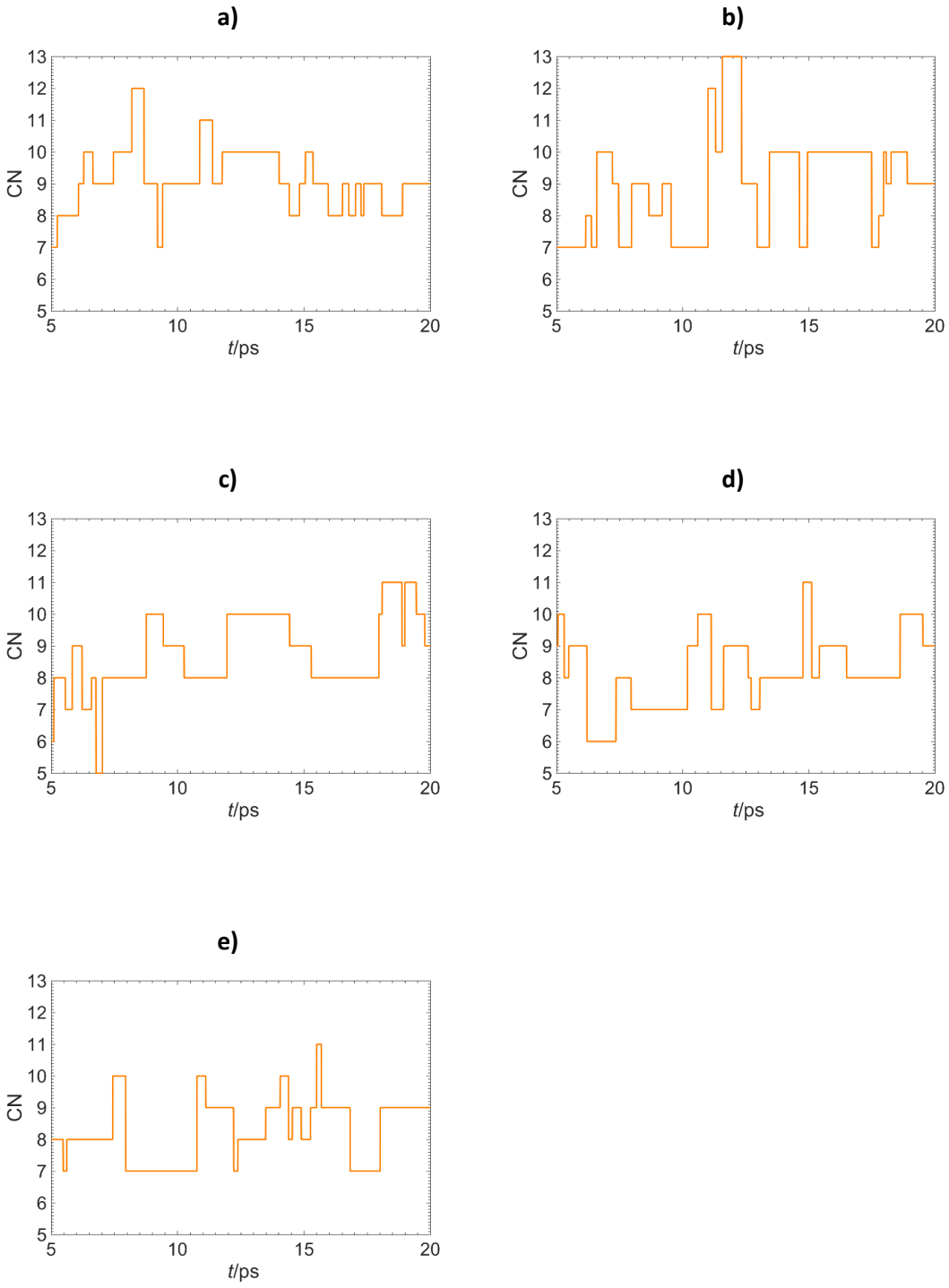

Figure 6.5(a-e): Total coordination number (CN) plots for each 15 ps trajectory of Cs^+ in water using a first shell cutoff of 3.7 Å.

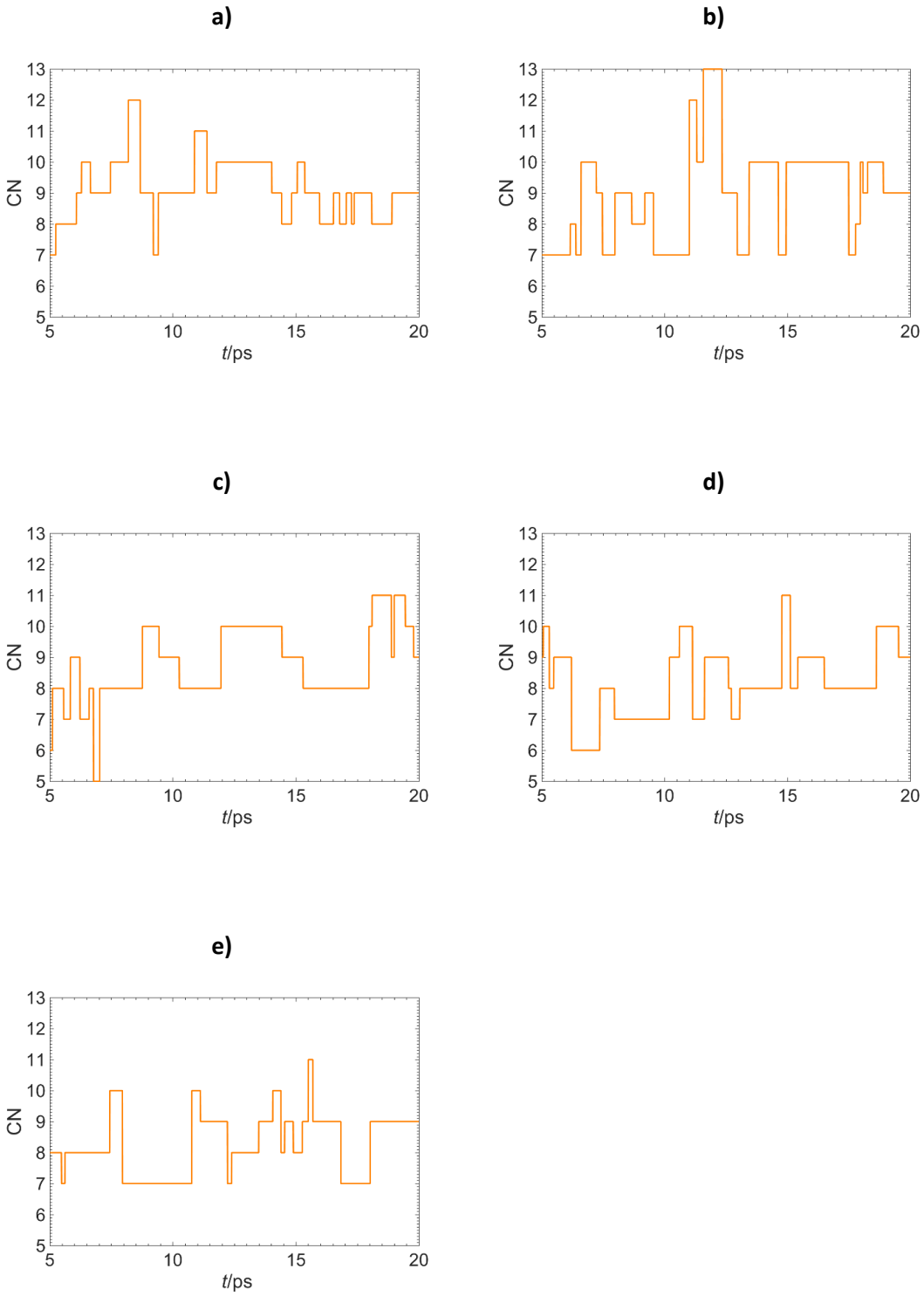

Figure 6.6(a-e): Total coordination number (CN) plots for each 15 ps trajectory of Cs^+ in water using a first shell cutoff of 3.8 Å.

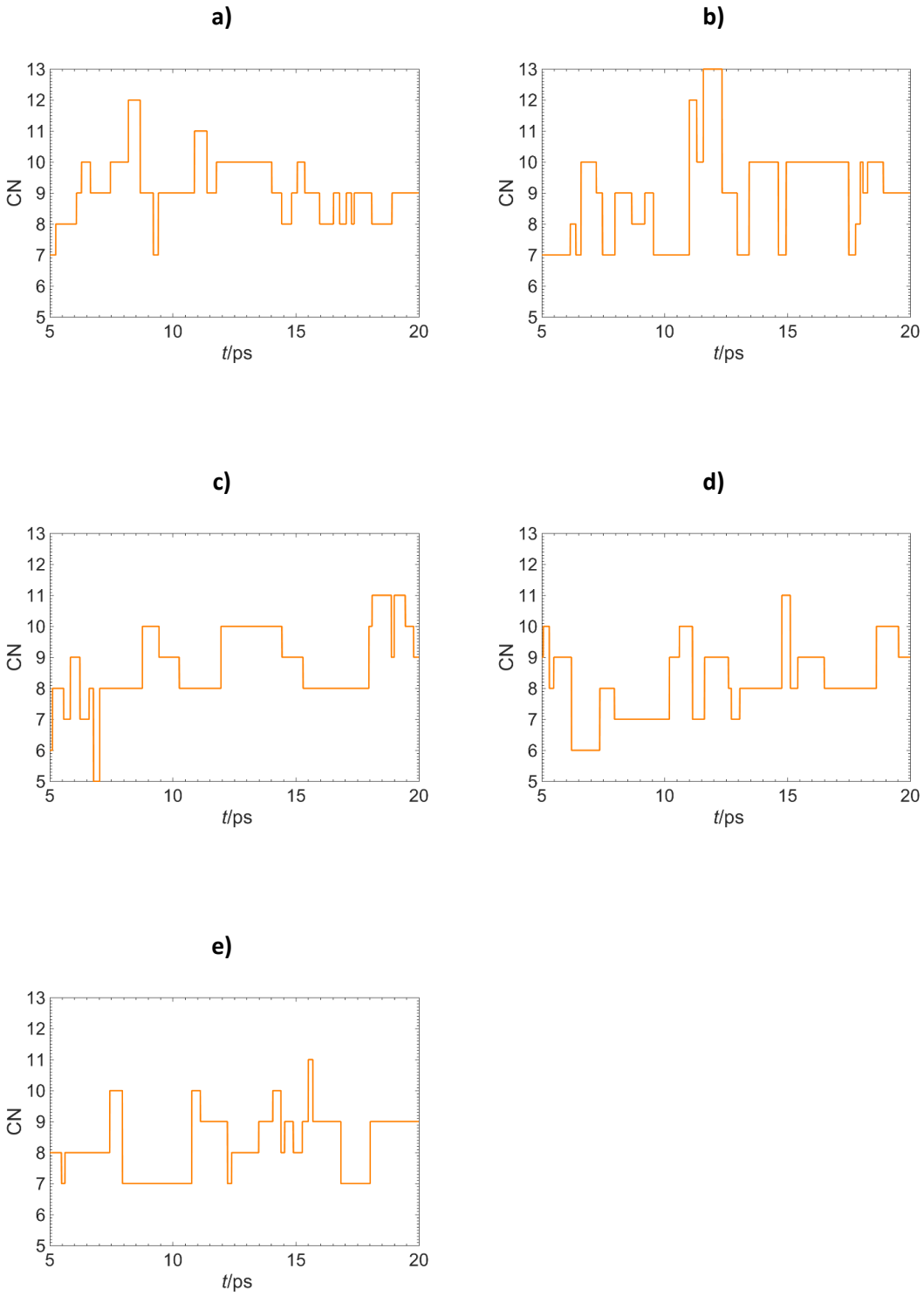

Figure 6.7(a-e): Total coordination number (CN) plots for each 15 ps trajectory of Cs^+ in water using a first shell cutoff of 3.9 Å.

6.2.2.2 Characterisation of Caesium Monohydroxide Complexes

The monohydroxide solvation structure of caesium was investigated with DFT and AIMD. To generate the initial starting structures, 5 snapshots were taken from separate aquo simulations of Cs^+ AIMD trajectories and a single proton was removed to make a OH^- ion. The initial hydroxide placement was varied prior to the optimisation. These 5 structures had both their cell parameters and geometry optimised simultaneously before being used in the AIMD simulations. The starting cell parameters $a = b = c = 12.50\,\text{Å}$ were used for all AIMD trajectories as in the aquo trajectories. Each AIMD trajectory lasted 20 ps with the initial 5 ps discarded for equilibrium. A total of 75 ps trajectory time was collected and analysed according to the methodology described in **Chapter 4** but accounting for only a single hydroxide in the systems.

The RDFs for the monohydroxide systems was calculated over the entire 75 ps, as shown in **Figure 6.8**. As in the aquo environments, the first solvation shell of Cs^+ is undefined with a shallow slope and there is no minimum indicating the end of the solvation shell. A full trajectory plot of all Cs—O distances across the entire timescale of the trajectory is shown in **Figure 6.9**, confirming the lack of a defined first solvation shell, as seen for the aquo systems.

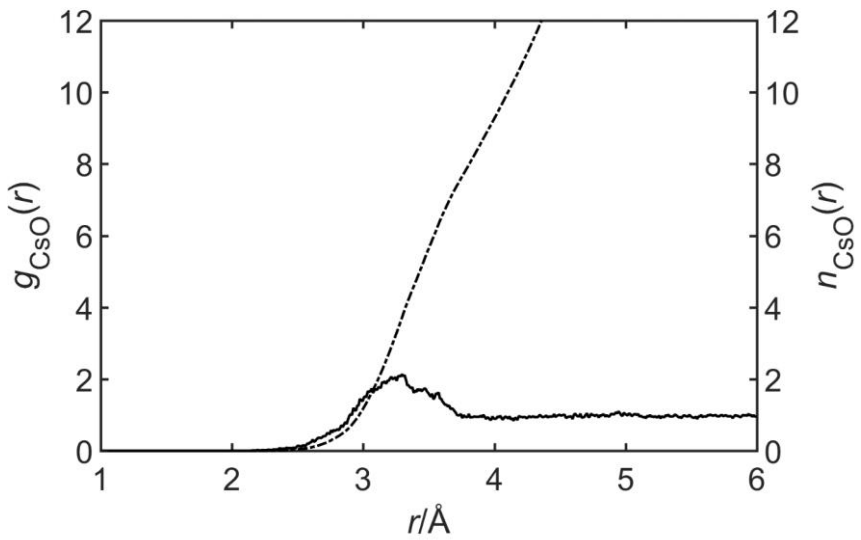

Figure 6.8: Cs—O radial distribution function, g(r), generated from 75 ps of simulation time for the caesium monohydroxide environment.

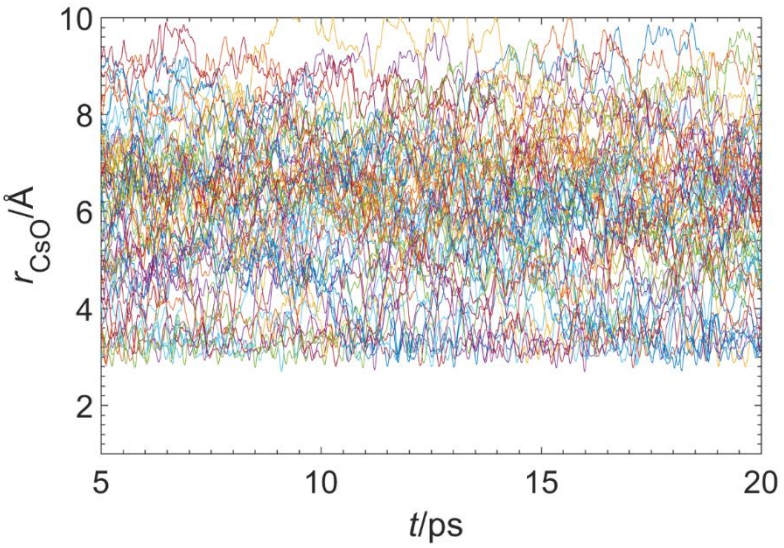

Figure 6.9: Full plot for all Cs—O bonds in a monohydroxide environment for one 15 ps AIMD trajectory.

As the first solvation shell was no more defined in the monohydroxide systems than in the aquo systems, the same approach for choosing a cutoff was taken. The average bond lengths and average CNs were calculated for cutoffs of 3.7, 3.8 and 3.9 Å. The calculated average Cs—O bond lengths and CNs are listed in **Table 6.10** and **Table 6.11** respectively. All three cutoffs produce similar average bond lengths, with a difference of 0.05 Å, and with little variation across trajectories. Comparing the 3.8 Å cutoff results for both the aquo and hydroxide environments, the trends are in line with the hydroxide investigations of previous ions in this thesis. As seen for other hydroxide species the average bond length decreases slightly, by 0.02 Å, with the addition of a hydroxide ion.

Table 6.10: Calculated Cs—O bond lengths (r_{Cs-O}) and mean bond length for each AIMD trajectory run and accompanying standard deviation (SD), at cutoffs of 3.7, 3.8 and 3.9 Å.

Trajectory	r_{Cs-O} (Å)		
Cutoff (Å)	3.7	3.8	3.9
1	3.317	3.359	3.397
2	3.324	3.361	3.399
3	3.321	3.350	3.390
4	3.318	3.352	3.408
5	3.316	3.352	3.407
Mean (SD)	3.319 (0.00)	3.355 (0.00)	3.400 (0.01)

A similar distribution of average CN was seen as for the aquo complexes, with the lowest CN found for the 3.7 Å cutoff and the highest CN at the 3.9 Å cutoff. The average CN found for the cutoffs range from 6.46 to 8.11, with average CNs reducing by 0.61, 1.06 and 0.56, respectively

with respect to the aquo values. The results from first shell cutoff using 3.8 Å indicated the largest reduction in CN with the introduction of a hydroxide, from 8.27 to 7.21. Across the trajectories there is also less variation in the coordination modes identified compared to the aquo trajectories. Although the introduction of the hydroxide has not impacted the bond lengths in the first solvation shell, it does appear to have followed the trend found previously where hydroxide systems have lower average CN than their aquo counterparts.

Table 6.11: Calculated total and mean coordination numbers (CN) for each AIMD trajectory run and accompanying standard deviation (SD), at cutoffs of 3.7, 3.8 and 3.9 Å.

Trajectory	CN		
Cutoff (Å)	3.7	3.8	3.9
1	6.69	7.47	8.11
2	6.65	7.26	7.87
3	6.33	7.12	7.78
4	6.64	7.25	8.19
5	5.98	6.94	7.81
Mean (SD)	6.46 (0.30)	7.21 (0.20)	8.110 (0.19)

The coordination of Cs^+ varies significantly in the hydroxide trajectories, as in the aquo trajectories but with some key differences. The difference in total CN with the inclusion of a hydroxide ion is evidenced in the percentage of trajectory time at each coordination environment, given in **Table 6.12**. The range of CNs identified shortens from 5 to 13 in the aquo systems to 4 to 11 in the hydroxides. The Cs^+ ion is predominantly 7 coordinated and the higher CNs of 12 and 13 which were briefly detected in the aquo systems are not present in the hydroxide systems for any cutoff, and 4 coordinated species are identified by the 3.7 and 3.8 Å cutoffs.

Table 6.12: Percentage residence time for coordination environments at cutoffs of 3.7, 3.8 and 3.9 Å averaged over 75 ps of simulation time.

Cutoff (Å)	CN							
	4	5	6	7	8	9	10	11
3.7	5.80	17.96	25.13	30.76	15.97	2.85	1.43	0.00
3.8	0.71	11.14	20.71	34.66	22.57	7.62	2.81	0.38
3.9	0.00	5.03	10.65	31.14	24.93	18.16	8.33	4.35

The results of the analysis of the hydroxide CN of caesium for each trajectory and the overall hydroxide CN for each cutoff are presented in **Table 6.13**. For all three cutoffs the hydroxide CN is very low, less than 0.1 in all cases, with multiple trajectories for the 3.7 and 3.8 Å cutoff, which indicate no coordination by the hydroxide ion. The percentage of time the central ion

spent at each hydroxide coordination mode is summarised in **Table 6.14**, which reinforces the lack of hydroxide coordination to the central ion. The cutoff used to define the first solvation shell has made little difference to the results as all three cutoffs have less than 4 % trajectory time with a hydroxide in the first solvation shell.

Table 6.13: Hydroxide coordination numbers (CN_{OH}) for each AIMD trajectory with accompanying standard deviation (SD).

Trajectory	CN_{OH}		
Cutoff (Å)	3.7	3.8	3.9
1	0.07	0.08	0.09
2	0.00	0.00	0.01
3	0.01	0.01	0.01
4	0.07	0.07	0.08
5	0.00	0.00	0.00
Mean (SD)	0.07 (0.03)	0.03 (0.04)	0.04 (0.04)

Table 6.14: Percentage residence time for hydroxide coordination environments at cutoffs of 3.7, 3.8 and 3.9 Å averaged over 75 ps.

Cutoff (Å)	CN	
	0	1
3.7	97.22	2.78
3.8	96.65	3.35
3.9	96.01	3.99

The dynamics of proton transfer were analysed according to the methodology in **Chapter 4**, with the calculated Mulliken charges on each atom identifying the hydroxides through each trajectory. **Table 6.15** summarises the PTEs that occurred in the monohydroxide systems for 75 ps for each cutoff. The total PTEs for each cutoff are the same, with the 3.8 and 3.9 Å cutoff identifying identical types of proton transfer. The total number of PTEs is not dissimilar to the number of PTEs found in the strontium monohydroxide systems, with a reduction in prevalence of PTES from 0.9 PTEs every ps to 0.73 PTEs every ps. In keeping with the trends seen across the hydroxide environments modelled in this thesis the most prevalent PTEs are those which occur outside the first solvation shell, with similar numbers of PTEs going into and out of the first solvation shell. In contrast to other ions studied, all of the PTEs going into and out of the first solvation shell are directly at, or very close to, the boundary of the first solvation shell; this suggests that the hydroxide is not, in fact, coordinating with the caesium at all, but rather interacting with the ion through chance.

Table 6.15: Number and characterisation of proton transfer events (PTE) for each cutoff, obtained from 75 ps of AIMD data for the caesium monohydroxide system, percentages in parenthesis.

Cutoff (Å)	PTE				
	1^{st}—1^{st}	1^{st}—2^{nd}	2^{nd}—1^{st}	2^{nd}—2^{nd}	Total
3.7	1(2)	2(4)	1(2)	51(93)	55
3.8	1(2)	2(4)	2(4)	50(91)	55
3.9	1(2)	2(4)	2(4)	50(91)	55

The full plots which indicate both the total and hydroxide coordination numbers for each of the 5 trajectories which have been analysed using the 3.8 Å cutoff are shown in **Figure 55**. The plots also indicate the first shell cutoff and the distance at which a PTE occurred away from the central ion. As in the aquo complexes, the total CN fluctuates frequently and does not centre on a particular coordination mode. Instead, over each trajectory a range of CNs is found, as reported in **Table 6.12**. It is clear that the majority of PTEs occur outside the first solvation shell, in the bulk water, with very few occurring at the boundary of the first solvation shell. Intrashell PTEs are only identified in **Figure 6.10d**, while in all other trajectories the hydroxide coordination is a result of proton migration into the first solvation shell. Due to the proximity of the intrashell PTEs of **Figure 6.10d** to the solvation shell cutoff, these could potentially be the result of the proton migration and rapid interchange of the CN coinciding, resulting in them being mischaracterised as PTEs.

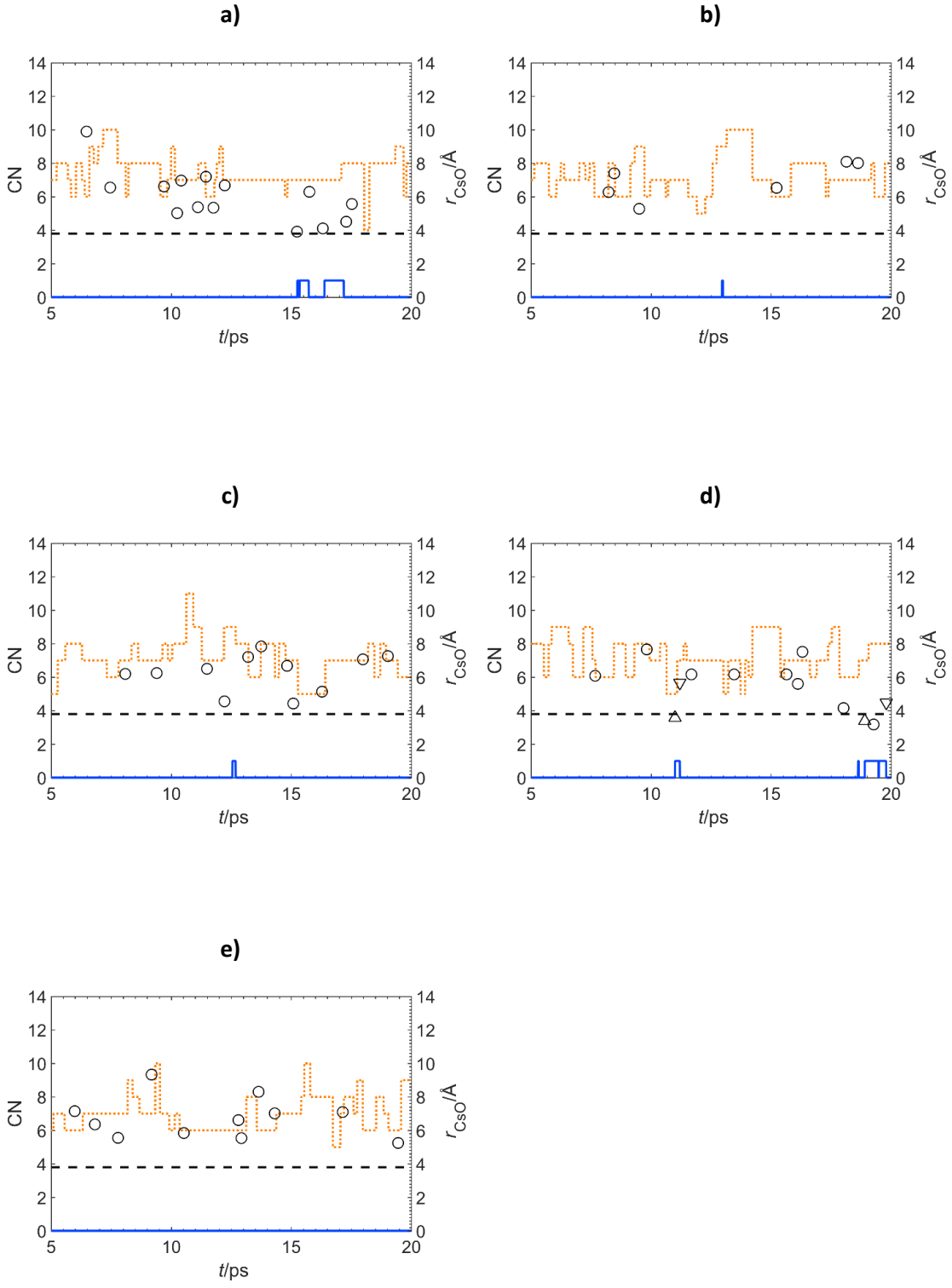

Figure 6.10(a-e): Total (dotted orange) and hydroxide (solid blue) coordination number and proton transfer events (Δ: 1st shell → 2nd shell, ∇: 2nd shell → 1st shell, ○: intrashell) for each 15 ps AIMD trajectory. The dashed black line indicates the first shell cutoff distance of 3.8 Å.

6.2.3 Part 2: Conclusion

This section focused on attempting to define the first solvation shell of caesium in both aquo and monohydroxide environments. 75 ps of analysable AIMD trajectories were collected for each environment. Initial structures were optimised using the PBE functional with a DFT-D3 dispersion correction and AIMD simulations were carried out using Born-Oppenheimer molecular dynamics.

Bonding in the first solvation shell was characterised by averaging the RDFs over the entire AIMD trajectory time, which identified a lack of definition in the first solvation shell. This lack of definition resulted in the investigation of the coordination environment using three different solvation shell cutoffs (3.7, 3.8 and 3.9 Å), which were then used for the hydroxide analysis to enable accurate comparison. For each cutoff, the average coordination numbers, average bond lengths, and where applicable, average hydroxide coordination numbers of the system were calculated. Analysis of the first solvation shell of the aquo systems was within the results found in existing experimental and computational literature. Overall, changing the first solvation shell cutoff did not have a large impact on the solvation features identified, with the primary difference being the range of caesium coordination numbers identified across the trajectory time.

The addition of a hydroxide to the solvation environment resulted in lower CNs and a smaller range of CN seen across the trajectories. However, hydroxide coordination to the caesium ion was found to be a rare occurrence, suggesting that the solvation of OH^- is competing with the solvation of Cs^+. Indicating that as with strontium, caesium will not be in a hydrated hydroxide form when removed from the nuclear storage ponds. Further, the migration of protons through the systems was analysed and proton transfer was found to occur on a slightly less frequent timescale than for the alkaline earth metals. Proton transfer events occurred mostly outside the first solvation shell, and the few intrashell events observed were found at the solvation shell boundary.

Overall, the investigation into the solvation structure of caesium revealed an ill-defined first solvation shell, with rapidly changing coordination environments across all trajectories. The investigation into the impact of a single hydroxide produced a similarly ill-defined solvation shell, however this lack of definition did not drastically alter the prevalence of proton transfer events which occurred on a slightly lower frequency than the strontium monohydroxide investigation.

6.3 Part 3: Aquo and Hydrated Hydroxide Complexes of La^{3+} and Lu^{3+}

As for the alkaline earth metals studied in **Chapter 3**, and for the uranyl complexes investigated in **Chapter 5**, the solvation shell structure of lanthanum ion (La^{3+}) and lutetium ion (Lu^{3+}) in aqueous environments has been well reported in both computational and experimental literature. However, the interactions between the ions and hydroxides, and the dynamics of hydroxide solvation structure, have not yet been investigated. Aside from their relevance to this thesis as products of the nuclear fuel cycle, as trications they offer a further opportunity to explore the impact of increasing ionic charge on the behaviour of hydroxides in an aqueous environment. Furthermore, as the 'book-ends' of the lanthanide series there is a size differential to be explored, with La^{3+} having a large ionic radius of 1.250 Å, and Lu^{3+} a smaller ionic radius of 0.995 Å.[275]

The hydration number for La^{3+} has been studied experimentally with methods including EXAFS[275–281], XRD[282–285],ND[286], Raman[287] and X-ray Scattering[288]. The majority of studies find the CN of La^{3+} to be around 9[275–282], with an overall CN range of 7.5[286] to 12[279] and accompanying first shell La—O bond distances from 2.52[281] to 2.86[275] Å. Näslund *et al*.[281], in a combined X-ray diffraction and X-ray absorption spectroscopy investigation, studied a solution of lanthanum perchlorate and concluded that the most probable structure was 9 coordinated, with 3 waters in the equatorial plane at an average distance of 2.52 Å, and 6 capping water molecules at a distance of 2.66 Å. In the EXAFS investigation of P. Allen *et al*.[276] the solvation structure of La^{3+} in increasing chloride concentration was studied and at low concentration a CN of 9.2 was identified with an average La—O bond length of 2.52 Å. Díaz-Moreno *et al*.[286] investigated the structure of 1 M aqueous $LaCl_3$ using H/D isotopic substitution neutron scattering and X-ray scattering, and found that La^{3+} is hydrated by 8 water molecules and 1 Cl^- ion, compared to being surrounded by 9 water molecules at lower concentrations. Solera *et al*.[279] investigated solvated La^{3+} with EXAFS and proposed a higher CN of 12 with a bond length of 2.56 Å, but this was an outlier amongst the experimental literature results.

The combined EXAFS and MD studies of Duvali *et al*.[289] identified a La—O distance of 2.52 Å and a CN of 9.02. A similar study by Migliorati *et al*.[290] found a slightly longer La—O distance of 2.57 Å and a CN of 9.5. Rudolph *et al*.[291] combined Raman spectroscopy and DFT to identify a La—O bond distance of 2.58 Å and a CN of 9.

Computational studies reflected trends similar to those found in experimental literature, with La—O bond distances from 2.50[292] Å to 2.9[293] Å and first shell CNs identified as 8[294] to 12[295],

with the majority finding a CN of 9[294,296–298]. Buzko *et al*.[294] used DFT to examine water clusters of La^{3+} with CNs of 8 and 9 and found that the 9 coordinated complex was the most stable. Whereas, Hofer *et al*.[296] used an *ab initio* QMMM approach to investigate the structure and dynamics of La^{3+} and found that 9 and 10 CN complexes coexist and interchange with an average CN of 9.5, the average La—O bond length was 2.65 Å. An MD study by Meier *et al*.[295] investigated aqueous solutions of $LaCl_3$ at different concentrations: at infinite dilution CN of 12 with an average La—O distance of 2.64 Å was found but at a concentration of 2M the CN lowered to 10.2 with a La—O distance of 2.50 Å.

Fujiwara *et al*.[297] used AIMD and DFT to identify a La^{3+} CN of 9 and a first shell La—O length of 2.64 Å when surrounded by 64 water molecules. The authors attempted a study using 24 water molecules which identified a lower La^{3+} CN of 8, it was observed that 24 waters resulted in a first solvation shell with large gaps suggesting that the 24 water model was too small. The Terrier *et al*.[298] CPMD study developed three potentials to study the solvation structure of La^{3+}, and found bond lengths of 2.58 Å, 2.58 Å and 2.84 Å with corresponding CNs of 9.00, 8.45 and 9.16. The authors identified that their most accurate potential had produced the CN of 9.16, but that the bond length of 2.84 Å was overly long.

The solvation structure of Lu^{3+} is similarly well studied, with experimental investigations finding a range of CN which cluster around 8 with NMR[299], EXAFS[275,277,278,280,300,301], XANES[302] finding CNs in the range of 7.7[300] to 8.7[299] with La—O bond lengths of 2.31[277] Å to 2.53[302] Å. Persson *et al*.[278] used EXAFS to characterise the solvation shell in aqueous solution at ambient temperature, and found a Lu—O bond length of 2.36 Å and a total CN of 8.4 with 6 bonds at an average distance of 2.28 Å and an average of 2.2 bonds at distance of 2.51 Å. Brücher *et al*.[299] used ^{1}H and ^{35}Cl NMR to investigate the hydration of the Lu^{3+} in a water and acetone mixture, finding that the CN decreased as the acetone to water ratio increased, with the ClO_4^- ions replacing coordinating water molecules. A CN of 8.7 was found for a 0.49 M solution and a CN above 9 was deduced for a dilute solution.

DFT[294,303–307] studies indicate an unambiguously 8 coordinated structure with first shell Lu—O bond lengths identified as 2.35[303] Å to 2.48[304] Å. Fujiwara *et al*.[297] used DFT and AIMD to investigate the hydration of La^{3+}, geometry optimisations of structures from the AIMD trajectories found a La—O of 2.36 Å with a CN of 8 to be the most stable. Buzko *et al*.[294] investigated the hydration and stability of $Lu(H_2O)_n^{3+}$ (n = 1 to 9), and found a maximum CN of 9, with calculations attempting to coordinate a 10th water molecule all resulting in the 10th water moving to the second solvation shell. Hay[308] calculated the geometries of 58 known structures with a CN from 8 to 12 using a molecular mechanics force field approach, for the 8

coordinated species the Lu—O length was 2.32 Å and for the 9 coordinated species the Lu—O length was 2.51 Å for the three capping water molecules and 2.34 Å for the other 6 water molecules.

Classical MD studies investigating the hydration of Lu^{3+} have found CNs of 8[289,308–310] with Lu—O bond lengths of around 2.32[289,308–310] Å. The MD study of Sessa *et al*.[310] found that the 8 CN species was dominant for 97% of the time with a low percentage of 9 coordinated complexes detected, and the 8 coordinated structure was a square antiprism geometry with a Lu—O of 2.32 Å. Duvail *et al*.[289] used classical MD to investigate the solvation structure of Lu^{3+} and compared the results to EXAFS data to identify a CN of 8.01 and bond length of 2.32 Å.

6.3.1 Computational Details

Born-Oppenheimer molecular dynamics simulations were performed using the QUICKSTEP module of CP2K version 3.0 on simulation cells with periodic boundary conditions.[94,115] Temperature and pressure were kept constant using a NPT_I ensemble, where the simulation cell is isotropic, the average temperature $T = 400\ K$ was maintained using a Nosè-Hoover thermostat and a barostat maintained pressure of 1 atm.[105] The GAPW[96] method was implemented using the PBE functional with the DFT-D3 dispersion correction applied.[76,166] The calculations used a double-ζ plus polarization Gaussian basis set (DZVP-MOLOPT-SR-GTH), a planewave cutoff of 600 Ry and relative cutoff of 80 Ry.[167] Convergence test results for both cutoffs can be found in **Appendix A5 and A6** for La^{3+}, and Lu^{3+} respectively.

5 initial structures with 64 water molecules and a central ion of either La^{3+} or Lu^{3+} were optimised. All initial structures underwent a cell optimisation prior to the start of the AIMD trajectory run, where both the cell parameters and the geometry were optimised simultaneously. For La^{3+}, the optimised cell parameters were $a = b = c = 11.65$ Å and for Lu^{3+} they were $a = b = c = 11.50$ Å, these were used for all starting structures. For the aquo environments, charge neutrality was achieved through the use of a uniform neutralising background charge. Each AIMD trajectory was made up of 40,000 steps, each of length 0.5 fs for a total of 20 ps. The first 5 ps of each trajectory was treated as an equilibration period and was not considered in subsequent analysis.

A total of 100 ps of trajectory time was collected for each lanthanide system, with 75 ps of trajectory time used in analysis once the equilibration period was discarded. The resulting post-equilibration trajectory time was analysed in the same method described in detail in **Chapter 3**.

6.3.2 Results

6.3.2.1 Characterisation of Lanthanide Aquo Complexes

RDFs were calculated for the entire 75 ps simulation time for each ion and are shown in **Figure 6.11**.

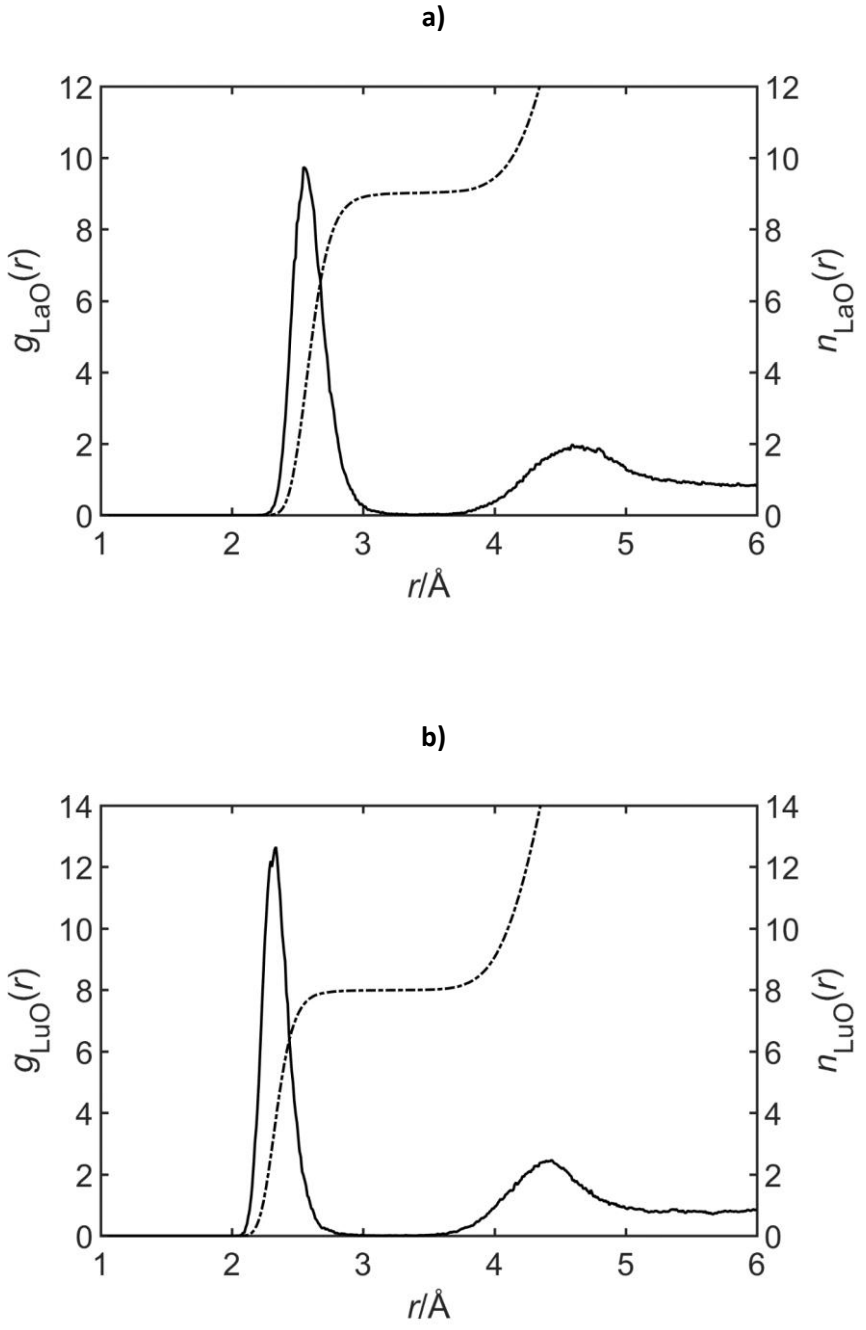

Figure 6.11: M—O radial distribution functions, g(r), generated using a total of 75 ps simulation time for **a)** La^{3+}, **b)** Lu^{3+} in aqueous environment.

For both ions a well-defined first solvation shell is evident, with peak maxima at 2.54 Å and 2.34 Å for La^{3+} and Lu^{3+} respectively. For La^{3+}, this indicated a La—O distance well within the

ranges of both experimental results of 2.51[281] Å to 2.56[288] Å, and computational results of 2.50[292] Å to 2.9[293] Å. In particular, this value is in excellent agreement with 2.54 Å value obtained by the EXAFS of Allen *et al*.[276] and Ishiguro *et al*.[277] The majority of EXAFS investigations found a Lu—O distance of around 2.3[275,277,278,289,300,301] Å, which is in excellent agreement with the RDF peak for Lu^{3+}. This value also agrees well with both experimentally derived values of 2.31[277,280,301] Å to 2.53[302] Å and the computational values of 2.32[309–311] Å to 2.48[304] Å.

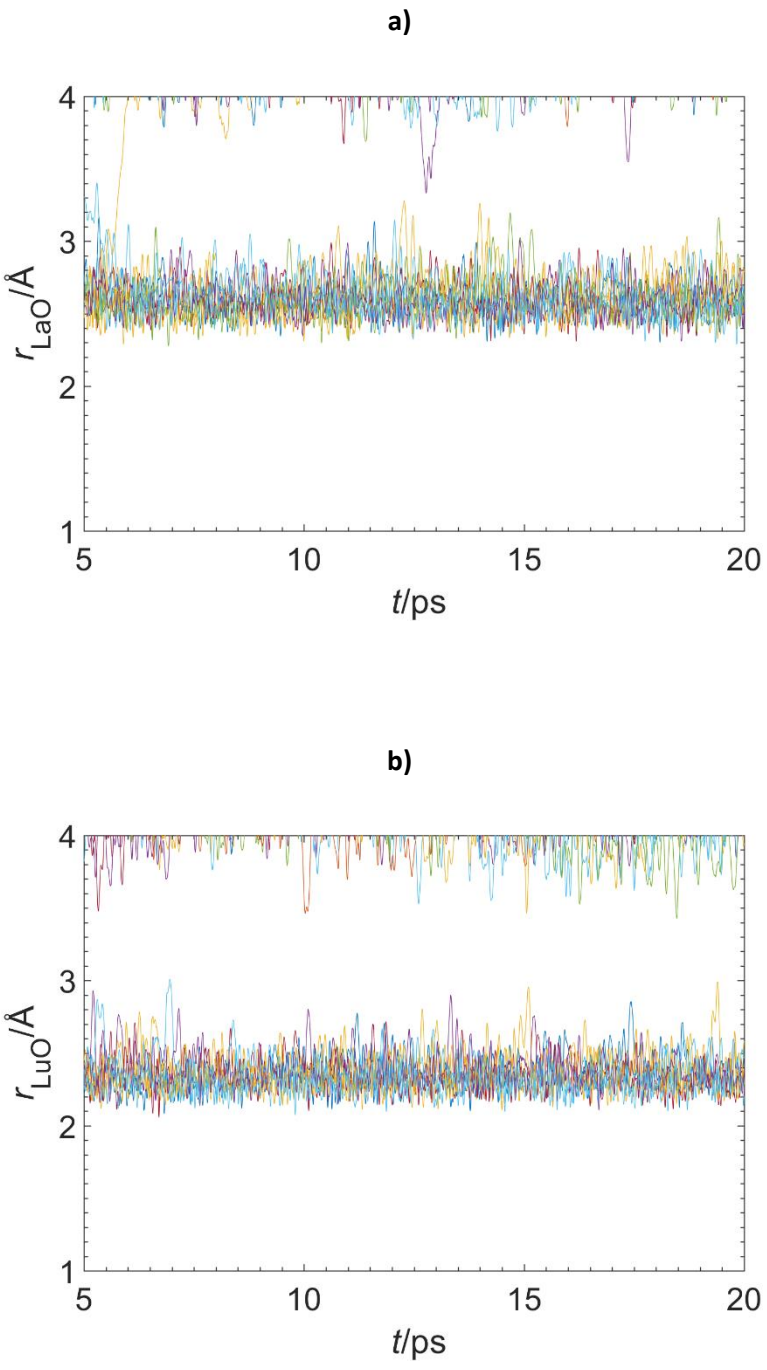

Figure 6.12: Example of a first shell trajectory plot for all M—O bonds at a distance < 4 Å for **a)** La^{3+} and **b)** Lu^{3+}.

All M—O bonds (where M = La^{3+} or Lu^{3+}) within 4 Å of the central ion over the timescale of the trajectory are plotted in **Figure 6.12**. The strong definition of the first solvation shells which is reflected in the RDF diagrams. The first shell bonds for both La^{3+} (**Figure 6.12a**) and Lu^{3+} (**Figure 6.12b**) indicate a tightly bound first solvation shell with a fairly constant number of M—O bonds. While in both cases there are instances of longer M—O bonds, these do not result in a change of overall coordination number in the two examples given.

Appropriate first shell cutoffs using the RDF + 0.5 Å (3.0 Å for La^{3+} and 2.8 Å for Lu^{3+}) for the analysis of average bond lengths and coordination numbers were chosen. **Table 6.16** summarises the calculated La—O and Lu—O bond lengths along with the total first shell CN which is listed for each trajectory. Both calculated values have small standard deviations, indicating a constant average bond length across the different trajectories. The overall means for the bond lengths, averaged over 75 ps, with accompanying standard deviations are also given. The average La—O bond length of 2.61 Å is well within the literature values of 2.50[292] Å to 2.9[293] Å and compares well with the 2.63 Å value obtained in the AIMD investigation of Fujiwara *et al*.[297] and the Hofer *et al*.[296] value of 2.65 Å. Similarly, the average Lu—O bond length of 2.36 Å is well within the literature range of 2.3[300] Å to 2.53[302] Å, and compares excellently with both the 2.36 Å value obtained in the Fujiwara *et al*.[297] AIMD investigation and the 2.36 Å value obtained in the DFT investigation of Zhang *et al*.[305] Furthermore, it is also in excellent agreement with the EXAFS studies of both Persson *et al*.[278] and D'Angelo *et al*.[275] which both obtained a value of 2.36 Å.

Table 6.16: Calculated M—O separations ($r_{M\text{-}O}$) and mean coordination numbers (CN) for each AIMD trajectory (Traj.) considered in this study, with accompanying standard deviations (SD)

Traj.	$r_{M\text{-}O}$ (Å)		CN	
	La	Lu	La	Lu
1	2.611	2.360	9.01	7.99
2	2.615	2.355	8.96	7.95
3	2.611	2.360	8.90	7.99
4	2.612	2.356	8.98	7.93
5	2.614	2.365	8.99	7.98
Mean (SD)	2.612 (0.002)	2.359 (0.004)	8.97 (0.04)	7.97 (0.03)

The CNs for both La^{3+} and Lu^{3+} compare excellently with the available literature values of 9[275,276,294,296–298,277–282,289,290] and 8[275,277,305–310,278,280,289,294,300,301,303,304] respectively and there is very little deviation in the values for the first shell CN across the trajectories. The percentage residence times for each ion at different coordination environments are given in **Table 6.17**

and reflect the decrease in ionic radius across the lanthanide series reflected in the coordination number change with La^{3+} ion existing primarily as a 9 CN species and Lu^{3+} ion as an 8 CN species, as evidenced extensively through the literature.

Table 6.17: Percentage residence time of different coordination environments, averaged over a total of 75ps for each ion.

Cation	CN			
	7	8	9	10
La^{3+}	0.00	4.20	94.71	1.09
Lu^{3+}	4.53	94.11	1.35	0.00

The coordination plots for the total first shell CN changing over time for each trajectory are given in **Figures 6.13** and **6.14** for La^{3+} and Lu^{3+} respectively. As confirmed by the calculated averages given in **Tables 34** and **35** the CN of La^{3+} is mostly 9, and the CN of Lu^{3+} is 8. There is some lability in the coordination with La^{3+} being found with CNs of 8 to 10, and Lu^{3+} coordination environments of 7 to 9. However, the majority of deviations from the primary coordination number are short lived, lasting less than 2 ps.

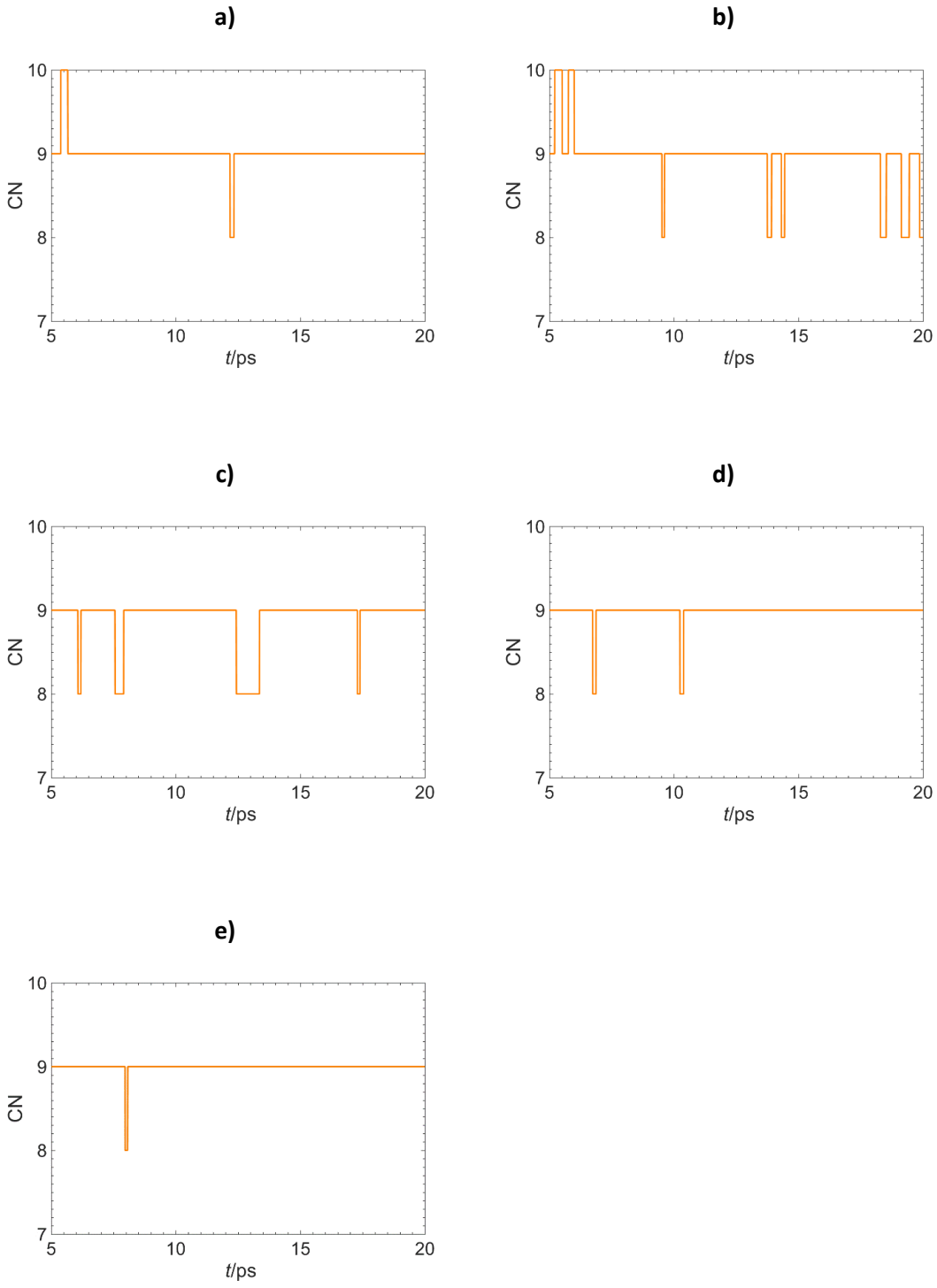

Figure 6.13(a-e): Total coordination number plots for each 15 ps AIMD trajectory of La^{3+}.

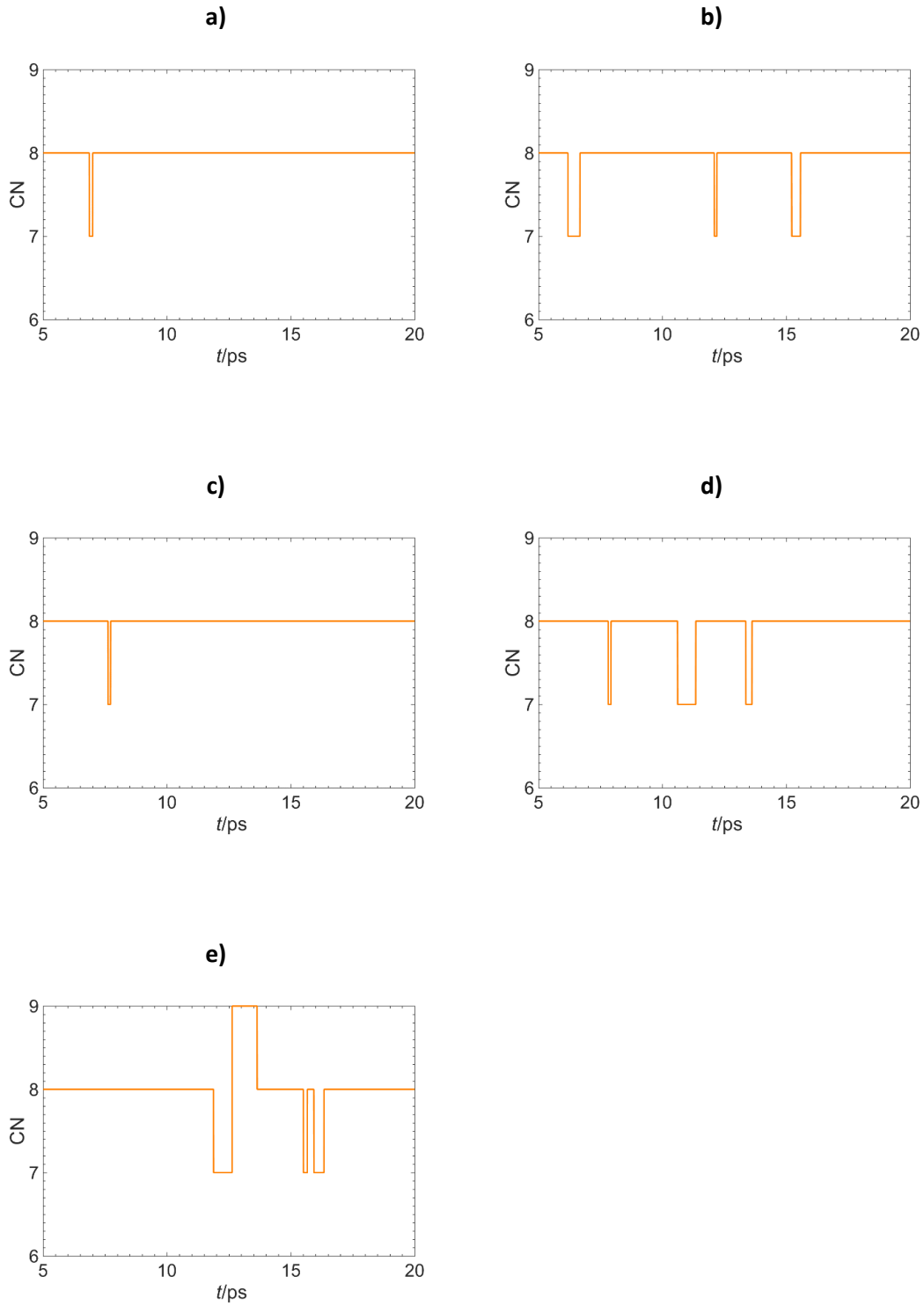

Figure 6.14(a-e): Total coordination number plots for each 15 ps AIMD trajectory of Lu^{3+}.

6.3.2.2 Characterisation of the Lanthanide Trihydroxide Complexes

In keeping with the methodology used throughout this thesis, the 5 hydroxide environments were created for each ion by taking snapshots of the AIMD trajectories for the aquo complexes. Three protons were removed from waters in each structure snapshot to generate three OH^- ions with the full simulation box containing 61 water molecules, 3 OH^- ions and a central ion of either La^{3+} or Lu^{3+}. These structures had both their geometry and cell parameters optimised simultaneously to generate the starting structures for each 20 ps AIMD trajectory. Initial cubic cell parameters for AIMD trajectories were set to $a = b = c = 11.65$ Å for La^{3+} and $a = b = c = 11.50$ Å for Lu^{3+}, in keeping with those used for the aquo trajectories. 5 ps of trajectory time was discarded for equilibration resulting in 75 ps of hydroxide simulation time for each ion. The resulting trajectories were analysed using the same methodology described in **Chapter 4**, this time taking into account the three hydroxides present in the system.

The RDFs for La^{3+} and Lu^{3+} were calculated over the entire 75 ps for each ion and are shown in **Figure 6.15**. The first solvation shells for both ions are well defined. In **Figure 6.15a** a peak of 2.61 Å indicates the La—O first shell distance and in **Figure 6.15b** a peak of 2.18 Å indicates the Lu—O distance. The introduction of hydroxide ions into the solvation environment has increased the La—O distance by 0.60 Å, although the La^{3+} peak is much broader than those in the aquo simulations. The peak indicating the Lu—O bond has decreased 0.15 Å compared to the water simulations, in keeping with previous hydroxide simulations of other ions where the hydroxide environments indicate a smaller first solvation shell compared to their aqueous environments.

a)

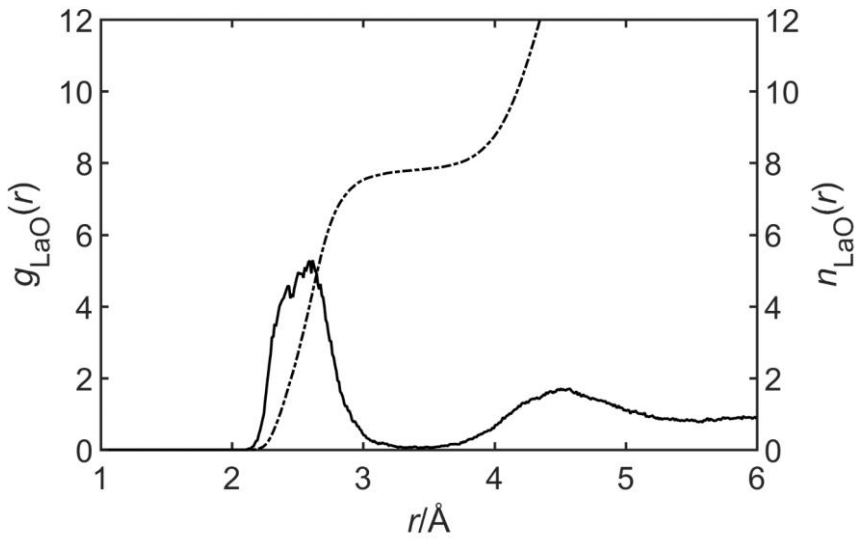

b)

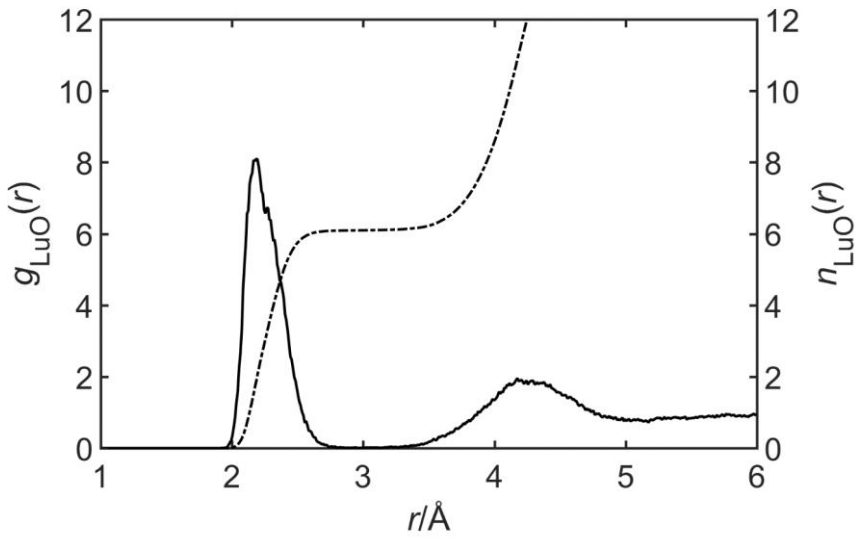

Figure 6.15: M—O radial distribution function, g(r), generated using a total of 75 ps simulation time for **a)** La^{3+}, **b)** Lu^{3+} in a trihydroxide environment.

a)

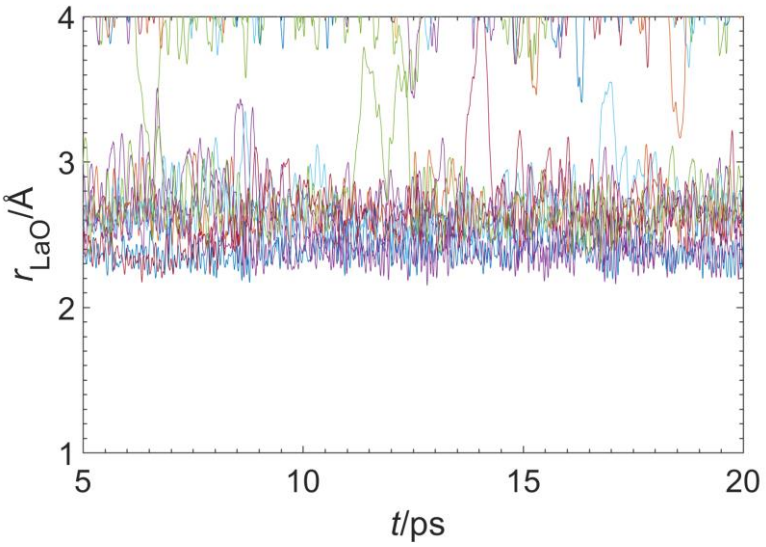

b)

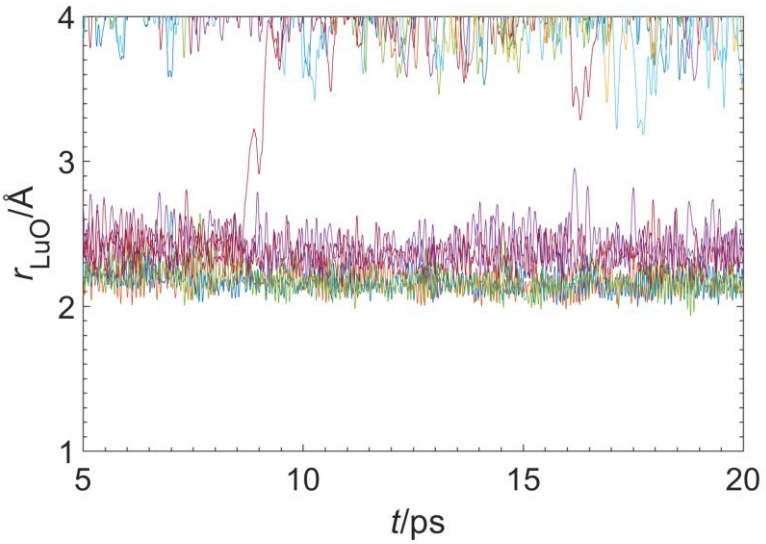

Figure 6.16: Example of a first shell trajectory plot for all M—O bonds at a distance < 4 Å for **a)** La^{3+} and **b)** Lu^{3+}.

Examples of full trajectory plots for all M—O distances less than 4 Å from the central atom are shown in **Figure 6.16**. Both **Figure 6.16a** and **Figure 6.16b**, which show the solvation environment for La^{3+} and Lu^{3+}, respectively, reveal defined solvation shells as indicated by the RDFs of **Figure 6.15**. However, in contrast to the aquo complexes, the solvation environment around La^{3+} is much more dynamic, with waters entering and leaving the first solvation shell multiple times over the trajectory period. The La—O bond lengths of the first solvation shell

fluctuate over a larger distance than seen for the aquo complexes as seen in **Figure 6.16a**. This is reflected in the RDF with the much broader peak for La^{3+} than for Lu^{3+}.

The calculated M—O average bond distances, total first shell CNs and hydroxide CNs are summarised **Table 6.18** for each trajectory. The overall averages of these values, calculated over 75 ps, are included along with the standard deviation. First shell cutoffs of 3 Å and 2.8 Å were used for La^{3+} and Lu^{3+} respectively, for consistency these are the same as those used for the aquo calculations. The calculated average bond lengths provide a clearer indication of the impact of hydroxides on the first solvation shell than the RDFs: values for both ions decreased with the introduction of hydroxides into the system, with a reduction of 0.028 Å and 0.083 Å for La—O and Lu—O respectively. The larger reduction in CN for the Lu^{3+} hydroxide system allows the remaining ligands to coordinated more closely to the ion which leads to the reduction in average bond length.

Table 6.18: Calculated M—O separations (r_{M-O}), mean coordination numbers (CN) and mean hydroxide coordination numbers (CN_{OH}) for each AIMD trajectory (Traj.) considered in this study with accompanying standard deviations (SD).

Traj.	r_{M-O} (Å)		CN		CN_{OH}	
	La^{3+}	Lu^{3+}	La^{3+}	Lu^{3+}	La^{3+}	Lu^{3+}
1	2.594	2.287	7.72	6.24	2.49	3.00
2	2.580	2.293	7.59	6.39	2.32	2.64
3	2.578	2.265	7.47	6.00	2.54	3.00
4	2.587	2.270	7.66	6.00	2.43	3.00
5	2.584	2.265	7.66	6.02	2.52	2.91
Mean	2.584	2.276	7.62	6.13	2.46	2.91
(SD)	(0.006)	(0.013)	(0.10)	(0.18)	(0.09)	(0.15)

In both cases the total CN reduced by more than 1 with the introduction of hydroxides. The hydroxide CN (CN_{OH}) indicate that the hydroxide ions preferentially coordinate to the ion over existing in the bulk water. This is more pronounced for Lu^{3+} with the majority of its CN_{OH} values equalling 3, indicating that overall there is little or no deviation from full hydroxide coordination. There is larger variation in the hydroxide coordination for La^{3+}, with most values at around 2.5, indicating there is some fluctuation in the number of hydroxides coordinating in the first solvation shell across all trajectories. This difference is likely due to the size difference between the two ions as the smaller and more charge dense Lu^{3+} cation will preferentially bind with the hydroxide ions, while the larger and more diffuse La^{3+} cation allows for more lability in the coordination of anions.

The residence times for each coordination environment and ion are given in **Table 6.19**. Interpreting the change of total CN in the contexts of these numbers, the range of coordination environments for La^{3+} has shifted from 8 to 10 in the aquo environment to 6 to 8, with the majority of trajectory time spent as 8 coordinated species compared to the 9 coordinated species found in the aquo species, but with significant time spent in 7-fold coordination. Lu^{3+} has a similar shift, with coordination environments of 5 to 7 found in the hydroxide species compared to a range of 7 to 9 for the aquo environments, the majority of trajectory time was spent in 6-fold coordination with a significant portion spent in 7-fold coordination.

Table 6.19: Percentage residence time of different coordination environments (CN), averaged over a total of 75ps for each ion.

Cation	CN			
	5	6	7	8
La^{3+}	0.00	1.85	34.36	63.79
Lu^{3+}	0.33	86.40	13.27	0.00

There is a clear difference in the hydroxide coordination to the ion, as shown by the residence times for each hydroxide coordination number given in **Table 6.20**. For the majority of the trajectory time Lu^{3+} is found as a trihydroxide with brief periods as a mono- or di- hydroxide, whereas La^{3+} is found as either a di- or tri-hydroxide for 98 % of time with a brief instance of monohydroxide coordination. This difference can again be attributed to the size difference of the ions and indicates the increased lability of the first shell of La^{3+} and the impact of a longer and weaker La—O bond. Neither ion is found to be uncoordinated by hydroxides at any point through the simulation time, in contrast to the dication alkaline earth metals, suggesting that the increased charge of the central ion increases the affinity for the hydroxide ions.

Table 6.20: Percentage residence time of different hydroxide coordination environments (CN_{OH}), along with mean coordination number, averaged over a total of 75 ps for each ion.

Cation	CN_{OH}			
	0	1	2	3
La^{3+}	0.00	1.91	50.30	47.79
Lu^{3+}	0.00	2.31	4.35	93.34

Each hydroxide trajectory is summarised in **Figure 6.17** and **Figure 6.18** for La^{3+} and Lu^{3+} respectively. Each figure shows the total coordination and hydroxide coordination to the central ion, and the movement of hydroxides through proton transfer is summarised, the first shell cutoffs are also indicated on these graphs. The clear difference between the ions at each end of the lanthanide series is evident. Both the total and hydroxide coordination number for

La^{3+} are highly variable throughout each trajectory. Conversely, for the smaller and charge dense Lu^{3+} the total CN and hydroxide CN remain relatively stable, and, in periods where these numbers do vary, it is for longer periods across a trajectory.

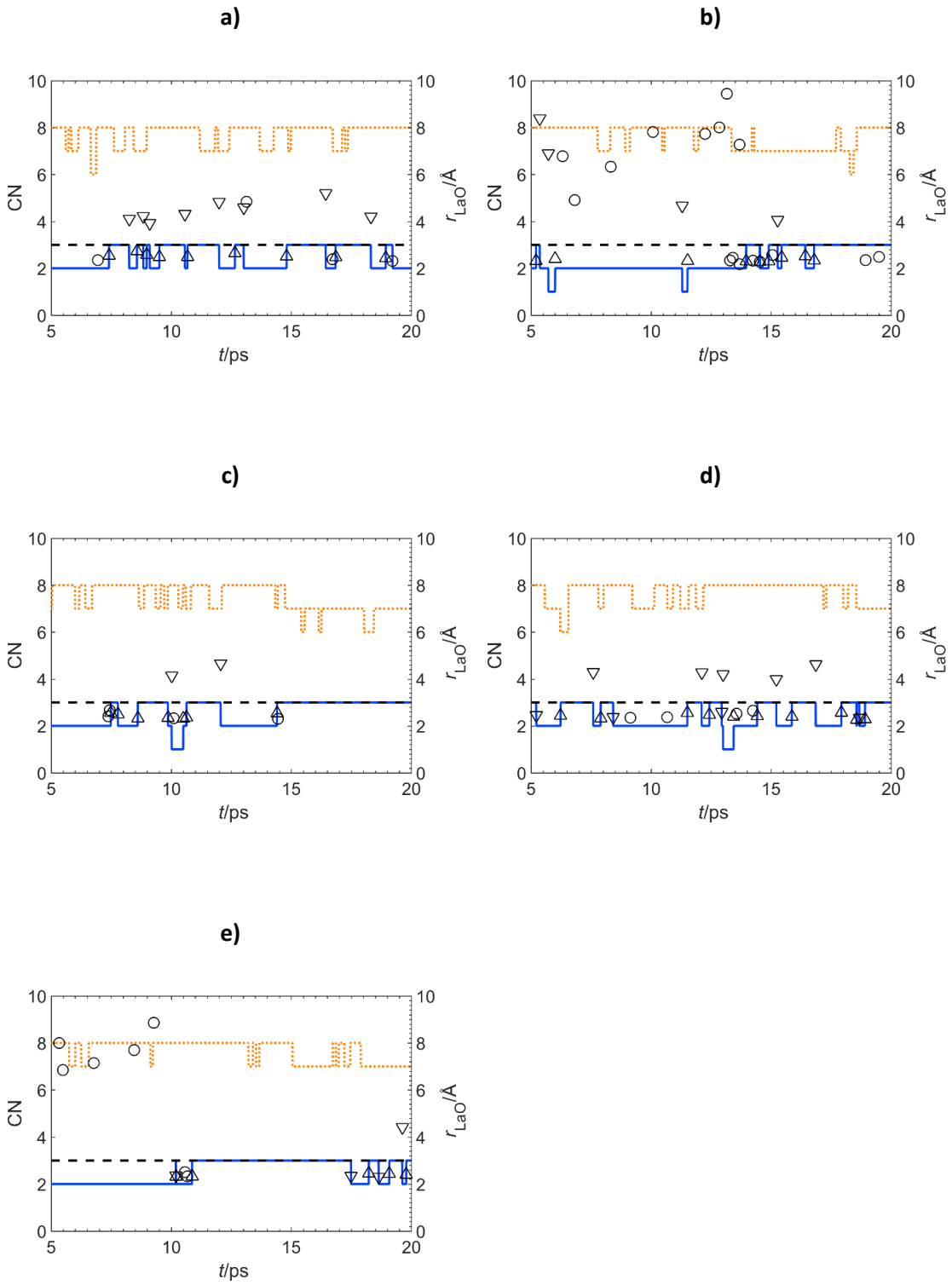

Figure 6.17(a-e): Total (dotted orange) and hydroxide (solid blue) coordination number and proton transfer events (Δ: 1st shell → 2nd shell, ∇: 2nd shell → 1st shell, ○: intrashell) for each 15 ps AIMD trajectory for La^{3+}. The dashed black line indicates the first shell cutoff distance of 3 Å.

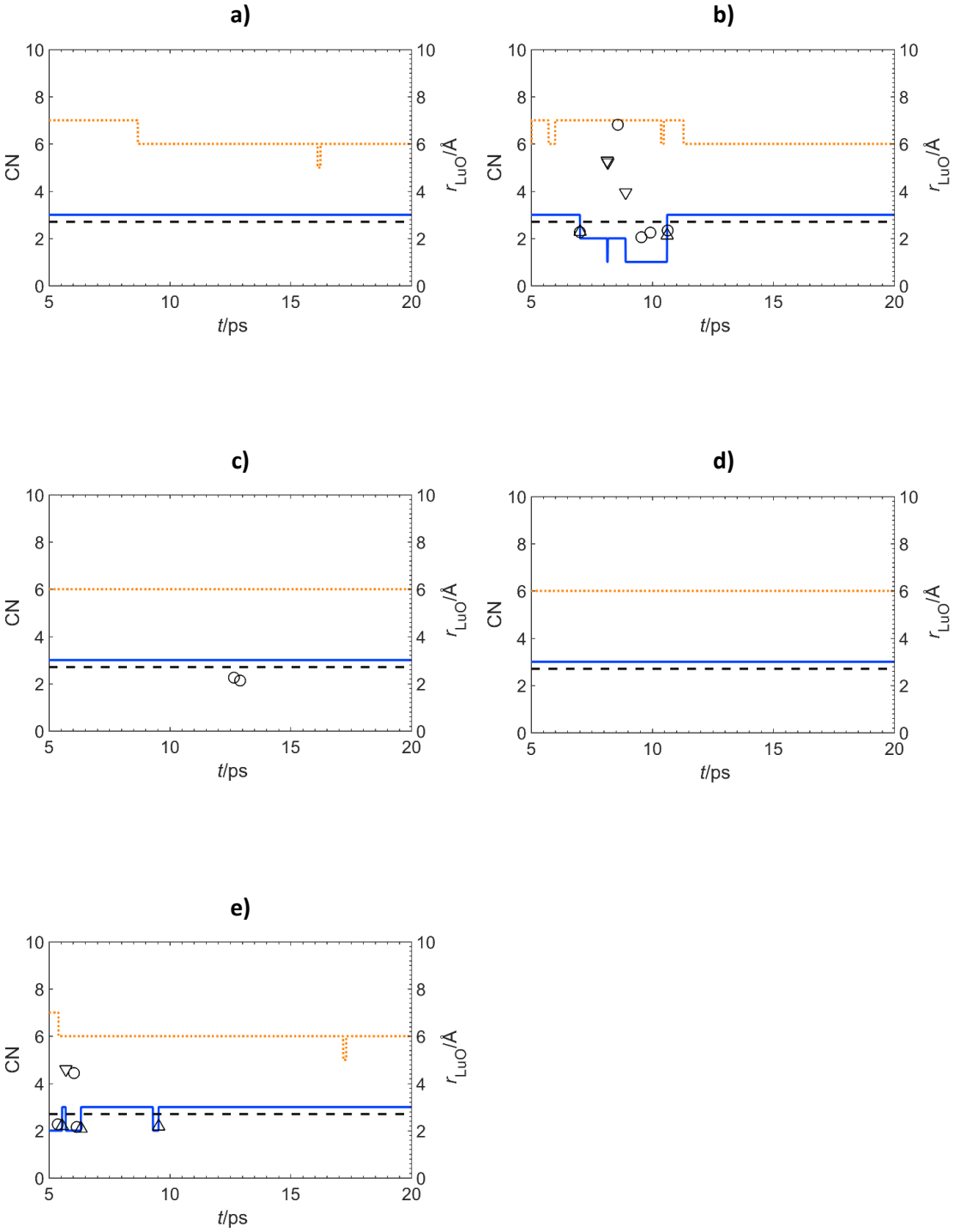

Figure 6.18(a-e): Total (dotted orange) and hydroxide (solid blue) coordination number and proton transfer events (Δ: 1st shell → 2nd shell, ∇: 2nd shell → 1st shell, ○: intrashell) for each 15 ps AIMD trajectory for Lu^{3+}. The dashed black line indicates the first shell cutoff distance of 2.8 Å.

The total number of PTEs, characterised by transfer of the protons related to the first solvation shell, are summarised in **Table 6.21**. The La^{3+} systems have 4 times as many PTEs compared to the Lu^{3+} systems. In both environments the intrashell PTEs outside the first solvation shell were not the most common, in contrast to all the other ions examined in the hydroxide environment. Instead, for La^{3+} the 1^{st} to 2^{nd} shell PTEs were most prevalent, with a significant number of 2^{nd} to 1^{st} and 1^{st} to 1^{st} shell PTEs were also observed. Significant amounts of hydroxide migration were indicated by the unequal flow of protons into and out of the first solvation shell, however this is not quantified in this analysis. This is likely linked to the increase in the hydroxide coordination to the ions, which increases the probability of PTEs in the first solvation shell. The low number of PTEs for Lu^{3+} makes it difficult to identify significant trends, although the most common type of PTE is an intra first shell PTE, which is again likely a reflection of the increase in CN_{OH} for Lu^{3+} throughout the simulations. The increase in the number of hydroxides in the simulation environment does not seem to have increased the total number of PTEs, again likely due to the coordination of the hydroxide to the central ion, indicating that the coordination of the hydroxides to the ion inhibits proton transfer.

Table 6.21: Number and characterisation of proton transfer events (PTE), obtained from 75 ps of AIMD data for each ion considered in this study. Percentage values are given in parentheses.

Cation	PTE				
	$1^{st}-1^{st}$	$1^{st}-2^{nd}$	$2^{nd}-1^{st}$	$2^{nd}-2^{nd}$	Total
La^{3+}	20 (20)	40 (39)	27 (26)	15 (15)	102
Lu^{3+}	9 (41)	7 (32)	4 (18)	2 (9)	22

The increased charge of the lanthanides compared to the alkaline earth metals appears to have an impact on the total number of PTEs. The higher ionic charge of the lanthanides results in higher hydroxide coordination, as well as a decrease in the number of PTEs. Furthermore, there is a decrease in the amount of PTEs for Lu^{3+} compared to La^{3+}. While both ions have the same overall charge, they differ in size, and the larger and less charge dense La^{3+} seems to be less able to influence the solvation structure than the smaller, more charge dense Lu^{3+} ion.

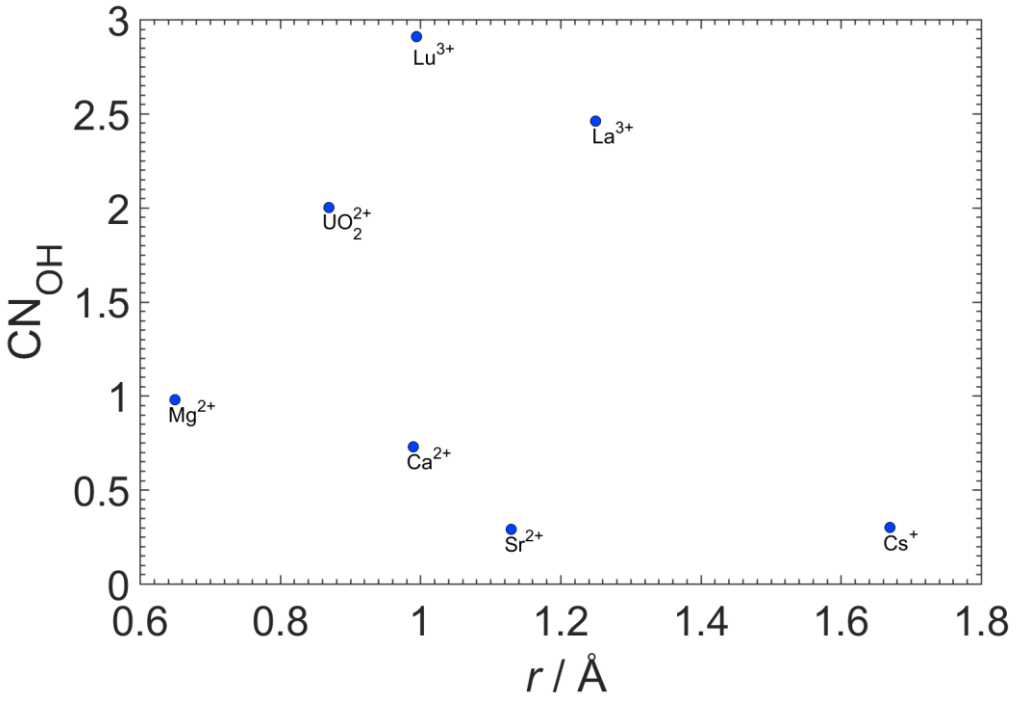

Figure 6.19: The hydroxide coordination (CN_{OH}) against the ionic radius[123] of each cation Cs^{+}, Mg^{2+}, Ca^{2+}, Sr^{2+}, UO_2^{2+}, La^{3+}, Lu^{3+}

The CN_{OH} of each ion studied in this thesis is compared with its ionic radius in **Figure 6.19**, highlighting similar trends as the ionic radii increases. Across both the trications of the lanthanides and the dications of the alkaline earths, higher charge density is correlated with a higher CN_{OH}. In all cases the larger less charge dense ions such as Cs^{+}, La^{3+} and Sr^{2+} have lower CN_{OH} numbers, indicating a reduced ability to attract the hydroxide anion.

6.3.3 Section 3: Conclusion

This section focused on the solvation structure of the lanthanides at each end of the lanthanide series, La^{3+} and Lu^{3+}, in the absence and presence of hydroxide ions. As trications, the lanthanides offered the opportunity to continue investigating the increase in central ionic charge and its impact on both water and hydroxide coordination. In addition, by studying the lanthanides at both ends of the lanthanide series the effect of the increased ionic radius from La^{3+} to Lu^{3+} and its impact on water and hydroxide coordination can also be investigated. Initial geometries were optimised using the PBE functional with a DFT-D3 dispersion correction and all AIMD simulations were carried out using Born-Oppenheimer molecular dynamics. For each ion, 75 ps of analysable AIMD trajectories were collected for both the aquo and the trihydroxide environments.

The first solvation shell for each ion was characterised by averaging the radial distribution functions over the entire AIMD trajectories collected, and by calculating the average bond lengths for M—O. The first shell coordination numbers were calculated alongside percentage residence times for each coordination environment. For the trihydroxide systems the coordination of the hydroxide ions to the cation was analysed and the migration of protons via proton transfer events was calculated.

The results characterising the aqueous environment for both La^{3+} and Lu^{3+} compared excellently with existing literature values. Both the average coordination number for the first solvation shell and the average bond lengths are well within the literature ranges given. The average coordination numbers correctly identified the change in CN from 9 to 8 across the lanthanide series.

The analysis of the solvation environment with the addition of three hydroxide ions resulted in a reduction of both average bond lengths and coordination number for both La^{3+} and Lu^{3+}. The calculated hydroxide coordination numbers indicated that the hydroxide ions preferentially coordinate to the ions over migrating through the bulk water, with no periods of time identified for either ion where no hydroxide coordination takes place. For Lu^{3+} the coordination of hydroxide ions was found to be more pronounced and the ion was coordinated by three hydroxides for the majority of the trajectory time. Proton transfer events were identified and quantified for each ion and were 5 times as frequent for La^{3+} compared to Lu^{3+}, which had two trajectories with no PTEs. Compared to the alkaline earth metals PTEs were less prevalent in the lanthanides and the most common classification of PTEs were first shell intra and inter shell PTEs.

6.4 Chapter 6: General Conclusions

This chapter further explored the relationship of different ions in aqueous environments and in the presence of hydroxide, by investigating a monocation and a dication with a single hydroxide ion, and then trications with three hydroxide ions. In **Part 1**, the dication Sr^{2+} with a single hydroxide was investigated and the results compared to the results of the AIMD simulations to those of the dication with two hydroxide ions. A single hydroxide ion had little impact on the solvation shell compared to simulations involving two hydroxides, with no change in Sr—O average bond lengths and a small reduction of 0.1 in CN compared to the aquo complexes whereas the dihydroxide systems found a reduction in both CN and bond length. Hydroxide coordination was limited and was found for less than 2 ps in the monohydroxide simulations compared to the dihydroxide simulations where it was evidenced

for periods of ~10 ps. However, similar proton transfer behaviour was witnessed in the monohydroxide systems and these events occurred predominantly away from the ion.

In **Part 2**, the solvation structure of the monocation Cs^+ was investigated in both water and in the presence of a monohydroxide. The Cs^+ solvation shell was difficult to characterise, with no solvation shell definition. The aqueous solvation environment was characterised and a range of first shell CNs of 5 to 11 was identified. The lack of definition was also found in the hydroxide environment which made it difficult to accurately compare the hydroxide environment to the Sr^{2+} monohydroxide AIMD trajectories. Similar to Sr^{2+}, there was a lack of coordination of the hydroxide to the ion, although this may be partly due to lack of defined solvation shell. While proton transfers did occur they were at a lower rate than all previous AIMD hydroxide simulations and all occurred at the boundary of the first solvation shell, or outside the first solvation shell.

In **Part 3**, the solvation structure of the trications La^{3+} and Lu^{3+}, were investigated in both water and in the presence of three hydroxide ions. The results for ions indicated well defined first solvation shells, and calculated bond lengths and coordination numbers compared excellently with literature. Both ions exhibited strong hydroxide coordination, likely due to the higher ionic charge of the ions compared to the investigations of the mono and di cations. The high hydroxide coordination had an altered the types of proton transfer events which were identified across the simulations. The most prevalent PTEs were inside first solvation shell in contrast to all other hydroxide simulations. A lower PTE rate was identified compared to that of the alkaline earths, further adding evidence to the theory that proton transfer occurs more readily away from the ion, in the bulk water.

Chapter 7: CeO_2(111) Surface Investigations

This chapter represents a probative investigation into a solvated CeO_2(111) material surface. In contrast to the previous chapters of this thesis, the study presented here is based on energetics and not dynamics. Initial calculations focus on the mineral surface itself, then the surface-water interface when a water model is included. Further calculations examine the adsorption of a Sr^{2+} ion onto the solvated mineral surface and the favourability of adsorption with the introduction of hydroxide ions. In this chapter, cerium oxide, or ceria, is used as an analogue of uranium dioxide, which is found in the legacy waste storage ponds. By doing so, the capability and viability of the computational model is tested for potential inclusion in future AIMD studies of the surfaces of minerals found in the nuclear waste storage ponds.

7.1 Introduction

While brucite is the main mineral found in the nuclear storage ponds, there are other minerals of interest present. As discussed in **Section 1.3,** the uranium from the fuel rods readily forms uranium dioxide (UO_2) in the ponds. Investigating the adsorption of radionuclides onto materials surfaces found in the waste storage ponds can contribute to the accurate characterisation of the chemical environment and behaviour of the stored nuclear waste in the storage ponds.

The accurate description of *f* electrons in actinides such as uranium poses a challenge for DFT. For example, the use of GGA functionals incorrectly predicts UO_2 to be metallic[83], which is usually overcome with the application of a U_{eff} term in the DFT+U method, as discussed in **Section 2.9.5**. However, modelling UO_2 even with the DFT+U method is not trivial due to the 2 unpaired f electrons of each uranium centre, which can result in multiple metastable states.[244,312]

CeO_2 has previously been used experimentally[313–318] as an analogue for UO_2 due to the structural similarities and because CeO_2 is characterised by unoccupied $4f$ states of Ce^{4+} ($4f^0$)[319], which make it significantly easier to model computationally. The ionic radii of cerium(IV) and uranium(IV) are of a similar size at 87 pm and 89 pm respectively.[320] In their respective dioxide forms the lattice parameters are also similar, for UO_2 the lattice parameter is $a = 5.47$ Å[321] and for CeO_2 it is $a = 5.41$ Å.[322] Both CeO_2 and UO_2 crystallise to the same fluorite type structure, are face centred cubic, and have the same Fm-3m space group.[323,324] The potential oxidation states of each metal differs as U(IV) can be oxidised to U(VI) whereas Ce(IV) cannot, but it can be reduced to Ce(III).[319] This difference in possible oxidation states

may be important for chemisorption processes, such as when CO forms carbonate-like CO_3^{2-} structures on a $CeO_2(111)$ surface[325]. However, for the expected physisorption of an ion coordinating weakly to the surface, where the surface lattice is not disrupted, CeO_2 is an appropriate analogue for UO_2.

Ceria (CeO_2) has been well studied as it is a well-known catalytic material. As such, most studies focus on the interaction of a single ion with the $CeO_2(111)$ surface or on the adsorption of water onto the $CeO_2(111)$ surface. An overview of the relevant literature is discussed here; for more in-depth evaluations of the full surface chemistry of CeO_2 the reader is directed to the extensive reviews by Paier *et al*.[326] and Mullins *et al*.[327]

The adsorption of single atoms such as Ag[328,329], Au[330–336], Pt[337] and Sn[338] on stoichiometric and reduced surfaces of $CeO_2(111)$ has been investigated using both experimental and computational methodologies. In general, it has been found that the adsorption of these clusters to the surface of $CeO_2(111)$ results in the transfer of charge from the oxide surface to the metal, reducing Ce^{4+} ions on the surface to Ce^{3+}.[329,330,332,333,337,338] Farmer *et al*.[328] examined the adsorption of Ag on $CeO_2(111)$ using micro calorimetry and found that Ag binds more strongly on reduced $CeO_2(111)$ because of the oxygen vacancies. Bruix *et al*.[337] used DFT + U with both LDA and GGA functionals to examine the adsorption of Pt onto a stoichiometric $CeO_2(111)$ surface, and found the oxidation of Pt to Pt^+ and the reduction of the surface Ce^{4+} to Ce^{3+} to be the most energetically favourable structure. This DFT study also predicted that the most favourable geometry corresponded to the adsorption of Pt on top of a site bridging two nearest-neighbour surface oxygens (O_s).

The bridge-like adsorption structure was also found in the Zhang *et al*.[333] DFT + U investigation on the adsorption of Au onto stoichiometric and defective $CeO_2(111)$. Theoretical studies[332,333], along with resonant photoemission spectroscopy experiments[334,339,340], found that the adsorption of Au on stoichiometric $CeO_2(111)$ surface leads to the spontaneous oxidation of Au^0 to Au^+. However, scanning tunnelling microscopy (STM) and x-ray photoelectron spectroscopy (XPS) analysis of single crystals reported by Baron *et al*.[330] and the DFT study by Castellani *et al*.[331] found that a reduced surface is required to produce the redox reaction where Ce^{4+} is reduced to Ce^{3+} and Au^0 is oxidized to Au^+. The origin of this difference is the closeness in energy between the two electronic states which correspond to a neutral or charged Au. This closeness in energy was identified by Branda *et al*.[335] who investigated the electronic structure of atomic Au adsorbed onto a stoichiometric $CeO_2(111)$ surface using DFT + U with LDA, GGA and the HSE06 hybrid functional, and found the results were highly dependent on the exchange correlation functional used.

Investigations of the interaction of water with the surface of CeO_2(111) have revealed that water adsorbs either molecularly[341–344], where the H_2O adsorbs on the surface of cerium and forms two hydrogen bonds with neighbouring surface oxygen (O_s), or dissociatively[345–347], where the H_2O donates a proton to the neighbouring O_s forming a hydroxide, and the remaining OH^- forms a bond with a surface Ce.[343,347] However, the literature is in disagreement about which of these adsorption methods is the most thermodynamically stable, as discussed below.[348–350]

Experimentally, water on CeO_2(111) surfaces has been well studied with a variety of methods[345,348,351] including X-ray Photoelectron Spectroscopy (XPS)[348,349,352,353], Temperature-Programmed Desorption (TPD)[348,349,352–354] and Atomic Force Microscopy (AFM)[345,346]. Henderson *et al*.[352] used XPS and TPD to investigate the surface chemistry of water on the CeO_2(111) surface. The investigation found three possible molecular configurations for water adsorption to the surface. The most likely adsorption configuration was in a C_{2V} geometry with the hydrogen atoms of water pointing directly away from the surface. For the alternative configurations, the water molecule was adsorbed with either a single hydrogen bond from the water oxygen to the surface, or with two hydogen bonds from the water hydrogens to surface oxygens. Several studies[348,349] including the non-contact AFM investigations by Gritschneder *et al*.[345] and Torbrügge *et al*.[346] noted the importance of oxygen vacancies and found that water preferentially dissociates onto the surface and forms hydroxide if oxygen vacancies are present.

There have been multiple theoretical studies of the interaction and adsorption of H_2O onto the CeO_2(111) surface, typically including 1 monolayer (ML) or less of water.[341,342,359,360,343,344,347,350,355–358] Fernández-Torre *et al*.[350] and Yang *et al*.[341] investigated H_2O adsorption on the CeO_2(111) surface using DFT and DFT+U approaches. All methods and surface models supported the findings that water adsorbs on to the Ce^{4+} atom and can be found in two states: either as a molecule forming one hydrogen bonds with a O_s or as a hydroxyl pair where a hydroxide forms on a surface cerium and a proton is donated to an adjacent O_s. Both structures are stabilised by a hydrogen bond and differ in energy by 10 - 30 meV depending on the functional used and the unit cell considered. The results of these studies rule out complete water dissociation as the thermodynamically stable phase.

Watkins *et al*.[347] used DFT and DFT+U, both with the GGA functional PW91, to investigate the process of dissociating water on the stoichiometric and reduced CeO_2(111) surface. The results led to the conclusion that water will dissociate upon adsorbing onto either form of the surface, in contrast to previous studies.[342,343,361] Molinari *et al*.[344] used DFT+U with the PBE functional

to examine molecular and dissociative adsorption of water and the formation of oxygen vacancies. In line with the Watkins *et al*.[347] study they concluded that dissociative adsorption was favoured over molecular adsorption but that the stability of the dissociative state decreases with an increasing amount of hydroxyl groups. However, the results from the study also indicated that molecular adsorption becomes more favourable as the water coverage increases.

As well as investigations of ceria it is important to understand the behaviour of the adsorption of the strontium ion which will be examined in this chapter. The adsorption of the Sr ion onto solid surfaces, such as clay, iron oxide and other sediments, has been studied.[45,362–364] In general, Sr^{2+} coordinates weakly as an outer-sphere complex at the surface-water interface[154,362,363,365], but this behaviour depends on ionic strength and the presence of other minerals in the system.[366] The adsorption of the dication onto a surface has been found to increase with increasing pH.[45,362,363,366–368] Sahai *et al*.[363] examined the sorption of Sr^{2+} on kaolinite clay, amorphous silica and the goethite mineral surface using X-Ray Absorption Spectroscopy (XAS). They examined the rate of absorption as a function of pH, strontium concentration, and the presence or absence of atmospheric CO_2. Sorption of Sr^{2+} was found to increase with pH, and an increase in strontium uptake on goethite was found in the presence of atmospheric CO_2.

Parkman *et al*.[365] investigated Sr^{2+} sorption in aqueous solution on the calcite and kaolinite mineral surfaces using XANES and EXAFS. For calcite, Sr^{2+} uptake increased linearly with Sr^{2+} concentration, but the highest update of Sr^{2+} by kaolinite was found at the lowest initial Sr^{2+} concentration and at higher concentrations the EXAFS data showed only weak binding of Sr^{2+} to kaolinite surfaces. The difference in adsorption behaviour was due to the ion exchange of Ca^{2+} with Sr^{2+} in calcite, which was corroborated by the XAS study by Pingitore *et al*.[49] who found that Sr^{2+} is incorporated into calcite by substituting with Ca^{2+}.

Wallace *et al*.[45] examined the sorption of Sr^{2+} to sediment samples taken from the Sellafield site, in sediment water systems made to emulate the ground water around Sellafield. The authors found that ion adsorption was observed between pH 4 and 6 with maximum sorption occurring at pH 6 to 8, and Sr^{2+} was found to adsorb as an outer sphere complex. The long-term sorption of Sr^{2+} was also examined and it was found that over periods of 365 days Sr^{2+} remained in weakly bound surface complexes, which if the groundwater ionic strength increased would lead to a substantial remobilisation of Sr^{2+}.

In the thesis of Eszter Makkos[368], computational investigations of Sr^{2+} on the surface of brucite using DFT and a COSMO solvation model found that interaction between the surface and the ion was not favoured at a pH below 11. However, Ashworth *et al*.[369] investigated the sorption-desorption interactions of ^{90}Sr with brucite ($Mg(OH)_2$) and the impact of adding natural organic matter. The experiments were conducted in pond-like conditions with a pH between 10.5 and 12.5 and ionic strength of either 2.5 x 10^{-3}, 0.01 or 0.1 M. It was found there is no impact on the sorption of Sr^{2+} to brucite with a change in either ionic strength or pH with no sorption found in either environment.[369]

7.2 Computational Details

All calculations in this chapter were DFT optimisations performed using the QUICKSTEP module of CP2K version 3.0 on simulation cells with periodic boundary conditions.[94,115] The GAPW[96] method was implemented using the PBE functional with Grimme's DFT-D3 dispersion correction applied.[76,166] The calculations used polarised double-ζ Gaussian basis sets (DZVP-MOLOPT-SR-GTH) and a planewave cutoff of 500 Ry.[167] The DFT+U approach was taken for all calculations and applied to the Ce^{4+} f orbitals, using a U value of 7.00 eV and a J value of 0.7 eV, consistent with previous DFT+U studies of CeO_2(111).[360,370–373]

7.3 Results

7.3.1 CeO_2(111) Surface Model

DFT was employed to optimise a surface model of CeO_2(111). The initial aim of the investigation was to combine the 64 water molecule model used in the aqueous AIMD investigations of previous chapters with the CeO_2(111) surface. To do this effectively, the surface model needed to have parameters approximately the same as the size of the periodic box used for the water model, corresponding to ~11.99 Å in length and width. To make a surface of this size a 4x3x2 supercell of CeO_2(111), was made using Gaussview[120], as is shown in **Figure 7.1**, due to the periodic nature of the calculations and the focus on the surface interactions a 15 Å vacuum, used in other similar studies[342,347,371,374,375], was applied in the *c* direction which is perpendicular to the surface, to prevent interactions between the surface atoms and the base of the surface in the box above and the starting cell parameters were set to $a = 11.65$ Å$, b = 13.5$ Å$, c = 20.80$ Å. The oxygens at the base of the surface model were fixed in place to allow the stability afforded by the bulk structure of the solid to be modelled without the computational cost of modelling extra layers. As the investigation is primarily interested in surface interactions, the bulk model is of lesser importance. The structure depicted in **Figure 7.1** underwent a cell optimisation to optimise the periodic cell parameters

and geometry simultaneously. The optimised cell parameters were $a = 11.19$ Å$, b = 12.90$ Å$, c = 21.24$ Å.

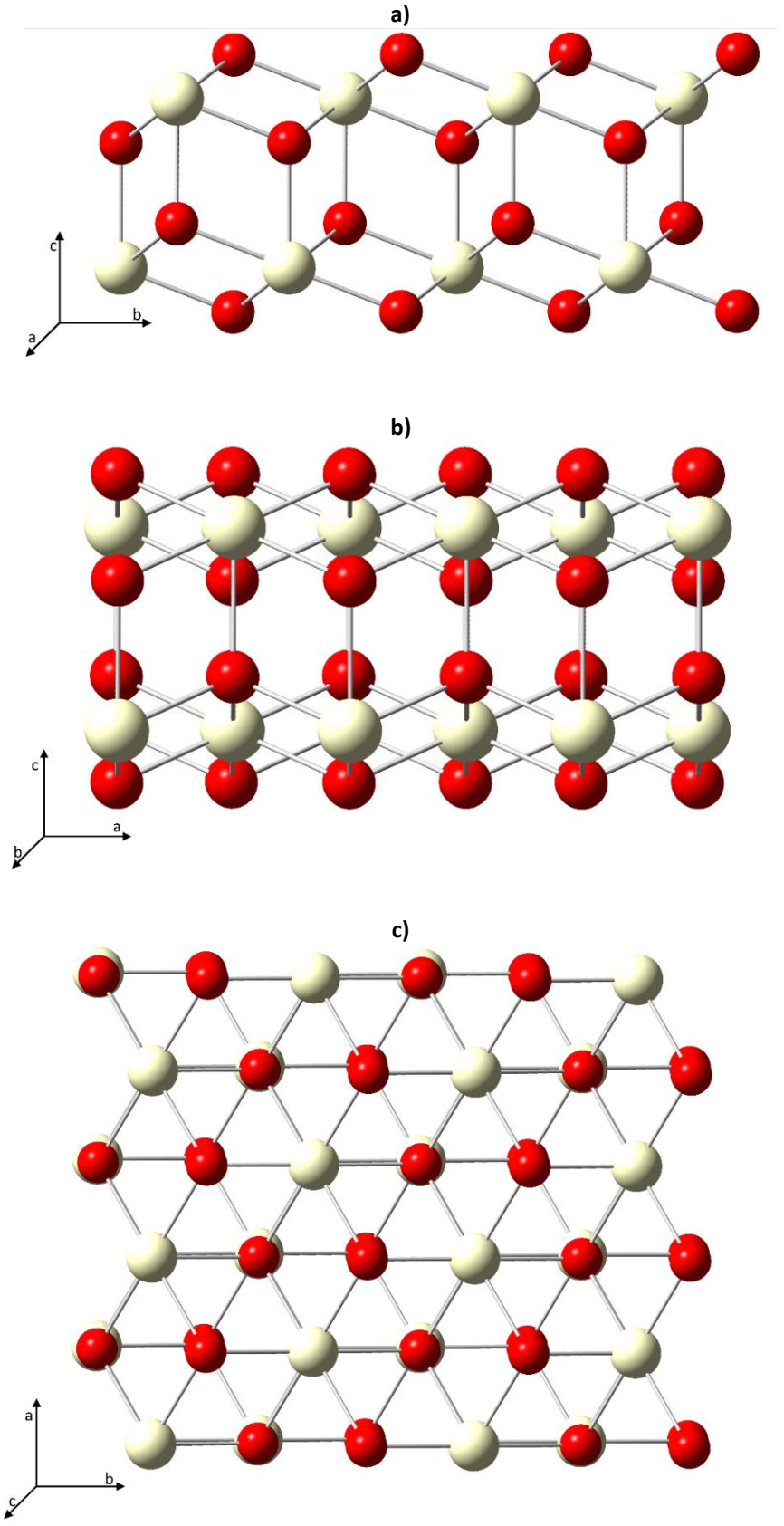

Figure 7.1: CeO_2(111) 4x3x2 surface. **a)** Front view, **b)** side view, **c)** top view.

7.3.2 CeO_2(111) Surface Interaction with Water

Initially, 3 previously optimised sets of 32 water molecules were added on top of the CeO_2(111) surface to generate 3 unique starting structures as the basis for the investigation of the interaction of water coverage on a surface, an example of which is shown in **Figure 7.2**. Previous theoretical investigations focused only on the adsorption of one water molecule onto the surface of CeO_2(111) with a maximum of 1 monolayer (ML) of water, as detailed in **Section 7.1**. In these calculations, 32 water molecules were used to provide a more realistic model of surface water coverage. To accommodate the addition of 32 water molecules and to maintain a 15 Å vacuum the cell parameters were increased in the c direction and were set to $a = 11.19$ Å, $b = 12.90$ Å, $c = 36.24$ Å. All calculations from this point are geometry optimisations with the cell parameters held constant, as this enables an accurate comparison of the total energies.

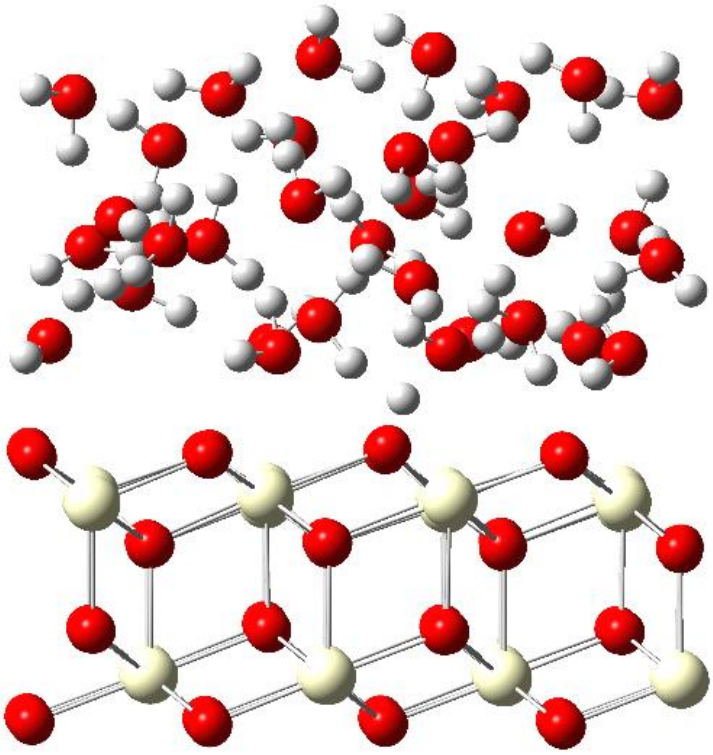

Figure 7.2: CeO_2(111) 4x3x2 surface model with 32 water molecules.

The relative energies of the first three optimised water surface structures are listed in **Table 7.1**. The two lowest energy structures optimised with a water molecule dissociatively adsorbed onto the surface. This water dissociation behaviour is similar to that seen in the computational studies of Molinari *et al*.[344] and Watkins *et al*.[347] although both these investigations focused on a single water molecule rather than full surface coverage. Structure

1 optimised with a H^+ protonating a O_s, and an OH^- coordinating the adjacent surface Ce^{4+}. Structure 2 had a H^+ protonating the surface but the OH^- did not coordinate a surface Ce^{4+}. Structure 3 had an unprotonated surface and the water molecules above the surface had become very spread apart, this structure was not used in further investigations. These preliminary results suggest that waters can spontaneously dissociate and form low energy structures, although 3 data points is not conclusive.

Table 7.1: The relative energies (E_{rel}) of the starting structures of CeO_2(111) 4x3x2 surface with 32 water molecules

Structure	E_{rel} (eV)
1	0.000
2	0.423
3	2.041

The next stage in the investigation was to examine the possibility of protonating the CeO_2(111) surface multiple times through manually dissociating multiple water molecules. The aim of this was to identify which surface environment was more energetically favourable: a surface with no protonation, a single protonation or multiple protonations. The two lowest energy structures listed in **Table 7.1** were taken and multiple water molecules were dissociated across the CeO_2(111) surface by separating a water molecule and coordinating the H^+ ion to a O_s and the OH^- ion to an adjacent surface Ce. Up to a maximum of 4 waters were dissociated on the CeO_2(111) surface before the structures were re-optimised. From these optimised geometries low energy structures were then identified and manipulated by dissociating different water molecules or recombining waters on the surface before being re-optimised to try to identify the most stable environment. In total 20 different structures were optimised and **Figure 7.3** summarises the relative energies of all the structures by the number of protons on the CeO_2(111) surface after geometry optimisation (n_{H^+}).

There is a general trend of the total energy increasing as the number of dissociated waters increases from 1 to 4, in line with the Molinari *et al*.[344] DFT study which suggested that the stability of the ground state decreases with increasing hydroxyl groups. Structures with a range of relative energies for each number of dissociated waters were found, likely due differences in the hydrogen bonding of the bulk water on the surface. However, due to the preliminary nature of this investigation only the lowest energy structures were compared. Overall, surfaces where E_{rel} < 0.5 eV are either unprotonated or protonated by a single proton. Multiple attempts were made to optimise structures with 0, 2, 3, 4 waters were adsorbed dissociatively;

however, as is evident in **Figure 7.3**, the majority of these structures optimised to structures with just a single proton on the CeO_2(111) surface.

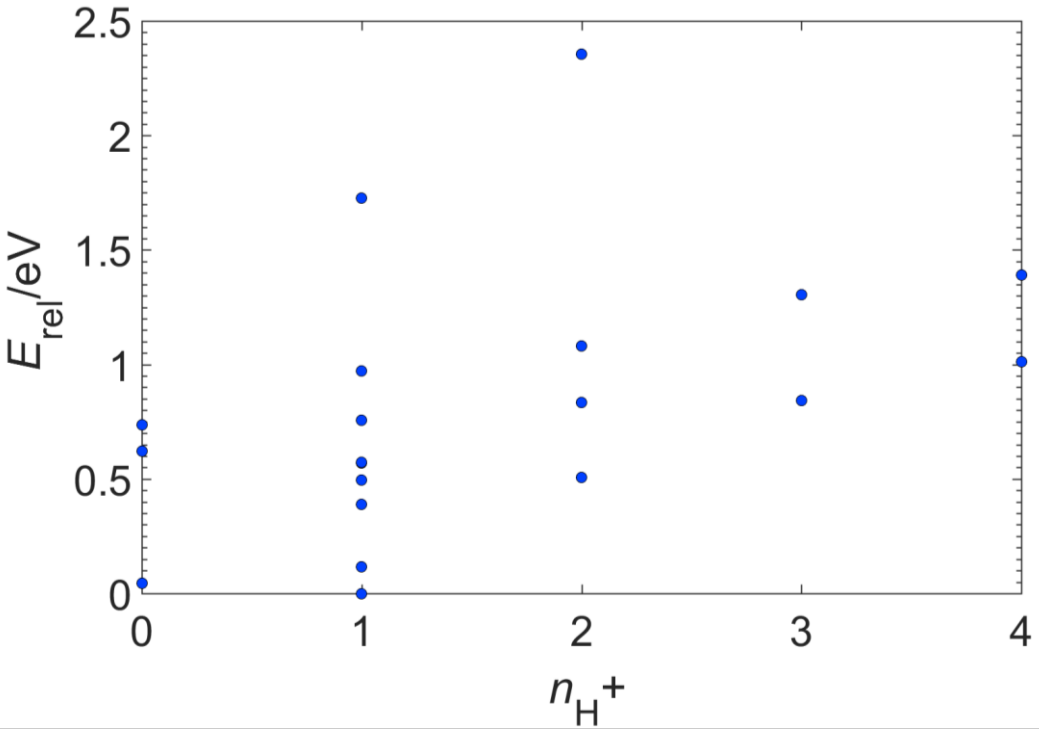

Figure 7.3: The relative energies (E_{rel}) of the optimised CeO_2(111) 4x3x2 surface model with 32 water molecules against the number of protons protonating the surface (n_{H^+}).

7.3.3 CeO_2(111) Surface interactions with Solvated Sr^{2+}

The interaction of Sr^{2+} with the CeO_2(111) surface was studied using DFT. A single Sr^{2+} ion was added to the water model above the surface in the 3 lowest energy optimised structures from **Section 7.3.2**. For each of the three starting structures the distance of the ion from the surface was varied to model either inner shell coordination, outer shell coordination, or not coordinated to the surface. These three structures were optimised to form the starting geometries for the investigation. Each optimised final structure was examined to obtain the Sr^{2+} coordination number (CN), Sr^{2+} distance from the surface (r_{Sr}), and surface protonation.

As in **Section 7.3.2**, the optimised structures were then altered to mimic the features of lower energy structures and more fully explore the different coordination environments of the ion and surface to find lower energy structures. Optimised low energy geometries were altered in one of three ways; by either changing the Sr^{2+} CN, the Sr^{2+} distance from the surface, or altering the protonation of the CeO_2(111) surface. In total, 40 separate geometries were optimised to try to identify common features in low energy configurations. The data produced from these optimisations can be found in **Appendix E Table E1**.

For the purposes of analysis, the distance of Sr^{2+} from the surface was used to classify the surface coordination of the Sr^{2+} as inner shell, outer shell or uncoordinated. As was established in the **Chapter 3** AIMD studies of Sr^{2+} in an aqueous environment, the chosen cutoff for the first solvation shell is 3.2 Å. Therefore, any coordination of Sr^{2+} to the surface at distances of $r_{Sr} < 3.2$ Å is classified here as inner shell. Outer shell coordination of Sr^{2+} to the surface, where a water in the first solvation shell is bonded to the surface via hydrogen bonds, was defined as $3.2 < r_{Sr} < 5$ Å based on the edge of the second solvation shell as defined in the Sr—O RDF reported in **Section 4.3.2**. Structures with no Sr^{2+} surface coordination where the ion was considered to be in bulk water were defined at a distance of $r_{Sr} > 5$ Å. All optimised structures were visually inspected to identify any direct coordination by the ion to surface species.

Previous investigations of Sr^{2+} adsorption onto surfaces have used different cutoffs to categorise the bonding of the ion with the surface. Kerridge and Kaltsoyannis[376], in their periodic electrostatic embedded cluster model (PEECM) of Sr^{2+} adsorption onto brucite, identified the inner shell as a distance of < 4 Å, outer shell complexes at a distance of > 4 Å and < 6 Å, and bulk structures at distances of > 6 Å.[376] The thesis of E Makkos[368] built on this study, examining the adsorption of Sr^{2+} onto brucite using similar parameters, considering only inner and outer shell complexes of Sr to the surface with all Sr—surface distances < 8 Å. However, cutoff values used in this chapter are consistent with the results from the AIMD simulations in **Chapter 3** and **Chapter 4** for Sr^{2+} coordination.

Figure 7.4 shows the relative energy (E_{rel}) of each geometry, relative to the lowest energy structure, plotted against the distance of the Sr^{2+} from the surface. Using the cutoffs for Sr—surface coordination, with inner shell coordination when $r_{Sr} < 3.2$ Å, outer shell coordination when $3.2 < r_{Sr} < 4.5$ Å, and bulk coordination when $r_{Sr} > 5$ Å, the majority of structures optimised to outer shell coordinated structures, with 15 inner shell coordinated structures, 23 outer shell coordinated structures and 2 bulk structures. The lowest energy structure has a Sr—surface distance of 4.45 Å, and is coordinated to the surface via two hydrogen bonds between first shell waters and O_s with bond lengths of 1.65 Å and 1.86 Å. When examining other low energy structures where $E_{rel} < 0.5$ eV they are either inner or outer shell coordination to the surface, indicating that those structures which have some surface coordination are more stable than those uncoordinated to the surface.

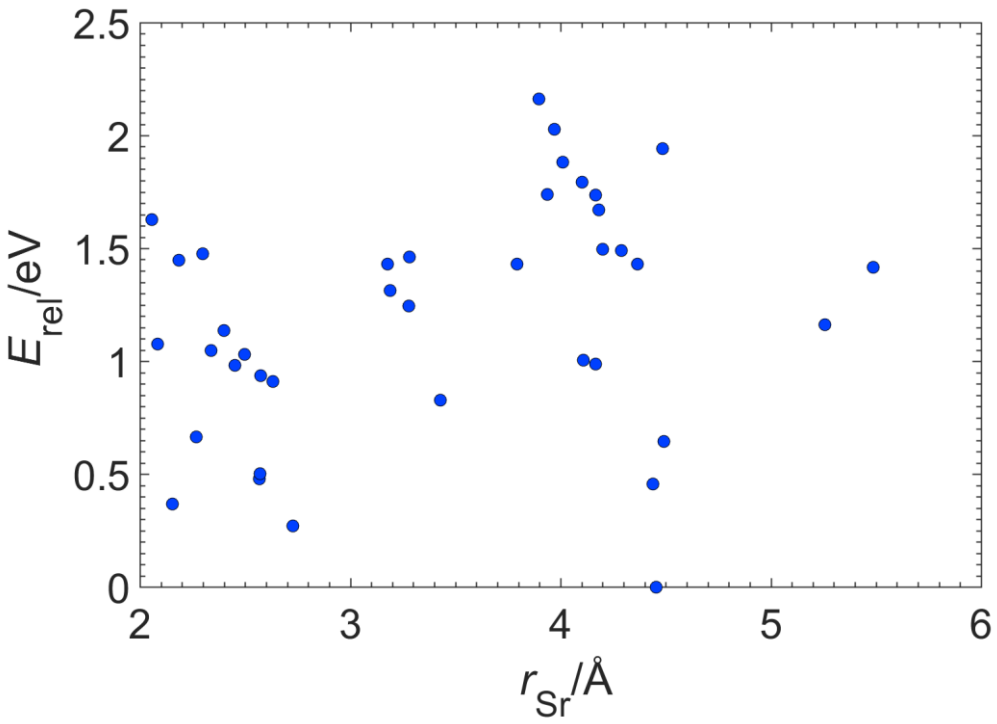

Figure 7.4: The relative energies (E_{rel}) of the optimised CeO_2(111) 4x3x2 surface model with a Sr^{2+} ion and 32 water molecules against Sr^{2+} distance from the surface (r_{Sr}).

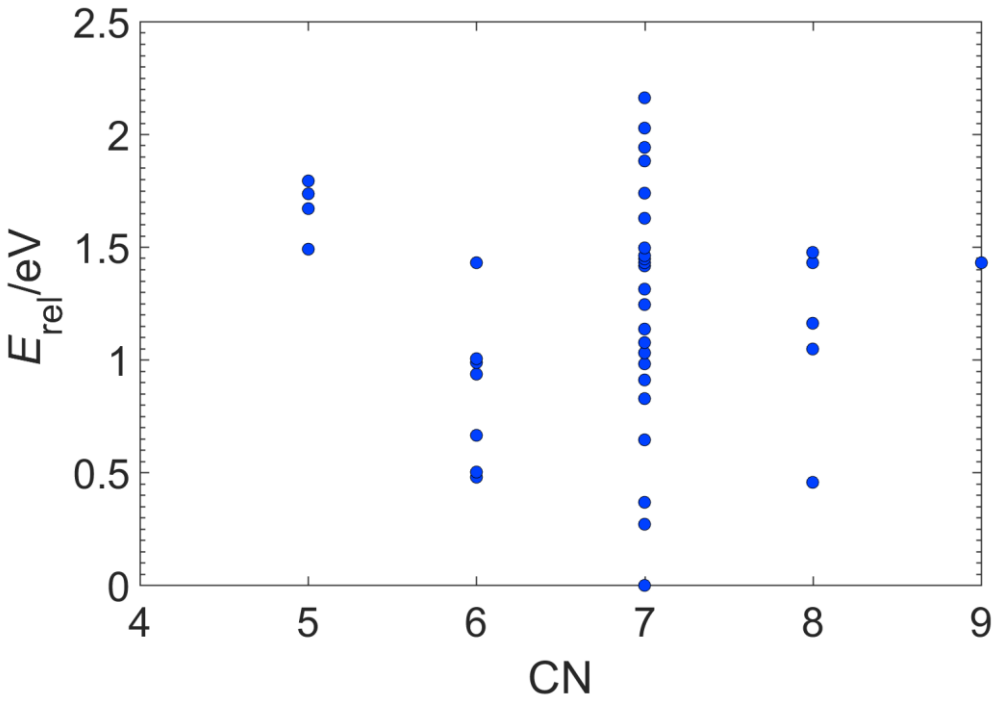

Figure 7.5: The relative energies (E_{rel}) of the optimised CeO_2(111) 4x3x2 surface model with a Sr^{2+} ion and 32 water molecules, against total Sr^{2+} CN.

The E_{rel} of each optimised geometry against the total Sr^{2+} CN is shown in **Figure 7.5**. The majority of structures optimised with a Sr^{2+} CN of 7 and the lowest energy structure is 7 coordinated. Multiple attempts were made to optimise low energy structures with CN other than 7, however the majority optimised to either a 7 CN structure, or a structure with a higher energy. Both 5 CN and 9 CN structures have higher energies (E_{rel} > ~1.5 eV) suggesting these CN are the least energetically favourable coordination environments. Optimised structures which have a E_{rel} < 0.5 eV are predominantly 7 coordinated but there are also 6 and 8 coordinated structures suggesting a stability for those coordination numbers.

In an attempt to identify structural features common to the lowest energy configurations, **Figure 7.4** was replicated but with each of the data points classified in different ways to clarify any trends between low energy structures and the final optimised geometry. The data were classified according to Sr^{2+} CN (**Figure 7.6**) and degree of surface protonation (**Figure 7.7**). When examining low energy structures where E_{rel} < 0.5 eV in **Figure 7.6**, they are all either inner or outer shell surface complex and have a predominantly 6 or 7 coordinated Sr^{2+} with one 8 coordinated structure. Overall the lowest energy structure is 7 coordinated with outer shell surface coordination.

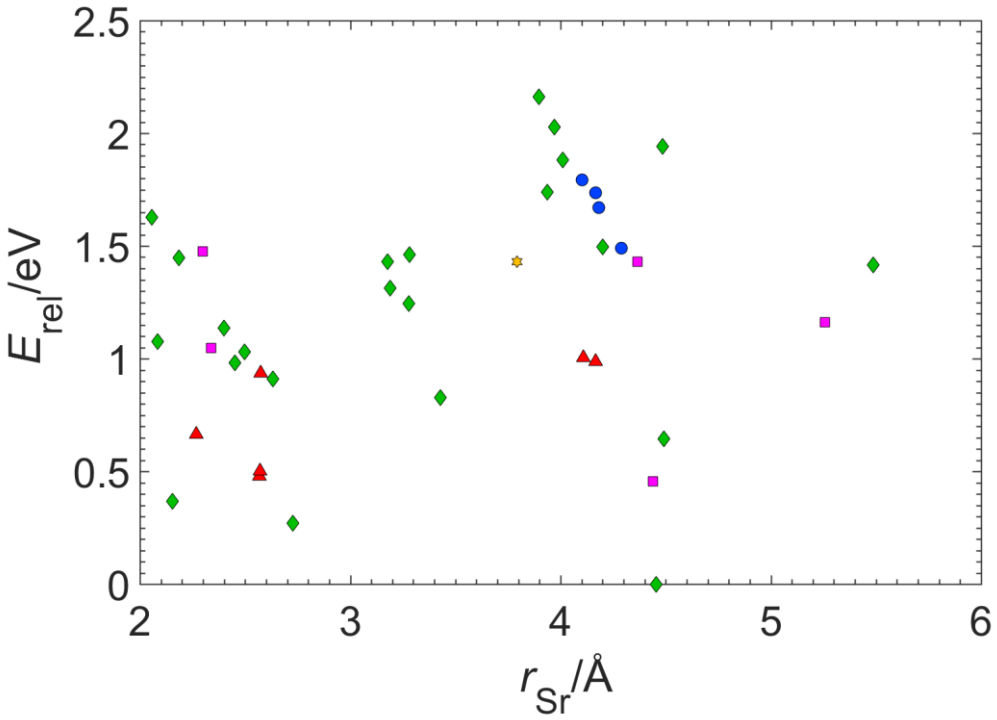

Figure 7.6: The relative energies (E_{rel}) of the optimised CeO_2(111) 4x3x2 surface model with a Sr^{2+} ion, and 32 water molecules, against Sr^{2+} distance from the surface (r_{Sr}). Each data point is coloured by Sr^{2+} CN. Blue circle = 5, red triangle = 6, green diamond = 7, magenta square = 8, yellow star = 9.

Based on the correlation between lower energy and lack of surface protonation in **Section 7.3.2**, the E_{rel} of the optimised structures were examined to identify any correlation between lower energy and surface protonation. These results are summarised in **Figure 7.7**, generally, the E_{rel} increases with increasing surface protonation. All structures with E_{rel} < 0.5 eV have an unprotonated CeO_2(111) surface, indicating that a protonated surface is not energetically favourable.

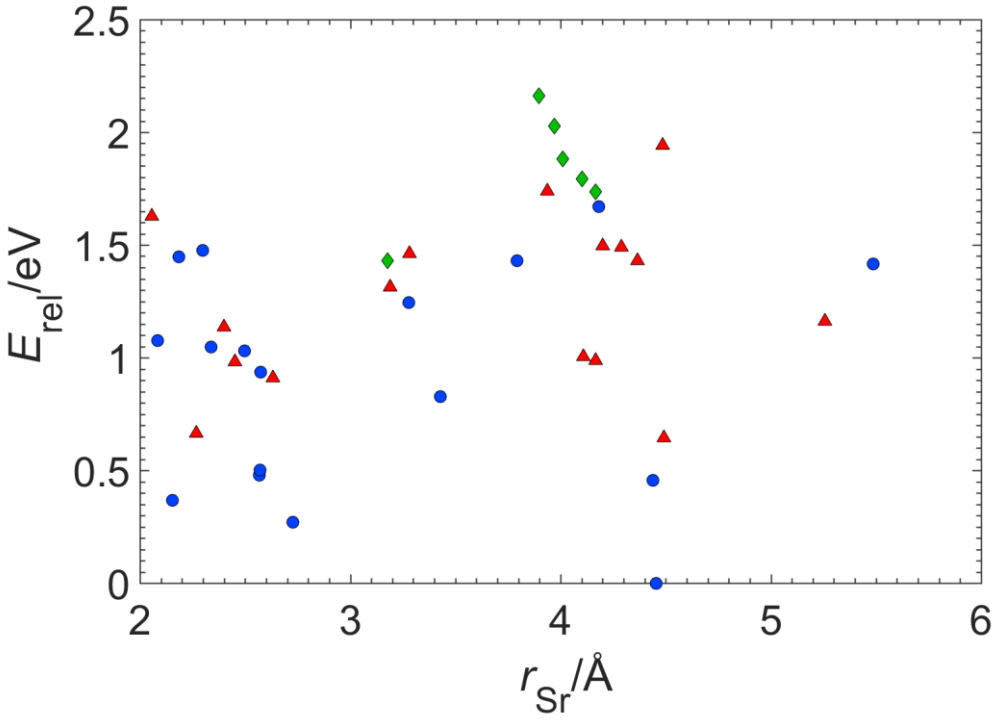

Figure 7.7: The relative energies (E_{rel}) of the optimised CeO_2(111) 4x3x2 surface model with a Sr^{2+} ion and 32 water molecules, against Sr^{2+} distance from the surface (r_{Sr}). Each data point is coloured by surface protonation. Blue circle = 0 H^+, red triangle = 1 H^+, green diamond = 2 H^+.

Overall the lowest energy structure has a Sr^{2+} ion outer shell coordinated to the CeO_2(111), a Sr^{2+} CN of 7 and a CeO_2(111) surface which is unprotonated. Examining the common structural features in structures where E_{rel} < 0.5 eV, the Sr^{2+} CN is 6, 7 or 8, they have an unprotonated CeO_2(111) surface, and the Sr^{2+} ion is coordinated to the surface via either inner or outer shell coordination.

7.3.4 CeO_2(111) Surface with Sr^{2+} and 64 Water Molecules

The previous chapters presented in this thesis used 64 water molecules to ensure the solvation model of the ions was adequate. The 32 water molecule model used in **Sections 7.2** and **7.3** provides a good starting point to model solvation. However, there were concerns that 32 water molecules were not sufficient to model the second shell behaviour of Sr^{2+} nor to provide

enough bulk water above the surface, which may cause an issue if it was more energetically favourable for the Sr^{2+} ion to remain uncoordinated.

To test if an increase in water molecules impacted the relative energies, an additional 16 water molecules were added above the existing 32 water molecules in the 4 lowest energy structures from **Section 7.3.2**, for a total of 48 water molecules. In the 4 lowest energy structures the coordination of the Sr^{2+} ion to the CeO_2(111) surface varied, one structure was outer shell coordinated, two inner shell coordinated and one with no surface coordination. Once the additional 16 water molecules were added, the 4 structures were then re-optimised and the relative energies for the 32 and 48 water molecule models compared.

The structural features of each optimised geometry with both 32 and 48 water molecule models are summarised in **Table 7.2**, each structure is numbered 1 to 4 (S1 to S4). There is no significant change in the surface—Sr distance (r_{Sr}) with the addition of more waters, with a slight increase in the r_{Sr} distance of 0.02 Å for S1 and 0.01 Å for S3 and S4. There is also a change in the Sr^{2+} CN in two geometries, in one case increasing by 1 for S4, and for S2 decreasing by 1. However, the classification of the surface coordination has remained unchanged in all cases, combined with the lack of a significant change in r_{Sr} this suggests that an increased number of waters is unnecessary for simulating bulk water and that the lower number of 32 waters does not prevent the Sr^{2+} from migrating away from the surface.

Table 7.2: The surface-Sr distance (r_{Sr}), Sr^{2+} coordination number (CN), Sr^{2+} coordination type (CT) and relative energies (E_{rel}) for low energy structures 1 to 4 (S1 to 4) optimised with either 32 water molecules (32 H_2O) or 48 water molecules (48 H_2O).

	r_{Sr} (Å)		CN		CT		E_{rel}/eV	
	32 H_2O	48 H_2O	32 H_2O	48 H_2O	32 H_2O	48 H_2O	32 H_2O	48 H_2O
S1	2.73	2.75	7	7	Inner shell	Inner shell	0.000	0.000
S2	4.44	4.43	8	7	Outer shell	Outer shell	0.186	0.217
S3	2.57	2.58	6	6	Inner shell	Inner shell	0.209	1.938
S4	6.86	6.87	6	7	None	None	1.161	1.965

The trend in relative energies remains the same, S1 is the lowest energy structure in both cases, and SN4 is the highest in energy. There is an increase in the relative energies with the increase in water molecules for S2, S3 and S4, however this does not appear to be attributed to the Sr^{2+} surface relationship. Rather the additional waters may have impacted the structure and bonding of the water in such a way that the total energies have been impacted for instance increased hydrogen bonding.

While the initial aim of these investigations was to have a total of 64 water molecules, the lack of evidence that the increased number of water molecules impacted the Sr—surface relationship suggests that 32 water molecules is sufficient to model bulk water in similar investigations. As there is also an increased computational cost associated with more explicit water molecules while maintaining a 15 Å vacuum between layers, using only 32 water molecules allows for cheaper calculations and appears to be sufficient for modelling a solvation environment for the Sr^{2+} ion.

7.3.5 Hydroxide Interaction with Solvated Sr^{2+} on the CeO_2(111) Surface

The next stage of the investigation was to examine the impact of introducing two hydroxide ions, and thus increased pH, on the adsorption of Sr^{2+} to the CeO_2(111) surface using DFT. As the Magnox storage ponds are kept at a high pH the aim of this investigation was to evaluate if an alkaline environment had any effect on ion adsorption. Protons were removed from two waters in five separate from **Section 7.3.4** to generate two OH^- ions. Each geometry was then optimised. The placement of the hydroxides, in relation to the distance from the ion, was varied in each of the structures.

The low energy optimised structures were then manipulated as in **Section 7.3.2** and **7.3.3**, altering either the Sr^{2+} CN, the Sr^{2+} hydroxide coordination or Sr—surface distance to explore if changes structural characteristics resulted in a lower total energy. A total of 54 different geometries of various configurations were optimised. The data produced from these optimisations can be found in **Appendix E Table E2**. The final structures were analysed in a similar way to the geometries in **Section 7.3.4**.

Figure 7.8 shows the relative energies (E_{rel}) of the optimised structures in relation to the distance of the Sr^{2+} ion from the surface. The lowest energy structure is 3.63 Å away from the surface and so is considered to be an outer shell Sr^{2+} complex. On examining the lowest energy structure, it has two hydrogen bonds to the surface oxygens, one with a length of 1.83 Å from the hydrogen of a first shell OH^- to O_s, and one with a length of 1.71 Å from a water hydrogen to a O_s.

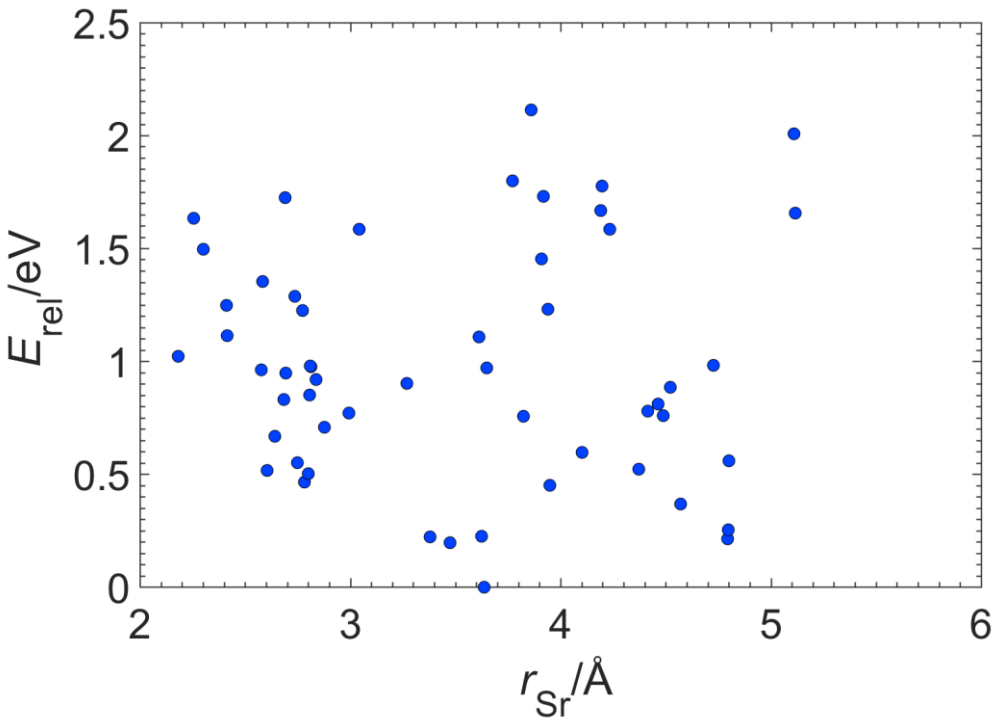

Figure 7.8: The relative energies (E_{rel}) of the optimised CeO_2(111) 4x3x2 surface model with a Sr^{2+}, 32 water molecules, and 2 OH^- against Sr^{2+} distance from the surface (r_{Sr}).

Examining structures where E_{rel} < 0.5 eV, these optimised geometries have an Sr^{2+} ion which is either outer shell coordinated or is uncoordinated to the surface, in contrast to the calculations which did not have hydroxide species. From these results it can be inferred that the presence of hydroxide ions makes it energetically less favourable for Sr^{2+} to adsorb fully onto the CeO_2(111) surface. However, this graph does not identify anything about the presence of the hydroxides in the optimised structures.

To investigate any structural features which were common to the lowest energy geometries **Figure 7.8** was replicated but with each of the data points colour coded according to number of Sr—OH bonds (**Figure 7.9**), degree of surface protonation (**Figure 7.10**), and Sr^{2+} CN (**Figure 7.11**).

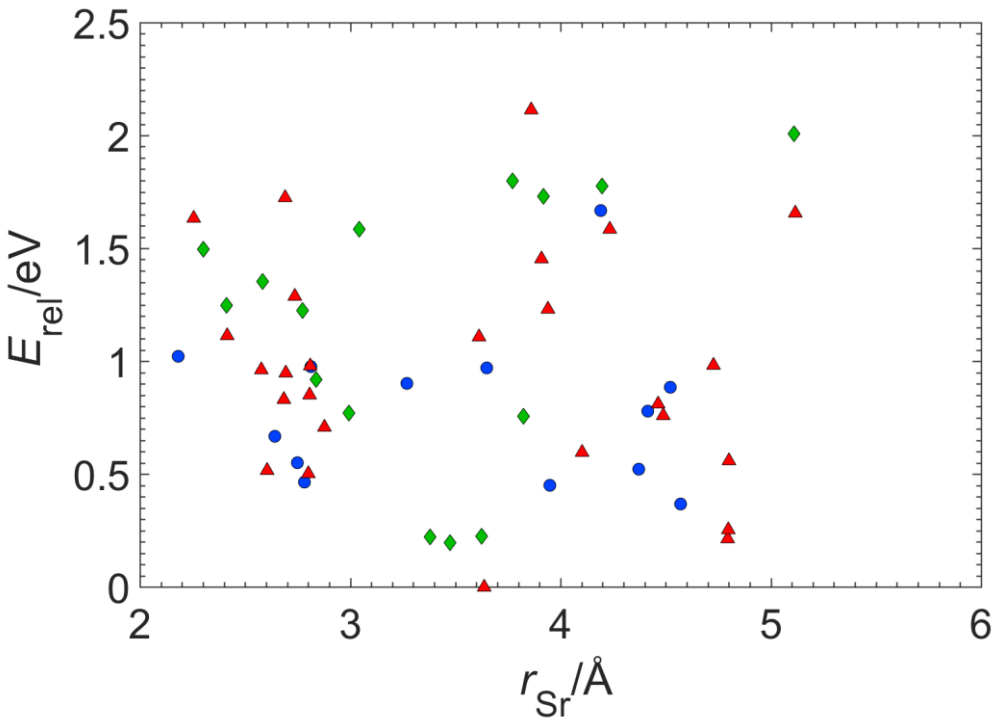

Figure 7.9: The relative energies (E_{rel}) of the optimised CeO_2(111) 4x3x2 surface model with a Sr^{2+}, 32 water molecules, and 2 OH^- against Sr^{2+} distance from the surface (r_{Sr}). Each data point is coloured according to the number of explicit Sr—OH bonds, blue circle = 0 bond, red triangle = 1, green diamond = 2.

As demonstrated by **Figure 7.9** there does not appear to be a clear trend between the number of Sr—OH bonds and the lowest energy structures. The lowest energy configuration has 1 Sr—OH bond, but 3 geometries with a E_{rel} < 0.25 eV have 2 Sr—OH bonds, and a further 2 geometries with E_{rel} < 0.25 eV have a single Sr—OH bond. Structures with no Sr—OH bonds are also found at E_{rel} < 0.5 eV, there does not appear to be a strong link between total energy and hydroxide ion bonding. In the context of the previous AIMD investigations of strontium monohydroxide in **Chapter 6** and strontium dihydroxide in **Chapter 4** where there was a low amount of hydroxide coordination to the ion it is perhaps unsurprising that there is no energetically stabilising effect from the hydroxide ions.

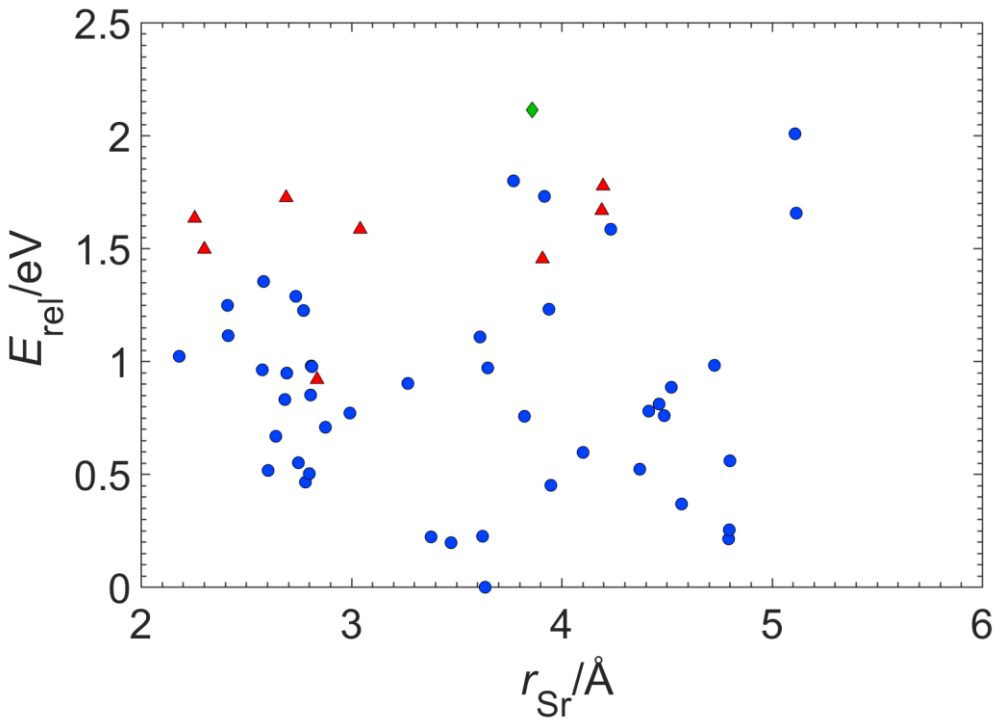

Figure 7.10: The relative energies (E_{rel}) of the optimised CeO_2(111) 4x3x2 surface model with a Sr^{2+}, 32 water molecules, and 2 OH^- against Sr^{2+} distance from the surface (r_{Sr}). Each data point is coloured according to the number of surface protonation, blue circle = 0 H^+, red triangle = 1 H^+, green diamond = 2 H^+.

In contrast to **Figure 7.7**, the analogous graph for the surface strontium structures without hydroxide, **Figure 7.10** shows that the overwhelming majority of geometries have an unprotonated surface; of the 54 structures, there are 8 geometries with 1 H^+ on the surface, and 1 geometry with 2 H^+ on the surface. All of the geometries where E_{rel} < 0.5 eV have an unprotonated surface, and the structure with the highest E_{rel} has two protons on the surface. These results suggest that the presence of hydroxide ions decreases the likelihood of water dissociating and protonating the CeO_2(111) surface. In a highly alkaline environment, such as that modelled here, protonation would be unexpected. The lack of surface protonation evidenced in these results suggests that the model is correctly mimicking a high pH.

Figure 7.11 identifies each optimised geometry by the total Sr—O CN coordination number. As in the aqueous surface investigation the lowest energy structure has a Sr^{2+} CN of 7 and has outer shell coordination to the surface. For structures where E_{rel} < 0.5 eV the Sr^{2+} CN is 6, 7 or 8 and are predominantly outer shell coordinated or uncoordinated to the surface.

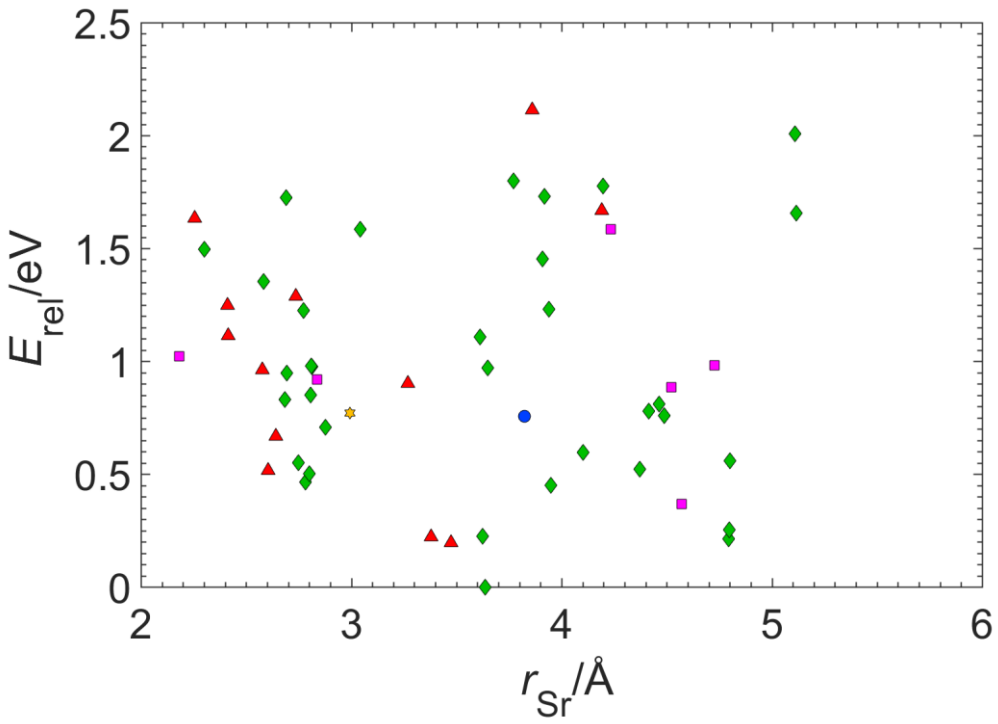

Figure 7.11: The relative energies (E_{rel}) of the optimised CeO_2(111) 4x3x2 surface model with 32 water molecules, a Sr^{2+}, and 2 OH^- against Sr^{2+} distance from the surface (r_{Sr}). Each data point is coloured according to the Sr^{2+} CN, yellow star = 4, blue circle = 5, red triangle = 6, green diamond = 7, magenta square = 8.

The total CNs which were identified in these optimisations are shown in **Figure 7.12,** which plots E_{rel} against the Sr^{2+} CN. Similar to **Figure 7.5**, the majority of structures optimised to a Sr^{2+} with a CN of 7 and a significant number of 6 and 8 coordinated structures were also optimised. The higher CN of 9 is not found in the hydroxide structures, this could be an indication of the presence of 2 OH^- affecting the overall CN, in the same way that the AIMD simulations of Sr^{2+} in a hydroxide environment the higher CNs of 10 were not identified and the average Sr^{2+} CN reduced.

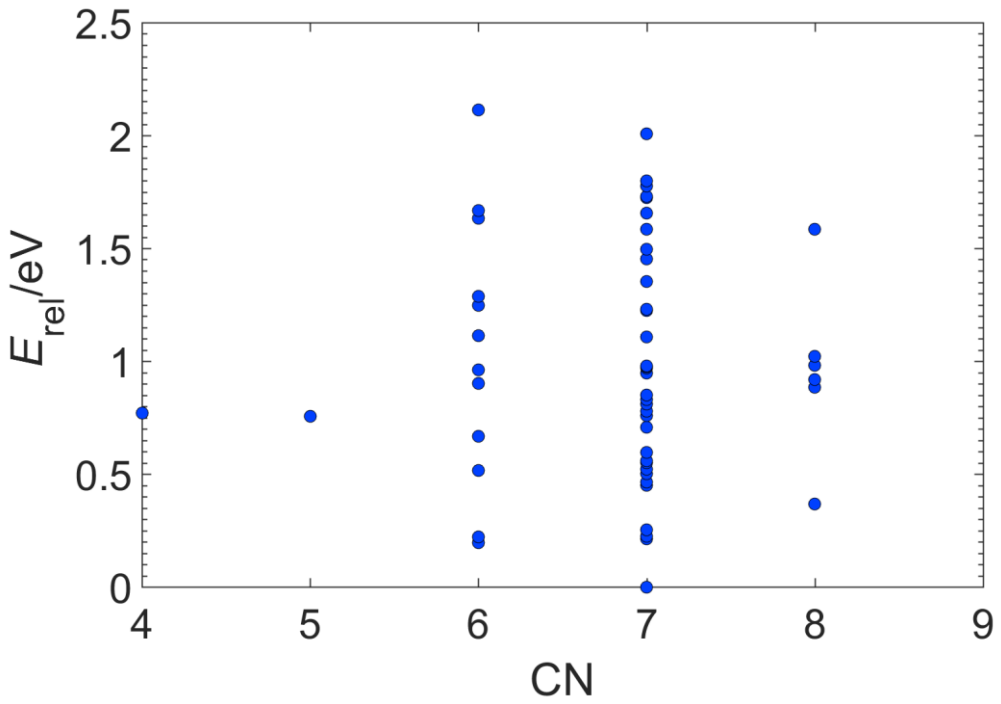

Figure 7.12: The relative energies (E_{rel}) of the optimised CeO_2(111) 4x3x2 surface model with 32 water molecules, a Sr^{2+}, and 2 OH^- against Sr^{2+} coordination number (CN).

Overall when looking at the surface interaction of Sr^{2+} in an aqueous dihydroxide environment the lowest energy structure is 7 CN, does not form Sr—O_s bonds, does not have a protonated surface, has a single Sr—OH bond, and is coordinated to the surface through outer shell coordination. Examining the trends for the structures where $E_{rel} < 0.5$ eV, there are structures with Sr^{2+} CN of 6, 7 and 8, with 0 or 1 Sr—O_s bonds, no surface protonation, either 0, 1 or 2 Sr—OH bonds and are coordinated to the surface via either outer shell coordination or not at all.

It is worth nothing that DFT calculations, such as those described in this chapter, reveal only what is energetically favourable with regards to the bonding environment of Sr^{2+}. As the AIMD investigations of previous chapters highlighted, when dynamics are introduced to a system the solvation environment can change. The most prevalent example of this is the strontium hydroxide solvation environment examined in **Chapter 4,** which in previous static calculations indicated that it would form energetically stable mono and dihydroxides[162,187], while in dynamic simulations the Sr^{2+} ion was mainly uncoordinated by hydroxide ions.

7.4 Conclusion

This chapter explores the feasibility of using a $CeO_2(111)$ surface model as an analogue for UO_2 to investigate the surface interactions of water, the possible surface adsorption of Sr^{2+} and the impact that an alkaline environment, modelled as two hydroxide ions, has on these interactions. In contrast to previous chapters of the thesis, the calculations were energetic calculations using the DFT+U method rather than dynamic simulations. A prototype 4x3x2 supercell of the $CeO_2(111)$ surface was built and optimised with 32 water molecules to act as the water model covering the surface.

To investigate the dissociation of multiple water molecules, and therefore protonation of the $CeO_2(111)$ surface, 20 separate structures were optimised with varying levels of surface protonation. The most energetically favourable structures were those with a single proton on the surface and these were most prevalent. As surface protonation increased, so did the relative energy (E_{rel}).

The adsorption of a single Sr^{2+} ion was investigated by taking previously optimised low energy structures and introducing a Sr^{2+} ion at various distances from the $CeO_2(111)$ surface and reoptimising the structure. In total, 40 different structures were examined to fully explore the impact of Sr^{2+} CN, surface protonation and Sr—surface distance on the E_{rel} of the structures. In general, the results showed favourability towards surface-ion interaction, with low energy structures which had E_{rel} < 0.5 eV had a Sr^{2+} with either inner or outer shell surface coordination. These low energy structures had stable Sr^{2+} CN of 6, 7 or 8, and an unprotonated $CeO_2(111)$ surface. The lowest energy structures typically had a Sr^{2+} ion which coordinated to the surface with either inner or outer shell coordination and with a varying number of Sr—O_s bonds.

To verify that 32 waters were sufficient to model the second solvation shell of the Sr^{2+} ion, the 4 lowest energy optimised water-surface models with a Sr^{2+} ion had an additional 16 water molecules added on top of the water model, for a total of 48 water molecules. These were then reoptimized and the relative energies of the 32 and 48 water models were compared. There was found to be no difference in the type of Sr^{2+} coordination to the surface as a result of the extra waters, suggesting that the 32 water model was sufficient for this type of investigation. However, the relative energies of the initial structures were strongly impacted, suggesting that the additional waters had an impact on the relative energy of the systems.

An alkaline environment was simulated by introducing 2 OH^- ions to the surface model with solvated Sr^{2+}. In total, 54 separate geometries were optimised and examined for common

bonding features related to the lowest energy structures. As in the aqueous model, the lowest energy structure was 7 CN, did not have a protonated surface but did have a single Sr—OH bond. The increase in pH appeared to make surface coordination less favourable, with low energy structures where E_{rel} < 0.5 eV having Sr^{2+} which was outer shell coordinated or uncoordinated to the surface. As in the aqueous structures the low energy structures had Sr^{2+} CNs of 6, 7 or 8 and 0, 1 or 2 Sr—OH bonds all prevalent in the low energy structures.

One aim of this thesis was to provide relevant information to the nuclear partners as to how their future research should be directed. This chapter begins a study into the adsorption of ions to a mineral surface in a high pH environment, finding that at a high pH environment appears to destabilise the surface coordination of the radionuclide Sr^{2+}. This can be expanded on in a future more involved study into the adsorption of ions onto a mineral surface, using different ions, such as those listed in this thesis, using a larger mineral surface more representative of the bulk surface and eventually moving onto different mineral surfaces such as uranium.

The purpose of this chapter was to investigate the possibility of using a 4x3x2 CeO_2(111) surface and a 32 water molecule model to examine Sr^{2+} adsorption, to identify structural features common to the most energetically stable structures and to investigate the impact of a hydroxide environment. The developed model has provided a good starting point for these types of simulations and shown that there is weak favourability for outer shell surface complexation of Sr^{2+} in a hydroxide environment.

Chapter 8: Conclusions

The aim of this thesis was to explore the solvation structure of a range of ions which are present in the nuclear waste storage ponds at Sellafield, and to investigate the impact of hydroxide ions on the solvation structure using quantum chemical methods. *Ab initio* molecular dynamics (AIMD) calculations provided a novel way to investigate the interactions between the ions found in the ponds and the pond conditions.

In **Chapter 3**, the solvation structures of the alkaline earth metals Mg^{2+}, Ca^{2+} and Sr^{2+} were investigated with AIMD using a 64 water molecule model. This chapter introduced the parameters used for all further solvation models and a robust analysis method using the results of AIMD simulations was tested and developed for use in the subsequent chapters. The structure of the first solvation shell of the alkaline earth metals was characterised using radial distribution functions (RDFs) and by calculating the average M—O bond lengths (where M = Mg, Ca or Sr), first shell coordination numbers (CN) and coordination environment residence times. The results of the AIMD calculations compared excellently with experimental and computational literature and correctly identified the trends down the group, Mg^{2+} to Sr^{2+}, of increasing average bond length and increasing coordination number. The results of this chapter indicated that an accurate solvation model had been developed and that the analysis method was correctly representing the data from each AIMD trajectory.

The solvation structure of the alkaline earth metals Mg^{2+}, Ca^{2+} and Sr^{2+} in the presence of hydroxide ions was investigated in **Chapter 4**. AIMD was used to collected 225 ps of analysable trajectory time for each ion, and an analysis method for quantifying proton transport and hydroxide dynamics was developed and tested. For all three ions the introduction of hydroxide ions resulted in a reduction in total CN. The average bond length of Mg—O increased in the hydroxide environment and the average bond length for Ca—O and Sr—O decreased. The quantification of proton transfer events (PTEs) identified that proton transfer was most likely to be an intrashell PTE which occurred outside the first solvation shell of the ion. PTEs were found to be most prevalent in Sr^{2+} systems and least prevalent in the Mg^{2+} systems. Snapshots of the AIMD simulations for Sr^{2+} with different hydroxide coordination environments, where Sr^{2+} was a monohydroxide or a dihydroxide species, were optimised to compare the energetics of the systems. The results found a small energy difference between the two coordination modes of 3.0 kJ mol^{-1}, which was in line with previous DFT investigations.

Chapter 5 used the solvation environments developed in **Chapters 3** and **4** and applied them to the more complex uranyl ion (UO_2^{2+}). AIMD was used to investigate the aquo,

monohydroxide and dihydroxide environments of the UO_2^{2+} ion. This chapter used the developed solvation model and applied it to a complex ion of nuclear relevance due to the prevalence of uranyl in the storage ponds. For the aquo complexes, the solvation structure compared well to existing experimental and computational literature. In the monohydroxide system both the axial and equatorial bond lengths increased compared to the aquo system, but there was no reduction in total first shell CN. The hydroxide ion remained coordinated to UO_2^{2+} at all times and there were no PTEs identified. In the dihydroxide uranyl environment there was an increase in axial and equatorial bond length as well as an increase in the uranyl hydroxide bond length. Compared to both the aquo and mono hydroxide systems there was a reduction in total CN. There was an increase in PTEs in the dihydroxide system with 3 PTEs identified, with no intrashell PTEs outside the first solvation shell. The high hydroxide coordination to the uranyl ion combined with the lack of PTEs provides further evidence that the coordination of hydroxide ions to a central cation inhibits proton transfer.

Chapter 6 examined proton transfer as a function of increasing ionic charge. **Part 1** examined the solvation structure of Sr^{2+} in a monohydroxide environment using AIMD, it was found that the Sr—O bond length was unchanged but the total CN of the Sr^{2+} reduces compared to the aquo species with the introduction of one hydroxide. Similar proton transfer behaviour to the Sr^{2+} dihydroxides was identified, with PTEs occurring more frequently outside the first solvation shell. The hydroxide ion was predominantly uncoordinated to the Sr^{2+} ion, with no intrashell PTEs inside the first solvation shell. **Part 2** examined the solvation structure of Cs^+ in both an aqueous and monohydroxide environments. The solvation structure of the ion was undefined in both cases likely due to the size of the Cs^+ ion and therefore low charge density compared to other ions studied. Three cutoffs were used to try to define the bonding structure but varying the cutoff did not have a large impact on the characterisation of the solvation structure. The introduction of a hydroxide ion resulted in a lower total CN and smaller range of CN identified across the AIMD trajectories, but there was a lack of direct coordination of hydroxide to the ion. **Part 3** examined the solvation structure of La^{3+} and Lu^{3+} in an aquo and trihydroxide environment. The solvation structure of the two lanthanides was compared to existing literature and found to be in good agreement with both computational and experimental literature. The results from the AIMD simulations of the trihydroxide environment found that hydroxide coordination was preferred for both ions with no periods of time where either ion was uncoordinated by hydroxides. Lu^{3+} was predominantly found to be a trihydroxide, whereas for La^{3+} the hydroxide coordination was more labile and frequently found to be a dihydroxide or trihydroxide. The proton transport behaviour was quantified and

PTEs were more frequent for La^{3+} compared to Lu^{3+}, likely due to the increased variation in hydroxide coordination for La^{3+} compared to Lu^{3+}. PTEs were less prevalent in lanthanides compared to the alkaline earth metals due to the high hydroxide coordination to the ion which appears to inhibit proton transfer.

Chapter 3 to **6** examine similar themes, firstly focusing on the solvation structure of an anion in water before examining the impact hydroxide ions and thus a higher pH impacts that solvation structure. As such the work presented can be extended in similar ways. While the dynamic trajectories focus on systems with a single cation, there is the potential to examine multiple cations if a larger number of water molecules is used, for example multiple of the alkaline earth meals, or to investigate competing interactions of an alkaline earth metal and a more complex ion such as a lanthanide, and how increasing pH affects this. Alternatively, this work could be extended by examining the solvation behaviour of the individual cations with different counter ions found in the storage ponds, for example carbonates, chloride or sulfates.

A preliminary investigation into the adsorption of Sr^{2+} onto a $CeO_2(111)$ surface was detailed in **Chapter 7**. This chapter used CeO_2 as a UO_2 analogue and energetic rather than dynamic calculations. A 4x3x2 supercell of $CeO_2(111)$ with a 32 water molecule model was built and various strontium-surface interactions modelled to determine which structure characteristics were most energetically favourable. It was determined that the most energetically favourable structure had a Sr^{2+} ion with a CN of 7 which coordinated to the surface through its outer shell. Stable low energy structures were also found with some form of inner or outer shell Sr^{2+} surface coordination and a Sr^{2+} CN of 6, 7 or 8. The impact on the ion-surface interactions of introducing hydroxide ions was also investigated and was found to reduce the stability of the structures with inner shell strontium-surface coordination, there was a weak favourability for outer shell surface Sr^{2+} complexation.

The surface model developed in **Chapter 7** also provides an opportunity for future work. Although a basic model has been developed, which showed a weak preference for strontium coordination to the surface, further computational calculations would provide more verification. This could be done through the use of a larger supercell, further calculations probing the surface coordination of an ion, or using AIMD to examine the impact of dynamics on the surface coordination. There is also the opportunity to study the absorption of other ions relevant to the nuclear waste clean-up process, such as Cs^{+}.

The work outlined in this thesis is the first example of an *ab initio* molecular dynamics investigation of the chemical species found in the nuclear waste storage ponds at Sellafield. The results have demonstrated that the developed solvation model is accurate and can be applied to a range of ions. The results also detail the successful use of AIMD to investigate hydroxide species and proton transport through an aqueous environment.

Appendix A: Convergence Tests

Prior to any experimental trajectories being run both the cutoff and relative cutoff were converges to an accuracy of 10^{-8} Ha, as per the instructions:

https://www.cp2k.org/howto:converging_cutoff

A1: Mg^{2+} Convergence Test Results

Chosen cutoff: 500 Ry **Chosen relative cutoff**: 60 Ry

Table A1: The results from converging the cutoff for Mg^{2+}, the cutoff, total energy and number of Gaussians distributed on Grids 1 to 5.

Cutoff /Ry	Total Energy/Ha	Grid 1	Grid 2	Grid 3	Grid 4	Grid 5
50	-1122.6662854047	382295	170490	1327	0	0
100	-1122.6535936449	348797	151288	53827	200	0
150	-1122.6974186454	327356	133407	93029	320	0
200	-1122.6968275573	267293	131965	154534	320	0
250	-1122.6965322500	265266	117029	170490	1327	0
300	-1122.6966547341	257631	113936	179063	3482	0
350	-1122.6967403726	227360	144007	128718	53827	200
400	-1122.6967114286	227160	121637	151288	53827	200
450	-1122.6967312108	214377	124911	156465	58159	200
500	-1122.6967902432	210454	117022	133287	93029	320
550	-1122.6967902432	208437	118919	133407	93029	320

Table A1.1: The results from converging the relative cutoff for Mg^{2+}, the cutoff, total energy and number of Gaussians distributed on Grids 1 to 5.

Rel_ Cutoff/Ry	Total Energy /Ha	Grid 1	Grid 2	Grid 3	Grid 4	Grid 5
10	-1125.8755478988	35968	70512	109909	122899	214824
20	-1122.7800483483	96768	70874	110379	121237	154854
30	-1122.6992111569	106480	109909	122899	158479	56345
40	-1122.6967781205	127379	114990	128998	128718	54027
50	-1122.6967904028	159239	106027	118438	169081	1327
60	-1122.6967902432	167642	110379	121237	154534	320
70	-1122.6967902432	206435	115335	138993	93029	320
80	-1122.6967902432	210454	117022	133287	93029	320
90	-1122.6967902432	216389	122899	158479	56145	200
100	-1122.6967902432	227360	121437	151288	53827	200

A2: Ca^{2+} Convergence Test Results

Chosen cutoff: 500 Ry **Chosen t relative cutoff**: 60 Ry

Table A2: The results from converging the cutoff for Ca^{2+}, the cutoff, total energy and number of Gaussians distributed on Grids 1 to 5.

Cutoff /Ry	Total Energy/Ha	Grid 1	Grid 2	Grid 3	Grid 4	Grid 5
50	-1098.7232244297	388763	168245	4420	0	0
100	-1098.3330717075	351489	155246	54453	240	0
150	-1098.4016127091	326246	144093	90729	360	0
200	-1098.4032505024	266436	140505	152668	1819	0
250	-1098.4033642738	262562	126201	168245	4420	0
300	-1098.4035425780	253705	121242	182061	4420	0
350	-1098.4034041848	217217	154872	134646	54453	240
400	-1098.4034962996	212828	138661	155246	54453	240
450	-1098.4035077300	201724	139609	162606	57249	240
500	-1098.4035537513	197638	131199	141502	90729	360
550	-1098.4035537513	197638	128608	144093	90729	360

Table A2.1: The results from converging the relative cutoff for Ca^{2+}, the cutoff, total energy and number of Gaussians distributed on Grids 1 to 5.

Cutoff/Ry	Total Energy /Ha	Grid 1	Grid 2	Grid 3	Grid 4	Grid 5
10	-1101.5612244425	2568	65075	136963	136727	220095
20	-1098.4856403422	50728	104933	123113	128167	154487
30	-1098.4057767430	67643	136963	136727	162606	57489
40	-1098.4035422984	105196	129889	139662	131988	54693
50	-1098.4035538849	149042	114961	124760	170846	1819
60	-1098.4035537513	155661	123113	128167	152668	1819
70	-1098.4035537513	197638	122342	150359	90729	360
80	-1098.4035537513	197638	131199	141502	90729	360
90	-1098.4035537513	204606	136727	162606	57249	240
100	-1098.4035537513	212828	138901	155006	54453	240

A3: Sr^{2+} Convergence Test Results

Chosen cutoff: 500 Ry **Chosen relative cutoff**: 60 Ry

Table A3: The results from converging the cutoff for Sr^{2+}, the cutoff, total energy and number of Gaussians distributed on Grids 1 to 5.

Cutoff /Ry	Total Energy/Ha	Grid 1	Grid 2	Grid 3	Grid 4	Grid 5
50	-1093.8003570372	388820	168232	4396	0	0
100	-1092.6145430271	346950	159866	54392	240	0
150	-1092.6422030370	321814	145714	93560	360	0
200	-1092.6420318184	263978	142926	152725	1819	0
250	-1092.6420101801	262537	126283	168232	4396	0
300	-1092.6421740954	246741	128241	182070	4156	240
350	-1092.6420689549	212944	158953	134919	54392	240
400	-1092.6420407374	207640	139310	159866	54392	240
450	-1092.6421324640	200375	139291	164125	57417	240
500	-1092.6420957122	197719	125752	146951	90666	360
550	-1092.6420957122	197719	124095	145714	93560	360

Table A3.1: The results from converging the relative cutoff for Sr^{2+}, the cutoff, total energy and number of Gaussians distributed on Grids 1 to 5.

Cutoff/Ry	Total Energy /Ha	Grid 1	Grid 2	Grid 3	Grid 4	Grid 5
10	-1095.6576504630	2560	76352	118807	128634	235095
20	-1092.7167114773	50248	83006	129283	144367	154544
30	-1092.6443084923	78912	118807	128634	144069	91026
40	-1092.6421183806	91202	121742	158953	134919	54632
50	-1092.6420958409	110547	145941	130891	169673	4396
60	-1092.6420957122	133254	129283	144367	152725	1819
70	-1092.6420957122	152296	137358	173917	96058	1819
80	-1092.6420957122	197719	124095	145714	93560	360
90	-1092.6420957122	197719	128634	144069	90666	360
100	-1092.6420957122	201839	137827	164125	57417	240

A4: Cs^+ Convergence Test Results

Chosen cutoff: 600 Ry **Chosen relative cutoff**: 80 Ry

Table A4: The results from converging the cutoff for Cs^+, the cutoff, total energy and number of Gaussians distributed on Grids 1 to 5.

Cutoff /Ry	Total Energy/Ha	Grid 1	Grid 2	Grid 3	Grid 4	Grid 5
50	-1045.6282335323	472001	54320	1707	0	0
100	-1081.7205469107	362955	159988	4845	240	0
150	-1082.1909731465	325228	146773	54320	1707	0
200	-1082.1536194466	292112	145763	88326	1587	240
250	-1082.1549750860	232083	151076	139784	4845	240
300	-1082.1543333052	209973	152982	159988	4845	240
350	-1082.1543298589	194878	155586	172239	3618	1707
400	-1082.1543895353	162757	182145	130173	51246	1707
450	-1082.1543896353	153089	172139	146773	54320	1707
500	-1082.1543548580	143158	168324	160519	54320	1707
550	-1082.1543548681	140614	161638	138220	85729	1827
600	-1082.1543866563	135794	156318	145763	88326	1827
650	-1082.1543866563	133608	131786	171040	89767	1827

Table A4.1: The results from converging the relative cutoff for Cs^+, the cutoff, total energy and number of Gaussians distributed on Grids 1 to 5.

Cutoff/Ry	Total Energy /Ha	Grid 1	Grid 2	Grid 3	Grid 4	Grid 5
10	-1085.0362442948	2560	44912	93142	163305	224109
20	-1082.2526684199	46408	50227	128489	155141	147763
30	-1082.1581852996	47472	93142	163305	136553	87556
40	-1082.1544060291	51880	110877	182145	130173	52953
50	-1082.1543873464	75042	129576	158337	159988	5085
60	-1082.1543868484	96635	128489	155141	142678	5085
70	-1082.1543867502	106699	152467	174710	92325	1827
80	-1082.1543866563	135794	156318	145763	88326	1827
90	-1082.1543866562	140614	163305	136553	85729	1827
100	-1082.1543866562	147011	167365	157625	54320	1707

A5: La^{3+} Convergence Test Results

Chosen cutoff: 600 Ry **Chosen relative cutoff**: 80 Ry

Table A5: The results from converging the cutoff for La^{3+}, the cutoff, total energy and number of Gaussians distributed on Grids 1 to 5.

Cutoff /Ry	Total Energy/Ha	Grid 1	Grid 2	Grid 3	Grid 4	Grid 5
50	-1068.5067025117	659114	73570	2907	0	0
100	-1092.8282680859	518761	204475	12035	320	0
150	-1093.1503491763	460251	198863	73570	2907	0
200	-1093.1320561375	426934	183779	121531	3347	0
250	-1093.1333008665	360460	178609	184167	12035	320
300	-1093.1333360679	360460	158301	204475	12035	320
350	-1093.1332461240	344693	157707	220836	12035	320
400	-1093.1333403499	291351	201718	169957	72245	320
450	-1093.1332922911	288128	172123	198863	73570	2907
500	-1093.1333103108	263622	185621	209551	73890	2907
550	-1093.1332918630	248478	181284	184041	118441	3347
600	-1093.1332918580	240136	186798	183779	121531	3347
650	-1093.1332918580	227321	164449	211374	129100	3347

Table A5.1: The results from converging the relative cutoff for La^{3+}, the cutoff, total energy and number of Gaussians distributed on Grids 1 to 5.

Cutoff/Ry	Total Energy /Ha	Grid 1	Grid 2	Grid 3	Grid 4	Grid 5
10	-1095.6378251129	2560	57712	188206	183329	303784
20	-1093.1858940790	59208	92657	208595	178609	196522
30	-1093.1345364079	60272	188206	183329	181996	121788
40	-1093.1332992260	78976	212375	201718	169957	72565
50	-1093.1332917616	109530	244379	162291	207036	12355
60	-1093.1332919013	151865	208595	178609	184167	12355
70	-1093.1332918454	174183	217587	211374	129100	3347
80	-1093.1332918580	240136	186798	183779	121531	3347
90	-1093.1332918580	248478	183329	181996	118761	3027
100	-1093.1332918580	276013	173230	209551	73890	2907

A6: Lu^{3+} Convergence Test Results

Chosen cutoff: 600 Ry **Chosen relative cutoff**: 80 Ry

Table A6: The results from converging the cutoff for Lu^{3+}, the cutoff, total energy and number of Gaussians distributed on Grids 1 to 5.

Cutoff /Ry	Total Energy/Ha	Grid 1	Grid 2	Grid 3	Grid 4	Grid 5
50	-1319.0635414129	732003	53755	400	0	0
100	-1323.2231276495	606907	170883	8368	0	0
150	-1321.6901204018	551029	180974	53755	400	0
200	-1321.7326818242	529875	156529	99234	520	0
250	-1321.7325630799	469181	154556	157882	4539	0
300	-1321.7325073758	455696	151211	170883	8368	0
350	-1321.7326293043	432690	164094	180606	8368	400
400	-1321.7326249948	391671	189868	150464	53755	400
450	-1321.7326471609	387644	163385	180974	53755	400
500	-1321.7326751347	381957	155704	181841	66256	400
550	-1321.7326750347	375393	154602	156409	99234	520
600	-1321.7326270847	362981	166894	156529	99234	520
650	-1321.7326270847	345803	153809	183580	102446	520

Table A6.1: The results from converging the relative cutoff for Lu^{3+}, the cutoff, total energy and number of Gaussians distributed on Grids 1 to 5.

Cutoff/Ry	Total Energy /Ha	Grid 1	Grid 2	Grid 3	Grid 4	Grid 5
10	-1324.9900100490	2560	163072	209761	154602	256163
20	-1321.8180308157	94568	194456	179757	154956	162421
30	-1321.7363269034	165632	209761	154602	156409	99754
40	-1321.7326559458	217285	174386	189868	150464	54155
50	-1321.7326270979	258040	181585	167282	170883	8368
60	-1321.7326272066	289024	179757	154956	157882	4539
70	-1321.7326270798	314705	174305	194182	98427	4539
80	-1321.7326270847	362981	166894	156529	99234	520
90	-1321.7326270847	375393	154602	156409	99234	520
100	-1321.7326270847	381957	158230	179315	66256	400

A7: UO_2^{2+} Convergence Test Results

Chosen cutoff: 600 Ry **Chosen relative cutoff**: 80 Ry

Table A7: The results from converging the cutoff for UO_2^{2+}, the cutoff, total energy and number of Gaussians distributed on Grids 1 to 5.

Cutoff /Ry	Total Energy/Ha	Grid 1	Grid 2	Grid 3	Grid 4	Grid 5
50	-1131.1898767481	737630	57781	440	0	0
100	-1143.1560452054	625885	150974	18992	0	0
150	-1142.8748585209	561168	176462	57781	440	0
200	-1142.8304687276	532476	163736	98639	1000	0
250	-1142.8129893943	479202	161790	149012	5847	0
300	-1142.7893639429	449881	176004	150974	18992	0
350	-1142.7840979677	429365	181432	166062	18552	440
400	-1142.7803245991	386589	197203	153838	57781	440
450	-1142.7803245991	379492	181676	176462	57781	440
500	-1142.7791932624	371657	171427	189420	62907	440
550	-1142.7782893393	369441	163155	173310	88945	1000
600	-1142.7782614385	365027	167449	163736	98639	1000
650	-1142.7782614384	364907	137452	190762	96883	5847

Table A7.1: The results from converging the relative cutoff for UO_2^{2+}, the cutoff, total energy and number of Gaussians distributed on Grids 1 to 5.

Cutoff/Ry	Total Energy /Ha	Grid 1	Grid 2	Grid 3	Grid 4	Grid 5
10	-1145.7851469054	2882	107867	258692	163155	263255
20	-1142.8606741289	100869	138262	230389	171472	154859
30	-1142.7813568305	110749	258692	163155	173310	89945
40	-1142.7782567489	139840	246749	197203	153838	58221
50	-1142.7782602535	174535	259562	191788	150974	18992
60	-1142.7782616312	239131	230389	171472	149012	5847
70	-1142.7782614239	339402	158512	182604	109486	5847
80	-1142.7782614385	365027	167449	163736	98639	1000
90	-1142.7782614385	369441	163155	173310	88945	1000
100	-1145.7851469054	376498	179012	177434	62467	440

Appendix B: Dispersion Correction Comparisons for Sr^{2+}

In order to check the impact of using Grimme's DFT-D2 dispersion[76,166] and not the improved DFT-D3 dispersion[93] two AIMD trajectories of Sr^{2+} in a periodic cell with 64 water molecules were run. The AIMD trajectories used the same computational parameters as listed in the methodology of **Chapter 3** and had identical starting configurations, the only change was the change in the dispersion correction used. Each trajectory was run for 20 ps, once the 5 ps of equilibration time was discarded the remaining 15 ps of time were analysed.

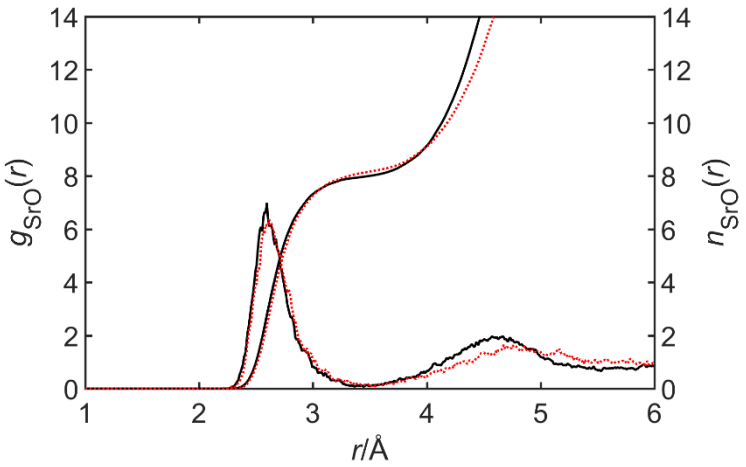

Figure B1: Sr—O radial distribution function, g(r), generated from 15ps simulations at 400K using a DFT-D2 dispersion correction (solid black) and DFT-D3 dispersion correction (dotted red).

The RDFs for each AIMD trajectory were averaged over the 15 ps trajectory time and are shown in **Figure B1**. Both dispersion corrections show a defined first and second shell, with the D2 correction having a more clearly defined second shell. Analysis of the RDF found that a minimal difference in first shell RDF peaks of 2.60 Å and 2.61 Å for D2 and D3 respectively, in line with what is expected experimentally for a Sr—O RDF. The average first shell Sr—O coordination numbers and first shell Sr—O bond lengths were also calculated. The calculated values for D2 gave an average CN of 7.94 and an Sr—O bond length of 2.67 Å, and the calculated values for the D3 trajectory have a slightly higher average CN of 7.98 and average Sr—O bond length of 2.68 Å. In the context of the values presented for both first shell average bond length and first shell Sr—O CN in **Table 3.4** there is no appreciable difference using the D3 dispersion correction in this case. It appears that D3 is not necessarily superior in this case, with minimal changes in both the RDF and first solvation shell bonding for Sr—O.

Appendix C: Cell Volume Fluctuations

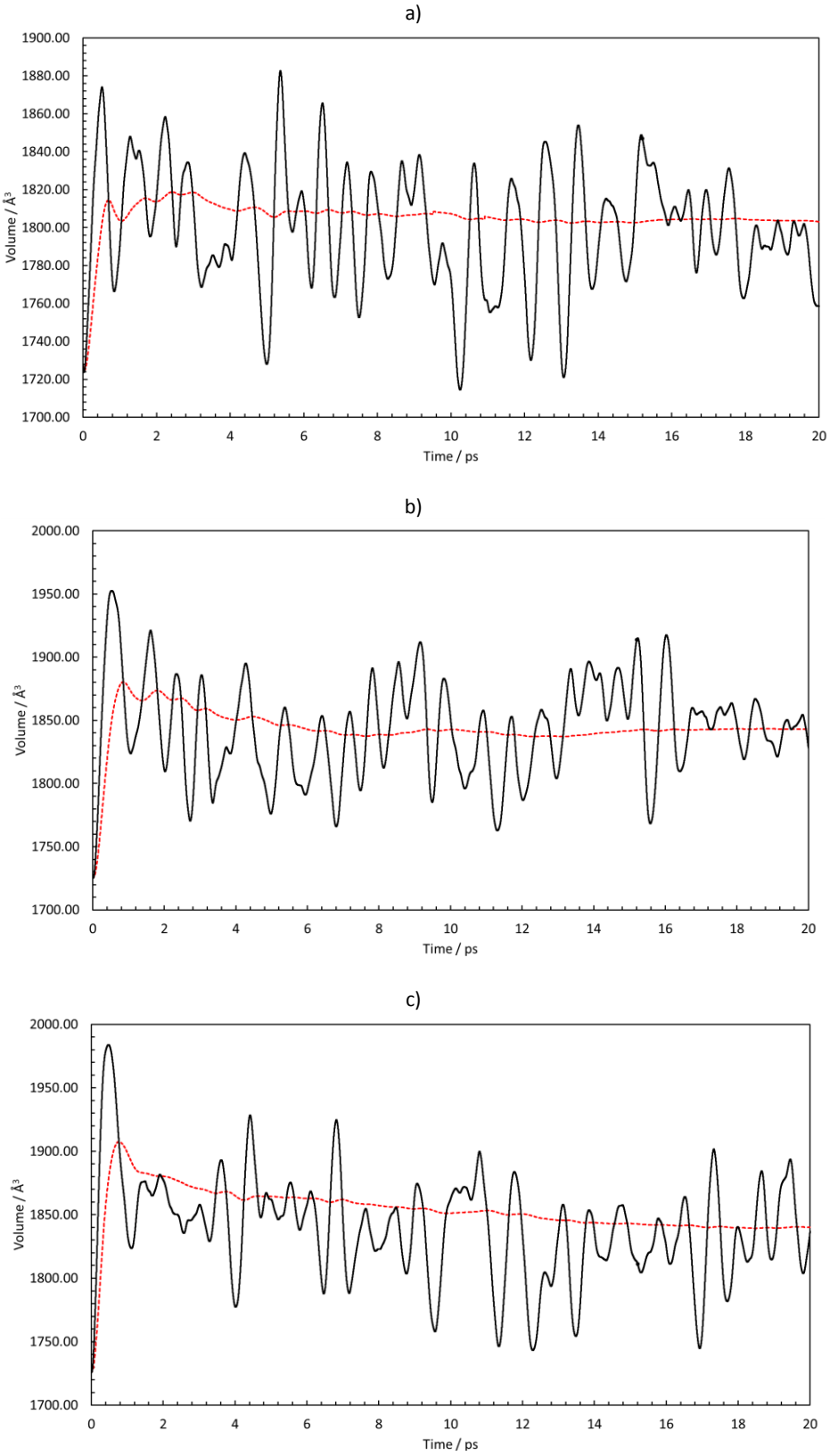

Figure C1: Instantaneous (black solid line) and average (red dotted line) cell volume fluctuations over a representative a) Mg^{2+} b) Ca^{2+} c) Sr^{2+} in a cell with 64 water molecules, NPT_I AIMD simulation.

A 5 ps equilibration time is used throughout this thesis to allow the variables, such as temperature and pressure, in the simulation cell to equilibrate before the trajectory time is sampled. As the NPT_I ensemble is used for all AIMD simulations, the cell volume is allowed to fluctuate across the timescale of a simulation.

Cell volume fluctuations for an example trajectory for each of the alkaline earth metals are shown in graph form in **Figure C1**. In each case the cell volume oscillates across the timescale of a trajectory, typical of a Nose-Hoover temperature controlled system. The magnitude of the cell volume oscillation for each example are within reasonable boundaries after 5 ps and do not increase as the trajectory progresses.

The lack of increase in the magnitude of the cell volume oscillations, combined with the accuracy of the first solvation shell structure for each ion as demonstrated in the results chapters instilled confidence that the 5 ps equilibration time was sufficient for the investigation purposes.

Appendix D: Timestep Choice

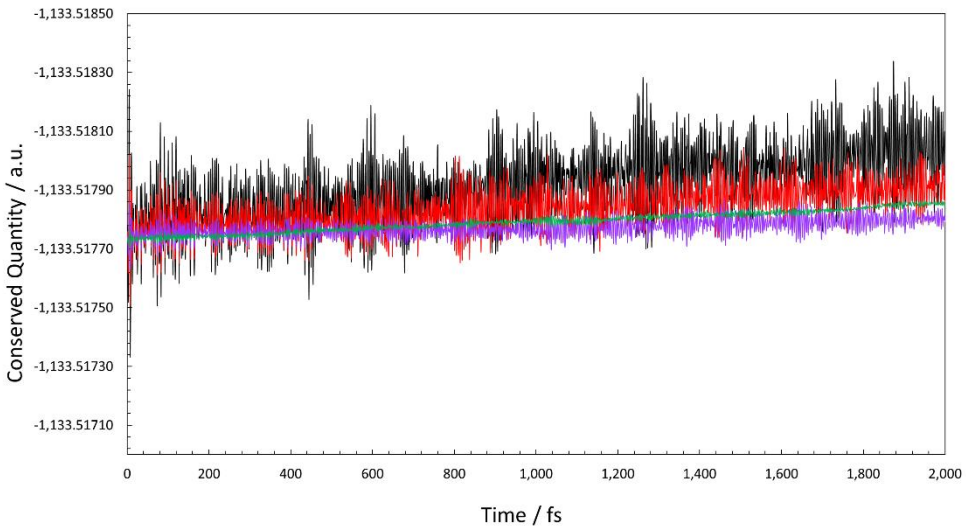

Figure D1: The variation of the conserved quantity over a 2 000 fs trajectory using timesteps 0.2 fs (green), 0.3 fs (purple), 0.4 fs (red) and 0.5 fs (black).

The timestep of a molecular dynamics simulation must be short enough to obtain the sampling of the smallest movement in the simulation cell, in this case the O—H bond. As a general rule, the time step should be no longer than 10% of the shortest vibrational period in the system being studied.[113] Timesteps of 0.2, 0.3, 0.4 and 0.5 fs were tested for a short 2000 fs AIMD trajectory of a Sr^{2+} ion in 64 molecules of water. The variation in the conserved quantity at each timestep, which is the sum of the potential and kinetic energy of a system, is depicted in **Figure D1**. Although the smaller timesteps, in particular 0.2 fs, have smaller variation over the trajectory the 0.5 fs timestep was selected for use in this thesis as the increased computational cost of using a smaller timestep outweighed the benefits. The variation in a 0.5 fs conserved quantity is less than 0.0005 a.u. for the 0.5 fs timestep and it is still smaller than $1/10^{th}$ the smallest vibration in the simulation shell and hence suitable for witnessing bond breaking and forming in the context of proton transfer.

Appendix E: Chapter 7 Data

Table E1: Data used to construct **Figure 7.4 – 7.7**; Sr surface distance (r_{Sr}), total Sr^{2+} CN, number of Sr—O_s bonds ($n_{Sr—Os}$), number of protons on the surface (n_{H^+}), bonding classification and relative energy (E_{rel}) for each optimised structure with a 4x3x2 CeO_2(111) surface, Sr^{2+} ion and 32 water molecules.

r_{Sr} /Å	Sr^{2+} CN	$n_{Sr—Os}$	n_{H^+}	Classification	E_{rel}/eV
4.455	7	0	0	Outer Shell	0.000
2.729	7	1	0	Inner Shell	0.270
2.156	7	3	0	Inner Shell	0.367
4.439	8	0	0	Outer Shell	0.456
2.570	6	1	0	Inner Shell	0.479
2.571	6	1	0	Inner Shell	0.501
4.492	7	0	1	Outer Shell	0.643
2.268	6	2	1	Inner Shell	0.665
3.428	7	0	0	Outer Shell	0.828
2.632	7	1	1	Inner Shell	0.911
2.573	6	1	0	Inner Shell	0.935
2.453	7	1	1	Inner Shell	0.982
4.166	6	0	1	Outer Shell	0.988
4.108	6	0	1	Outer Shell	1.004
2.498	7	1	0	Inner Shell	1.030
2.339	8	2	0	Inner Shell	1.048
2.083	7	3	0	Inner Shell	1.075
2.399	7	2	1	Inner Shell	1.137
5.256	8	0	1	Bulk	1.161
3.278	7	0	0	Outer Shell	1.246
3.191	7	0	1	Inner Shell	1.312
5.487	7	0	0	Bulk	1.416
3.178	7	0	2	Inner Shell	1.430
6.860	6	0	0	Bulk	1.431
4.365	8	0	1	Outer Shell	1.431
3.792	9	0	0	Outer Shell	1.431
2.184	7	3	0	Inner Shell	1.448
3.281	7	0	1	Outer Shell	1.461
2.300	8	3	0	Inner Shell	1.474
4.288	5	0	1	Outer Shell	1.489
4.202	7	0	1	Outer Shell	1.496
2.058	7	3	1	Inner Shell	1.628
4.183	5	0	0	Outer Shell	1.670
4.167	5	0	2	Outer Shell	1.735
3.936	7	0	1	Outer Shell	1.740
4.103	5	0	2	Outer Shell	1.792
4.011	7	0	2	Outer Shell	1.882
4.485	7	0	1	Outer Shell	1.942
3.970	7	0	2	Outer Shell	2.027
3.898	7	0	2	Outer Shell	2.161

Table E2: Data used to construct **Figure 7.8 – 7.12**; Sr surface distance (r_{Sr}), total Sr^{2+} CN, number of Sr—OH bonds ($n_{Sr—OH}$), number of Sr—O_s bonds ($n_{Sr—Os}$), number of protons on the surface (n_{H^+}), bonding classification and relative energy (E_{rel}) for each optimised structure with a 4x3x2 CeO_2(111) surface, Sr^{2+} ion and 32 water molecules and 2 OH^-.

r_{Sr} /Å	Sr^{2+}CN	$n_{Sr—OH}$	$n_{Sr—Os}$	n_{H^+}	Classification	E_{rel}/eV
3.637	7	1	0	0	Outer Shell	0.000
3.474	6	2	0	0	Outer Shell	0.195
4.794	7	1	0	0	Bulk	0.213
3.379	6	2	0	0	Outer Shell	0.221
3.624	7	2	0	0	Outer Shell	0.226
4.799	7	1	0	0	Bulk	0.252
4.570	8	0	0	0	Bulk	0.367
3.949	7	0	0	0	Outer Shell	0.450
2.783	7	0	1	0	Inner Shell	0.464
2.799	7	1	1	0	Inner Shell	0.502
2.604	6	1	1	0	Inner Shell	0.516
4.372	7	0	0	0	Outer Shell	0.521
2.748	7	0	0	0	Inner Shell	0.550
4.800	7	1	0	0	Bulk	0.558
4.104	7	1	0	0	Outer Shell	0.596
2.640	6	0	1	0	Inner Shell	0.667
2.878	7	1	1	0	Inner Shell	0.708
3.824	5	2	0	0	Outer Shell	0.756
4.488	7	1	0	0	Bulk	0.760
2.994	4	2	0	0	Inner Shell	0.769
4.416	7	0	0	0	Outer Shell	0.780
4.465	7	1	0	0	Outer Shell	0.809
2.685	7	1	1	0	Inner Shell	0.831
2.807	7	1	1	0	Inner Shell	0.850
4.523	8	0	0	0	Bulk	0.885
3.269	6	0	0	0	Outer Shell	0.902
2.838	8	2	0	1	Inner Shell	0.918
2.695	7	1	1	0	Inner Shell	0.947
2.577	6	1	1	0	Inner Shell	0.960
3.650	7	0	0	0	Outer Shell	0.971
2.812	7	0	1	0	Inner Shell	0.976
2.811	7	1	1	0	Inner Shell	0.980
4.726	8	1	0	0	Bulk	0.980
2.182	8	0	3	0	Inner Shell	1.023
3.611	7	1	0	0	Outer Shell	1.106
2.416	6	1	2	0	Inner Shell	1.111
2.773	7	2	1	0	Inner Shell	1.223
3.939	7	1	0	0	Outer Shell	1.231
2.413	6	2	2	0	Inner Shell	1.247
2.738	6	1	1	0	Inner Shell	1.287

Table E2 cont: Data used to construct **Figure 7.8** – **7.12**; Sr surface distance (r_{Sr}), total Sr^{2+} CN, number of Sr—OH bonds ($n_{Sr—OH}$), number of Sr—O_s bonds ($n_{Sr—Os}$), number of protons on the surface (n_{H^+}), bonding classification and relative energy (E_{rel}) for each optimised structure with a 4x3x2 CeO_2(111) surface, Sr^{2+} ion and 32 water molecules and 2 OH^-.

r_{Sr} /Å	Sr^{2+} CN	$n_{Sr—OH}$	$n_{Sr—Os}$	n_{H^+}	Classification	E_{rel}/eV
2.583	7	2	1	0	Inner Shell	1.353
3.908	7	1	0	1	Outer Shell	1.453
2.301	7	2	2	1	Inner Shell	1.497
3.042	7	2	0	1	Inner Shell	1.583
4.235	8	1	0	0	Outer Shell	1.584
2.255	6	1	1	1	Inner Shell	1.632
5.117	7	1	0	0	Bulk	1.657
4.192	6	0	0	1	Outer Shell	1.667
2.691	7	1	1	1	Inner Shell	1.725
3.918	7	2	0	0	Outer Shell	1.729
4.199	7	2	0	1	Outer Shell	1.774
3.773	7	2	0	0	Outer Shell	1.798
5.110	7	2	0	0	Bulk	2.006
3.861	6	1	0	2	Outer Shell	2.112

References

(1) NIRAB, “UK Nuclear Innovation and Research Programme Recommendations,” 2016.

(2) “Department for Business, Innovation & Skills and Department of Energy & Climate Change,” 2013.

(3) “NDA Annual Report and Accounts, 2017/18.”

(4) Nuclear Decommissioning Authority (NDA), “End of reprocessing at Thorp signals new era for Sellafield,” *16 November 2018*. [Online]. Available: https://www.gov.uk/government/news/end-of-reprocessing-at-thorp-signals-new-era-for-sellafield.

(5) Nuclear Decommisioning Authority (NDA), “The historic UK nuclear legacy (1940s to 1970s).” [Online]. Available: https://www.gov.uk/government/publications/nuclear-provision-explaining-the-cost-of-cleaning-up-britains-nuclear-legacy/nuclear-provision-explaining-the-cost-of-cleaning-up-britains-nuclear-legacy#the-historic-uk-nuclear-legacy-1940s-to-1970s.

(6) S. Owens, M. Higgins-Bos, M. Bankhead, and J. Austin, “Using Chemical And Process Modelling to Design and Improve an Effluent Treatment Plant,” *NNL Sci.*, no. 3, pp. 4–13, 2015.

(7) Electrowatt-Ekono (UK), “A Review of the Processes Contributing to Radioactive Waste in the UK,” 1999.

(8) R. Hancock, J. R. Parkinson, and R. M. Sellers, “Waste arising from power generation in Magnox reactors,” *Interdiscip. Sci. Rev.*, vol. 23, no. 3, pp. 289–291, 1998.

(9) “The role of nuclear power in a low carbon economy. Paper 1: An introduction to nuclear power – science, technology and UK policy context,” 2006.

(10) N. Kaltsoyannis and P. Scott, *The f elements*. Oxford University Press, 1999.

(11) C. V. Sundaram and S. L. Mannan, “Nuclear fuels and development of nuclear fuel elements,” *Sadhana*, vol. 14, no. 1, pp. 21–57, 1989.

(12) M. M. Bé, V. Chisté, C. Dulieu, E. Browne, C. Baglin, V. Chechev, Kuzmenko, R. Helmer, F. Kondev, T. D. MacMahon, and K. B. Lee, *Table of radionuclides (Vol.3 - A = 3 to 244)*, vol. 3. 2006.

(13) A. L. Nichols, D. L. Aldama, and M. Verpelli, “C-3.3. U-235 cumulative fission yields for selected fission products,” *Handb. Nucl. Data Safeguards Database Extensions*, no. August, pp. 105–106, 2008.

(14) G. R. Choppin, J. O. Liljenzin, and J. Rydberg, *Radiochemistry and Nuclear Chemistry*, no. 3. Elsevier, 2002.

(15) L. S. Natrajan and M. H. Langford Paden, “CHAPTER 6. F-block Elements Recovery,” in *Element Recovery and Sustainability*, 2013, pp. 140–184.

(16) S. E. Jensen and E. Nonbel, *Description of the Magnox Type of Gas Cooled Reactor (MAGNOX)*, vol. 2, no. November. 1999.

(17) M. E. Pick, “Magnox Graphite Core Decommissioning and Disposal Issues,” *IAEA TECDOC-1647*, pp. 1–14, 2010.

(18) D. E. Shropshire, “Lessons Learned From GEN I Carbon Dioxide Cooled Reactors,” in *12th International Conference on Nuclear Engineering*, 2004, pp. 463–473.

(19) Nuclear Decommissioning Authority, “The Magnox operating programme 9 (MOP 9),” 2012.

(20) C. R. F. Azevedo, “Selection of fuel cladding material for nuclear fission reactors,” *Eng. Fail. Anal.*, vol. 18, no. 8, pp. 1943–1962, 2011.

(21) P. Greenfield, “A comparison of magnox A 12 and ZA alloys as canning materials for nuclear reactors,” *J. Nucl. Mater.*, vol. 11, no. 2, pp. 121–134, Feb. 1964.

(22) A. Laferrere, R. Burrows, C. Glover, R. N. Clark, O. Payton, L. Picco, S. Moore, and G. Williams, “In situ imaging of corrosion processes in nuclear fuel cladding,” *Corros. Eng. Sci. Technol.*, vol. 52, no. 8, pp. 596–604, 2017.

(23) R. Lindström, J. E. Svensson, and L. G. Johansson, “The Influence of Carbon Dioxide on the Atmospheric Corrosion of Some Magnesium Alloys in the Presence of NaCl,” *J. Electrochem. Soc.*, vol. 149, no. 4, p. B103, 2002.

(24) J. E. S. R. Lindstrom, L. G. Johansson, “The influence of NaCl and CO_2 on the atmospheric corrosion of magnesium alloy AZ91,” *Mater. Corros.*, vol. 54, pp. 587–594, 2003.

(25) The Institution of Electrical Engineers, “Nuclear Reactor Types,” 2005.

(26) Office for Nuclear Regulation, “Sellafield Programme: ONR review of the FGMSP LTPR submission,” 2016.

(27) Sellafield LTD, “Sellafield Magazine: issue 4. This information is licensed under the Open Government Licence v3.0. To view this licence, visit http://www.nationalarchives.gov.uk/doc/open-government-licence/,” 2016.

(28) R. Burrows, S. Harris, and N. P. C. Stevens, “Corrosion electrochemistry of fuel element materials in pond storage conditions,” *Chem. Eng. Res. Des.*, vol. 83, no. 7 A, pp. 887–892, 2005.

(29) Sellafield LTD, “Sellafield Integrated Waste Strategy (Version 2 Report and Recommendations),” 2007.

(30) PoyryEnergyLimited and AmecFosterWheeler, “2016 UK Radioactive Waste and Materials Inventory: UK Radioactive Waste Inventory Report,” 2017.

(31) G. R. Bochkarev and G. I. Pushkareva, “Stronitum Removal from Aqueous Media by Natural and Modified Sorbents,” *J. Min. Sci.*, vol. 45, no. 3, pp. 104–109, 2009.

(32) S. F. Jackson, S. D. Monk, and Z. Riaz, “An investigation towards real time dose rate monitoring, and fuel rod detection in a First Generation Magnox Storage Pond (FGMSP),” *Appl. Radiat. Isot.*, vol. 94, pp. 254–259, 2014.

(33) NNL, *UK National Nuclear Laboratory, The FGMSP Feed Envelope*, vol. Issue 3. p. NNL (08) 9212.

(34) C. R. Gregson, D. T. Goddard, M. J. Sarsfield, and R. J. Taylor, “Combined electron microscopy and vibrational spectroscopy study of corroded Magnox sludge from a legacy spent nuclear fuel storage pond,” *J. Nucl. Mater.*, vol. 412, no. 1, pp. 145–156, 2011.

(35) J. D. Farr, M. P. Neu, R. K. Schulze, and B. D. Honeyman, “Plutonium uptake by brucite and hydroxylated periclase,” *J. Alloys Compd.*, vol. 444–445, pp. 533–539, Oct. 2007.

(36) S. A. Parry, L. O'Brien, A. S. Fellerman, C. J. Eaves, N. B. Milestone, N. D. Bryan, and F. R. Livens, "Plutonium behaviour in nuclear fuel storage pond effluents," *Energy Environ. Sci.*, vol. 4, no. 4, p. 1457, 2011.

(37) S. Wallace, S. Shaw, K. Morris, and J. Small, "Effect of groundwater pH and ionic strength on strontium sorption in aquifer sediments: Implications for ^{90}Sr mobility at contaminated nuclear sites," *Appl. Geochemistry*, pp. 1–17, 2012.

(38) R. G. Denning, "Electronic structure and bonding in actinyl ions and their analogs," *J. Phys. Chem. A*, vol. 111, no. 20, pp. 4125–4143, 2007.

(39) M. Atkins and F. P. Glasser, "Application of portland cement-based materials to radioactive waste immobilization," *Waste Manag.*, vol. 12, no. 2–3, pp. 105–131, 1992.

(40) M. Chino, H. Nakayama, H. Nagai, H. Terada, G. Katata, and H. Yamazawa, "Preliminary estimation of release amounts of ^{131}I and ^{137}Cs accidentally discharged from the Fukushima Daiichi nuclear power plant into the atmosphere," *J. Nucl. Sci. Technol.*, vol. 48, no. 7, pp. 1129–1134, 2011.

(41) N. Kinoshita, K. Sueki, K. Sasa, J. -i. Kitagawa, S. Ikarashi, T. Nishimura, Y.-S. Wong, Y. Satou, K. Handa, T. Takahashi, M. Sato, and T. Yamagata, "Assessment of individual radionuclide distributions from the Fukushima nuclear accident covering central-east Japan," *Proc. Natl. Acad. Sci.*, vol. 108, no. 49, pp. 19526–19529, 2011.

(42) Sellafield Ltd, "Groundwater monitoring at Sellafield: Annual Data review 2016," 2016.

(43) J. Gray, S. R. Jones, and A. D. Smith, "Related content Discharges to the environment from the Sellafield site , 1951-1992 Discharges to the environment from the Sellafield Site," *J. Radiol. Prot.*, vol. 15, no. 2, pp. 99–131, 1995.

(44) R. A. Zielinski, D. T. Chafin, E. R. Banta, and B. J. Szabo, "Use of ^{234}U and ^{238}U isotopes to evaluate contamination of near-surface groundwater with uranium-mill effluent: A case study in south-central Colorado, U.S.A.," *Environ. Geol.*, vol. 32, no. 2, pp. 124–136, 1997.

(45) S. H. Wallace, S. Shaw, K. Morris, J. S. Small, A. J. Fuller, and I. T. Burke, "Effect of groundwater pH and ionic strength on strontium sorption in aquifer sediments: Implications for ^{90}Sr mobility at contaminated nuclear sites," *Appl. Geochemistry*, vol. 27, no. 8, pp. 1482–1491, 2012.

(46) D. Di Tommaso and N. H. de Leeuw, "First Principles Simulations of the Structural and Dynamical Properties of Hydrated Metal Ions Me^{2+} and Solvated Metal Carbonates (Me = Ca, Mg, and Sr)," *Cryst. Growth Des.*, vol. 10, no. 10, pp. 4292–4302, Oct. 2010.

(47) T. M. Nakanishi, "Agricultural aspects of radiocontamination induced by the Fukushima nuclear accident — A survey of studies by the Univ. of Tokyo Agricultural Dept. (2011–2016)," *Proc. Japan Acad. Ser. B*, vol. 94, no. 1, pp. 20–34, 2018.

(48) F. Cadini, E. Tosoni, and E. Zio, "Modeling the release and transport of 90Sr radionuclides from a superficial nuclear storage facility," *Stoch. Environ. Res. Risk Assess.*, vol. 30, no. 2, pp. 693–712, 2016.

(49) N. E. Pingitore, F. W. Lytle, B. M. Davies, M. P. Eastman, P. G. Eller, and E. M. Larson, "Mode of incorporation of Sr^{2+} in calcite: Determination by X-ray absorption spectroscopy," *Geochim. Cosmochim. Acta*, vol. 56, no. 4, pp. 1531–1538, Apr. 1992.

(50) L. A. Warren, P. A. Maurice, N. Parmar, and F. G. Ferris, "Microbially mediated calcium

carbonate precipitation: Implications for Interpreting calcite precipitation and for solid-phase capture of inorganic contaminants," *Geomicrobiol. J.*, vol. 18, no. 1, pp. 93–115, 2001.

(51) D. Delacroix, J. P. Guerre, P. Leblanc, and C. Hickman, "Radionuclide and radiation protection data handbook 2nd edition (2002).," *Radiat. Prot. Dosimetry*, vol. 98, no. 1, pp. 9–168, 2002.

(52) E. Schrödinger, "Quantisierung als Eigenwertproblem," *Ann. Phys.*, vol. 384, no. 6, pp. 489–527, 1926.

(53) G. R. Fowles, "Solution of the Schrödinger Equation for the Hydrogen Atom in Rectangular Coordinates," *Am. J. Phys.*, vol. 30, no. 4, p. 308, 1962.

(54) M. Born and R. Oppenheimer, "Zur Quantentheorie der Molekeln," *Ann. Phys.*, vol. 389, no. 20, pp. 457–484, Jan. 1927.

(55) E. Lewars, *Computational Chemistry Introduction to the Theory and Applications of Molecular and Quantum Mechanics*. 2004.

(56) J. C. Slater, "Atomic Shielding Constants," *Phys. Rev.*, vol. 36, no. 1, pp. 57–64, Jul. 1930.

(57) Boys S.F., "A General Method of Calculation for the Stationary States of Any Molecular System," *Proc. R. Soc. Lond. A*, vol. 200, pp. 542–554, 1950.

(58) C. J. Cramer, *Essentials of Computational Chemistry Theories and Models*, vol. 42, no. 2. 2004.

(59) P. E. Blöchl, "Electrostatic decoupling of periodic images of plane-wave-expanded densities and derived atomic point charges," *J. Chem. Phys.*, vol. 103, no. 17, pp. 7422–7428, 1995.

(60) F. Jensen, *Introduction to Computational Chemistry Computational Chemistry*. 2007.

(61) P. Pyykkö, "Relativistic Effects in Chemistry: More Common Than You Thought," *Annu. Rev. Phys. Chem.*, vol. 63, no. 1, pp. 45–64, May 2012.

(62) P. Pyykkö, "Relativistic effects in structural chemistry," *Chem. Rev.*, vol. 88, pp. 563–594, 1988.

(63) S. Goedecker, M. Teter, and J. Hutter, "Separable dual-space Gaussian pseudopotentials," *Phys. Rev. B*, vol. 54, no. 3, pp. 1703–1710, Jul. 1996.

(64) D. R. Hartree, "The Wave Mechanics of an Atom with a non-Coulomb Central Field. Part III. Term Values and Intensities in Series in Optical Spectra," *Math. Proc. Cambridge Philos. Soc.*, vol. 24, no. 03, p. 426, Jul. 1928.

(65) L. Pauling, "The application of the quantum mechanics to the structure of the hydrogen molecule and hydrogen molecule-ion and to related problems," *Chem. Rev.*, vol. 5, no. 2, pp. 173–213, 1928.

(66) J. C. Slater, "The theory of complex spectra," *Phys. Rev.*, vol. 34, no. 10, pp. 1293–1322, 1929.

(67) V. Fock, "Näherungsmethode zur Losung des quantenmechanischen Mehrkorperproblems," *Zeitschrift fur Phys.*, vol. 61, no. 1–2, pp. 126–148, 1930.

(68) J. Kohanoff, *Electronic Structure Calculations for Solids and Molecules*, 1st ed. Cambridge University Press, 2006.

(69) L. H. Thomas, “The calculation of atomic fields,” *Math. Proc. Cambridge Philos. Soc.*, vol. 23, no. 05, p. 542, Jan. 1927.

(70) E. Fermi, “Un Metodo Statistico per la Determinazione di alcune Prioprietà dell’Atomo,” *Rend. Accad. Naz. Lincei*, vol. 6, pp. 602–607, 1927.

(71) W. Koch and M. C. Holthausen, *A Chemist’s Guide to Density Functional Theory*, vol. 3. 2001.

(72) P. Hohenberg and W. Kohn, “Inhomogeneous electron gas,” *Phys. Rev.*, vol. 155, no. 1962, 1964.

(73) W. Kohn and L. Sham, “Self-consistent equations including exchange and correlation effects,” *Phys. Rev.*, 1965.

(74) J. P. Perdew and K. Schmidt, “Jacob’s ladder of density functional approximations for the exchange-correlation energy,” in *AIP Conference Proceedings*, 2001, vol. 577, pp. 1–20.

(75) J. P. Perdew and Y. Wang, “Accurate and simple analytic representation of the electron-gas correlation energy,” *Phys. Rev. B*, vol. 45, no. 23, pp. 13244–13249, 1992.

(76) J. Perdew, K. Burke, and M. Ernzerhof, “Generalized Gradient Approximation Made Simple.,” *Phys. Rev. Lett.*, vol. 77, no. 18, pp. 3865–3868, Oct. 1996.

(77) A. D. Becke, “Density-functional exchang-energy approximation with correct asymptotic behavior,” *Phys. Rev. A*, vol. 38, no. 6, pp. 3098–3100, 1988.

(78) J. Tao, J. Perdew, V. Staroverov, and G. Scuseria, “Climbing the Density Functional Ladder: Nonempirical Meta–Generalized Gradient Approximation Designed for Molecules and Solids,” *Phys. Rev. Lett.*, vol. 91, no. 14, p. 146401, Sep. 2003.

(79) J. Perdew, K. Burke, and Y. Wang, “Generalized gradient approximation for the exchange-correlation hole of a many-electron system,” *Phys. Rev. B*, vol. 54, no. 23, pp. 533–539, 1996.

(80) J. P. Perdew, M. Ernzerhof, and K. Burke, “Rationale for mixing exact exchange with density functional approximations,” *J. Chem. Phys.*, vol. 105, no. 22, p. 9982, 1996.

(81) A. D. Becke, “A new mixing of Hartree–Fock and local density-functional theories,” *J. Chem. Phys.*, vol. 98, no. 2, pp. 1372–1377, 1993.

(82) C. Lee, W. Yang, and R. G. Parr, “Development of the Colle- Salvetti correlation energy formula into a functional of the electron density,” *Phys Rev B*, vol. 37, no. 2, pp. 785–789, 1988.

(83) B. Dorado, B. Amadon, M. Freyss, and M. Bertolus, “DFT+U calculations of the ground state and metastable states of uranium dioxide,” *Phys. Rev. B*, vol. 79, no. 23, p. 235125, Jun. 2009.

(84) V. I. Anisimov, J. Zaanen, and O. K. Andersen, “Band theory and Mott insulators: Hubbard U instead of Stoner I,” *Phys. Rev. B*, vol. 44, no. 3, pp. 943–954, 1991.

(85) O. Gunnarsson, O. K. Andersen, O. Jepsen, and J. Zaanen, “Density-functional calculation of the parameters in the Anderson model: Application to Mn in CdTe,” *Phys. Rev. B*, vol. 39, no. 3, pp. 1708–1722, 1989.

(86) V. I. Anisimov and O. Gunnarsson, “Density-functional calculation of effective Coulomb interactions in metals,” *Phys. Rev. B*, vol. 43, no. 10, pp. 7570–7574, 1991.

(87) S. L. Dudarev, D. N. Manh, and A. P. Sutton, “Effect of Mott-Hubbard correlations on the electronic structure and structural stability of uranium dioxide,” *Philos. Mag. Part B*, vol. 75, no. 5, pp. 613–628, 1997.

(88) A. I. Liechtenstein, V. I. Anisimov, and J. Zaanen, “Density-functional theory and strong interactions: Orbital ordering in Mott-Hubbard insulators,” *Phys. Rev. B*, vol. 52, no. 8, pp. R5467–R5470, Aug. 1995.

(89) J. P. W. Wellington, A. Kerridge, J. Austin, and N. Kaltsoyannis, “Electronic structure of bulk AnO_2 (An = U, Np, Pu) and water adsorption on the (111) and (110) surfaces of UO_2 and PuO_2 from hybrid density functional theory within the periodic electrostatic embedded cluster method,” *J. Nucl. Mater.*, vol. 482, pp. 124–134, 2016.

(90) M. Capdevila-Cortada, Z. Łodziana, and N. López, “Performance of DFT+U approaches in the study of catalytic materials,” *ACS Catal.*, vol. 6, no. 12, pp. 8370–8379, 2016.

(91) S. Grimme, “Density functional theory with London dispersion corrections,” *Wiley Interdiscip. Rev. Comput. Mol. Sci.*, vol. 1, no. 2, pp. 211–228, 2011.

(92) S. Grimme, “Semiempirical GGA-type density functional constructed with a long-range dispersion correction,” *J. Comput. Chem.*, vol. 27, no. 15, pp. 1787–1799, Nov. 2006.

(93) S. Grimme, J. Antony, S. Ehrlich, and H. Krieg, “A consistent and accurate ab initio parametrization of density functional dispersion correction (DFT-D) for the 94 elements H-Pu.,” *J. Chem. Phys.*, vol. 132, no. 15, p. 154104, Apr. 2010.

(94) J. Vandevondele, M. Krack, F. Mohamed, M. Parrinello, T. Chassaing, and J. Hutter, “Quickstep: Fast and accurate density functional calculations using a mixed Gaussian and plane waves approach,” *Comput. Phys. Commun.*, vol. 167, no. 2, pp. 103–128, Apr. 2005.

(95) G. Lippert, J. Hutter, M. Parrinello, B. G. Lippert, J. H. and M. Parrinello, G. Lippert, J. Hutter, and M. Parrinello, “A hybrid Gaussian and plane wave density functional scheme,” *Mol. Phys.*, vol. 92, no. 3, pp. 477–488, Oct. 1997.

(96) J. Hutter, M. Parrinello, and G. Lippert, “The Gaussian and augmented-plane-wave density functional method for ab initio molecular dynamics simulations,” *Theor. Chem. Acc.*, vol. 103, pp. 124–140, 1999.

(97) D. Marx and J. Hutter, *Ab initio molecular dynamics: Theory and implementation*, vol. 1. 2000.

(98) R. Petrenko and J. Meller, “Molecular Dynamics,” *Encycl. Life Sci.*, May 2010.

(99) V. Brazdova and D. R. Bowler, *Atomistic Computer Simulations*, 1st editio. Wiley-VCH, 2013.

(100) M. Praprotnik and D. Janežič, “Molecular dynamics integration and molecular vibrational theory. III. the infrared spectrum of water,” *J. Chem. Phys.*, vol. 122, no. 17, pp. 1–10, 2005.

(101) L. Verlet, “Computer ‘Experiments’ on Classical Fluids. I. Thermodynamical Properties of Lennard-Jones Molecules,” *Phys. Rev.*, vol. 159, no. 1, pp. 98–103, Jul. 1967.

(102) W. C. Swope, “A computer simulation method for the calculation of equilibrium constants for the formation of physical clusters of molecules: Application to small water clusters,” *J. Chem. Phys.*, vol. 76, no. 1, p. 637, 1982.

(103) D. Young, *Computational chemistry: a practical guide for applying techniques to real world problems*. 2004.

(104) J. E. Jones, "On the Determination of Molecular Fields. II. From the Equation of State of a Gas," *Proc. R. Soc. London A Math. Phys. Eng. Sci.*, vol. 106, no. 738, pp. 463–477, Oct. 1924.

(105) S. Nosé, "A molecular dynamics method for simulations in the canonical ensemble," *Mol. Phys.*, vol. 52, no. 2, pp. 255–268, Jun. 1984.

(106) W. Hoover, "Canonical Dynamics:equilibrium phase-space distributions," *Phys. Rev. A*, vol. 31, pp. 1695–97, 1985.

(107) F. R. Mohamed, "Advanced Methods in Ab-Initio Molecular Dynamics," *Physiol. Res.*, vol. 59 Suppl 1, no. 16893, 2006.

(108) A. R. Leach, *Molecular Modelling Principles and Applications*, 2nd editio. Prentice Hall, 2001.

(109) X. He, Y. Zhu, A. Epstein, and Y. Mo, "Statistical variances of diffusional properties from ab initio molecular dynamics simulations," *npj Comput. Mater.*, vol. 4, no. 1, 2018.

(110) A. A. Hassanali, J. Cuny, V. Verdolino, and M. Parrinello, "Aqueous solutions: state of the art in *ab initio* molecular dynamics," *Philos. Trans. R. Soc. A Math. Phys. Eng. Sci.*, vol. 372, no. 2011, pp. 20120482–20120482, 2014.

(111) J. M. Herbert and M. Head-Gordon, "Accelerated, energy-conserving Born-Oppenheimer molecular dynamics via Fock matrix extrapolation," *Phys. Chem. Chem. Phys.*, vol. 7, no. 18, pp. 3269–3275, 2005.

(112) B. Kirchner, P. J. di Dio, and J. Hutter, "Real-World Predictions from Ab Initio Molecular Dynamics Simulations," pp. 109–153, 2011.

(113) M. Allen, "Introduction to molecular dynamics simulation," *Comput. Soft Matter From Synth. Polym. to …*, vol. 23, no. 2, pp. 1–28, 2004.

(114) R. Car and M. Parrinello, "Unified Approach for Molecular Dynamics and Density-Functional Theory," *Phys. Rev. Lett.*, vol. 55, no. 22, pp. 2471–2474, Nov. 1985.

(115) J. Hutter, M. Iannuzzi, F. Schiffmann, and J. VandeVondele, "cp2k: atomistic simulations of condensed matter systems," *Wiley Interdiscip. Rev. Comput. Mol. Sci.*, vol. 4, no. 1, pp. 15–25, Jan. 2014.

(116) M. Krack and M. Parrinello, "All-electron ab-initio molecular dynamics," *Phys. Chem. Chem. Phys.*, vol. 2, no. 10, pp. 2105–2112, 2000.

(117) J. VandeVondele, F. Mohamed, M. Krack, J. Hutter, M. Sprik, and M. Parrinello, "The influence of temperature and density functional models in ab initio molecular dynamics simulation of liquid water.," *J. Chem. Phys.*, vol. 122, no. 1, p. 14515, 2005.

(118) W. Humphrey, A. Dalke, and K. Schulten, "VMD: Visual molecular dynamics," *J. Mol. Graph.*, vol. 14, no. 1, pp. 33–38, Feb. 1996.

(119) The MathWorks Inc., *MATLAB and statistics toolbox, Release 2010b [computer software]*. 2010.

(120) R. Dennington, T. A. Keith, and J. M. Millam, "GaussView, Version 6,." Semichem Inc., Shawnee Mission, KS, 2016.

(121) J. Cowan, “Structural and catalytic chemistry of magnesium dependent enzymes,” *Biometals*, vol. 15, pp. 225–235, 2002.

(122) J. J. R. F. da. Silva and R. J. P. (Robert J. P. Williams, *The biological chemistry of the elements : the inorganic chemistry of life*. Oxford University Press, 2001.

(123) E. Bellion, “The Biological Chemistry of the Elements: The Inorganic Chemistry of Life (da Silva, J. J. R. Frausto; Williams, R. J. P.),” *J. Chem. Educ.*, vol. 69, no. 12, p. A326, Dec. 1992.

(124) G. Pálinkás and T. Radnai, “Hydration Shell Structures in an $MgCl_2$ Solution from X-Ray and MD Studies,” *Zeitschrift für Naturforsch. A*, vol. 37, no. 9, pp. 1049–1060, Jan. 1982.

(125) P. R. Smirnov and V. N. Trostin, “Structural parameters of hydration of Be^{2+} and Mg^{2+} ions in aqueous solutions of their salts,” *Russ. J. Gen. Chem.*, vol. 78, no. 9, pp. 1643–1649, Sep. 2008.

(126) F. Bruni, S. Imberti, R. Mancinelli, and M. A. Ricci, “Aqueous solutions of divalent chlorides: Ions hydration shell and water structure,” *J. Chem. Phys.*, vol. 136, no. 6, p. 064520, Feb. 2012.

(127) K. M. Callahan, N. N. Casillas-Ituarte, M. Roeselová, H. C. Allen, and D. J. Tobias, “Solvation of magnesium dication: molecular dynamics simulation and vibrational spectroscopic study of magnesium chloride in aqueous solutions.,” *J. Phys. Chem. A*, vol. 114, no. 15, pp. 5141–5148, 2010.

(128) M. A. Marques, M. I. Cabaco, M. I. de B. Marques, and A. M. Gaspar, “Intermediate-range order in aqueous solutions of salts constituted of divalent ions combined with monovalent counter-ions,” *J. Phys. Condens. Matter*, vol. 14, no. 32, p. 303, Aug. 2002.

(129) C. W. Bock, G. D. Markham, A. K. Katz, and J. P. Glusker, “The Arrangement of First- and Second-shell Water Molecules Around Metal Ions: Effects of Charge and Size,” *Theor. Chem. Acc.*, vol. 115, no. 2–3, pp. 100–112, 2006.

(130) C. W. Bock, A. Kaufman, and J. P. Glusker, “Coordination of Water to Magnesium Cations,” *Inorg. Chem.*, vol. 33, no. 3, pp. 419–427, 1994.

(131) J. P. Larentzos and L. J. Criscenti, “A Molecular Dynamics Study of Alkaline Earth Metal−Chloride Complexation in Aqueous Solution,” *J. Phys. Chem. B*, vol. 112, no. 45, pp. 14243–14250, Nov. 2008.

(132) T. Ikeda, M. Boero, and K. Terakura, “Hydration properties of magnesium and calcium ions from constrained first principles molecular dynamics,” *J. Chem. Phys.*, vol. 127, no. 7, p. 074503, Aug. 2007.

(133) L. Bernasconi, E. J. Baerends, and M. Sprik, “Long-range solvent effects on the orbital interaction mechanism of water acidity enhancement in metal ion solutions: A comparative study of the electronic structure of aqueous Mg and Zn dications,” *J. Phys. Chem. B*, vol. 110, no. 23, pp. 11444–11453, 2006.

(134) F. C. Lightstone, E. Schwegler, R. Q. Hood, F. Gygi, and G. Galli, “A first principles molecular dynamics simulation of the hydrated magnesium ion,” *Chem. Phys. Lett.*, vol. 343, no. 5–6, pp. 549–555, Aug. 2001.

(135) M. Pavlov, P. E. M. Siegbahn, and M. Sandström, “Hydration of Beryllium, Magnesium, Calcium, and Zinc Ions Using Density Functional Theory,” *J. Phys. Chem. A*, vol. 102, no. 1, pp. 219–228, Jan. 1998.

(136) J. N. Albright, “X-Ray Diffraction Studies of Aqueous Alkaline-Earth Chloride Solutions,” *J. Chem. Phys.*, vol. 56, no. 8, pp. 3783–3786, Apr. 1972.

(137) R. Caminiti, G. Licheri, G. Piccaluga, and G. Pinna, “X-ray diffraction study of $MgCl_2$ aqueous solutions,” *J. Appl. Crystallogr.*, vol. 12, no. 1, pp. 34–38, 1979.

(138) W. Bol, G. J. a. Gerrits, and C. L. van Panthaleon Eck, “The hydration of divalent cations in aqueous solution. An X-ray investigation with isomorphous replacement,” *J. Appl. Crystallogr.*, vol. 3, no. 6, pp. 486–492, 1970.

(139) E. Spohr, G. Palinkas, K. Heinzinger, P. Bopp, and M. . Probst, “Molecular Dynamics Study of an Aqueous $SrCl_2$ Solution.,” *J.Phys. Chem*, vol. 92, no. 23, pp. 6754–6761, 1988.

(140) S. Obst and H. Bradaczek, “Molecular Dynamics Study of the Structure and Dynamics of the Hydration Shell of Alkaline and Alkaline-Earth Metal Cations,” *J. Phys. Chem.*, vol. 100, no. 39, pp. 15677–15687, Jan. 1996.

(141) T. Yamaguchi, S. I. Hayashi, and H. Ohtaki, “X-ray Diffraction Study of Calcium(II) Chloride Hydrate Melts: $CaCl_2$-RH_2O (R = 4.0. 5.6. 6.0. 8.6),” *Inorg. Chem.*, vol. 28, no. 12, pp. 2434–2439, 1989.

(142) G. Licheri, “X-ray diffraction study of the average solute species in $CaCl_2$ aqueous solutions,” *J. Chem. Phys.*, vol. 64, no. 6, p. 2437, 1976.

(143) S. Cummings, J. E. Enderby, and R. A. Howe, “Ion hydration in aqueous $CaCl_2$ solutions,” *J. Phys. C Solid State Phys.*, vol. 13, no. 1, pp. 1–8, Jan. 1980.

(144) V. I. Chizhik, A. V. Egorov, M. S. Pavlova, M. I. Egorova, and A. V. Donets, “Structure of hydration shell of calcium cation by NMR relaxation, Car-Parrinello molecular dynamics and quantum-chemical calculations,” *J. Mol. Liq.*, vol. 224, pp. 730–736, 2016.

(145) D. Spångberg, K. Hermansson, P. Lindqvist-Reis, F. Jalilehvand, M. Sandström, and I. Persson, “Model Extended X-ray Absorption Fine Structure (EXAFS) Spectra from Molecular Dynamics Data for Ca^{2+} and Al^{3+} Aqueous Solutions,” *J. Phys. Chem. B*, vol. 104, no. 45, pp. 10467–10472, 2000.

(146) L. X. Dang, G. K. Schenter, and J. L. Fulton, “EXAFS Spectra of the Dilute Solutions of Ca^{2+} and Sr^{2+} in Water and Methanol,” *J. Phys. Chem. B*, vol. 107, no. 50, pp. 14119–14123, Dec. 2003.

(147) A. K. Katz, J. P. Glusker, S. A. Beebe, and C. W. Bock, “Calcium Ion Coordination: A Comparison with That of Beryllium, Magnesium, and Zinc,” *J. Am. Chem. Soc.*, vol. 118, no. 24, pp. 5752–5763, Jan. 1996.

(148) M. Kohagen, P. E. Mason, and P. Jungwirth, “Accurate Description of Calcium Solvation in Concentrated Aqueous Solutions,” *J. Phys. Chem. B*, vol. 118, no. 28, pp. 7902–7909, Jul. 2014.

(149) S. Koneshan, J. C. Rasaiah, R. M. Lynden-Bell, and S. H. Lee, “Solvent Structure, Dynamics, and Ion Mobility in Aqueous Solutions at 25 °C,” *J. Phys. Chem. B*, vol. 102, no. 21, pp. 4193–4204, May 1998.

(150) T. Tofteberg, A. Öhrn, and G. Karlström, “Combined quantum chemical statistical mechanical simulations of Mg^{2+}, Ca^{2+} and Sr^{2+} in water,” *Chem. Phys. Lett.*, vol. 429, no. 4–6, pp. 436–439, Oct. 2006.

(151) M. M. Naor, K. Van Nostrand, and C. Dellago, “Car–Parrinello molecular dynamics

simulation of the calcium ion in liquid water," *Chem. Phys. Lett.*, vol. 369, no. 1–2, pp. 159–164, Feb. 2003.

(152) S. Bogatko, E. Cauët, E. Bylaska, G. Schenter, J. Fulton, and J. Weare, "The Aqueous Ca^{2+} System, in Comparison with Zn^{2+} , Fe^{3+}, and Al^{3+} : An Ab Initio Molecular Dynamics Study," *Chem. - A Eur. J.*, vol. 19, no. 9, pp. 3047–3060, Feb. 2013.

(153) A. Y. Mehandzhiyski, E. Riccardi, T. S. van Erp, T. T. Trinh, and B. A. Grimes, "Ab Initio Molecular Dynamics Study on the Interactions between Carboxylate Ions and Metal Ions in Water," *J. Phys. Chem. B*, vol. 119, no. 33, pp. 10710–10719, Aug. 2015.

(154) P. A. O'Day, M. Newville, P. S. Neuhoff, N. Sahai, and S. A. Carroll, "X-Ray Absorption Spectroscopy of Strontium(II) Coordination," *J. Colloid Interface Sci.*, vol. 222, no. 2, pp. 184–197, Feb. 2000.

(155) P. D'Angelo, H. F. Nolting, and N. V. Pavel, "Evidence for multielectron resonances at the Sr K edge," *Phys. Rev. A*, vol. 53, no. 2, pp. 798–805, Feb. 1996.

(156) L. Axe, G. B. Bunker, P. R. Anderson, and T. a Tyson, "An XAFS Analysis of Strontium at the Hydrous Ferric Oxide Surface," *J. Colloid Interface Sci.*, vol. 199, no. 1, pp. 44–52, Mar. 1998.

(157) D. M. Pfund, J. G. Darab, J. L. Fulton, and Y. Ma, "An XAFS Study of Strontium Ions and Krypton in Supercritical Water," *J. Phys. Chem.*, vol. 98, no. 50, pp. 13102–13107, 1994.

(158) I. Persson, M. Sandstrom, H. Yokoyama, and M. Chaudhry, "Structure of the Solvated Stronitum and Barium Ions in Aqueous, Dimethyl Sulfoxide and Pyridine Solution, and Crystal Structure of Strontium and Barium Hydroxide Octahydrate," *Z. Naturforsch*, vol. 50a, pp. 21–37, 1995.

(159) M. I. Cabaço, M. I. De Barros Marques, M. A. Marques, A. M. Gaspar, and M. L. De Almeida, "X-ray diffraction and Raman spectroscopy investigations in concentrated aqueous solutions of yttrium and strontium nitrates," *J. Mol. Liq.*, vol. 117, no. 1–3, pp. 69–76, 2005.

(160) S. Ramos, G. W. Neilson, A. C. Barnes, and M. J. Capitán, "Anomalous x-ray diffraction studies of $Sr^{[2+]}$ hydration in aqueous solution," *J. Chem. Phys.*, vol. 118, no. 12, p. 5542, 2003.

(161) G. W. Neilson and R. D. Broadbent, "The structure of Sr^{2+} in aqueous solution," *Chem. Phys. Lett.*, vol. 167, no. 5, pp. 429–431, Apr. 1990.

(162) A. Kerridge and N. Kaltsoyannis, "Quantum Chemical Studies of the Hydration of Sr^{2+} in Vacuum and Aqueous Solution," *Chem. - A Eur. J.*, vol. 17, no. 18, pp. 5060–5067, Apr. 2011.

(163) T. S. Hofer, B. R. Randolf, and B. M. Rode, "Sr(II) in water: A labile hydrate with a highly mobile structure," *J. Phys. Chem. B*, vol. 110, no. 41, pp. 20409–20417, 2006.

(164) D. J. Harris, J. P. Brodholt, and D. M. Sherman, "Hydration of Sr^{2+} in Hydrothermal Solutions from ab Initio Molecular Dynamics," *J. Phys. Chem. B*, vol. 107, no. 34, pp. 9056–9058, Aug. 2003.

(165) P. D'Angelo, V. Migliorati, F. Sessa, G. Mancini, and I. Persson, "XANES Reveals the Flexible Nature of Hydrated Strontium in Aqueous Solution," *J. Phys. Chem. B*, vol. 120, no. 17, pp. 4114–4124, May 2016.

(166) S. Grimme, "Accurate description of van der Waals complexes by density functional

theory including empirical corrections," *J. Comput. Chem.*, vol. 25, no. 12, pp. 1463–1473, 2004.

(167) J. VandeVondele and J. Hutter, "Gaussian basis sets for accurate calculations on molecular systems in gas and condensed phases.," *J. Chem. Phys.*, vol. 127, no. 11, p. 114105, Oct. 2007.

(168) J. C. Grossman, E. Schwegler, E. W. Draeger, F. Gygi, and G. Galli, "Towards an assessment of the accuracy of density functional theory for first principles simulations of water," *J. Chem. Phys.*, vol. 120, no. 1, pp. 300–11, 2004.

(169) M. V. Fernández-Serra and E. Artacho, "Network equilibration and first-principles liquid water," *J. Chem. Phys.*, vol. 121, no. 22, p. 11136, 2004.

(170) P. H.-L. Sit and N. Marzari, "Static and dynamical properties of heavy water at ambient conditions from first-principles molecular dynamics," *J. Chem. Phys.*, vol. 122, no. 20, p. 204510, May 2005.

(171) S. Yoo, X. C. Zeng, and S. S. Xantheas, "On the phase diagram of water with density functional theory potentials: The melting temperature of ice I_h with the Perdew–Burke–Ernzerhof and Becke–Lee–Yang–Parr functionals," *J. Chem. Phys.*, vol. 130, no. 22, p. 221102, 2009.

(172) S. Yoo and S. S. Xantheas, "Communication: The effect of dispersion corrections on the melting temperature of liquid water.," *J. Chem. Phys.*, vol. 134, no. 12, p. 121105, 2011.

(173) E. Schwegler, J. C. Grossman, F. Gygi, and G. Galli, "Towards an assessment of the accuracy of density functional theory for first principles simulations of water. II," *J. Chem. Phys.*, vol. 121, no. 11, pp. 5400–5409, Sep. 2004.

(174) R. A. DiStasio, B. Santra, Z. Li, X. Wu, and R. Car, "The individual and collective effects of exact exchange and dispersion interactions on the ab initio structure of liquid water," *J. Chem. Phys.*, vol. 141, no. 8, p. 084502, Aug. 2014.

(175) A. K. Soper, "The Radial Distribution Functions of Water as Derived from Radiation Total Scattering Experiments: Is There Anything We Can Say for Sure?," *ISNR Phys. Chem.*, vol. 2013, p. 1, 2013.

(176) I. Persson, H. Yokoyama, M. Chaudhry, and M. Sandström, "Structure of the Solvated Strontium and Barium Ions in Aqueous, Dimethyl Sulfoxide and Pyridine Solution, and Crystal Structure of Strontium and Barium Hydroxide Octahydrate," *Zeitschrift fur Naturforsch. - Sect. A J. Phys. Sci.*, vol. 50, no. 1, pp. 21–37, Jan. 1995.

(177) T. S. Hofer, H. T. Tran, C. F. Schwenk, and B. M. Rode, "Characterization of dynamics and reactivities of solvated ions by ab initio simulations.," *J. Comput. Chem.*, vol. 25, no. 2, pp. 211–7, 2004.

(178) A. Hassanali, F. Giberti, J. Cuny, T. D. Kühne, and M. Parrinello, "Proton transfer through the water gossamer," *Proc. Natl. Acad. Sci.*, vol. 110, no. 34, pp. 13723–13728, Aug. 2013.

(179) C. A. Wraight, "Chance and design-Proton transfer in water, channels and bioenergetic proteins," *Biochim. Biophys. Acta - Bioenerg.*, vol. 1757, no. 8, pp. 886–912, 2006.

(180) E. Codorniu-Hernández and P. G. Kusalik, "Probing the mechanisms of proton transfer in liquid water," *Proc. Natl. Acad. Sci.*, vol. 110, no. 34, pp. 13697–13698, Aug. 2013.

(181) G. D. Markham, J. P. Glusker, and C. W. Bock, "The Arrangement of First- and Second-

Sphere Water Molecules in Divalent Magnesium Complexes: Results from Molecular Orbital and Density Functional Theory and from Structural Crystallography," *J. Phys. Chem. B*, vol. 106, no. 19, pp. 5118–5134, May 2002.

(182) S. Kluge and J. Weston, "Can a hydroxide ligand trigger a change in the coordination number of magnesium ions in biological systems?," *Biochemistry*, vol. 44, no. 12, pp. 4877–4885, 2005.

(183) A. R. Felmy, D. A. Dixon, J. R. Rustad, M. J. Mason, and L. M. Onishi, "The hydrolysis and carbonate complexation of strontium and calcium in aqueous solution. Use of molecular modeling calculations in the development of aqueous thermodynamic models," *J. Chem. Thermodyn.*, vol. 30, no. 9, pp. 1103–1120, 1998.

(184) H. G. Smith, "The crystal structure of strontium hydroxide octahydrate, $Sr(OH)_2.8H_2O$," *Acta Crystallogr.*, vol. 6, no. 7, pp. 604–609, Jul. 1953.

(185) J. S. Ricci, R. C. Stevens, R. K. McMullan, and W. T. Klooster, "Structure of strontium hydroxide octahydrate, $Sr(OH)_2{\cdot}8H_2O$, at 20, 100 and 200 K from neutron diffraction," *Acta Crystallogr. Sect. B Struct. Sci.*, vol. 61, no. 4, pp. 381–386, 2005.

(186) A. Kerridge and N. Kaltsoyannis, "The coordination of Sr^{2+} by hydroxide: a density functional theoretical study," *Dalt. Trans.*, vol. 40, no. 42, p. 11258, Nov. 2011.

(187) E. Makkos, A. Kerridge, and N. Kaltsoyannis, "The importance of second shell effects in the simulation of hydrated Sr^{2+} hydroxide complexes," *Dalt. Trans.*, vol. 44, no. 25, pp. 11572–11581, 2015.

(188) R. S. Mulliken, "Electronic population analysis on LCAO-MO molecular wave functions. I," *J. Chem. Phys.*, vol. 23, no. 10, pp. 1833–1840, 1955.

(189) N. Agmon, "The Grotthuss mechanism," *Chem. Phys. Lett.*, vol. 244, no. 5–6, pp. 456–462, 1995.

(190) D. Marx, "Proton Transfer 200 Years after von Grotthuss: Insights from Ab Initio Simulations," *ChemPhysChem*, vol. 7, no. 9, pp. 1848–1870, Sep. 2006.

(191) H.-S. H. Lee and M. E. M. Tuckerman, "The structure and proton transport mechanisms in the superprotonic phase of CsH_2PO_4: An ab initio molecular dynamics study," *J. Phys. Chem. C*, vol. 112, pp. 9917–9930, 2008.

(192) K. D. Kreuer, "On the complexity of proton conduction phenomena," *Solid State Ionics*, vol. 136–137, pp. 149–160, 2000.

(193) M. Tuckerman, K. Laasonen, M. Sprik, and M. Parrinello, "Ab Initio Molecular Dynamics Simulation of the Solvation and Transport of H_3O^+ and OH^- Ions in Water," *J. Phys. Chem.*, vol. 99, no. 16, pp. 5749–5752, 1995.

(194) P. L. Geissler, C. Dellago, D. Chandler, J. Hutter, and M. Parinello, "Autoionization in Liquid Water," *Sci. Mag*, vol. 291, no. 5511, pp. 2121–2124, Mar. 2001.

(195) G. Tocci and A. Michaelides, "Solvent-Induced Proton Hopping at a Water−Oxide Interface," *J. Phys. Chem. C*, vol. 5, p. 474, 2014.

(196) M. Hellström and J. Behler, "Concentration-Dependent Proton Transfer Mechanisms in Aqueous NaOH Solutions: From Acceptor-Driven to Donor-Driven and Back," *J. Phys. Chem. Lett.*, vol. 7, no. 17, pp. 3302–3306, Sep. 2016.

(197) E. L. Mühr-Ebert, F. Wagner, and C. Walther, "Speciation of uranium: Compilation of a

thermodynamic database and its experimental evaluation using different analytical techniques," *Appl. Geochemistry*, 2019.

(198) C. A. Krestou and D. Panias, "Uranium (VI) speciation diagrams in the UO_2^{2+} /CO_3^{2-} /H_2O system at 25," *Eur. J. Miner. Process. Environ. Prot.*, vol. 4, no. 2, pp. 1303–868, 2004.

(199) A. Martínez-Torrents, S. Meca, N. Baumann, V. Martí, J. Giménez, J. De Pablo, and I. Casas, "Uranium speciation studies at alkaline pH and in the presence of hydrogen peroxide using time-resolved laser-induced fluorescence spectroscopy," *Polyhedron*, vol. 55, pp. 92–101, 2013.

(200) U. Wahlgren, H. Moll, I. Grenthe, B. Schimmelpfennig, L. Maron, V. Vallet, and O. Gropen, "Structure of Uranium(VI) in Strong Alkaline Solutions. A Combined Theoretical and Experimental Investigation," *J. Phys. Chem. A*, vol. 103, no. 41, pp. 8257–8264, 1999.

(201) C. Hennig, J. Tutschku, A. Rossberg, G. Bernhard, and A. C. Scheinost, "Comparative EXAFS investigation of uranium(VI) and -(IV) aquo chloro complexes in solution using a newly developed spectroelectrochemical cell," *Inorg. Chem.*, vol. 44, no. 19, pp. 6655–6661, 2005.

(202) L. Soderholm, S. Skanthakumar, and J. Neuefeind, "Determination of actinide speciation in solution using high-energy X-ray scattering," *Anal. Bioanal. Chem.*, vol. 383, no. 1, pp. 48–55, 2005.

(203) N. Bardin, P. Rubini, and C. Madie, "Hydration of Actinyl(VI), MO^{2+}_{2aq} (M = U, Np, Pu). An NMR Study," *Radiochim. Acta*, vol. 83, no. 4, pp. 189–194, Jan. 1998.

(204) M. A. Denecke, "Actinide speciation using X-ray absorption fine structure spectroscopy," *Coord. Chem. Rev.*, vol. 250, no. 7–8, pp. 730–754, 2006.

(205) J. Neuefeind, L. Soderholm, and S. Skanthakumar, "Experimental Coordination Environment of Uranyl(VI) in Aqueous Solution," *J. Phys. Chem. A*, vol. 108, no. 14, pp. 2733–2739, 2004.

(206) C. Den Auwer, D. Guillaumont, P. Guilbaud, S. D. Conradson, J. J. Rehr, A. Ankudinov, and E. Simoni, "Theoretical chemical contribution to the simulation of the LIII X-ray absorption edges of uranyl, neptunyl and osmyl hydrates and hydroxides," *New J. Chem.*, vol. 28, no. 8, p. 929, 2004.

(207) P. G. Allen, J. J. Bucher, D. K. Shuh, N. M. Edelstein, and T. Reich, "Investigation of Aquo and Chloro Complexes of UO_2^{2+} , NpO_2^{+} , Np^{4+} , and Pu^{3+} by X-ray Absorption Fine Structure Spectroscopy," *Inorg. Chem.*, vol. 36, no. 21, pp. 4676–4683, 1997.

(208) M. Aaberg, D. Ferri, J. Glaser, and I. Grenthe, "Structure of the hydrated dioxouranium(VI) ion in aqueous solution. An X-ray diffraction and proton NMR study," *Inorg. Chem.*, vol. 22, no. 26, pp. 3986–3989, 1983.

(209) C. Hennig, K. Schmeide, V. Brendler, H. Moll, S. Tsushima, and A. C. Scheinost, "EXAFS investigation of U(VI), U(IV), and Th(IV) sulfato complexes in aqueous solution," *Inorg. Chem.*, vol. 46, no. 15, pp. 5882–5892, 2007.

(210) N. W. Alcock and S. Esperås, "Crystal and molecular structure of uranyl diperchlorate heptahydrate," *J. Chem. Soc., Dalt. Trans.*, no. 9, pp. 893–896, 1977.

(211) B. Siboulet, C. J. Marsden, and P. Vitorge, "A theoretical study of uranyl solvation: Explicit modelling of the second hydration sphere by quantum mechanical methods,"

Chem. Phys., vol. 326, no. 2–3, pp. 289–296, 2006.

(212) K. E. Gutowski and D. A. Dixon, "Predicting the energy of the water exchange reaction and free energy of solvation for the uranyl ion in aqueous solution," *J. Phys. Chem. A*, vol. 110, no. 28, pp. 8840–8856, 2006.

(213) N. Kumar and J. M. Seminario, "Solvation of Actinide Salts in Water Using a Polarizable Continuum Model," *J. Phys. Chem. A*, vol. 119, no. 4, pp. 689–703, Jan. 2015.

(214) P. J. Hay, R. L. Martin, and G. Schreckenbach, "Theoretical studies of the properties and solution chemistry of AnO_2^{2+} and AnO^{2+} aquo complexes for An = U, Np, and Pu," *J. Phys. Chem. A*, vol. 104, no. 26, pp. 6259–6270, 2000.

(215) D. Hagberg, G. Karlstro, B. O. Roos, and L. Gagliardi, "The Coordination of Uranyl in Water : A Combined Quantum Chemical and Molecular Simulation Study," *J. Am. Chem. Soc.*, vol. 127, no. 6, pp. 14250–14256, 2005.

(216) C. Clavaguéra-Sarrio, V. Brenner, S. Hoyau, C. J. Marsden, P. Millié, and J. P. Dognon, "Modeling of uranyl cation-water clusters," *J. Phys. Chem. B*, vol. 107, no. 13, pp. 3051–3060, 2003.

(217) V. Vallet, U. Wahlgren, B. Schimmelpfennig, Z. Szabó, and I. Grenthe, "The Mechanism for Water Exchange in $[UO_2(H_2O)_5]^{2+}$ and $[UO_2(oxalate)^2(H_2O)]^{2-}$, as Studied by Quantum Chemical Methods," *J. Am. Chem. Soc.*, vol. 123, no. 48, pp. 11999–12008, 2001.

(218) H. P. Hratchian, J. L. Sonnenberg, P. J. Hay, R. L. Martin, B. E. Bursten, and H. B. Schlegel, "Theoretical investigation of uranyl dihydroxide: Oxo ligand exchange, water catalysis, and vibrational spectra," *J. Phys. Chem. A*, vol. 109, no. 38, pp. 8579–8586, 2005.

(219) M. Bühl, R. Diss, and G. Wipff, "Coordination Environment of Aqueous Uranyl(VI) Ion," *J. Am. Chem. Soc.*, vol. 127, no. 39, pp. 13506–13507, Oct. 2005.

(220) P. Nichols, E. J. Bylaska, G. K. Schenter, and W. de Jong, "Equatorial and apical solvent shells of the UO_2^{2+} ion," *J. Chem. Phys.*, vol. 128, no. 12, p. 124507, Mar. 2008.

(221) R. Atta-Fynn, D. F. Johnson, E. J. Bylaska, E. S. Ilton, G. K. Schenter, and W. A. de Jong, "Structure and Hydrolysis of the U(IV), U(V), and U(VI) Aqua Ions from Ab Initio Molecular Simulations," *Inorg. Chem.*, vol. 51, no. 5, pp. 3016–3024, Mar. 2012.

(222) S. P. Tiwari, N. Rai, and E. J. Maginn, "Dynamics of actinyl ions in water: a molecular dynamics simulation study," *Phys. Chem. Chem. Phys.*, vol. 16, no. 17, pp. 8060–8069, 2014.

(223) P. Guilbaud and G. Wipff, "Hydration of uranyl (UO_2^{2+}) cation and its nitrate ion and 18-crown-6 adducts studied by molecular dynamics simulations," *J. Phys. Chem.*, vol. 97, no. 21, pp. 5685–5692, 1993.

(224) S. Kerisit and C. Liu, "Structure, kinetics, and thermodynamics of the aqueous uranyl(VI) cation," *J. Phys. Chem. A*, vol. 117, no. 30, pp. 6421–6432, 2013.

(225) S. Kerisit and C. Liu, "Molecular simulation of the diffusion of uranyl carbonate species in aqueous solution," *Geochim. Cosmochim. Acta*, vol. 74, no. 17, pp. 4937–4952, 2010.

(226) N. Rodríguez-Jeangros and J. M. Seminario, "Density functional theory and molecular dynamics study of the uranyl ion $(UO_2)^{2+}$," *J. Mol. Model.*, vol. 20, no. 3, 2014.

(227) R. J. Frick, T. S. Hofer, A. B. Pribil, B. R. Randolf, and B. M. Rode, "Structure and dynamics

of the UO^{+2} ion in aqueous solution: an ab initio QMCF-MD study," *Phys. Chem. Chem. Phys.*, vol. 12, no. 37, p. 11736, Sep. 2010.

(228) D. L. Clark, S. D. Conradson, R. J. Donohoe, D. W. Keogh, D. E. Morris, P. D. Palmer, R. D. Rogers, and C. D. Tait, "Chemical Speciation of the Uranyl Ion under Highly Alkaline Conditions. Synthesis, Structures, and Oxo Ligand Exchange Dynamics," *Inorg. Chem.*, vol. 38, no. 7, pp. 1456–1466, 1999.

(229) H. Moll, T. Reich, and Z. Szabó, "The hydrolysis of dioxouranium(VI) investigated using EXAFS and ^{17O}-NMR," *Radiochim. Acta*, vol. 88, no. 7, p. 411, Jan. 2000.

(230) G. Schreckenbach, P. J. Hay, and R. L. Martin, "Density functional calculations on actinide compounds: Survey of recent progress and application to $[UO_2X_4]^{2?}$ (X=F, Cl, OH) and AnF_6 (An=U, Np, Pu)," *J. Comput. Chem.*, vol. 20, no. 1, pp. 70–90, 1999.

(231) G. Schreckenbach, P. J. Hay, and R. L. Martin, "Theoretical Study of Stable Trans and Cis Isomers in $[UO_2(OH)_4]^{2-}$ Using Relativistic Density Functional Theory," *Inorg. Chem.*, vol. 37, no. 17, pp. 4442–4451, 1998.

(232) J. L. Sonnenberg, P. J. Hay, R. L. Martin, and B. E. Bursten, "Theoretical investigations of uranyl-ligand bonding: Four- and five-coordinate uranyl cyanide, isocyanide, carbonyl, and hydroxide complexes," *Inorg. Chem.*, vol. 44, no. 7, pp. 2255–2262, 2005.

(233) M. García-Hernández, C. Willnauer, S. Krüger, L. V. Moskaleva, and N. Rösch, "Systematic DFT Study of Gas Phase and Solvated Uranyl and Neptunyl Complexes $[AnO_2$ X 4] n (An = U, Np; X = F, Cl, OH, n = −2; X = H_2O, n = +2)," *Inorg. Chem.*, vol. 45, no. 3, pp. 1356–1366, Feb. 2006.

(234) K. I. M. Ingram, L. J. L. Häller, and N. Kaltsoyannis, "Density functional theory investigation of the geometric and electronic structures of $[UO_2(H_2O)_m(OH)_n]^{(2-n)}$ (n + m = 5) ," *Dalton Trans.*, vol. 2, pp. 2403–2414, 2006.

(235) G. A. Shamov and G. Schreckenbach, "Theoretical Study of the Oxygen Exchange in Uranyl Hydroxide. An Old Riddle Solved?," *J. Am. Chem. Soc.*, vol. 130, no. 41, pp. 13735–13744, Oct. 2008.

(236) J. P. Austin, M. Sundararajan, M. A. Vincent, and I. H. Hillier, "The geometric structures, vibrational frequencies and redox properties of the actinyl coordination complexes ($[AnO_2(L)n]m$; An = U, Pu, Np; L = H_2O, Cl^-, CO_3^{2-}, $CH_3CO_2^-$, OH^-) in aqueous solution, studied by density functional theory methods," *Dalt. Trans.*, no. 30, p. 5902, 2009.

(237) V. Vallet, U. Wahlgren, B. Schimmelpfennig, H. Moll, Z. Szabó, and I. Grenthe, "Solvent Effects on Uranium(VI) Fluoride and Hydroxide Complexes Studied by EXAFS and Quantum Chemistry," *Inorg. Chem.*, vol. 40, no. 14, pp. 3516–3525, Jul. 2001.

(238) S. Tsushima and T. Reich, "A theoretical study of uranyl hydroxide monomeric and dimeric complexes," *Chem. Phys. Lett.*, vol. 347, no. 1–3, pp. 127–132, 2001.

(239) Z. Cao and K. Balasubramanian, "Theoretical studies of $UO_2(OH)(H_2O)^{n+}$, $UO_2(OH)_2(H_2O)n$, $NpO_2(OH)(H_2O)n$, and $PuO_2(OH)(H_2O)^{n+}$ (n≤21) complexes in aqueous solution," *J. Chem. Phys.*, vol. 131, no. 16, p. 164504, 2009.

(240) X. Cao and M. Dolg, "Density functional studies on lanthanide (III) texaphyrins (Ln-Tex^{2+} , Ln = La, Gd, Lu): structure, stability and electronic excitation spectrum," *Mol. Phys.*, vol. 101, no. 15, pp. 2427–2435, Aug. 2003.

(241) M. Bühl and G. Schreckenbach, "Oxygen Exchange in Uranyl Hydroxide via Two

'Nonclassical' Ions," *Inorg. Chem.*, vol. 49, no. 8, pp. 3821–3827, Apr. 2010.

(242) K. Matthias, "On the ground state electronic structure of uranium dioxide," *Phys. Scr.*, vol. 90, no. 9, p. 94014, 2015.

(243) J. Rabone and M. Krack, "A procedure for bypassing metastable states in local basis set DFT+U calculations and its application to uranium dioxide surfaces," *Comput. Mater. Sci.*, vol. 71, pp. 157–164, 2013.

(244) B. Dorado, M. Freyss, B. Amadon, M. Bertolus, G. Jomard, and P. Garcia, "Advances in first-principles modelling of point defects in UO_2 : f electron correlations and the issue of local energy minima," *J. Phys. Condens. Matter*, vol. 25, no. 33, p. 333201, Aug. 2013.

(245) S. L. Dudarev, G. A. Botton, S. Y. Savrasov, Z. Szotek, W. M. Temmerman, and A. P. Sutton, "Electronic Structure and Elastic Properties of Strongly Correlated Metal Oxides from First Principles: LSDA + U, SIC-LSDA and EELS Study of UO_2 and NiO," *Phys. status solidi*, vol. 166, no. 1, pp. 429–443, Mar. 1998.

(246) A. Kotani and T. Yamazaki, "Systematic Analysis of Core Photoemission Spectra for Actinide Di-Oxides and Rare-Earth Sesqui-Oxides," *Prog. Theor. Phys. Suppl.*, vol. 108, pp. 117–131, Feb. 1992.

(247) M. Bühl, H. Kabrede, R. Diss, and G. Wipff, "Effect of hydration on coordination properties of uranyl(VI) complexes. A first-principles molecular dynamics study," *J. Am. Chem. Soc.*, vol. 128, no. 19, pp. 6357–6368, 2006.

(248) S. Ramos, G. W. Neilson, A. C. Barnes, and P. Buchanan, "An anomalous x-ray diffraction study of the hydration structures of Cs^+ and I^- in concentrated solutions," *J. Chem. Phys.*, vol. 123, no. 21, p. 214501, Dec. 2005.

(249) S. Ansell, A. C. Barnes, P. E. Mason, G. W. Neilson, and S. Ramos, "X-ray and neutron scattering studies of the hydration structure of alkali ions in concentrated aqueous solutions," *Biophys. Chem.*, vol. 124, no. 3, pp. 171–179, Dec. 2006.

(250) R. M. Lawrence and R. F. Kruh, "X-Ray Diffraction Studies of Aqueous Alkali-Metal Halide Solutions," *J. Chem. Phys.*, vol. 47, no. 11, pp. 4758–4765, Dec. 1967.

(251) Y. Tamura, I. Okada, H. Ohtaki, and T. Yamaguchi, "An X-Ray Diffraction Study on the Structure of Concentrated Aqueous Caesium Iodide and Lithium Iodide Solutions," *Zeitschrift für Naturforsch. A*, vol. 42, no. 4, pp. 367–376, Jan. 1987.

(252) G. Pálinkás, T. Radnai, and F. Hajdu, "Ion-Solvent and Solvent-Solvent Interactions. X-ray Study of Aqueous Alkali Chloride Solutions," *Zeitschrift für Naturforsch. A*, vol. 35, no. 1, Jan. 1980.

(253) P. R. Smirnov and V. N. Trostin, "Structures of the nearest surroundings of the K^+, Rb^+, and Cs^+ ions in aqueous solutions of their salts," *Russ. J. Gen. Chem.*, vol. 77, no. 12, pp. 2101–2107, Dec. 2007.

(254) J. Mähler and I. Persson, "A Study of the Hydration of the Alkali Metal Ions in Aqueous Solution," *Inorg. Chem.*, vol. 51, no. 1, pp. 425–438, Jan. 2012.

(255) Z. Yongquan, S. Yoshie, Y. Toshio, F. Yan, and F. Chunhui, "Structure of Aqueous RbCl and CsCl Solutions Using X-Ray Scattering and Empirical Potential Structure Refinement Modelling," *ACTA PHYSICO-CHIMICA Sin.*, vol. 34, no. 5, pp. 483–491, 2018.

(256) A. G. Novikov, M. N. Rodnikova, V. V. Savostin, and O. V. Sobolev, "The study of hydration effects in aqueous solutions of LiCl and CsCl by inelastic neutron scattering,"

J. Mol. Liq., vol. 82, no. 1–2, pp. 83–104, Sep. 1999.

(257) N. Ohtomo and K. Arakawa, "Neutron Diffraction Study of Aqueous Ionic Solutions. I. Aqueous Solutions of Lithium Chloride and Caesium Chloride," *Bull. Chem. Soc. Jpn.*, vol. 52, no. 10, pp. 2755–2759, Oct. 1979.

(258) V. I. Chizhik, V. I. Mikhailov, and P. C. Su, "NMR relaxation data on the microstructure of aqueous solutions of alkali-metal salts and hydroxides," *Theor. Exp. Chem.*, vol. 22, no. 4, pp. 480–483, 1987.

(259) M. Kołaski, H. M. Lee, Y. C. Choi, K. S. Kim, P. Tarakeshwar, D. J. Miller, and J. M. Lisy, "Structures, energetics, and spectra of aqua-cesium (I) complexes: An ab initio and experimental study," *J. Chem. Phys.*, vol. 126, no. 7, p. 074302, Feb. 2007.

(260) D. Z. Caralampio, J. M. Martínez, R. R. Pappalardo, and E. S. Marcos, "The hydration structure of the heavy-alkalines Rb^+ and Cs^+ through molecular dynamics and X-ray absorption spectroscopy: surface clusters and eccentricity," *Phys. Chem. Chem. Phys.*, vol. 19, no. 42, pp. 28993–29004, 2017.

(261) C. F. Schwenk, T. S. Hofer, and B. M. Rode, "'Structure breaking' effect of hydrated Cs^+," *J. Phys. Chem. A*, vol. 108, no. 9, pp. 1509–1514, 2004.

(262) S. Deublein, J. Vrabec, and H. Hasse, "A set of molecular models for alkali and halide ions in aqueous solution," *J. Chem. Phys.*, vol. 136, no. 8, 2012.

(263) G. Lamoureux and B. Roux, "Absolute hydration free energy scale for alkali and halide ions established from simulations with a polarizable force field," *J. Phys. Chem. B*, vol. 110, no. 7, pp. 3308–3322, 2006.

(264) S. H. Lee and J. C. Rasaiah, "Molecular dynamics simulation of ionic mobility. I. Alkali metal cations in water at 25 °C," *J. Chem. Phys.*, vol. 101, no. 8, pp. 6964–6974, 1994.

(265) V. Mile, O. Gereben, S. Kohara, and L. Pusztai, "On the structure of aqueous cesium bromide solutions: Diffraction experiments, molecular dynamics simulations and Reverse Monte Carlo modeling," *J. Mol. Liq.*, vol. 157, no. 1, pp. 36–42, 2010.

(266) Y. Tamura, H. Ohtaki, and I. Okada, "An MD Simulation of Concentrated Aqueous Solutions of Caesium Iodide," *Zeitschrift für Naturforsch. A*, vol. 46, no. 12, Jan. 1991.

(267) T. Ikeda and M. Boero, "Communication: Hydration structure and polarization of heavy alkali ions: A first principles molecular dynamics study of Rb + and Cs +," *J. Chem. Phys.*, vol. 137, no. 4, p. 041101, Jul. 2012.

(268) R. L. Kuczkowski, D. R. Lide, and L. C. Krisher, "Microwave spectra of alkali hydroxides: Evidence for linearity of CsOH and KOH," *J. Chem. Phys.*, vol. 44, no. 8, pp. 3131–3132, 1966.

(269) D. R. Lide and R. L. Kuczkowski, "Structure of the alkali hydroxides. I. Microwave spectrum of gaseous CsOH," *J. Chem. Phys.*, vol. 46, no. 12, pp. 4768–4774, 1967.

(270) M.-A. D. Stiakaki, A. C. Tsipis, C. A. Tsipis, and C. E. Xanthopoulos, "Molecular geometries and energetics of metal-containing systems using an improved ASED-MO model: a systematic test to group 1 and 2 metal containing systems in the gas phase," *Chem. Phys.*, vol. 189, no. 3, pp. 533–555, Dec. 1994.

(271) E. P. F. Lee and T. G. Wright, "Theoretical study of RbOH, CsOH, FrOH, and their cations: Geometrics, vibrational frequencies, and the ionization energies," *J. Phys. Chem. A*, vol. 107, no. 26, pp. 5233–5240, 2003.

(272) C. W. Bauschlicher, S. R. Langhoff, and H. Partridge, “A b initio study of the alkali and alkaline-earth monohydroxides,” *J. Chem. Phys.*, vol. 84, no. 2, pp. 901–909, Jan. 1986.

(273) R. D. Brown, P. D. Godfrey, B. Kleibömer, and D. McNaughton, “Structures and flexibilities of the alkali hydroxides,” *J. Mol. Struct.*, vol. 327, no. 1, pp. 99–106, 1994.

(274) S. Odde, C. Pak, H. M. Lee, K. S. Kim, and B. J. Mhin, “Aqua dissociation nature of cesium hydroxide,” *J. Chem. Phys.*, vol. 121, no. 1, p. 204, 2004.

(275) P. Dangelo, A. Zitolo, V. Migliorati, G. Chillemi, M. Duvail, P. Vitorge, S. Abadie, and R. Spezia, “Revised ionic radii of lanthanoid(III) ions in aqueous solution,” *Inorg. Chem.*, vol. 50, no. 10, pp. 4572–4579, 2011.

(276) P. G. Allen, J. J. Bucher, D. K. Shuh, N. M. Edelstein, and I. Craig, “Coordination Chemistry of Trivalent Lanthanide and Actinide Ions in Dilute and Concentrated Chloride Solutions,” *Inorg. Chem.*, vol. 39, no. 3, pp. 595–601, Feb. 2000.

(277) S. Ishiguro, Y. Umebayashi, and M. Komiya, “Thermodynamic and structural aspects on the solvation steric effect of lanthanide(III)—dependence on the ionic size,” *Coord. Chem. Rev.*, vol. 226, no. 1–2, pp. 103–111, Mar. 2002.

(278) I. Persson, P. D’Angelo, S. De Panfilis, M. Sandström, and L. Eriksson, “Hydration of lanthanoid(III) ions in aqueous solution and crystalline hydrates studied by EXAFS spectroscopy and crystallography: The myth of the ‘gadolinium break,’” *Chem. - A Eur. J.*, vol. 14, no. 10, pp. 3056–3066, 2008.

(279) J. A. Solera, J. García, and M. G. Proietti, “Multielectron excitations at the L edges in rare-earth ionic aqueous solutions,” *Phys. Rev. B*, vol. 51, no. 5, pp. 2678–2686, 1995.

(280) P. D’Angelo, S. De Panfilis, A. Filipponi, and I. Persson, “High-Energy X-ray Absorption Spectroscopy: A New Tool for Structural Investigations of Lanthanoids and Third-Row Transition Elements,” *Chem. - A Eur. J.*, vol. 14, no. 10, pp. 3045–3055, Mar. 2008.

(281) J. Näslund, P. Lindqvist-Reis, I. Persson, and M. Sandström, “Steric Effects Control the Structure of the Solvated Lanthanum(III) Ion in Aqueous, Dimethyl Sulfoxide, and N , N ‘-Dimethylpropyleneurea Solution. An EXAFS and Large-Angle X-ray Scattering Study,” *Inorg. Chem.*, vol. 39, no. 18, pp. 4006–4011, Sep. 2000.

(282) A. Habenschuss and F. H. Spedding, “The coordination (hydration) of rare earth ions in aqueous chloride solutions from x-ray diffraction. II. $LaCl_3$, $PrCl_3$, and $NdCl_3$ a),” *J. Chem. Phys.*, vol. 70, no. 8, pp. 3758–3763, 1979.

(283) L. S. Smith and D. L. Wertz, “Solute Structuring in Aqueous Lanthanum(III) Chloride Solutions,” *J. Am. Chem. Soc.*, vol. 97, no. 9, pp. 2365–2368, 1975.

(284) L. S. Smith and D. L. Wertz, “On the coordination of La^{3+} in aqueous $LaBr_3$ solutions,” *J. Inorg. Nucl. Chem.*, vol. 39, no. 1, pp. 95–98, Jan. 1977.

(285) M. A. Marques, M. I. Cabaço, M. I. De Barros Marques, A. M. Gaspar, and C. M. De Morais, “Local order in aqueous solutions of lanthanum chloride and bromide by x-ray diffraction, EXAFS and raman spectroscopy,” *J. Phys. Condens. Matter*, vol. 13, no. 20, pp. 4367–4385, 2001.

(286) S. Díaz-Moreno, S. Ramos, and D. T. Bowron, “Solvation structure and ion complexation of La^{3+} in a 1 molal aqueous solution of lanthanum chloride,” *J. Phys. Chem. A*, vol. 115, no. 24, pp. 6575–6581, 2011.

(287) W. W. Rudolph and G. Irmer, “Raman spectroscopic characterization of light rare earth

ions: La^{3+} , Ce^{3+} , Pr^{3+} , Nd^{3+} and Sm^{3+} – hydration and ion pair formation," *Dalt. Trans.*, vol. 46, no. 13, pp. 4235–4244, 2017.

(288) G. Johansson and H. Wakita, "X-ray investigation of the coordination and complex formation of lanthanoid ions in aqueous perchlorate and selenate solutions," *Inorg. Chem.*, vol. 24, no. 19, pp. 3047–3052, Sep. 1985.

(289) M. Duvail, P. D'Angelo, M.-P. Gaigeot, P. Vitorge, and R. Spezia, "What first principles molecular dynamics can tell us about EXAFS spectroscopy of radioactive heavy metal cations in water," *Radiochim. Acta*, vol. 97, no. 7, pp. 339–346, Jan. 2009.

(290) V. Migliorati, A. Serva, F. Sessa, A. Lapi, and P. D'Angelo, "Influence of Counterions on the Hydration Structure of Lanthanide Ions in Dilute Aqueous Solutions," *J. Phys. Chem. B*, vol. 122, no. 10, pp. 2779–2791, 2018.

(291) W. W. Rudolph and G. Irmer, "Hydration and ion pair formation in common aqueous La(III) salt solutions – a Raman scattering and DFT study," *Dalt. Trans.*, vol. 44, no. 1, pp. 295–305, 2015.

(292) M. Montagna, R. Spezia, and E. Bodo, "Structural and energetic properties of La^{3+} in water/DMSO mixtures," *J. Mol. Struct.*, vol. 1148, pp. 381–387, 2017.

(293) T. Ikeda, M. Hirata, and T. Kimura, "Hydration structure of Y^{3+} and La^{3+} compared: an application of metadynamics.," *J. Chem. Phys.*, vol. 122, no. 24, p. 244507, 2005.

(294) V. Buzko, I. Sukhno, and M. Buzko, "Ab initio and DFT study of Lu^{3+}hydration," *J. Mol. Struct. THEOCHEM*, vol. 894, no. 1–3, pp. 75–79, 2009.

(295) W. Meier, P. Bopp, M. M. Probst, E. Spohr, and J. L. Lin, "Molecular dynamics studies of lanthanum chloride solutions," *J. Phys. Chem.*, vol. 94, no. 11, pp. 4672–4682, 1990.

(296) T. S. Hofer, H. Scharnagl, B. R. Randolf, and B. M. Rode, "Structure and dynamics of La(III) in aqueous solution - An ab initio QM/MM MD approach," *Chem. Phys.*, vol. 327, no. 1, pp. 31–42, 2006.

(297) T. Fujiwara, H. Mori, Y. Mochizuki, H. Tatewaki, and E. Miyoshi, "Theoretical study of hydration models of trivalent rare-earth ions using model core potentials," *J. Mol. Struct. THEOCHEM*, vol. 949, no. 1–3, pp. 28–35, 2010.

(298) C. Terrier, P. Vitorge, M.-P. Gaigeot, R. Spezia, and R. Vuilleumier, "Density functional theory based molecular dynamics study of hydration and electronic properties of aqueous La^{3+}," *J. Chem. Phys.*, vol. 133, no. 4, p. 044509, 2010.

(299) E. Brücher, J. Glaser, I. Grenthe, and I. Puigdomènech, "On the hydration of the lutetium(III) Ion in water acetone mixtures. A ^{1}H and ^{35}Cl NMR study," *Inorganica Chim. Acta*, vol. 109, no. 2, pp. 111–116, Mar. 1985.

(300) A. Munoz-Paez, M. D. Alba, M. A. Castro, R. Alvero, and J. M. Trillo, "Geometric structures of lanthanide ions within layered clays as determined by EXAFS. From the Lu(III) hydrate to the disilicate," *J. Phys. Chem.*, vol. 98, no. 39, pp. 9850–9860, 1994.

(301) T. Yamaguchi, M. Nomura, H. Wakita, and H. Ohtaki, "An extended x-ray absorption fine structure study of aqueous rare earth perchlorate solutions in liquid and glassy states," *J. Chem. Phys.*, vol. 89, no. 8, pp. 5153–5159, 1988.

(302) P. D'Angelo, A. Zitolo, V. Migliorati, and I. Persson, "Analysis of the detailed configuration of hydrated lanthanoid(III) ions in aqueous solution and crystalline salts by using K- And L3-edge XANES spectroscopy," *Chem. - A Eur. J.*, vol. 16, no. 2, pp. 684–

692, 2010.

(303) A. E. Clark, “Density Functional and Basis Set Dependence of Hydrated Ln(III) Properties,” *J. Chem. Theory Comput.*, vol. 4, no. 5, pp. 708–718, May 2008.

(304) S. Hengrasmee and M. M. Probst, “A Study of Hydrated Rare Earth Ions,” *Zeitschrift für Naturforsch. A*, vol. 46, no. 1–2, pp. 0–4, Jan. 1991.

(305) J. Zhang, N. Heinz, and M. Dolg, “Understanding Lanthanoid(III) Hydration Structure and Kinetics by Insights from Energies and Wave functions,” *Inorg. Chem.*, vol. 53, no. 14, pp. 7700–7708, Jul. 2014.

(306) J. Ciupka, X. Cao-Dolg, J. Wiebke, and M. Dolg, “Computational study of lanthanide(III) hydration,” *Phys. Chem. Chem. Phys.*, vol. 12, no. 40, p. 13215, 2010.

(307) J. Kuta and A. E. Clark, “Trends in aqueous hydration across the 4f period assessed by reliable computational methods,” *Inorg. Chem.*, vol. 49, no. 17, pp. 7808–7817, 2010.

(308) B. P. Hay, “Extension of Molecular Mechanics to High-Coordinate Metal Complexes. Calculation of the Structures of Aqua and Nitrato Complexes of Lanthanide(III) Metal Ions,” *Inorg. Chem.*, vol. 30, no. 14, pp. 2876–2884, 1991.

(309) M. Duvail, P. Vitorge, and R. Spezia, “Building a polarizable pair interaction potential for lanthanoids(III) in liquid water: A molecular dynamics study of structure and dynamics of the whole series,” *J. Chem. Phys.*, vol. 130, no. 10, p. 104501, Mar. 2009.

(310) F. Sessa, R. Spezia, and P. D’Angelo, “Lutetium(III) aqua ion: On the dynamical structure of the heaviest lanthanoid hydration complex,” *J. Chem. Phys.*, vol. 144, no. 20, p. 204505, May 2016.

(311) K. Miyakawa, Y. Kaizu, and H. Kobayashi, “An electrostatic approach to the structure of hydrated lanthanoid ions. $[M(OH_2)_9]^{3+}$ versus$[M(OH_2)8]^{3+}$,” *J. Chem. Soc. Faraday Trans. 1 Phys. Chem. Condens. Phases*, vol. 84, no. 5, pp. 1517–1529, 1988.

(312) F. Jollet, G. Jomard, B. Amadon, J. P. Crocombette, and D. Torumba, “Hybrid functional for correlated electrons in the projector augmented-wave formalism: Study of multiple minima for actinide oxides,” *Phys. Rev. B - Condens. Matter Mater. Phys.*, vol. 80, no. 23, pp. 1–8, 2009.

(313) M. C. Stennett, C. L. Corkhill, L. A. Marshall, and N. C. Hyatt, “Preparation, characterisation and dissolution of a CeO_2 analogue for UO_2 nuclear fuel,” *J. Nucl. Mater.*, vol. 432, no. 1–3, pp. 182–188, 2013.

(314) C. L. Corkhill, E. Myllykylä, D. J. Bailey, S. M. Thornber, J. Qi, P. Maldonado, M. C. Stennett, A. Hamilton, and N. C. Hyatt, “Contribution of energetically reactive surface features to the dissolution of CeO_2 and ThO_2 analogues for spent nuclear fuel microstructures,” *ACS Appl. Mater. Interfaces*, vol. 6, no. 15, pp. 12279–12289, 2014.

(315) C. L. Corkhill, D. J. Bailey, F. Y. Tocino, M. C. Stennett, J. A. Miller, J. L. Provis, K. P. Travis, and N. C. Hyatt, “Role of Microstructure and Surface Defects on the Dissolution Kinetics of CeO_2, a UO_2 Fuel Analogue,” *ACS Appl. Mater. Interfaces*, vol. 8, no. 16, pp. 10562–10571, 2016.

(316) J. Roleček, Š. Foral, K. Katovský, and D. Salamon, “A feasibility study of using CeO_2 as a surrogate material during the investigation of UO_2 thermal conductivity enhancement,” *Adv. Appl. Ceram.*, vol. 116, no. 3, pp. 123–131, 2017.

(317) S. Fernandez, M. I. Nieto, J. Cobos, and R. Moreno, “CeO_2 pellet fabrication as spent

fuel matrix analogue," *J. Eur. Ceram. Soc.*, vol. 36, no. 14, pp. 3505–3512, 2016.

(318) A. T. Nelson, D. R. Rittman, J. T. White, J. T. Dunwoody, M. Kato, and K. J. McClellan, "An Evaluation of the Thermophysical Properties of Stoichiometric CeO_2 in Comparison to UO_2 and PuO_2," *J. Am. Ceram. Soc.*, vol. 97, no. 11, pp. 3652–3659, 2014.

(319) S. Fabris, S. de Gironcoli, S. Baroni, G. Vicario, and G. Balducci, "Taming multiple valency with density functionals: A case study of defective ceria," *Phys. Rev. B*, vol. 71, no. 4, p. 041102, Jan. 2005.

(320) B. D. Shannon, M. H, N. H. Baur, O. H. Gibbs, M. Eu, and V. Cu, "Revised Effective Ionic Radii and Systematic Studies of Interatomie Distances in Halides and Chaleogenides Central Research and Development Department , Experimental Station , E . L Du Pont de Nemours The effective ionic radii of Shannon & Prewitt Acta," 1976.

(321) L. Lynds, W. A. Young, J. S. Mohl, and G. G. Libowitz, "X-Ray and Density Study of Nonstoichiometry in Uranium Oxides," 1963, pp. 58–65.

(322) K. K. Babitha, A. Sreedevi, K. P. Priyanka, B. Sabu, and T. Varghese, "Structural characterization and optical studies of CeO_2 nanoparticles synthesized by chemical precipitation," *Indian J. Pure Appl. Phys.*, vol. 53, no. September, pp. 596–603, 2015.

(323) P. Villars, "CeO2 Crystal Structure: Datasheet from 'PAULING FILE Multinaries Edition – 2012,'" 2016. [Online]. Available: https://materials.springer.com/isp/crystallographic/docs/sd_1923902.

(324) P. Villars, "UO2 Crystal Structure: Datasheet from 'PAULING FILE Multinaries Edition – 2012,'" 2016. [Online]. Available: https://materials.springer.com/isp/crystallographic/docs/sd_0456101.

(325) Z. Yang, T. K. Woo, and K. Hermansson, "Strong and weak adsorption of CO on CeO_2 surfaces from first principles calculations," *Chem. Phys. Lett.*, vol. 396, no. 4–6, pp. 384–392, 2004.

(326) J. Paier, C. Penschke, and J. Sauer, "Oxygen Defects and Surface Chemistry of Ceria: Quantum Chemical Studies Compared to Experiment," *Chem. Rev.*, vol. 113, no. 6, pp. 3949–3985, Jun. 2013.

(327) D. R. Mullins, "The surface chemistry of cerium oxide," *Surf. Sci. Rep.*, vol. 70, no. 1, pp. 42–85, 2015.

(328) J. A. Farmer, J. H. Baricuatro, and C. T. Campbell, "Ag Adsorption on Reduced CeO_2 (111) Thin Films," *J. Phys. Chem. C*, vol. 114, no. 40, pp. 17166–17172, Oct. 2010.

(329) M. M. Branda, N. C. Hernández, J. F. Sanz, and F. Illas, "Density Functional Theory Study of the Interaction of Cu, Ag, and Au Atoms with the Regular CeO_2(111) Surface," *J. Phys. Chem. C*, vol. 114, no. 4, pp. 1934–1941, Feb. 2010.

(330) M. Baron, O. Bondarchuk, D. Stacchiola, S. Shaikhutdinov, and H.-J. Freund, "Interaction of Gold with Cerium Oxide Supports: CeO_2(111) Thin Films vs CeO x Nanoparticles," *J. Phys. Chem. C*, vol. 113, no. 15, pp. 6042–6049, Apr. 2009.

(331) N. J. Castellani, M. M. Branda, K. M. Neyman, and F. Illas, "Density Functional Theory Study of the Adsorption of Au Atom on Cerium Oxide: Effect of Low-Coordinated Surface Sites," *J. Phys. Chem. C*, vol. 113, no. 12, pp. 4948–4954, Mar. 2009.

(332) Z. P. Liu, S. J. Jenkins, and D. A. King, "Origin and activity of oxidized gold in water-gas-shift catalysis," *Phys. Rev. Lett.*, vol. 94, no. 19, pp. 1–4, 2005.

(333) C. Zhang, A. Michaelides, D. A. King, and S. J. Jenkins, “Structure of gold atoms on stoichiometric and defective ceria surfaces,” *J. Chem. Phys.*, vol. 129, no. 19, p. 194708, Nov. 2008.

(334) M. Škoda, M. Cabala, I. Matolínová, K. C. Prince, T. Skála, F. Šutara, K. Veltruská, and V. Matolín, “Interaction of Au with CeO_2(111): A photoemission study,” *J. Chem. Phys.*, vol. 130, no. 3, p. 034703, Jan. 2009.

(335) M. M. Branda, N. J. Castellani, R. Grau-Crespo, N. H. de Leeuw, N. C. Hernandez, J. F. Sanz, K. M. Neyman, and F. Illas, “On the difficulties of present theoretical models to predict the oxidation state of atomic Au adsorbed on regular sites of CeO_2(111),” *J. Chem. Phys.*, vol. 131, no. 9, p. 094702, 2009.

(336) D. Tibiletti, A. A.- Fonseca, R. Burch, Y. Chen, J. M. Fisher, A. Goguet, C. Hardacre, P. Hu, and D. Thompsett, “DFT and In Situ EXAFS Investigation of Gold/Ceria−Zirconia Low-Temperature Water Gas Shift Catalysts: Identification of the Nature of the Active Form of Gold,” *J. Phys. Chem. B*, vol. 109, no. 47, pp. 22553–22559, Dec. 2005.

(337) A. Bruix, K. M. Neyman, and F. Illas, “Adsorption, Oxidation State, and Diffusion of Pt Atoms on the CeO_2(111) Surface,” *J. Phys. Chem. C*, vol. 114, no. 33, pp. 14202–14207, Aug. 2010.

(338) Y. Zhao, B. Teng, Z. Yang, Y. Zhao, L. Zhao, and M. Luo, “Density Functional Theory Study of Sn Adsorption on the CeO_2 Surface,” *J. Phys. Chem. C*, vol. 115, no. 33, pp. 16461–16466, Aug. 2011.

(339) J. Guzman, S. Carrettin, and A. Corma, “Spectroscopic evidence for the supply of reactive oxygen during CO oxidation catalyzed by gold supported on nanocrystalline CeO_2,” *J. Am. Chem. Soc.*, vol. 127, no. 10, pp. 3286–3287, 2005.

(340) Y. Zhou, N. J. Lawrence, L. Wang, L. Kong, T. S. Wu, J. Liu, Y. Gao, J. R. Brewer, V. K. Lawrence, R. F. Sabirianov, Y. L. Soo, X. C. Zeng, P. A. Dowben, W. N. Mei, and C. L. Cheung, “Resonant photoemission observations and DFT study of s-d hybridization in catalytically active gold clusters on ceria nanorods,” *Angew. Chemie - Int. Ed.*, vol. 52, no. 27, pp. 6936–6939, 2013.

(341) Z. Yang, Q. Wang, S. Wei, D. Ma, and Q. Sun, “The Effect of Environment on the Reaction of Water on the Ceria (111) Surface : A DFT+U Study,” *J. Phys. Chem. C*, no. 114, pp. 14891–14899, 2010.

(342) H. T. Chen, Y. M. Choi, M. Liu, and M. C. Lin, “A theoretical study of surface reduction mechanisms of CeO_2(111) and (110) by H_2,” *ChemPhysChem*, vol. 8, no. 6, pp. 849–855, 2007.

(343) M. Fronzi, S. Piccinin, B. Delley, E. Traversa, and C. Stampfl, “Water adsorption on the stoichiometric and reduced CeO_2(111) surface: A first-principles investigation,” *Phys. Chem. Chem. Phys.*, vol. 11, no. 40, pp. 9188–9199, 2009.

(344) M. Molinari, S. C. Parker, D. C. Sayle, and M. S. Islam, “Water adsorption and its effect on the stability of low index stoichiometric and reduced surfaces of ceria,” *J. Phys. Chem. C*, vol. 116, no. 12, pp. 7073–7082, 2012.

(345) S. Gritschneder and M. Reichling, “Structural elements of CeO_2(111) surfaces,” *Nanotechnology*, vol. 18, no. 4, p. 044024, Jan. 2007.

(346) S. Torbrügge, O. Custance, S. Morita, and M. Reichling, “Manipulation of individual water molecules on CeO_2(111),” *J. Phys. Condens. Matter*, vol. 24, no. 8, p. 084010, Feb.

2012.

(347) M. B. Watkins, A. S. Foster, and A. L. Shluger, “Hydrogen Cycle on CeO_2(111) Surfaces: Density Functional Theory Calculations,” *J. Phys. Chem. C*, vol. 111, no. 42, pp. 15337–15341, 2007.

(348) V. Matolín, I. Matolínová, F. Dvořák, V. Johánek, J. Mysliveček, K. C. Prince, T. Skála, O. Stetsovych, N. Tsud, M. Václavů, and B. Šmíd, “Water interaction with CeO_2(111)/Cu(111) model catalyst surface,” *Catal. Today*, vol. 181, no. 1, pp. 124–132, 2012.

(349) D. R. Mullins, P. M. Albrecht, T. L. Chen, F. C. Calaza, M. D. Biegalski, H. M. Christen, and S. H. Overbury, “Water dissociation on CeO_2(100) and CeO_2(111) thin films,” *J. Phys. Chem. C*, vol. 116, no. 36, pp. 19419–19428, 2012.

(350) D. Fernández-Torre, K. Kośmider, J. Carrasco, M. V. Ganduglia-Pirovano, and R. Pérez, “Insight into the adsorption of water on the clean CeO_2(111) surface with van der waals and hybrid density functionals,” *J. Phys. Chem. C*, vol. 116, no. 25, pp. 13584–13593, 2012.

(351) L. Gill, A. Beste, B. Chen, M. Li, A. K. P. Mann, S. H. Overbury, and E. W. Hagaman, “Fast MAS1H NMR Study of Water Adsorption and Dissociation on the (100) Surface of Ceria Nanocubes: A Fully Hydroxylated, Hydrophobic Ceria Surface,” *J. Phys. Chem. C*, vol. 121, no. 13, pp. 7450–7465, 2017.

(352) M. A. Henderson, C. L. Perkins, M. H. Engelhard, S. Thevuthasan, and C. H. F. Peden, “Redox properties of water on the oxidized and reduced surfaces of CeO_2(1 1 1),” *Surf. Sci.*, vol. 526, no. 1–2, pp. 1–18, 2003.

(353) B. Chen, Y. Ma, L. Ding, L. Xu, Z. Wu, Q. Yuan, and W. Huang, “Reactivity of hydroxyls and water on a CeO_2(111) thin film surface: The role of oxygen vacancy,” *J. Phys. Chem. C*, vol. 117, no. 11, pp. 5800–5810, 2013.

(354) C. T. Campbell and J. R. V Sellers, “Erratum: Enthalpies and entropies of adsorption on well-defined oxide surfaces: Experimental results (Chemical Reviews (2013) 113 (4106-4135) DOI:10.1021/cr300329s),” *Chem. Rev.*, vol. 113, no. 8, p. 6902, 2013.

(355) S. Kumar and P. K. Schelling, “Density functional theory study of water adsorption at reduced and stoichiometric ceria (111) surfaces,” *J. Chem. Phys.*, vol. 125, no. 20, p. 204704, Nov. 2006.

(356) J. Fan, B. Xu, J. Z. Zhao, and H. Xu, “Controllable dissociation of H_2O on a CeO_2(111) surface,” *Phys. Chem. Chem. Phys.*, vol. 20, no. 3, pp. 1575–1582, 2018.

(357) M. V. Ganduglia-Pirovano, J. L. F. Da Silva, and J. Sauer, “Density-functional calculations of the structure of near-surface oxygen vacancies and electron localization on CeO_2(111),” *Phys. Rev. Lett.*, vol. 102, no. 2, pp. 1–4, 2009.

(358) H. Y. Li, H. F. Wang, X. Q. Gong, Y. L. Guo, Y. Guo, G. Lu, and P. Hu, “Multiple configurations of the two excess 4*f* electrons on defective CeO_2(111): Origin and implications,” *Phys. Rev. B - Condens. Matter Mater. Phys.*, vol. 79, no. 19, pp. 2–5, 2009.

(359) C. Zhang, A. Michaelides, D. A. King, and S. J. Jenkins, “Oxygen vacancy clusters on ceria: Decisive role of cerium *f* electrons,” *Phys. Rev. B*, vol. 79, no. 7, p. 075433, Feb. 2009.

(360) H.-T. Chen, J.-G. Chang, H.-L. Chen, and S.-P. Ju, “Identifying the O_2 diffusion and

reduction mechanisms on CeO_2 electrolyte in solid oxide fuel cells: A DFT+U study," *J. Comput. Chem.*, vol. 30, no. 15, pp. 2433–2442, Nov. 2009.

(361) D. Marrocchelli and B. Yildiz, "First-principles assessment of H_2S and H_2O reaction mechanisms and the subsequent hydrogen absorption on the CeO 2(111) surface," *J. Phys. Chem. C*, vol. 116, no. 3, pp. 2411–2424, 2012.

(362) J. Chorover, S. Choi, P. Rotenberg, R. J. Serne, N. Rivera, C. Strepka, A. Thompson, K. T. Mueller, and P. A. O'Day, "Silicon control of strontium and cesium partitioning in hydroxide-weathered sediments," *Geochim. Cosmochim. Acta*, vol. 72, no. 8, pp. 2024–2047, Apr. 2008.

(363) N. Sahai, S. a. Carroll, S. Roberts, and P. a. O'Day, "X-Ray Absorption Spectroscopy of Strontium(II) Coordination," *J. Colloid Interface Sci.*, vol. 222, no. 2, pp. 198–212, 2000.

(364) R. Rahnemaie, T. Hiemstra, and W. H. van Riemsdijk, "Inner- and outer-sphere complexation of ions at the goethite–solution interface," *J. Colloid Interface Sci.*, vol. 297, no. 2, pp. 379–388, May 2006.

(365) R. H. Parkman, J. M. Charnock, F. R. Livens, and D. J. Vaughan, "A study of the interaction of strontium ions in aqueous solution with the surfaces of calcite and kaolinite," *Geochim. Cosmochim. Acta*, vol. 62, no. 9, pp. 1481–1492, 1998.

(366) C. L. Thorpe, J. R. Lloyd, G. T. W. Law, I. T. Burke, S. Shaw, N. D. Bryan, and K. Morris, "Strontium sorption and precipitation behaviour during bioreduction in nitrate impacted sediments," *Chem. Geol.*, vol. 306–307, pp. 114–122, 2012.

(367) S. Forsberg, K. Rosén, and F. Bréchignac, "Chemical availability of ^{137}Cs and ^{90}Sr in undisturbed lysimeter soils maintained under controlled and close-to-real conditions," *J. Environ. Radioact.*, vol. 54, no. 2, pp. 253–265, Jan. 2001.

(368) E. Makkos, "Computational investigations of the speciation of Sr^{2+} in aqueous solution, and its interactions with the hydrated brucite (0001) surface," University College London, 2017.

(369) H. Ashworth, L. Abrahamsen-Mills, N. Bryan, L. Foster, J. R. Lloyd, S. Kellet, and S. Heath, "Effect of humic acid & bacterial exudates on sorption–desorption interactions of 90 Sr with brucite," *Environ. Sci. Process. Impacts*, vol. 20, no. 6, pp. 956–964, 2018.

(370) Y.-G. Wang, D. Mei, J. Li, and R. Rousseau, "DFT+U Study on the Localized Electronic States and Their Potential Role During H_2O Dissociation and CO Oxidation Processes on CeO 2 (111) Surface," *J. Phys. Chem. C*, vol. 117, no. 44, pp. 23082–23089, Nov. 2013.

(371) Y.-G. Wang, D. Mei, V.-A. Glezakou, J. Li, and R. Rousseau, "Dynamic formation of single-atom catalytic active sites on ceria-supported gold nanoparticles," *Nat Commun*, vol. 6, p. 6511, 2015.

(372) J.-H. Lan, W.-Q. Shi, L.-Y. Yuan, J. Li, Y.-L. Zhao, and Z.-F. Chai, "Recent advances in computational modeling and simulations on the An(III)/Ln(III) separation process," *Coord. Chem. Rev.*, vol. 256, no. 13–14, pp. 1406–1417, Jul. 2012.

(373) Y. Jiang, J. B. Adams, and M. van Schilfgaarde, "Density-functional calculation of CeO2 surfaces and prediction of effects of oxygen partial pressure and temperature on stabilities.," *J. Chem. Phys.*, vol. 123, no. 6, p. 64701, 2005.

(374) Z. Yang, X. Yu, Z. Lu, S. Li, and K. Hermansson, "Oxygen vacancy pairs on CeO2(110): A DFT + U study," *Phys. Lett. Sect. A Gen. At. Solid State Phys.*, vol. 373, no. 31, pp. 2786–

2792, 2009.

(375) G. Carchini, M. García-Melchor, Z. Łodziana, and N. López, “Understanding and Tuning the Intrinsic Hydrophobicity of Rare-Earth Oxides: A DFT+U Study,” *ACS Appl. Mater. Interfaces*, vol. 8, no. 1, pp. 152–160, 2016.

(376) A. Kerridge and N. Kaltsoyannis, “Theoretical studies of the surface complexation of strontium hydrates with brucite,” *Proc. Diam. 2011 Conf. Coventry*.